Université du Québec
Institut National de la Recherche Scientifique
Énergie, Matériaux et Télécommunications

MORPHOLOGY CONTROL AND PHOTOVOLTAIC PERFORMANCE ENHANCEMENT FOR NON-FULLERENE BASED ORGANIC SOLAR CELLS

Par

Ting Yu

Thèse présentée pour l'obtention du grade de
Philosophiae doctor (Ph.D.)
en sciences de l'énergie et des matériaux

Jury d'évaluation

Président du jury et examinateur interne	Prof. Andreas Peter Ruediger INRS-EMT
Examinateur externe	Prof. Nianqiang (Nick) Wu University of Massachusetts Amherst
Examinateur externe	Prof. Zhifeng Ding Western University
Directeur de recherche	Prof. Dongling Ma INRS-EMT

ACKNOWLEDGEMENTS

I would like to express my most sincere gratitude to my supervisor, Prof. Dongling Ma, for providing me with a valuable opportunity to pursue my Ph.D. in her research group of INRS-EMT. She always gave me a warm, open, and rigorous research atmosphere. Meanwhile, throughout my research work, she gave me constant and excellent guidance, strong support, and constructive advice, which supports me to complete my research work. I learned a lot from her, especially her attitude toward academic research, which greatly inspired me to continue my research career.

Meanwhile, I would like to give my sincere acknowledgment to my collaborators, Prof. Izquierdo Ricardo and his students for kindly providing me with instruments and assistance for photovoltaic device fabrication, Prof. Gregory C. Welch and his students for providing me with non-fullerene materials and the characterization of indoor photovoltaic performance, Prof. Aycan Yurtsever and Prof. Quinn Qiao for providing me with advanced characterization instruments and data analysis. It is my pleasure to work with them. With the help of my collaborators, I am able to successfully complete my Ph.D. dissertation with the investigation of morphology optimization and photovoltaic performance enhancement, and thus successfully publish my research results.

I would like to appreciate Prof. Andreas Peter Ruediger at INRS-EMT, Prof. Nianqiang (Nick) Wu from University of Massachusetts Amherst and Prof. Zhifeng Ding from Western University to be my thesis defense jury members.

I am grateful to all group members for their significant help throughout my work in Prof. Ma's group, including Prof. Zhonglin Du, Dr. Pandeng Li, Dr. Yannan Liu, Dr. Fan Yang, Dr. Deepak Thrithamarassery Gangadharan, Dr. Qingzhe Zhang, Dr. Shenyun Huang, Dr. Cristina Rodriguez-Seco, Wanting He, Yong Wang, Chen Wang, Ruiqi Yang, Guolong Song, Sina Moradi, and Zahra Kalantari. Especially, I would like to thank Prof. Zhonglin Du for the synthesis of nanomaterials and related property characterization. Also, I really appreciate Wanting He for performing the advanced electron microscopy on the photoactive layer, and related simulation and calculation, which provides an effective way to understand the complex nanoscale morphology.

I am eternally grateful to my parents for their constant support and encouragement throughout all my studies. I would like to thank my dear husband Tianxu Wang, who loves me deeply and selflessly supports me in my study, work and life. When I encountered depression and pressure in

my research work, he always tried to help me get through the difficulties. Because of his love and support, I can move forward in my scientific research career without any worries.

ABSTRACT

As people become more aware of environmental protection, the replacement of non-renewable fossil fuels is imminent to alleviate the unsustainable consequences. Solar energy is a promising candidate as an alternative to meet the increasing energy demand, which can be converted to electricity through photovoltaic devices. In 1954, Bell laboratories successfully fabricated crystalline silicon (c-Si) solar cells for the first time, and achieved an efficiency of 6%, thus opening new horizons for photovoltaic technology to harness solar energy. After the development of first- and second-generation solar cells, c-Si solar cells have reached an efficiency of 26% and realized commercial and industrial production. However, the complicated manufacturing processes of Si and inorganic film solar cells, the high cost of raw materials, and the inherent limitations of inorganic materials limit the further use of solar energy. In order to address the above issues, third-generation solar cells have been widely developed, with organic solar cells (OSCs) being one of the most promising photovoltaic devices due to their significant advantages such as low cost, flexibility, lightweight, and simple manufacturing process. The best power conversion efficiency (PCE) of single-junction OSCs has now reached over 19% in the laboratory, making them more attractive than ever for possible commercial applications.

For decades, significant efforts have been made to enhance the photovoltaic performance of OSCs through the innovation of the device configuration and the development of materials in photoactive layers, interfacial layers, and electrodes. Researchers developed three main configurations for the enhancement of photovoltaic performance, including single-layer OSCs, bilayer OSCs and bulk heterojunction (BHJ) OSCs. Among them, BHJ-OSCs are considered to be the most efficient device structure because of the largely increased contact area between the donor and acceptor materials, which favors exciton dissociation and charge transport. Moreover, BHJ-OSC configurations can be further optimized by employing a ternary blend strategy, which endows the photovoltaic efficiency of over 19%. It's worth noting that the ideal morphology of the BHJ blend film with interpenetrating nanostructures, suitable phase separation and proper domain size is of vital importance for the achievement of state-of-the-art OSCs. The introduction of the guest components in ternary OSCs is a simple and effective approach to yield the desirable morphology. However, the ternary blend film with three components usually brings more complex morphology. Therefore, the morphology of ternary blend film requires to be characterized in depth, which helps

to optimize the device performance. In addition, while breakthroughs in photoactive layer materials have led to rapid improvements in device efficiency, the contribution of interface materials to device performance cannot be ignored. Appropriate interfacial materials can also optimize the surface morphology of the photoactive layer, enhance optical absorption, promote Ohmic contact, and tune work functions of electrodes. Accordingly, some researchers have dedicated to developing interfacial materials, which further enhance photovoltaic performance. Based on the above discussion, the following three parts in this thesis provide meaningful explorations.

In the first part, in order to achieve the high-efficient OSCs, we integrated highly air-stable perylene diimide (PDI) based non-fullerene material (PDI-DPP-PDI) into OSCs as the guest acceptor. These three components exhibited cascaded energy band structure and complimentary absorption, thus facilitating the increase of photovoltage and photocurrent. Besides, the morphology of the ternary blend film was optimized by adjusting the content of the PDI-DPP-PDI. The three-dimensional nanoscale morphology was characterized in depth by photo-induced force microscopy (PiFM) coupled with infrared laser spectroscopy and energy-filtered transmission electron microscopy (EF-TEM), which could qualitatively and quantitatively "view" the surface and cross-sectional morphology. The results provided strong evidence that the PDI-DPP-PDI guest acceptor could suppress the aggregation of the fullerene molecules and generate the homogenous morphology with a higher level of the molecularly mixed phase, thus preventing the charge recombination and stabilizing the morphology of the photoactive layer. This work represented very promising approaches to deeply explore the morphology of the ternary blend film, which contributes to achieving a stable device and simultaneously improved photovoltaic performance.

In the second part, we fabricated non-fullerene based ternary OSCs by incorporating the PDI-EH non-fullerene guest acceptor. The nearly orthogonal structure of the PDI-EH molecule was designed to suppress its aggregation. In addition to obtaining broadened spectral absorption and a well-matched energy band, the PDI-EH guest acceptor serves to adjust the miscibility of the blend film, facilitating the acquisition of 'ideal' morphology. Flory-Huggins interaction parameters and differential scanning calorimetry (DSC) measurements revealed that the PDI-EH guest acceptor was compatible with host donor and acceptor materials so that it could fine-tune the miscibility to form an optimally intermixed phase. Selective PiFM imaging of donor and acceptor materials suggested the formation of well-mixed films after the incorporation of PDI-EH. In addition,

grazing incidence wide-angle X-ray scattering (GIWAXS) measurements demonstrated that the PDI-EH could promote favorable molecular ordering, leading to effective charge transport. Lastly, the relationship between the optimized morphology and local charge carrier dynamics at the nanoscale was explored by a novel transient photo-response atomic force microscopy (TP-AFM) technique. The results demonstrated that the ternary blend film containing 10% PDI-EH showed reduced charge transport time, increased charge recombination lifetime and extended charge diffusion length, thus improving the performance of OSCs under 1-sun, and indoor 2700 K and 6500 K LED illuminations with efficiencies enhancement of 12%, 14% and 16%, respectively. This work offers insights into morphology modulation and the resulting charge carrier dynamics, thereby facilitating the development of OSCs.

In the third part, to further enhance the photovoltaic performance of non-fullerene-based OSCs for their practical applications, integrating plasmonic metallic nanoparticles as interfacial modifiers and sunlight concentrators offers an attractive pathway to optimize the surface morphology of the photoactive layer to reduce surface defects, improve sunlight capture to promote more photon harvesting, and increase interfacial contact to facilitate charge extraction. However, at present, this approach has not attracted enough attention in the field of non-fullerene OSCs. In this work, the facile polyelectrolyte polystyrene sulfonate (PSS)-coated plasmonic gold nanorods (named GNRs@PSS) were synthesized by Dr. Zhonglin Du. I firstly incorporated GNRs@PSS into the inverted non-fullerene OSCs as rear interfacial modifiers, which led to nearly 20% PCE enhancement due to the dramatically increased photocurrent. It was found that GNRs could improve sunlight absorption and exciton generation via the near-field plasmonic and back scattering effects. The electric field distribution of individual GNRs was measured by PiFM measurements under tunable laser irradiation to reveal the surface plasmon resonance (SPR) effect. Meanwhile, advanced EF-TEM measurements exhibited that the PSS organic shell was uniformly coated on the surface of GNRs with a thickness of ~2.2 nm. This ultrathin surface organic layer not only ensured the strong SPR effect but also prevented direct contact between the GNRs and the photoactive layer. As a result, the integration of plasmonic GNRs@PSS contributed to sunlight absorption, surface morphology optimization, and interfacial contact, leading to an enhancement of photovoltaic performance.

CONTENTS

LIST OF FIGURES

LIST OF CHEMICAL COMPOUNDS, ABBREVIATIONS AND SYMBOLS

Chemical Compounds

$Zn(CH_3COO)_2 \cdot 2H_2O$	Zinc acetate dehydrate
$NH_2CH_2CH_2OH$	Ethanolamine
ZnO	Zinc oxide
$CH_3OCH_2CH_2OH$	2-methoxyethanol
MoO_3	Molybdenum oxide
Ag	Silver
LiF	Lithium fluoride
Au	Gold
ITO	Indium tin oxide
PEDOT: PSS	poly(3,4-ethylenedioxythiophene): polystyrene sulfonate
CB	Chlorobenzene
DIO	1,8-diiodooctane
PTB7	Poly [[4,8-bis[(2-ethylhexyl)oxy]benzo[1,2-b:4,5-b']dithiophene-2,6-diyl][3-fluoro-2-[(2-ethylhexyl)carbonyl]thieno[3,4-b]thiophenediyl]]
$PC_{61}BM$	[6,6]-Phenyl-C61-butyric acid methyl ester
PBDB-T	Poly[(2,6-(4,8-bis(5-(2-ethylhexyl)thiophen-2-yl)-benzo[1,2-b:4,5-b']dithiophene))-alt-(5,5-(1',3'-di-2-thienyl-5',7'-bis(2-ethylhexyl)benzo[1',2'-c:4',5'-c']dithiophene-4,8-dione)]
ITIC-4F/ITIC-2F	3,9-bis(2-methylene-((3-(1,1-dicyanomethylene)-6,7-difluoro)-indanone))-5,5,11,11-tetrakis(4-hexylphenyl)-dithieno[2,3-d:2',3'-d']-s-indaceno[1,2-b:5,6-b'] dithiophene
$HAuCl_4 \cdot H_2O$	Gold (III) chloride trihydrate
$NaBH_4$	Sodium borohydride
CTAB	Cetyltrimethylammonium bromide
ITO	Indium tin oxide
PSS	Polystyrene sulfonate

Abbreviations

OSCs	Organic solar cells
iOSCs	Indoor organic solar cells
BHJ	Bulk heterojunction

NFAs	Non-fullerene acceptors
AM	Air mass
EQE	External quantum efficiency
HOMO	Highest occupied molecular orbital
LUMO	Lowest unoccupied molecular orbital
J-V	Current density versus voltage
AFM	Atomic force microscopy
C-AFM	Current sensing atomic force microscopy
PiFM	Photo-induced force microscopy
EF-TEM	Energy-filtered transmission electron microscopy
TEM	Transmission electron microscope
EELS	Electron energy loss spectroscopy
FIB	Focused ion beam
TP-AFM	Transient photo-response atomic force microscopy
TPV	Transient photovoltage
TPC	Transient photocurrent
DSC	Differential scanning calorimetry
2D-GIWAXS	Two-dimensional grazing incidence wide-angle X-ray scattering
UV-vis	Ultraviolet visible
RMS	Root-mean-square roughness
CV	Cyclic voltammetry
DFT	Density functional theory
SCLC	Space charge limited current

Symbols

nm	Nanometer
min	Minute
^{o}C	Degree
λ	Wavelength
E_g	Bandgap
eV	Electonvolt
cm	Centimeter
μm	Micrometer
μ_h	Hole mobility
μ_e	Electron mobility
PCE	Power conversion efficiency
V_{oc}	Open-circuit voltage
J_{sc}	Short-circuit current
FF	Fill factor
P_{light}	Light intensity

P (E, T)	Exciton dissociation probability
J_{ph}	Net photocurrent density
J_{sat}	Saturated photocurrent density
γ	Surface energies
χ	Flory-Huggins interaction parameter
θ	Contact angle

LIST OF PUBLICATIONS AND CONFERENCE PRESENTATIONS

Journal Publications

1. **Ting Yu**, Francesco Tintori, Yuchen Zhang, Wanting He, Edward Cieplechowicz, Raja Sekhar Bobba, Poojan Indrajeet Kaswekar, Maziar Jafari, Yuxuan Che, Yong Wang, Mohamed Siaj, Ricardo Izquierdo, Dmytro F. Perepichka, Quinn Qiao, Gregory C. Welch and Dongling Ma. Miscibility driven morphology modulation in ternary solar cells, *J. Mater. Chem. A,* **2023**, *11*, 5037-5047.

2. **Ting Yu[1]**, Wanting He[1], Qingzhe Zhang, and Dongling Ma. Towards making advanced functional materials for photon-enabled applications, *Acc. Mater. Res.* **2023**, Accepted.

3. Zhonglin Du[1], **Ting Yu[1] (co-first author),** Wanting He, Aycan Yurtsever, Ricardo Izquierdo, and Dongling Ma. Improving organic photovoltaic efficiency via incorporating heterophase homojunction copper indium sulfide nanocrystals, *Solar RRL.* **2023,** under revision**.**

4. Yong Wang, Xiaolei Liu, Qingzhe Zhang, Chen Wang, Shengyun Huang, Yannan Liu, **Ting Yu**, Ruiqi Yang, Guozhu Chen, Mohanmed Chaker, Dongling Ma. Stable, cost-effective TiN-based plasmonic nanocomposites with over 99% solar steam generation efficiency. *Adv. Funct. Mater.* **2023**, 2212301.

5. Yuxuan Che, Muhammad Rizwan Niazi, **Ting Yu**, Thierry Maris, Cheng-Hao Liu, Dongling Ma, Ricardo Izquierdo, Igor F. Perepichka and Dmytro F. Perepichka. Nitrofluorene-based A-D-A acceptors for organic photovoltaics. *J. Mater. Chem. C* **2023**, DOI: 10.1039/D2TC05127C.

6. **Ting Yu**, Wanting He, Jafari Maziar, Tugrul Guner, Pandeng Li, Mohamed Siaj, Ricardo Izquierdo, Baoquan Sun, Gregory C. Welch, Aycan Yurtsever and Dongling Ma. Three-dimensional nanoscale morphology characterization of ternary organic solar cells, *Small Methods*, **2022**, *6*, 2100916.

7. Zhonglin Du[1], **Ting Yu[1](co-first author)**, Wanting He, Aycan Yurtsever, Ricardo Izquierdo, Maziar Jafari, Mohamed Siaj and Dongling Ma. Enhancing efficiency of non-fullerene organic solar cells via using polyelectrolyte-coated plasmonic gold nanorods as rear interfacial modifiers, *ACS Appl. Mater. Interfaces* **2022**, *14*, 16185-16196.

8. Shengyun Huang, Yannan Liu, Fan Yang, Yong Wang, **Ting Yu**, Dongling Ma. Metal nanowires for transparent conductive electrodes in flexible chromatic devices: a review, *Environ. Chem. Lett*. **2022**, *20*, 3005-3037.

9. Pandeng Li, Yuliang Zhang, **Ting Yu**, Qingzhe Zhang, Jean-Philippe. Masse, Yingguo Yang, Ricardo Izquierdo, Baoquan Sun, Dongling Ma, Unveiling photovoltaic performance enhancement mechanism of polymer solar cells via synergistic effect of binary solvent additives. *Solar RRL*, **2020**, *4*, 2000239.

Conference Presentations

1. **Ting Yu**, Wanting He, Ricardo Izquierdo, Dongling Ma. Three-dimensional Nanoscale Morphology Characterization of Ternary Organic Solar Cells. Canadian Society for Analytical Sciences and Spectroscopy, 64th International Conference on Analytical Sciences and Spectroscopy, Kinston, Canada, **2022**, August 8-10. (Oral presentation, *Burgener Research Graduate Student Travel Award*)

2. **Ting Yu**, Wanting He, Dongling Ma. Three - dimensional Nanoscale Morphology Characterization of Ternary Organic Solar Cells. Canadian Chemistry Conference and Exhibition, CCCE2022, Calgary, Canada, **2022**, July 13-17. (Oral presentation, *Book Prize with a book and certification*).

3. **Ting Yu**, Ricardo Izquierdo, Dongling Ma. Highly Efficient and Air Stable Ternary Organic Solar Cell Enabled by Employing a Perylenediimide-Based Acceptor. The 20th IEEE International Conference on Nanotechnology, NANO 2020, Montreal, Canada, **2020**, July 29-31 (Oral presentation).

CHAPTER 1   INTRODUCTION

1.1 Background of Solar Cells

The nuclear fusion process in the sun generates an enormous amount of solar energy, which is the most important energy source for the survival of life on earth. With the continuous consumption of fossil fuels and the environmental issues caused, solar energy, as sustainable and green energy, is a promising candidate to replace non-renewable fossil fuels, e.g., coal, petroleum and natural gas, in industrial and commercial applications. The sun radiates energy to the earth's surface in one hour, which is enough to meet human needs for a year.[1] Therefore, the effective utilization of solar energy can not only alleviate the energy crisis but also reduce environmental pollution problems. Solar cells can directly convert solar energy into electricity, which is a considerable way to use solar energy.

Bell laboratories first demonstrated the first generation of solar cells – crystalline silicon (c-Si) solar cells in 1954, opening a new era for photoelectric conversion. Since then, researchers have made great efforts to fabricate solar cells with low cost, simplified manufacturing process, and high photo-conversion efficiency, yielding c-Si solar cells with efficiencies exceeding 26%.[2] However, the production of c-Si solar cells requires large amounts of highly crystalline Si materials and the absorption of c-Si solar cells at the long wavelength is weak, which limits the further development of Si solar cells.[3] In addition, thin-film solar cells as second-generation solar cells, including polycrystalline Si, amorphous Si and cadmium telluride (CdTe) solar cells, have attracted widespread attention owing to the ease of the large-area fabrication. But the complex thin-film growth technologies, e.g., fast thermal chemical vapor deposition method, plasma enhanced chemical vapor deposition method, low-pressure chemical vapor deposition method, and liquid phase epitaxy growth method, are not conducive to their sustainable development in the industry.[4]

In order to obtain highly efficient thin-film solar cells with a simple fabrication process, third-generation solar cells have been developed. Third-generation solar cells mainly include new high-efficiency solar cells such as dye-sensitized solar cells, quantum dot solar cells, perovskite solar cells, multi-junction solar cells and organic solar cells (OSCs).[5] Among them, OSCs exhibit the following advantages: low manufacturing cost, lightweight, good processing performance, roll-to-roll or spray printing technologies, and can be fabricated into flexible devices that are easy to

1

carry.[6] Since the first OSC device with a single active layer between two electrodes was fabricated and exhibited a low efficiency below 0.1%, tremendous efforts have been made to increase device efficiencies, such as the innovation of device architecture, device fabrication engineering, and the design of high-efficient materials, thereby obtaining high efficiencies over 19% for single-junction OSCs.[7-10] Therefore, the high-efficient OSCs have a great potential to be commercialized in photovoltaic (PV) markets.

1.2 Fundamentals of Organic Solar Cells

1.2.1 Architectures of organic solar cells

Generally, the architecture of OSCs consists of an organic photoactive layer sandwiched in two electrodes with different work functions (WFs). Indium tin oxide (ITO)-coated glass has been widely used as the bottom electrode due to its high electrical conductivity and optical transparency. Also, ITO-coated glass has low absorption in the ultraviolet (UV) and visible light regions, which allows photons to penetrate the photoactive layer.[11] Based on the structure of the photoactive layer, the architecture of OSCs can be divided into single-layer device structure, bilayer (or planar heterojunction) device structure, and bulk heterojunction (BHJ) device structure. (**Figure 1.1**) The single-layer OSC is composed of a p-type organic layer and two different electrodes. Under sunlight illumination, the organic semiconductor material absorbs photons and generates excitons, which can be separated into free electrons and holes when they diffuse near the Schottky barrier (a Schottky barrier is formed between the low WF electrode and the organic semiconductor). However, the short exciton diffusion length of the organic semiconductor limits exciton dissociation, thereby leading to poor efficiency. For example, in 1982, Weinberger et al.[12] fabricated a polyacetylene-based single-layer device, which efficiency was only 0.3%, since excitons rarely reached the interface between the polyacetylene layer and the metal electrode, and separated charge carriers could easily recombine. In bilayer OSCs, a p-type organic layer with the electron-donating semiconductor (donor) and an n-type organic layer with the electron-accepting semiconductor (acceptor) are stacked into a planar heterojunction, which was first proposed and fabricated by Tang et al in 1986.[13] Photo-generated excitons can be effectively dissociated to be free charge carriers on the donor/acceptor interface. However, the limited contact area of the donor and acceptor organic layers limits the number of charge carriers generated, which is detrimental to the device efficiency. In 1995, Heeger and Wudl [14] first proposed a new BHJ concept to fabricate

the photoactive layer with blended donor and acceptor materials. The interpenetrating network of the photoactive layer largely increases the contact area of donor and acceptor materials, beneficial to eliminate the effect of short excitons diffusion length. Thus, BHJ-OSCs can favor effective exciton dissociation and charge transport to electrodes.
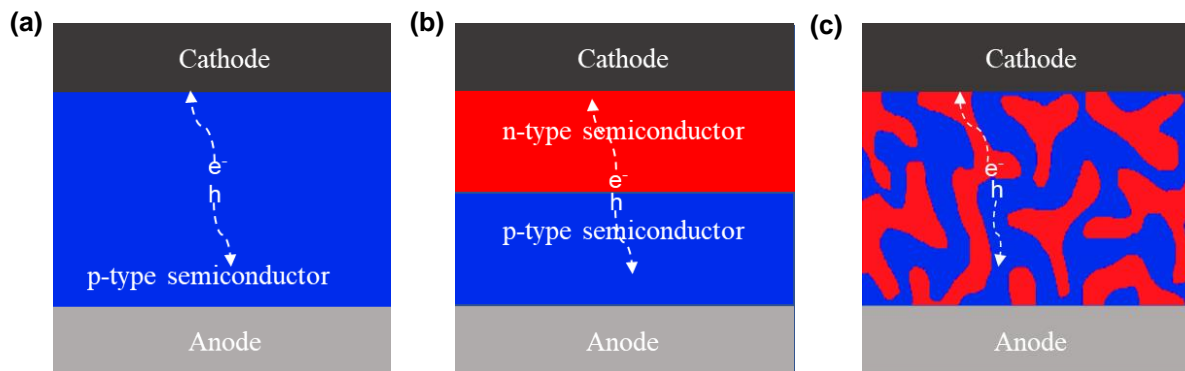
Figure 1.1. The architectures of (a) single-layer OSCs, (b) bilayer OSCs, and (c) BHJ OSCs.

In BHJ-OSCs, there are mainly two device structures: the conventional device structure and the inverted device structure. (**Figure 1.2**) In the conventional OSCs with a structure of ITO transparent electrode/hole transport layer (HTL)/photoactive layer/electron transport layer (ETL)/metal electrode, where the metal electrode with a low WF (e.g., Al) is sensitive to oxygen and moisture in the air. In addition, poly (3, 4-ethylene dioxythiophene)-poly (styrene sulfonate) (PEDOT: PSS) as the hole-transporting material can easily corrode the ITO glass due to the strong acidic nature of PSS, leading to device degradation. Considering the stability of OSCs, the inverted OSC has been developed with a structure of ITO transparent electrode/ETL/photoactive layer/HTL/metal electrode. Metal electrodes with high WFs (e.g., Ag and Au) can effectively avoid the oxidation of electrodes, while introducing metal oxides (e.g., ZnO and TiO_2) on the surface of ITO as a substitute for PEDOT: PSS can help improve the stability of the device.
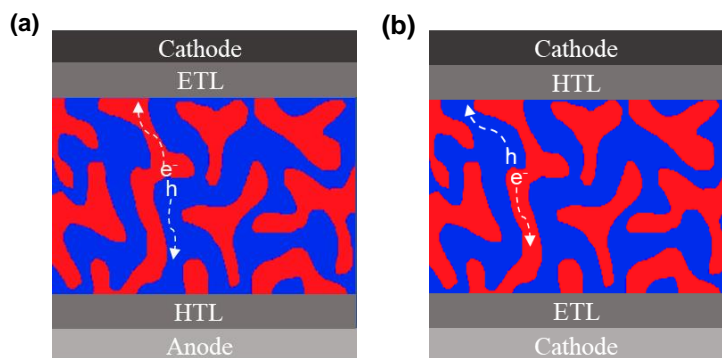
Figure 1.2 (a) Conventional structure of BHJ-OSCs, and (b) inverted structure of BHJ-OSCs.

1.2.2 Photovoltaic parameters of organic solar cells

The photovoltaic parameters of OSCs are obtained from the current density-voltage (*J-V*) curve under the AM 1.5G simulated illumination, which determines the photovoltaic performance of OSCs. (**Figure 1.3**) The fundamental parameters are as followed:
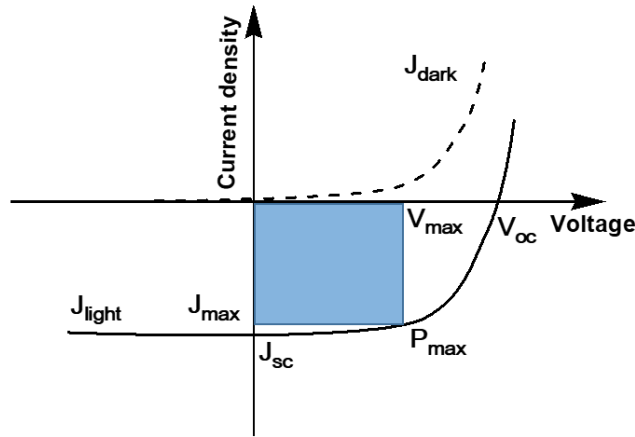
Figure 1.3 *J-V* curve of OSCs under the dark and the AM 1.5G simulated illumination.

Short-circuit current density (J_{sc}): When the applied potential is zero under the short circuit condition, the measured photocurrent is the short-circuit current. The J_{sc} is the maximum photocurrent density, which represents the number of photo-generated charge carriers and collected by respective electrodes.[15]

Open circuit voltage (V_{oc}): When the current is zero under the open circuit condition, the measured voltage is the open circuit voltage. Generally, the V_{oc} in BHJ-OSCs is related to the energy level difference between the highest occupied molecular orbital (HOMO) of the donor and the lowest unoccupied molecular orbital (LUMO) of the acceptor.[16]

Fill factor (FF): The FF is one of the important parameters, which reveals the quality of devices and is generally related to the charge carrier mobility and extraction, the morphology of the photoactive layer and the contact of the electrode. In **Figure 1.3**, the blue rectangle represents the FF, it indicates how fast or slow photo-generated charge carriers are extracted by respective electrodes.[15] The FF value can be calculated by the ratio of the product of current (J_{max}) and voltage (V_{max}) corresponding to the maximum output power to the product of J_{sc} and V_{oc}, and its formula is as followed:

$$FF = \frac{J_{max}V_{max}}{J_{sc}V_{oc}}$$

Power conversion efficiency (PCE): The PCE of the OSC is the efficiency of converting light into electricity under sunlight illumination, which is defined as the ratio of the product of the current (I_{max}) and voltage (V_{max}) corresponding to the maximum output power (expressed as the product of V_{oc}, Jsc and FF) to the incident optical power (P_{in}), and its formula is as followed:

$$PCE = \frac{V_{max}I_{max}}{P_{in}} = \frac{J_{sc}V_{oc}FF}{P_{in}}$$

Therefore, these parameters play key roles in enhancing and optimizing the device performance. The V_{oc}, J_{sc} and FF of OSCs can be enhanced by the design of photoactive layer materials, the modulation of the nanoscale morphology, and the optimization of the interface and electrodes, thus facilitating the achievement of the best efficiency.

In addition to the above four parameters, external quantum efficiency (EQE) and internal quantum efficiency (IQE) can also characterize the device performance. The EQE is defined as the ratio of the number of charge carriers (N_c) collected by a solar cell to the number of incident photons (N_p), while the IQE is the ratio of the N_c to the number of absorbed photons (N_{pa}) in a solar cell.

1.2.3 Mechanism of organic solar cells

The photoelectric conversion mechanisms of OSCs mainly consist of four steps as followed: (1) photons absorption and excitons generation; (2) excitons diffusion to the donor/acceptor interface; (3) excitons dissociation into free charge carriers; and (4) charge transport and collection by respective electrodes.[15, 17]

Photons absorption and excitons generation (**Figure 1.4** a): when the sunlight illuminates on the OSC, the donor and acceptor in the photoactive layer can absorb photons. Then, electrons are excited from the ground state to the excited state, generating electron-hole pairs (i.e., excitons). In order to harvest more photons, the absorption spectra of the donor and acceptor materials should match the photo flux of the AM 1.5G solar irradiation. In general, materials with a lower band gap (< 2.0 eV) are favorable for absorbing more photons, thus increasing the photo-generated charge carriers. In addition, the thickness of the photoactive layer is limited to less than 200 nm due to the

low charge-carrier mobility of photoactive layer materials, which affects the photon absorption density.[18]

Excitons diffusion (**Figure 1.4** b): Before excitons dissociate into free charge carriers, excitons will diffuse to the interface between the donor and the acceptor by hopping from high excitonic energy to low excitonic energy. However, because of the short exciton lifetime and short diffusion length (5-20 nm), excitons will decay when they are far from the donor/acceptor interface.[19]

Excitons dissociation (**Figure 1.4** c): Excitons can dissociate into free electrons and holes at the donor/acceptor interface due to the energetic offset between donor and acceptor materials. The free electrons are transferred to the acceptor material through the LUMO energy level, and the holes are transferred to the donor material through the HOMO energy level.

Charge transport and collection (**Figure 1.4** d): When excitons dissociation and charge separation occur at the donor/acceptor interface, free electrons and free holes will drift toward the cathode and anode, respectively, due to the built-in electric field caused by different work functions of electrodes. Finally, the electrons and holes are collected by the respective electrodes to generate the current.
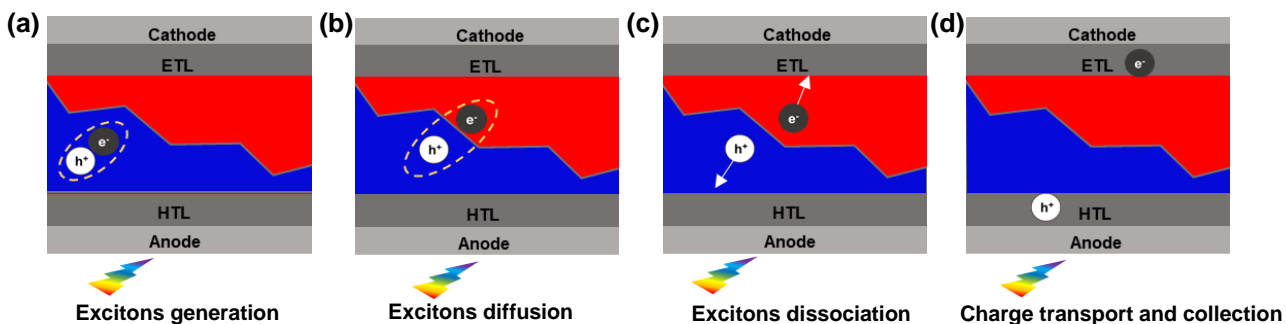
Figure 1.4 The photoelectric conversion mechanisms of OSCs, and the process mainly consists of four steps: (a) photons absorption and excitons generation, (b) excitons diffusion, (c) excitons dissociation, and (d) charge transport and collection.

1.3 Research Progress on Improving Photovoltaic Performance

1.3.1 Design and synthesis of acceptors

Constructing a BHJ structure in the photoactive layer is a major breakthrough in the research field of OSCs. On the basis of the BHJ structure, great efforts have been made to design the high-

efficient photoactive layer materials to achieve state-of-the-art efficiency. The development of acceptor materials plays a crucial role in modulating the spectral absorption, energy structure and nanoscale morphology, resulting in OCSs with excellent efficiencies. Therefore, the OSCs based on acceptor materials are classified into fullerene-based solar cells and non-fullerene-based solar cells.

1.3.1.1 Fullerene and its derivatives acceptors

In the past decades, the acceptor materials in OSCs are mainly fullerenes and their derivatives because of their high charge transfer capability and molar extinction coefficient at short wavelengths. In 1992, Sariciftci et al.[20] prepared the first fullerene-based bilayer p-n type OSCs using MEH-PPV polymer as a p-type material and C60 as an n-type material, which determined the photo-induced electron transfer from the polymer to the fullerene. As a result, fullerenes exhibit strong electron-accepting properties and have potential as acceptors in the OSC field. However, the C60 cage possesses low solubility in organic solvents, limiting the formation of high-concentrated blend solution. In order to overcome the drawbacks of fullerene cages, a series of fullerene functionalized derivatives have been developed by replacing phenyl groups,[21-23] changing the length of alkyl chains,[24, 25] modifying terminal ester groups[26, 27] and substituting the fullerene cage (e.g., C70),[28] which not only improve the solubility but also optimize photophysical properties.[29] The common fullerene derivatives are $PC_{61}BM$, $PC_{71}BM$ and ICBA used in OSCs. In 1995, Yu et al.[14] used a soluble C60 derivative, $PC_{61}BM$ as an acceptor and blended with MEH-PPV to fabricate the BHJ-OSCs. This device achieved an efficiency of 2.9%. In 2001, a new thiophene-based polymer (P3HT) was designed and synthesized by Kowalik et al.,[30] which has good optical absorption and high hole mobility. Afterward, P3HT: PCBM-based OSCs have led to extensive research for decades and achieved remarkable improvements in photovoltaic performance.[31] According to the device optimization, P3HT: PCBM-based OSCs achieved the National renewable energy laboratory (NREL)-certified record PCE of 5.4%.[32] Meanwhile, a large number of conjugated polymers with alternating donor-acceptor (D-A) backbones have been investigated as donor materials in OSCs. The 'push-pull' approach in polymers aims to promote intermolecular interactions that allows to tune their bandgap, facilitate charge transfer and improve light absorption abilities.[33, 34] In 2001, Duren et al.[35] synthesized a novel low-bandgap conjugated polymer (PTPTB) based on the benzothiadiazole (BDT) unit and introduced it as the donor into OSCs. It demonstrated for the first time that the photoinduced electron transfer occurred from the

D-A conjugated polymer donor to the fullerene acceptor. Since then, BDT-based polymer donors have attracted extensive attention. The BDT as an acceptor unit, is often copolymerized with thiophene,[36-40] benzodithiophene, fluorine, carbazole,[41-50] and dithienocyclopentadiene,[51-54] the resulting polymers have good photovoltaic performance. In 2010, Liang et al.[55] successfully synthesized an excellent polymer donor, PTB7, which has good solubility and light absorption ability. The PTB7: PC$_{71}$BM-based blend film exhibited an absorption range from 300 nm to 800 nm, leading to a PCE of over 7%. This paved a new path for the development of future solar cells. In 2015, He et al.[56] obtained a new polymer PTB7-Th by replacing alkoxy side chains on BDT unit with alkylthiophene side chains, which improved the degree of conjugation of the polymer and led to a photovoltaic conversion efficiency up to 10.61%. In 2017, Huang et al.[57] prepared a fullerene-based interfacial modifier (OPCBM) and integrated on the ZnO layer to improve the conductivity of interlayer and energetic alignment due to its photoconductive properties, leading to a high PCE value of 11.3% for OSCs based on the PTB7-Th: PC$_{71}$BM photoactive layer. In 2021, Usmani et al.[58] introduced Au nanoparticles into the ZnO ETL in PTB7-Th: PC$_{71}$BM-based OSCs, the plasmonic effect of Au could improve the light absorption and optimize the interface, contributing to the efficiency of 11.8%. The chemical structures of the above fullerene and its derivatives, and polymer donors were shown in **Figure 1.5**.
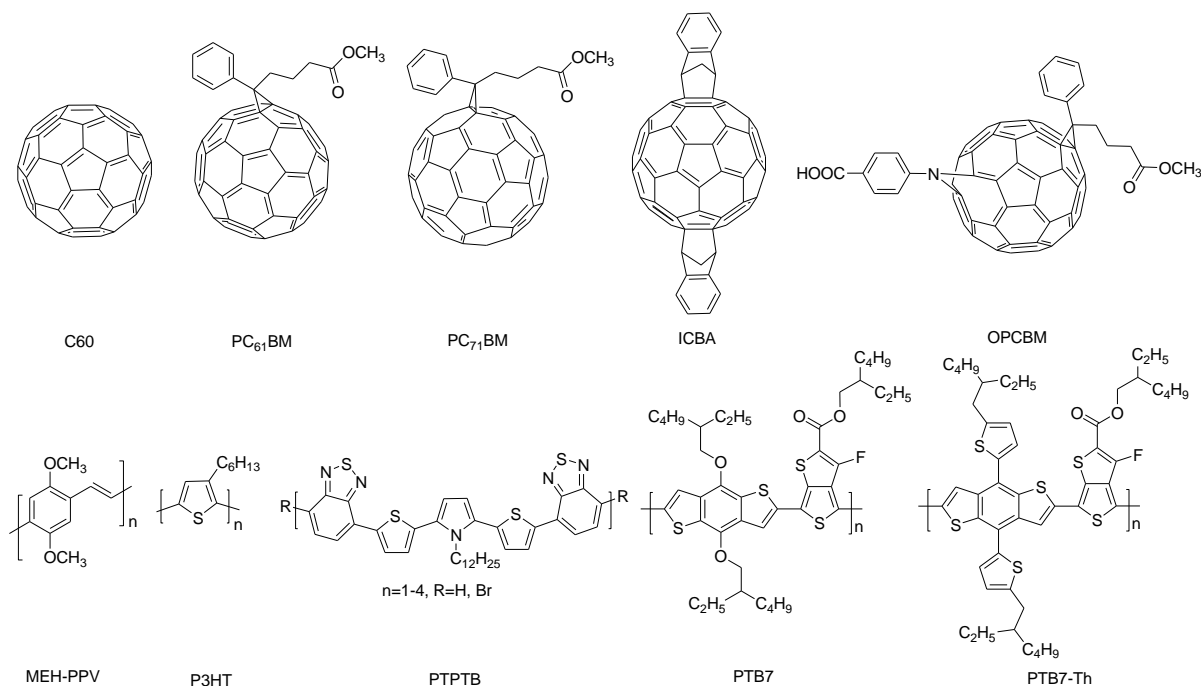
Figure 1.5 The chemical structures of fullerene and its derivatives, and polymer donors in fullerene-based OSCs.

1.3.1.2 Non-fullerene acceptors (NFAs)

Although great efforts have been made to trigger increasing efficiencies of fullerene-based OSCs, the considerable limitations of the chemical modification on the backbone of fullerene derivatives hinder the achievement of high-efficient photovoltaic performance, such as weak absorption ability in the visible or near-infrared (NIR) light regions and limited energy level tunability, resulting in relatively lower photocurrent and photovoltage.[59, 60] Moreover, the poor miscibility of fullerenes with donor materials enables excessive aggregation behavior, which causes the poor efficiency and stability. Compared to fullerene acceptors, the most attractive advantages of NFAs are flexible chemical structures and synthetic approaches, which is beneficial to improve the solubility, broaden spectral absorption in the visible and NIR light regions, tune energy levels, and increase electron mobility. The development and innovation of NFAs in OSCs have made great breakthroughs and achievements in device performance owing to these favorable properties, thus endowing OSCs with great potential in practical applications.[9, 10] To date, several types of NFAs have been brought into NFA-based OSCs, mainly including rylene diimide-based NFAs and A-D-A type NFAs.

Rylene diimide-based NFAs

Rylene diimide is one of the promising n-type organic semiconductors, which mainly involves perylene diimide (PDI) and naphthalene diimides (NDI). This class of the NFA exhibits several features: 1) feasible chemical structure modification at various positions; 2) large absorption coefficient; 3) strong electron affinity because of electron-deficient imide groups; 4) high electron mobility due to large conjugated backbones and intermolecular π stacking; and 5) high thermal, chemical and photo stability.[61, 62] Since Tang et al.[13] first used a perylene tetracarboxylic derivative (PV) as a NFA acceptor in photovoltaic devices in 1986 and yielded an efficiency close to 1%, the best efficiencies of PDI- and NDI-based single-junction OSCs have exceeded 11%,[63-65] The excellent photovoltaic performance of OSCs based on rylene diimide-based acceptors mainly arises from the structural evolution to address their inherent drawbacks such as the strong aggregation tendency due to large π-conjugated backbones, resulting in undesirable phase separation.

9

PDI-based acceptors: The structures of PDI-based acceptors are shown in **Figure 1.6**. The PDI molecule has three symmetric reactive positions: bay position, ortho position (α-position) and N position. These reactive sites can be modified to form a certain torsion angle in the molecular planar structure, thereby improving the solubility, inhibiting aggregation, and adjusting the optoelectronic properties. Among them, the modification of the N position by a series of alkyl and other groups can improve the solubility to adjust the morphology in the photoactive layer with little effect on optoelectronic properties. For example, Rajaram et al.[66] synthesized a asymmetric perylene with different lengths of alkyl chains on two N positions, which could form a smaller domain size in the photoactive layer due to their different degree of solubility. In addition, the α-position substitution has been regarded as a wide approach to balance the issue between the distortion and the coplanarity. Zhao et al.[67] synthesized an α-position substituted PDI acceptor (αPBDT) with the BDT unit. Compared with the bay position substituted PDI acceptor (βPBDT), the αPBDT molecule showed a better planarity and thus facilitated electron mobility. As a result, the OSC based on the PTB7-Th: αPBDT photoactive layer achieved a higher PCE value. Wu et al.[68] reported a PDI tetramer (TPB) by substituting the α-position with a BDT unit. α-substituted PDI derivatives showed better planarity so that the TPB molecule has good molecular packing of conjugated backbone. Therefore, the device based on the PTB7-Th: TPB photoactive layer exhibited a high J_{sc} value of 18 mA cm^{-2} and a PCE value of 8.47%.

The substitution of the bay position is a simple and effective strategy to obtain twisted PDI derivatives, which can reduce the intermolecular aggregation, and tune optical and electrical properties. The first approach is to introduce alkyl chains or aromatic groups at the bay position of the PDI monomer. Sharma et al.[69] synthesized a symmetrical PDI-based acceptor (P-A) with tert-butylphenoxy side groups at the 1, 7-bay position, which exhibited a broad absorption band ranging from 450 nm to 620 nm and a high LUMO level. The blend film containing the P-A acceptor showed good spectral coverage in the visible and NIR light ranges, yielding an efficiency of 2.85%. Kozma et al.[70] introduced the bay-position substitution with fused aromatic rings to obtain two acceptors, PDI-2 and PDI-3. According to theoretical calculations, these two PDI-based acceptors formed dihedral angles between substituted groups and the PDI backbone to hinder the intermolecular π-π stacking. In addition to functionalized PDI monomers, one straightforward and effective strategy is to link two PDIs together by inserting bonds (e.g., single, double, and triple bonds) or aromatic groups (e.g., thiophene, benzene, bithiophene, and spirobifluorene, etc.) to

form a twisted PDI dimer. In 2014, Wang's group[71] designed a series of bay-linked PDI acceptors that were linked by a single bond (s-diPBI), double bond (d-diPBT) and triple bond (t-diPBI), resulting in different optoelectronic properties based on the different degree of distortion between two PDIs. In 2015, their group[72, 73] modified s-diPBI acceptor by introducing thiophene or selenophene units on the PDI core to obtain two novel acceptors, SdiPBI-S and SdiPBI-Se. Due to the introduction of aromatic groups, there two acceptors showed more twisted structures and higher lying LUMO levels compared to the s-diPBI molecule linked by a single bond, which provided high PCEs of 7.16% and 8.42%, respectively. In addition, Yan et al.[74] synthesized a series of PDI dimers by various aromatic linkers in the bay positions (e.g., *par*a-phenylene, *meta*-phenylene, thiophene-2,5-diyl, 2,2'-bithiophene-5,5'-diyl, spirobifluorene-2,2'-diyl, and spirobifluorene-2,7-diyl) to form non-planar geometry. These electron-donating linkers could up-shift energy levels, produce extended conjugation, and broaden the spectral absorption. Moreover, these non-planar structures effectively inhibited the aggregation and crystallization of PDI units, thus favoring their photovoltaic performance. Among them, PDI-5 and PDI-6 with three-dimensional (3D) spirobifluorene linkers could form electron-transport networks that leaded to high photocurrent. Furthermore, bounding with three or four PDIs by a core has been extensively investigated. Lin et al.[75] linked three PDIs with a triphenylamine (TPA) core to get a non-planar and star-shaped PDI acceptor, S(TPA-PDI), which formed a quasi-3D structure, and thus had weak intermolecular interactions and molecular aggregation. Duan et al.[76] introduced an electron-deficient core (1, 3, 5-triazine) to bound three PDIs, thereby reporting a novel PDI trimer acceptor, Ta-PDI. According to the density functional theory (DFT) calculation, two PDIs in the Ta-PDI molecule showed relatively co-planar geometry with a torsion angle of 19°, while the third PDI had large torsion angles (83 ° and 74 °) with the other two PDIs. Therefore, Ta-PDI acceptor exhibited relatively high crystallinity and electron mobility, leading to a high PCE of 9.15% in the OSCs based on PTB7-Th: Ta-PDI photoactive layer. In addition, Lin et al.[77] rationally modulated the twisting degree of PDI-based acceptors, because the insufficient twisting could cause the formation of large domain size, and the excessive twisting could decrease charge mobility. Therefore, they synthesized TPPz-PDI4 acceptor with a less crowded tetraphenylpyrazine (TPPz) core, which exhibited a smaller torsion angle due to the reduced crowding of four PDIs, leading to better charge mobility and higher efficiency of 7.1%. The chemical structures of the above non-fused PDI-based NFAs are shown in **Figure 1.6**.
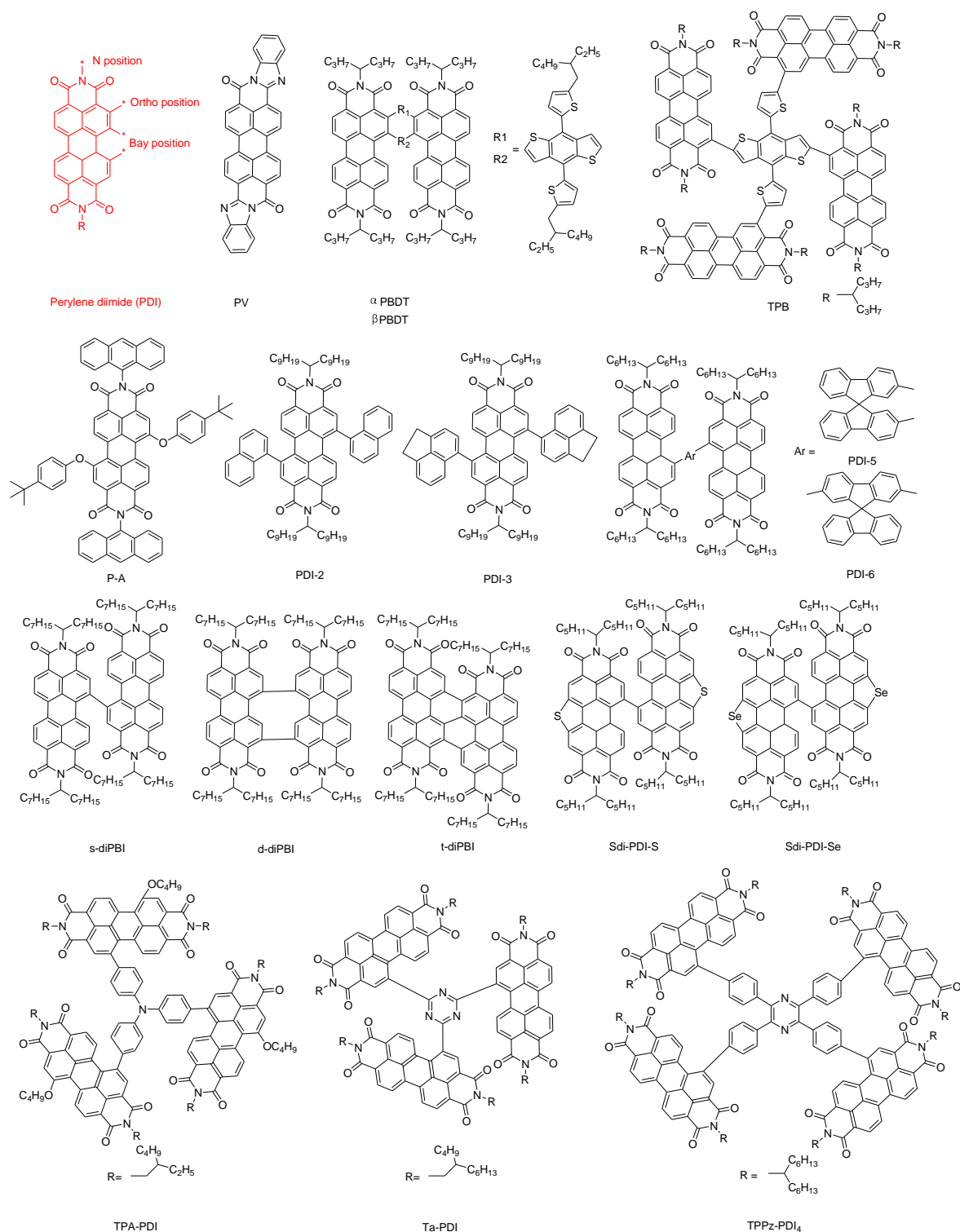
Figure 1.6 The chemical structures of non-fused PDI-based acceptors in NFA-based OSCs.

Compared to the above non-fused PDI molecules, the ring fusion of PDI is a promising approach to enhance molecular coplanarity. Considerable efforts have been made to design and synthesize

ring-fused PDI molecules that possess sufficient torsion and proper extent of ring-fusion, thereby enabling appropriate crystallinity and increased charge transport. For example, Zhong et al.[78] synthesized a helical PDI dimer with an ethylene spacer, which contributed to ultrafast electron and hole transfer between the polymer donor and the helical PDI acceptor. As a result, helical PDI NFA-based OSCs achieved excellent efficiency up to 6.05%. Furthermore, they reported two helical PDI acceptors with three PDIs and four PDIs (hPDI$_3$ and hPDI$_4$).[79] The photoactive layer based on the PTB7-Th: hPDI$_3$ (hPDI$_4$) presented a mesh-like network, the pores in this network showed tens of nanometers in diameter. In addition, holes and electrons transfer at the interface between donor and acceptor were found, thus contributing to device efficiencies of 7.9% and 8.3%, respectively. Moreover, Zhang et al.[64] reported a novel PDI-tetramer acceptor (FTTB-PDI4), which linked a tetrathienylbezene (TTB) core with four PDI units via a ring-fusion between the thiophene and PDI unit. Compared to non-fused PDI-tetramers, this fused NFA exhibited a 'double-decker' geometry with two pairs of parallel PDI units, thereby offering stronger light absorption and intermolecular packing. In addition, the photoactive layer showed a high domain purity of the acceptor, which was beneficial to maintain its molecule packing and electron transfer. As a result, an excellent efficiency of 10.58% the device was yielded for this device. The chemical structures of the above fused PDI-based NFAs are shown in **Figure 1.7.**
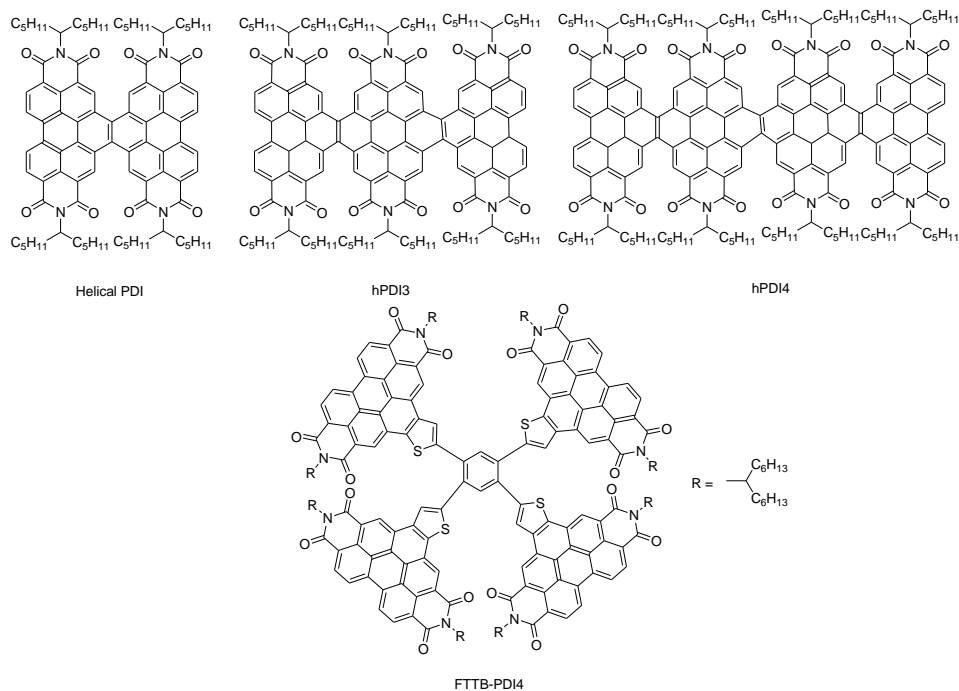
Figure 1.7 The chemical structures of fused PDI-based acceptors in NFA-based OSCs.

NDI-based acceptors: In addition to PDI, researchers have done a lot of work in studying its homologue molecule NDI and building NDI acceptor-based OSCs. Compared to PDI acceptors, NDI acceptors show relatively low light absorption and electron mobility due to their smaller conjugated backbones. In addition, the NDI unit has fewer reaction sites, which limits the chemical structural diversity of NDI molecules and the adjustment of their optical and electrical properties. Therefore, NDI-based small molecules cannot achieve high-efficient photovoltaic performance. Accordingly, NDI generally serves as an electron-deficient moiety to synthesize the NDI-based polymer acceptors. In 2008, Guo et al.[80] pioneered the synthesis of a series of n-type polymers based on NDI unit (P1 and P2a-2d), which showed deep-lying LUMO energy levels. According to the introduction of different electron-donating moieties, optical energy gaps could be adjusted ranging from 1.7 to 1.1 eV. Subsequently, Yan et al. [81] used an electron-transporting polymer, P(NDI2OD-T2) (also known as N2200) in organic thin-film transistor (OFET). The N2200 polymer had a high OFET electron mobility up to 0.85 cm^2 V^{-1} s^{-1} under ambient conditions, a broad spectral absorption from 300 nm to 900 nm, and remarkable stability under humidity conditions because of its planar structure and dense molecular packing. To date, the N2200 polymer is the most widely used polymer acceptor in OSCs and yields excellent efficiencies. In 2019, Li et al.[63] reported an all-polymer solar cell based on the PTzBI-Si: N2200 photoactive layer, and yielded a benchmark PCE value of 11.0% through employing a non-chlorinated cyclopentyl methyl ether solvent (CPME). The PTzBI-Si: N2200 blend in the CPME solvent exhibited stronger aggregation, leading to a higher absorption coefficient, efficient energy transfer and enhanced charge mobility. Besides, Zhu et.al[65] used the slot die printing to prepare the PTzBI-Si: N2200 photoactive layer. In this work, the volatile solvent of 2-methyltetrahydrofuran (MTHF) could freeze the morphology in a short time, which led to strong intermolecular interaction and the formation of more rigid conformations. The limited solubility of PTzBI-Si polymer donor and N2200 polymer acceptor in the MTHF solvent could induce the formation of fibril networks in the blend film, resulting in a high PCE of 11.76%. The chemical structures of the above NDI-based polymer acceptors and polymer donors are shown in **Figure 1.8**.
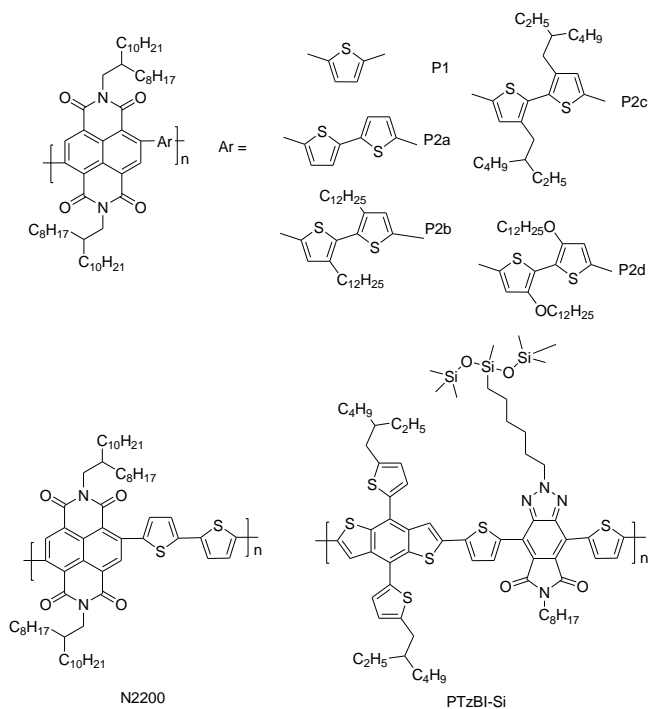
Figure 1.8 The chemical structures of NDI-based polymer acceptors, and polymer donors in NFA-based OSCs.

A-D-A type NFAs

A-D-A type NFAs generally are comprised of the electron-donating core (D) connected two electron-withdrawing (A) end-caps to form a 'push-pull' structure, which has the following attractive features: 1) the 'push-pull' effect can promote strong intramolecular interaction and intramolecular charge transfer to afford a broaden spectral absorption and a narrow bandgap; 2) this rigid and conjugated molecular conformation can facilitate the intermolecular charge transfer to adjacent acceptors or donors;[82] 3) A-D-A type NFA with a good planarity enables high electron mobility in the solid film.[83] Therefore, A-D-A type NFAs, especially ITIC-series and Y-series, have excellent optoelectronic properties, which provides breakthrough photovoltaic efficiencies.

ITIC-series NFAs: In 2015, Zhan's group[84] synthesized and reported a novel A-D-A type electron acceptor, ITIC, consisting of an indacenodithieno[3,2-b]thiophene (IDTT) core and two 2-(3-oxo-2,3-dihydroinden-1-ylidene)malononitrile (INCN) end groups. The ITIC NFA possesses low LUMO and HOMO energy levels due to INCN electron-withdrawing groups and broad absorption range arising from the pull-push structure. The introduction of 4-hexylphenyl groups plays a role in suppressing aggregation, leading to good miscibility with PTB7-Th polymer donor.

15

Thus, OSCs based on the PTB7-Th: ITIC blend film yielded a record efficiency of 6.8%. Since then, the field of A-D-A type NFAs has become a hot research topic. However, the overlapped absorption spectra of PTB7-Th donor and ITIC acceptor limited the improvement of the efficiency. Therefore, a series of polymers have been used as donors into ITIC-based OSCs to obtain high-efficient photovoltaic performance. For example, Zhao et al.[85] demonstrated a combination of the PBDB-T polymer donor and ITIC acceptor to achieve an outperforming PCE up to 11.21%. The PBDB-T and ITIC showed better complementary absorption to support more photons harvesting, as well as a well-aligned energy level to reduce the energy loss and increase the photovoltage. In addition, Xu et al.[86] reported a novel polymer donor (PBDTS-TDZ) with a wide bandgap, and then blended with ITIC acceptor with a low bandgap to yield a certified PCE of 13.19% without any additives and post-treatment.

Besides, a series of ITIC derivatives have been developed by the replacement of side chains, terminal groups and conjugated cores to tune their optoelectronic properties, which can match with polymer donors and enhance the photovoltaic performance of devices. Lin et al.[87] reported a promising ITIC derivative, ITIC-Th, via replacing phenyl side chains with thienyl side chains, which could downshift the energy level. Compared to phenyl side chains, thienyl side chains were able to increase intermolecular interactions, and facilitate molecular π-stacking and charge transport due to the easily polarized sulfur atoms and strong sulfur-sulfur interaction. Moreover, Li et al.[88] introduced a weak and small electron-donating substituent, methyl, on terminal groups of the ITIC molecule to obtain an electron acceptor (IT-M), which could lift the energy level without inducing steric hindrance for intermolecular packing. The device based on the PBDB-T: IT-M photoactive layer demonstrated a high V_{oc} of 0.94 V and a high PCE of 12.05%. Similarly, Zhao et al.[89] fluorinated the INCN end-groups to synthesize a novel electron acceptor (IT-4F). Meanwhile, they reported a newly fluorinated-polymer donor (PBDB-T-SF). The fluorinated donor and acceptor displayed high absorption coefficients and low-lying HOMO and LUMO energy levels, thereby achieving a record efficiency of 13.1%. Zhang et al.[90] introduced the chlorine substituents on the INCN end-groups to synthesize the IT-4Cl molecule. The IT-4Cl molecule possessed a large dipole-moment of the C-Cl bond to cause the molecular stacking and enhanced the intermolecular charge-transfer effect so that the OSC with PBDB-T-SF: IT-4Cl blend film achieved an outstanding PCE of 14.2%. In addition, the optimization of the conjugated core of the ITIC molecule is also a promising strategy to modulate the optical and physical properties

of ITIC-based acceptors. Lin et al.[91] reported a novel NFA (IDIC) by substituting phenyl side chains on the core of the ITIC molecule with alkyl chains, which showed a narrow bandgap of 1.6 eV. The IDIC acceptor blended with a medium bandgap FTAZ donor could result in complementary absorption from 400 nm to 800 nm. In addition, the FTAZ donor and IDIC acceptor had matched energy levels and relatively high hole and electron mobilities, yielding a certified PCE of 12.14%. In order to further broaden the spectral absorption, Zhu et al.[92] developed a fused ring NFA (IOIC3) with an eight-ring fused naphtho[1,2-b:5,6-b']dithiophene core and alkoxy side chains. The extended core and σ-inductive oxygen atoms were able to induce red-shifted absorption, decrease optical bandgap of 1.45 eV and enhance electron mobility of 1.5×10^{-3} cm^2 V^{-1} s^{-1}, which facilitated the achievement of a high efficiency of 13.1%. Similarly, Dai et al.[93] extended the seven-ring fused core of the ITIC molecule to the nine-ring fused core. The bandgap of the novel electron acceptor (INIC) and fluorinated-INIC (INIC3) could be reduced to 1.57 eV and 1.48 eV, respectively, and showed high extinction coefficients of $(2.1\text{-}2.5) \times 10^5$ M^{-1} cm^{-1}. The OSCs based on FTAZ: INIC3 exhibited an efficiency as high as 11.5%. The chemical structures of the above ITIC-series acceptors and polymer donors are shown in **Figure 1.9**.
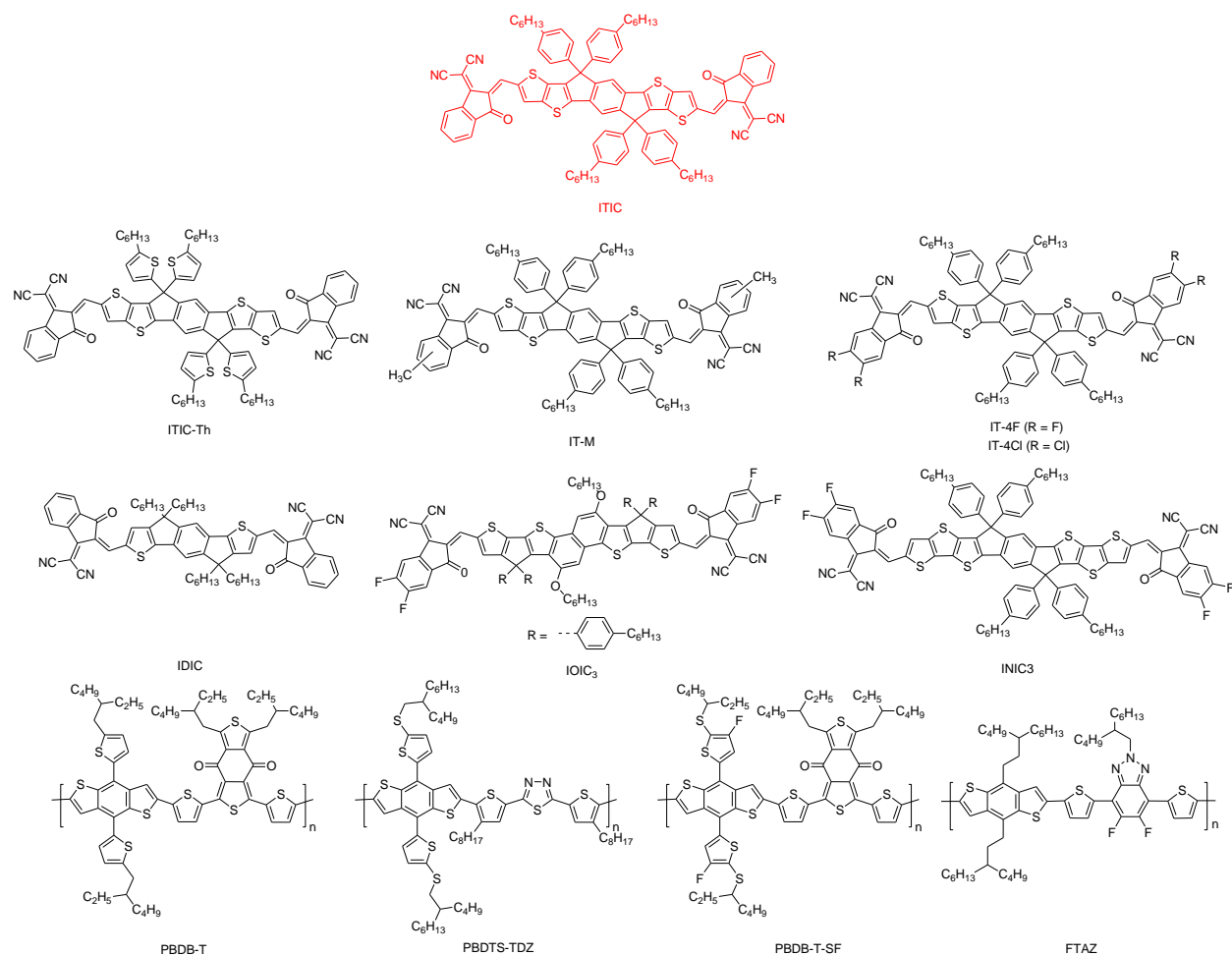
Figure 1.9 ITIC-series acceptors and polymer donors in NFA-based OSCs.

Y-series NFAs: A new class of the NFA was developed by Zou's group[94], which employed a ladder-type core of the dithienothiophen [3.2-b]-pyrrolobenzothiadiazole (TPBT) and 2-(5,6-difluoro-3-oxo-2,3-dihydro-1H-inden-1-ylidene)ma-lononitrile (2FIC) end groups to construct the Y6 acceptor with an A-DAD-A structure. The central fused TPBT core was used to tune electron affinity, while 2FIC end groups could contribute to the optical absorption and intermolecular interaction by forming noncovalent F-S and F-H bonds, thereby facilitating effective charge transport and obtaining a narrow bandgap of 1.33 eV. By blending with a medium bandgap PM6 polymer donor, the optimized efficiency reached 15.7% with a J_{sc} value as high as 25.2 mA cm^{-2}, breaking the historical efficiency record of single-junction OSCs. This photovoltaic performance has made Y6-based NFAs recent research hotspots. Afterward, a series of new donors were developed to match with the Y6 acceptor, thereby achieving remarkable device efficiencies. For example, Ma et al.[95] synthesized a polymer donor (PM7) by the chlorination of the PM6 polymer.

The PM7 donor exhibited a deeper HOMO energy level, blending with the Y6 acceptor could offer a higher V_{oc} and a breakthrough PCE of 17.04%. Furthermore, Liu et al.[96] reported a high-efficient copolymer donor, D18, with a fused-ring acceptor unit (dithieno[30, 20: 3, 4; 200, 300: 5, 6]benzo[1, 2-c][1, 2, 5]thiadiazole, DTBT), which showed a large molecular plane and high hole mobility. Thus, the OSC based on the D18: Y6 photoactive layer achieved a record PCE of 18.22%.

Moreover, Y6 derivatives have been developed to increase device efficiency through materials engineering. Firstly, the modification of the end groups as the flanking unit is beneficial to tune energy levels. A major achievement was made by Cui et al.[97], who conducted a new Y-series acceptor to study the influence of halogen atoms on geometries and electrical properties of acceptors. In this work, they replaced fluorine atoms on the Y6 molecule with chlorine atoms to generate a new acceptor, BTP-4Cl (Y7), which exhibited a downshifted energy level and a narrow optical bandgap. Additionally, the PBDB-TF (PM6): BTP-4Cl-based blend film had a high electroluminescence quantum efficiency (EQE$_{EL}$) of 3.47×10^{-4}, indicative of a reduced non-radiative energy loss. Thus, the devices based on PBDB-TF (PM6): BTP-4Cl blend film exhibited an efficiency as high as 16.5%. The modification of the conjugated core is another strategy to modulate the optoelectronic properties. For example, Zhang et al.[98] reported a new acceptor (Y6Se) by introducing a facile method of the selenium substitution on the TPBT core, which could effectively reduce the Urbach energy of 20.4 meV to decrease non-radiative energy loss. Combining the optimal properties with the strong absorption and high electron mobility, OSCs based on the D18: Y6Se active layer recorded a PCE of up to 17.7%.

Furthermore, researchers worked to modify the alkyl chain of the Y6 molecule, which helps to improve the solubility and control intermolecular stacking. Jiang et al.[99] optimized the branched alkyl chains on the nitrogen atom of the pyrrole unit of the Y6 molecule to synthesize a new acceptor N3 with the 3rd-position branched alkyl chain. The photoactive layer containing the N3 acceptor exhibited optimal properties associated with appropriate domain size, crystallinity, and more dominant face-on orientation, resulting in the best efficiency of 16.0%. In order to increase solubility and the processability of the BTP-4Cl molecule, Cui et al.[100] optimized alky chains on the central core from 2-ethylhexy (EH) to 2-bultyloctyl (BO) to obtain a new acceptor (BTP-4Cl-12), which had suitable solubility, and thus generated a high PCE of 17.0% for spin-coated devices and 15.5% for blade-coated devices. Furthermore, they reported a BTP-4Cl-12 analog (BTP-eC9) by shortening alkyl chains on the edge groups from n-undecyl (C11) to n-nonyl (C9).[101] The BTP-

eC9 acceptor displayed suitable solubility, decreased Urbach energy, and enhanced electron mobility, which led to a maximum PCE of up to 17.8% for the single-junction OSCs based on the PBDB-TF: BTP-eC9 blend film. Recently, a breakthrough molecule (L8-BO) was synthesized by Sun's group,[102] which substituted the β-position of the thiophene unit on the TPBT core of the Y6 with branched BO alkyl chains. The L8-BO molecule showed better molecular packing behavior, leading to improved structural order and charge transport in thin films. In addition, the blue-shifted optical absorption and the upshifted LUMO energy level of the L8-BO molecule are better matched with the PM6 donor, leading to an unprecedented PCE of 18.32% with an FF of 81.5% for single-junction OSCs. Afterward, researchers made efforts to maximize the device efficiency through device fabrication engineering. Song et al.[103] reported a new strategy by introducing a solvent additive (diiodomethane, DIM) to reduce the voltage loss (V_{loss}), resulting in increased V_{oc} of 0.893 V and PCE of 18.60%. Meng et al.[104] utilized the cobalt(II) acetate to prepare an efficient HTL on the PM6: L8-BO-based OSC, which could enhance the WF and conductivity of HTL and promote the improvement of V_{oc}, J_{sc}, and FF, and then obtain a champion efficiency of 18.77%. The chemical structures of the above Y-series acceptors and polymer donors are shown in **Figure 1.10**.
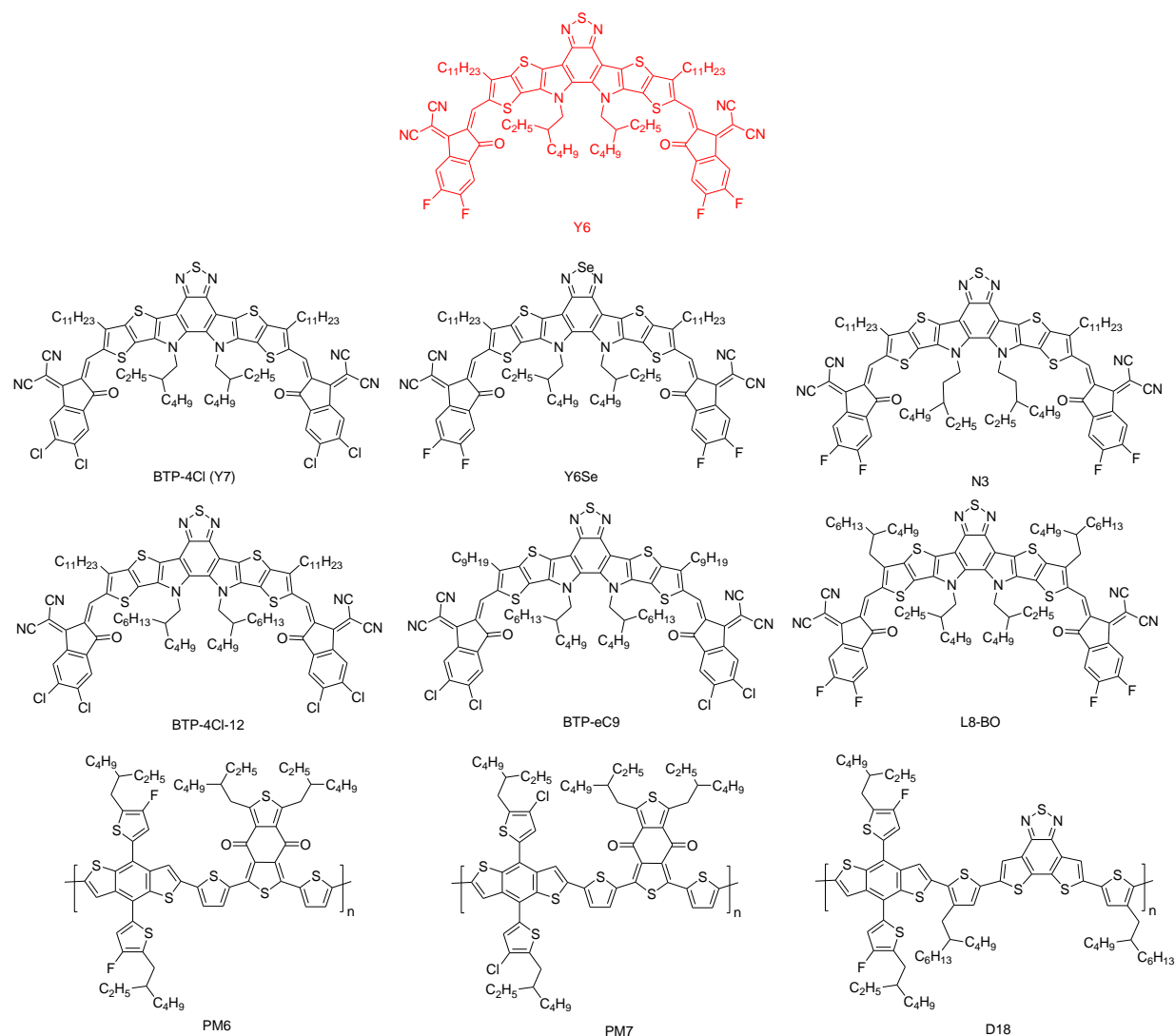
Figure 1.10 Y-series acceptors and polymer donors in NFA-based OSCs.

1.3.2 Morphology optimization

The OSC progress simultaneously depends on the evolution of materials and the optimization of the morphology. Accordingly, an ideal BHJ morphology of the photoactive layer is a prerequisite for the achievement of state-of-the-art OSCs. The control of the BHJ morphology through processing solvents, post-treatment and ternary blend strategy can facilitate the formation of suitable phase separation, proper domain size (10-30 nm), high domain purity, which is of vital importance for effective exciton dissociation and charge transport.[105]

1.3.2.1 Processing solvents

Solvents

For solution-processed photoactive layers, the selection of the casting solvent is crucial for the formation of the optimal morphology with appropriate phase separation, which should meet some requirements: 1) enabling enough solubility of donors and acceptors to process the film from the solution, and 2) possessing suitable boiling point and saturation vapor pressure for the formation of the crystalline film after spin-casting. In 2001, Shaheen et al.[106] for the first time discussed the influence of solvents on the morphology of the blend film. They used two solvents, toluene and chlorobenzene (CB), to cast the MDMO-PPV: PCBM blend film. According to atomic force microscopy (AFM) measurements, the CB-cast film showed a smaller phase-separated size and smoother surface morphology compared to the toluene-cast film. It pointed out that the good solubility of the PCBM in the CB could provide better morphology of the blend film. Since then, choosing the proper casting solvent has attracted more attention for optimizing the morphology. Park et al.[107] analyzed the effect of chloroform (CF), CB and dichlorobenzene (DCB) as casting solvents on the phase separation and percolated networks of the PCDTBT: $PC_{71}BM$ blend film with the help of the transmission electron microscopy (TEM) characterization. The results demonstrated that the DCB-cast film exhibited smaller nanoscale phase separation and better-connected percolated networks, resulting in the IQE approaching 100%. Researchers also made great efforts to optimize the morphology by using the mixed solvents. Wienk et al.[108] used a mixture of CF and o-dichlorobenzene (ODCB) (4:1) as the casting solvent to obtain optimized morphology with an appropriate domain size of 20-30 nm and phase separation. In this work, the mixed solution not only avoided the limited solubility of the pBBTDPP2 donor in the ODCB but also facilitated the formation of a semi-crystalline thin film due to the slow evaporation of solvents. In addition, different solvent treatments in the Y6 system can have a significant effect on the morphology. Zhu et al.[109] revealed that the CF-processed Y6 film was preferential to form the polymer-like extended crystal transport channels, while CB-processed Y6 film tended to exhibit small and discrete oriented crystallites, as confirmed by 2D grazing incidence wide-angle X-ray scattering (GIWAXS) measurements (**Figure 1.11**).
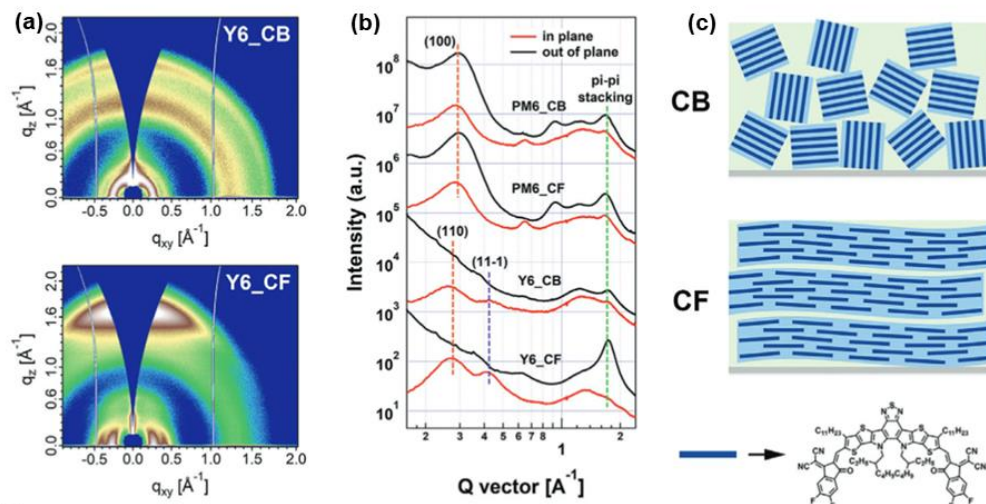
Figure 1.11 (a) 2D GIWAXS patterns for pure Y6 processed with CB and CF, and (b) related scattering profiles. (c) The arrangement sketch map of molecules in films processed by CB and CF. Reprinted from ref. 109. Copyright 2020 Wiley.

Halogenated solvents have been widely used to form favorable morphology and enhance photovoltaic performance, while they are toxic to harm human health and the environment. Halogen-free solvents are more attractive in OSC processing. So far, great progress has been made in the development of green solvent processable OSCs. Daynek et al.[110] synthesized a twisted PDI dimer (tPDI-Hex), which showed good solubility by incorporating alkyl chains on the N-annulation at the bay position of the PDI chromophore. OSCs based on the PTB7: tPDI-Hex blend film could achieve a PCE of 4.8% processed from the 2-methyl-tetrahydrofuran (2Me-THF) or o-xylene halogen-free solvents. Park et al.[111] reported a regionally random 3MT-Th polymer with good solubility in the non-halogenated toluene solvent. The 3MT-Th: ITIC blend film from the toluene solution demonstrated the finest interpenetrating network with the relatively small crystallite domain size, yielding a maximum PCE of 9.73%. Xu et al.[86] chose an appropriate green solvent (o-xylene) to finely control the morphology of PBDTS-TDZ: ITIC blend film, the resulting PCE was up to 13.35% with an extremely low energy loss (E_{loss}) of 0.48 eV. Recently, Kim et al.[112] developed three new green-solvent-processable NFAs, YSe-C3, YSe-C6 and YSe-C9. Among them, the o-xylene-processed PM6: YSe-C6 blend film exhibited an optimal morphology, leading to an excellent PCE of over 16%. However, blend films containing YSe-C3 and YSe-C9 acceptors formed aggregate-containing morphologies, limiting efficiencies to only 11%-14%. In addition, Pang et al.[113] incorporated B-N covalent bonds into the polymer donor (PBNT-TzTz)

with the aim of using a real green and eco-compatible anisole solvent. The anisole solvent is recommended by the "Globally Harmonized System of Classification and Labelling of Chemicals (GHS)" of the United Nations as the green solvent. The PBNT-TzTz polymer with B-N bonds exhibited a dipole moment of 1.84 Debye to improve the polarity, which could promote the solubility of PBNT-TzTz polymer in the anisole solvent and achieved a high PCE of 15.65%. The chemical structures of the above polymer donors and acceptors are shown in **Figure 1.12**.
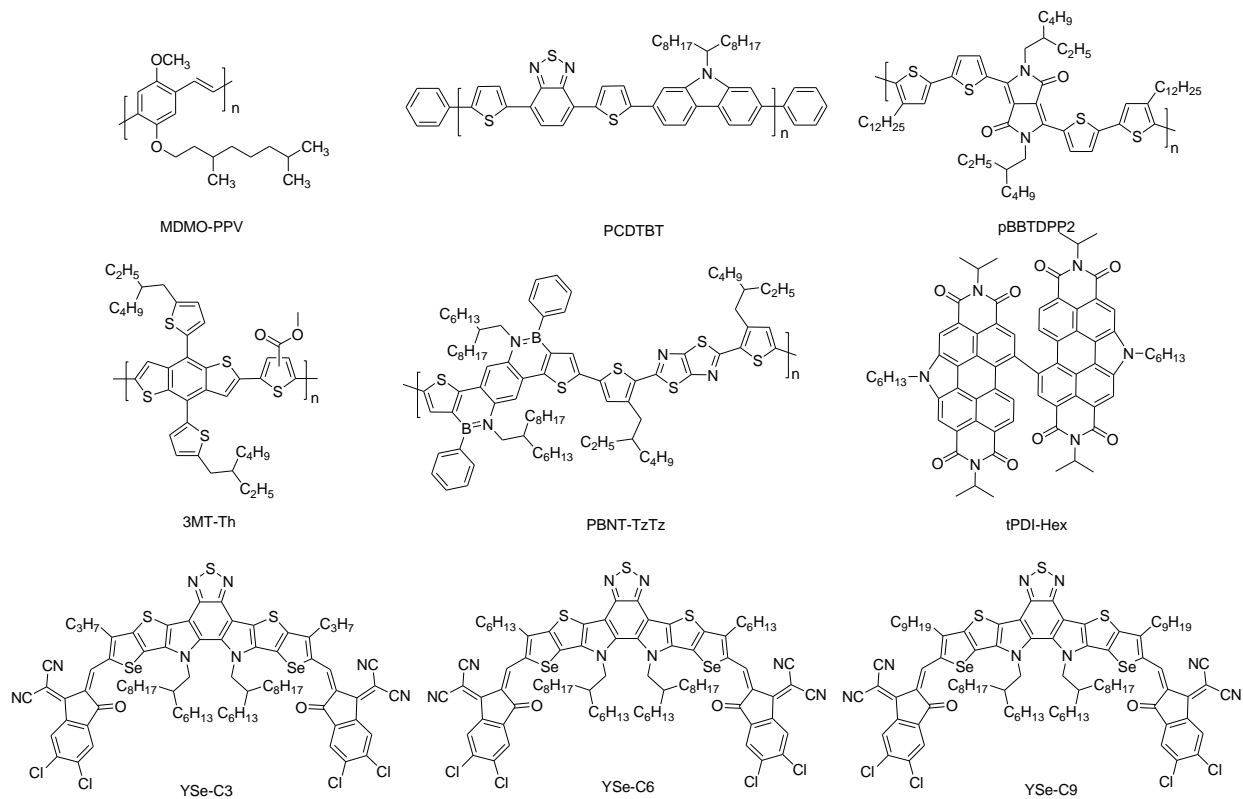
Figure 1.12 Polymer donors and acceptors in OSCs with processing solvent-induced morphology optimization.

Solvent additives

The addition of processing additives to blend solutions is a facial and effective strategy toward creating desirable BHJ morphology correlation with high photovoltaic performance. Solvent additives have been revealed to affect phase separation, molecular ordering, and crystalline nanostructures. In 2007, Heeger's group[114] for the first time reported a meaningful result in the effect of the alkanedithiol additive on morphology control, leading to an increased PCE from 2.8% to 5.5% without thermal annealing. Later, they clarified the mechanism of the processing additive

for morphology optimization.[115] Two criteria for the solvent additive have been identified: 1) the selective solubility for one of the components in the blend solution; and 2) a higher boiling point than the host processing solvent to ensure the interaction of processing additives and one of the components. They pointed out that alkanedithiol additives could selectively dissolve PCBM acceptors, while polymer donors were insoluble in alkanedithiol additives, resulting in the formation of three separate phases in fullerene-based blend films. In addition, they investigated a class of 1, 8-di(R)octanes as processing additives, and demonstrated that the 1, 8-diiodooctane (DIO) as the solvent additive provided the best efficiency. Since then, the DIO additive has been extensively used in fullerene-based OSCs to reduce fullerene aggregation and promote phase separation. Apart from the control of phase separation by the DIO additive, Guo et al.[116] found the influence of the DIO additive on the surface composition of the photoactive layer. The polymer donor would be enriched near the top surface, which could facilitate hole transport in the inverted device structure. Many successful studies proved that the incorporation of the DIO additive could boost the improvement of OSC efficiencies, especially in inverted device structures. However, stability studies have revealed that the DIO additive could accelerate the device degradation, since the residual DIO additive is difficult to be fully removed due to the high boiling point.[117, 118] Doumon et al.[119] investigated the degradation mechanism of OSCs caused by DIO additive. It indicated that the DIO additive could result in electron traps by the formation of iodine, dissolved hydroiodic acid and carbon-centered radicals under UV irradiation, which was detrimental to the device stability. In addition to the DIO additive, some halogenated additives have been reported in OSCs to control the morphology and enhance photovoltaic performance. Among them, 1-chloronaphthalene (1-CN) is one of the most widely used halogenated additives because of its selective solubility and high boiling point.[120, 121] Schmidt et al.[122] proposed the roles of 1-CN additive on the BHJ film. It indicated that the 1-CN additive could induce short stiff chain segments and short-range ordering in polymer aggregates, resulting in the crystallization of the polymer donor. Moreover, the BHJ blend film exhibited fine and intermixed phase-separated networks with the addition of the 1-CN, thereby favoring highly efficient OSCs with 1-CN as the solvent additive. Song et al.[103] employed a solvent additive strategy to reduce the E_{loss} by introducing diiodomethane (DIM) additive instead of DIO additive. DIM-processed PM6:L8-BO blend film possessed good morphology and charge transfer ability, leading to an excellent PCE of 18.6%.

Taking consideration of environmentally friendly processing OSCs, non-halogenated additives have been developed and chosen for future OSC technologies. Widely used green additives include 1, 8-octanedithiol (ODT),[123-125] 1-methylnaphthalene (MN),[126] diphenyl ether (DPE),[127-129] 1-phenylnaphthalene (PN),[128, 130, 131] and 3-methylthiophene (MT)[132, 133], etc. The ODT was the first reported green additive, which has been used in various systems. Salim et al.[123] systematically investigated the effect of alkanedithiols additives with different lengths of alkyl chains in the P3HT: $PC_{61}BM$ system. It was found that the boiling point and solubility of additives were critical to the degree of intermolecular interaction in the blend film. The ODT additive could provide optimized morphology and yield the best efficiency. In addition, Zhao et al.[134] introduced a novel green PN additive with an optimal alkyl chain length, which could drive the donor molecular orientation from edge-on to face-on relative to the substrate, and optimize the domain size and domain purity. Hence, the device efficiency dramatically increased from 6.4% to 11.7% with the addition of 2.5% PN into the blend solution. Xue et al.[135] reported a non-halogenated additive (methyl salicylate, MeSA) to modulate the morphology of the blend film. The addition of 7% MeSA was favorable to increase the crystallinity and form good interpenetrating network, leading to the significant improvement of the FF value in the PTB7-Th: $PC_{71}BM$ system from 49.26% to 70.11%. The structures of the above halogen and non-halogen solvent additives are shown in **Figure 1.13**.
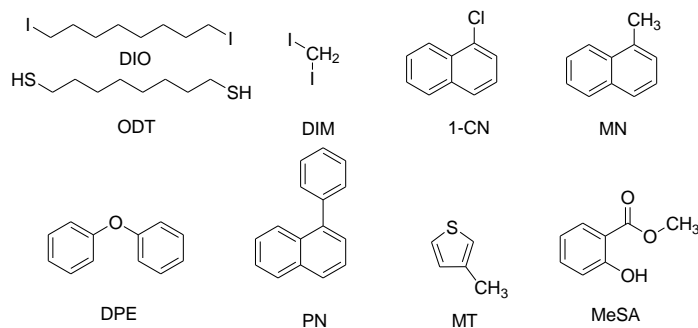
Figure 1.13 Halogen and non-halogen solvent additives for morphology optimization.

1.3.2.2 Post-treatment of the photoactive layer

Thermal annealing

Thermal annealing is a common post-treatment method for morphological rearrangement in BHJ photoactive layers, which is performed by heating the photoactive layer at a certain temperature for a certain period time after spin-coating the blending solution. This method is more effective

for highly crystalline materials to tune the crystallinity, molecular packing and domain size, which was for the first time successfully applied in the P3HT: PCBM system.[136, 137] After thermal annealing, grazing incidence XRD showed a sharp peak at $2\theta = 5.4^o$, revealing increased crystallinity of the P3HT. Furthermore, an ordered nanostructure was generated through the formation of the P3HT matrix and PCBM clusters, leading to an increase of the optical absorption. Moreover, NFA-based systems also need thermal annealing to control the morphology. Take high-performance NFA systems as examples, Li et al.[138] found that thermal annealing could control the vertical phase separation and increase the crystallinity of the PBDB-T: IT-M system. The PBDB-T would be rich on the top of the blend film at an annealing temperature of 80 °C, while the PBDB-T-rich on the top would be inhibited at an annealing temperature of 160 °C. Also, the crystallinity of the PBDB-T: ITIC system was increased after conducting thermal annealing, which thus achieved an excellent PCE exceeded 10%.[139, 140] Köntges et al.[140] found that the semi-crystalline ITIC acceptor could be formed from the polymorph in the photoactive layer due to the strong π-π interaction of electron-withdrawing groups during thermal annealing, which facilitated the formation of charge transport paths. In addition, Zhu et al.[141] investigated the influence of thermal annealing on the PM6: Y6 BHJ system through a series of characterization techniques. It was revealed that thermal annealing had a negligible effect on the molecular orientation, crystallinity, domain size and purities, while it forced Y6 vertical migration to the top surface of the blend film and changed the vertical phase separation of the PM6: Y6 blend film. As a result, the device showed increased charge mobility.

Solvent vapor annealing (SVA)

The SVA treatment is another effective method to control morphology and molecular rearrangement at room temperature, which is performed by placing the sample in a covered petri dish with a small amount of solvent after spin-coating. Because of the different solubility of donor and acceptor materials, their crystallinity and aggregation can be individually controlled by the SVA treatment. In 2005, Yang's group[136] employed this cost-effective SVA method to slow down the growth rate of the P3HT: PCBM photoactive layer for the first time, which facilitated the formation of a self-organized ordered structure, and thus achieved increased hole mobility and balanced charge transport. From then on, different solvents were chosen to anneal P3HT: PCBM blend films, which enabled increased molecular ordering and crystallinity of the P3HT.[142-144] The SVA post-treatment is also important for D-A polymer-based systems to optimize morphology

and improve photovoltaic performance. Chen et al.[145] reported that the solubility of the PCPDTBT donor and ICBA fullerene acceptor in annealing solvents played a significant role in the morphology of the blend film. The bromobenzene as an annealing solvent showed preferential solubility for the PCPDTBT donor, resulting in forming a non-uniform distribution of the ICBA, and thus deteriorating the device performance. However, the PCDTBT donor and ICBA acceptor had similar solubility in the DCB annealing solvent. After conducting the DCB solvent annealing, the blend film exhibited a better molecular ordering of the polymer and phase separation of the fullerene so as to obtain increased charge transport and enhanced device efficiency. In addition, Zheng et al.[146] systematically investigated the influence of the SVA treatment with different polar solvents (methanol, ethanol, dimethylsulfoxide, acetone and isopropanol) on the morphology of PTB7: $PC_{71}BM$ blend film. These polar solvents had different degrees of solubility and viscosity for the PTB7 donor and $PC_{71}BM$ acceptor. Among them, the methanol had high solubility and low viscosity so that the methanol SVA treatment could promote the formation of crystalline of PTB7: $PC_{71}BM$ blend and the properly aggregated $PC_{71}BM$. As a result, the device efficiency could be increased from 6.55% to 8.13%. According to the development of the SVA technology, researchers proposed an upside-down SVA (UD-SVA) technique to further optimize the morphology of the blend film and boost the device efficiency.[147] Jiao et al[148] applied the UD-SVA treatment on the NFA-based system with the PM7: IT-4Cl blend film (**Figure 1.14**). Four solvents, including dichloromethane (CH_2Cl_2), chloroform ($CHCl_3$), tetrahydrofuran (THF) and carbon disulfide (CS_2), were selected for the UD-SVA treatment. Among them, the OSC with the CS_2 UD-SVA treatment exhibited a well-developed morphology, which could promote efficient exciton dissociation and charge transport. Accordingly, the PCE of the PM7: IT-4Cl-based OSC could be up to 13.76%, which was more than 15% improvement in comparison with the as-cast OSC.
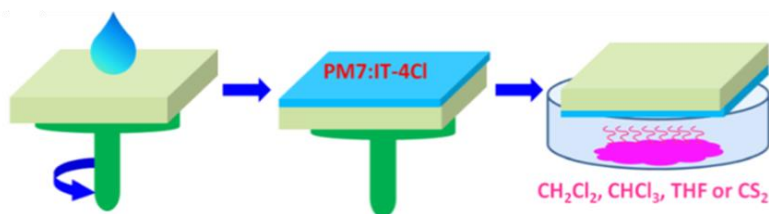
Figure 1.14 Schematic illustration of the photoactive layer fabrication with the UD-SVA treatment. Reprinted from ref. 148. Copyright 2020 Wiley.

1.3.2.3 Ternary blend strategy

The ternary blend strategy is a promising and extensive approach to optimize optoelectronic properties and morphology for achieving state-of-the-art photovoltaic performance, which consists of three components (D1: D2: A or D: A1: A2) in the photoactive layer. In particular, the third component can play a considerable role in modulating the crystallinity and miscibility of the photoactive layer and facilitating molecular stacking and phase separation. So far, the ternary blend strategy made great progress in morphology optimization, leading to a breakthrough efficiency of single-junction OSC over 19%.[9]

Crystallinity

In BHJ OSCs, the crystallinity of donor and acceptor materials is desirable to facilitate charge transport and increase charge mobility. However, excessive or poor crystallinity is not conducive to form appropriate domain size, which can induce charge recombination because of the short exciton lifetimes and diffusion length.[149] The crystallinity of host materials in the photoactive layer can be regulated by the ternary blend strategy. For instance, introducing a high crystalline component (the guest donor or acceptor) into the amorphous/relatively low crystalline host blend film can promote the molecular arrangement, thus improving the crystallinity and facilitating the charge mobility. For some conjugated polymers, their crystallinity is usually low owing to the high molecular weight.[150] For example, PTB7 and its derivative (PTB7-Th) have poor crystallinity, which leads to low hole mobility of OSCs based on PTB7: $PC_{71}BM$. Zhao et al.[151] incorporated a high crystalline PffBT4T-2OD polymer as the guest donor to increase the crystallinity of PTB7-Th: $PC_{71}BM$ blend film and optimize the morphology. 2D-GIWAXS measurements showed that introducing more content of the PffBT4T-2OD in the blend film could increase the crystallinity of the blend film. (**Figure 1.15**) The ternary film containing 15% PffBT4T-2OD exhibited appropriate domain size (25 nm) and domain purity, which was favorable to increase hole mobility and inhibit charge recombination, and thus afford a high J_{sc} value of 19.02 mA cm^{-2} and an FF value of 72.62%. Zhang et al.[152] introduced a high crystalline small molecule (p-DTS(FBTTH$_2$)$_2$) as the guest donor into the PTB7:$PC_{71}BM$ blend film, which increased the crystallinity and formed the face-on orientation without causing the change of the domain size. As a result, the hole mobility and the FF value in the ternary system were significantly increased. In contrast, poorly crystalline or amorphous guest components can interfere with the π-π stacking of host materials that show

29

high crystallinity, thus helping to alleviate too high crystallinity of the host blend film and form a homogeneous morphology with appropriate phase separation behavior. Xie et al.[153] introduced an amorphous fullerene acceptor (ICBA) as the guest acceptor into the PBT1-C: ITIC-2Cl blend film. It was found that the addition of the ICBA guest acceptor could decrease intermolecular π-π interactions of the crystalline ITIC-2Cl acceptor, which was beneficial for the film morphology, and efficient exciton dissociation and charge mobility. This ternary system containing 20% ICBA acceptor yielded a high PCE of 13.4% and FF of 76.8%.
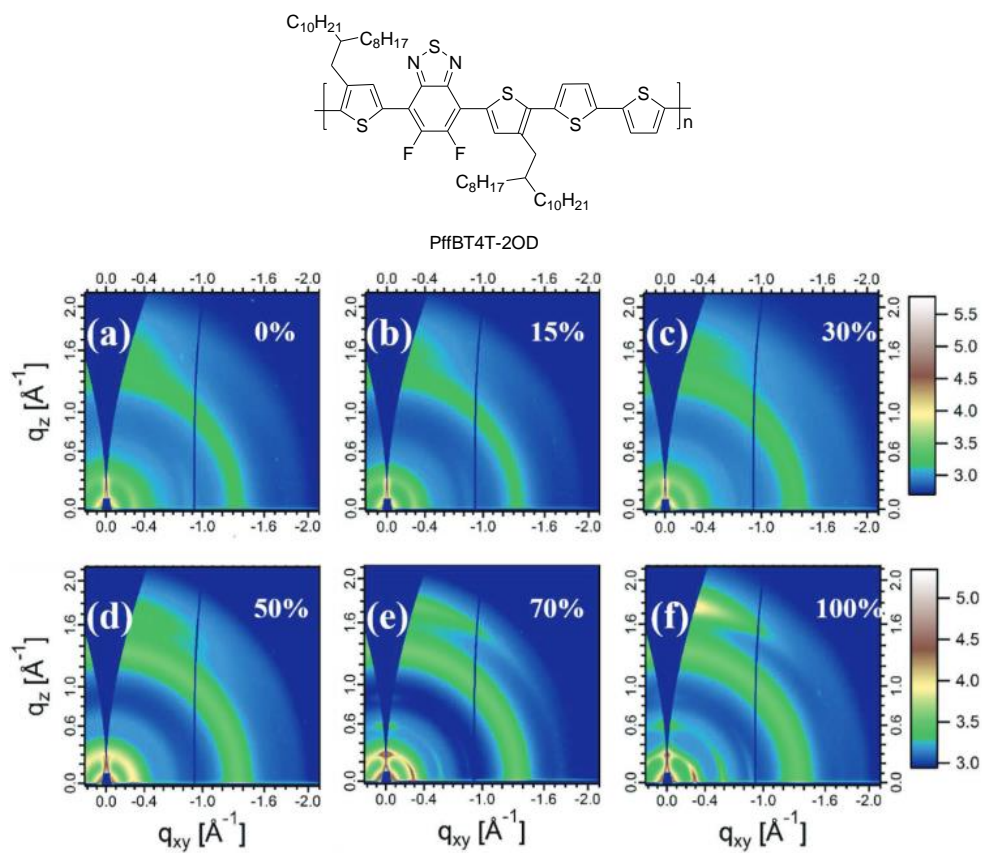
Figure 1.15 The chemical structure of the PffBT4T-2OD polymer. (a-f) 2D GIWAXS patterns of blend films with different weight ratio of the PffBT4T-2OD guest donor. Reprinted from ref. 151. Copyright 2017 Wiley.

Miscibility

The appropriate miscibility of photoactive layer materials is of vital importance for phase separation in BHJ photoactive layers. Excessively miscible materials tend to form small and impure phase domains in BHJ thin films, while immiscible materials favor high domain purity

with very large phase separation.[154] Herein, significant efforts have been made to increase or reduce the miscibility of materials by the introduction of guest components so as to achieve a near-ideal morphology. Thompson proposed the concept of an alloy model in BHJ blend films, in which the host component and the guest component are properly mixed to form alloy-like domains with a small Flory-Huggins interatcion.[155] Introducing guest component that has good compatibility with the host materials supports to form the alloy-like model in BHJ blend films, thus contributing to the formation of the desirable film morphology. Gao et al.[156] fabricated a highly efficient ternary OSCs with the host donor/acceptor materials (PM6 and BTP-4F-12) and the guest acceptor (IT-M). Due to good compatibility of BTP-4F-12 and IT-M acceptors, they could form an alloy-like state in the blend film. Thus, the IT-M guest acceptor could effectively regulate molecular arrangement and phase separation, which yielded a high-efficient thick-film OSC with an excellent PCE of 15.34%. Moreover, An et al.[157] synthesized a new polymer donor S3 that could form an alloy-like state with the PM6 donor due to their good compatibility, as confirmed by the small interfacial tension of these two donors in contact angle measurements. Thus, the morphology of the ternary blend film was optimized to form a more ordered molecular packing of the donors, which supported the increase of hole mobility. Besides, an effective strategy for the rational selection of guest components in the ternary system is proposed, i.e., the introduction of a guest component with similar chemical structures to the host material is beneficial to improve the miscibility. Li et al[158] replied on this strategy to select the BTP-F molecule as the guest acceptor that has the same central unit as the host BTP-eC9 acceptor, resulting in good compatibility between two acceptors. The 2D GIWAXS measurements indicated that the introduction of the BTP-F guest acceptor facilitated the formation of a more orderly molecular packing, yielding an impressive efficiency of 18.45%. Similarly, Cai et al.[159] reported highly efficient ternary OSCs by incorporating a novel guest acceptor, L8-BO-F, into the PM6: BTP-eC9 blend film. Two acceptors exhibited high miscibility due to their very similar chemical structures, which led to forming a homogenous mixed-phase and improve molecular ordering. As a result, a record efficiency of 18.66% was achieved in this best-performing ternary system. The chemical structures of the above acceptors and donors in ternary OSCs are shown in **Figure 1.16**.
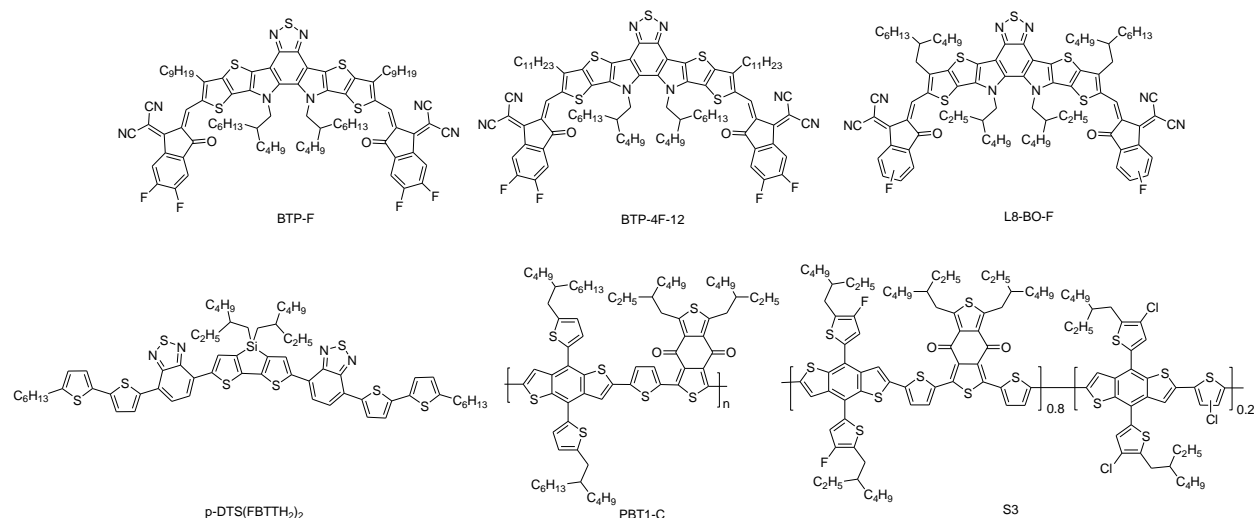
Figure 1.16 The chemical structures of acceptors and donors in ternary OSCs.

1.3.3 Interfacial modification

The contribution of interfacial layers to the OSC performance cannot be ignored. Interfacial layers have the inevitable potential to form Ohmic contacts between electrodes and the photoactive layer, tune the WFs of electrodes, optimize the surface morphology of the photoactive layer, modulate the light absorption of the photoactive layer by introducing nanomaterials with the plasmonic effect, and improve the device stability.[160] Herein, an appropriate interfacial layer is of vital importance for charge extraction and transport, and boost the device performance. There are two interfacial layers (i.e., HTL and ETL) in the OSC configuration that build bridges to transport electrons to the cathode and holes to the anode. In the past decade, researchers have made dramatic progress in the development of hole- and electron-transporting materials, which have helped to make a huge breakthrough in photovoltaic performance.

Generally, the HTL should meet some requirements: 1) the WF of the HTL is required to match the energy level of the donor material for hole transport; 2) the HTL has good compatibility with the photoactive layer and electrode to avoid surface defects; and 3) in an inverted device structure, the HTL should be highly transparent to transmit sunlight. Among the family of hole-transporting materials, PEDOT: PSS is a representative conducting polymer as the HTL in the conventional device structure due to its proper WF (~5.1 eV), high conductivity, ease of the solution processing and good transparency, which thus provided one of the best device efficiencies.[160, 161] In addition, vacuum-deposited metal oxides (e.g., MoO$_x$) are widely used as hole-transporting materials in an

inverted device structure owing to the high WF and excellent environmental stability.[162] Similar to properties of hole-transporting materials, electron-transporting materials should have low WF to match the energy level of the acceptor material for electron extraction or hole blocking, and good compatibility with the photoactive layer and the electrode. To date, a great number of polymers/organic small molecules, metal oxides, and hybrids/composites, have been widely used as electron-transporting materials. For example, metal oxides are currently predominant electron-transporting materials in the inverted OSC structure due to their high transparency, well-matched energy levels, and good ambient stability, such as ZnO, TiO_2, SnO_x and their doped composites. ZnO is the most representative metal oxide in the ETL, which is prepared by a sol-gel strategy using zinc salts as the precursor.[160] Very recently, Li et al.[161] fabricated an inverted OSC with the sol-gel-derived ZnO film as the ETL to achieve a high efficiency of over 16%. Furthermore, they introduced a 2-(3-(dimeth-ylamino) propyl)-1,3-dioxo-2,3-dihydro-1H-benzo[de]-isoquinoline-6,7-dicarboxylicacid (NMA) as the ZnO-modified material to address the photo-induced catalysis issue of the ZnO film. It was found that the hybrid ZnO/NMA film showed largely fewer oxygen defects, resulting in an increased PCE of 18.20% and enhanced device stability. (**Figure 1.17** a and b) In the conventional OSC structure, PDI-based electron-transporting materials (PDINN and PDINO) exhibits promising performances, since they have high conductivity, thickness-insensitive property, ability to downshift WFs of the metal electrodes, and good interfacial compatibility. (**Figure 1.17** c and d)[163, 164] With the help of PDI-based ETLs, the single-junction OSCs achieved the efficiency breakthrough.[165]
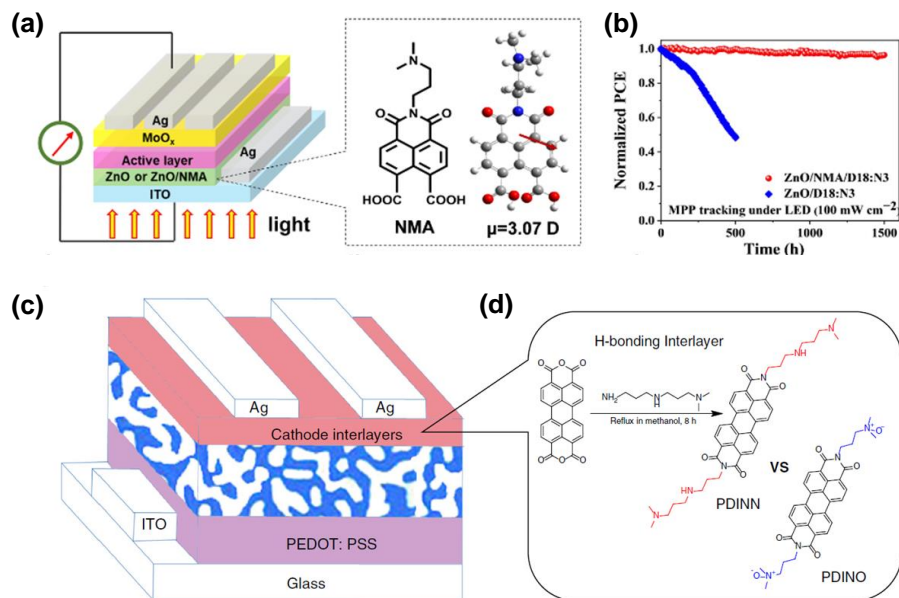
Figure 1.17 (a) The inverted device structure and chemical structure of NMA, and (b) photo-stability of devices based on ZnO and ZnO/NMA ETLs under light illumination. Reprinted from ref. 161. Copyright 2022 Wiley. (c) The conventional device structure, and (d) the synthetic route of the PDINN along with the chemical structures of PDINN and PDINO. Reprinted from ref. 164. Copyright 2020 Nature.

1.4 Research Objectives and Organization

1.4.1 Research objectives

With the aims of enhancement of photovoltaic performance through various approaches, such as ternary blend strategy, morphology optimization and interfacial modification, three research parts in the thesis were carried out as following:

Part I: Investigating photovoltaic performance enhancement of ternary solar cells via in-depth understanding the 3D morphology of ternary blend film

As all know, the introduction of a guest component with complementary absorption and well-matched energy level is a promising strategy to improve device efficiency. In addition, the desirable morphology of the photoactive layer with suitable phase separation and domain size can be achieved by adjusting the content of the guest component. However, it is still challenging to visualize 3D morphology of the blend film through traditional characterization techniques, such as AFM, TEM and scanning electron microscopy (SEM), especially for complex ternary blend morphology. The photoinduced force microscopy (PiFM) combining a high-resolution AFM with

infrared (IR) laser spectroscopy can characterize the surface morphology and the distribution of components in the photoactive layer by chemical identification. Moreover, the energy-filtered transmission electron microscopy (EF-TEM) with electron energy loss spectra (EELS) can probe the cross-sectional morphology of OSCs. Herein, the combination of these two advanced characterization techniques for 3D morphology characterization can gain insight into the role of the PDI-DPP-PDI acceptor in the morphological optimization of ternary blend films, thus helping to achieve highly efficient and stable OSCs.

Part II: Miscibility-driven morphological optimization enabling a high-efficient ternary solar cells via integrating non-fullerene guest acceptor (PDI-EH)

The BHJ morphological optimization in the photoactive layer is crucial and cannot be neglected, since the device performance is directly correlated with interpenetrating nanostructures, phase separation, domain size and domain purity. In most BHJ-OSCs, the crystallinity of donor and acceptor materials usually affects their miscibility and thus the phase separation. Too low or too high miscibility of donor and acceptor materials lead to the formation of large-scale or fully mixed phases, which can deteriorate device performance. Up to now, owing to the lack of quantitative information on the miscibility for achieving the optimal morphology, empirically fine-tuning the miscibility is also of vital importance. In ternary OSCs, the selection of a suitable guest molecule can fine-tune the miscibility of host donor and acceptor materials, and thus facilitate effective photo-generated charge carrier dynamic. Herein, in collaboration with Prof. Gregory C. Welch, a non-fullerene guest acceptor (PDI-EH) was rationally designed and synthesized to tune the miscibility of host donor and acceptor materials. In addition, in-depth understanding of the relationship between the optimal morphology and the resulting local charge carrier dynamic could facilitate the achievement of the desirable morphology.

Part III: Synergistic effect of polyelectrolyte PSS-coated plasmonic gold nanorods (GNRs@PSS) as rear interfacial modifiers on efficiency enhancement of non-fullerene-based solar cells

The photovoltaic performance of non-fullerene OSCs has made considerable progress. However, their efficiencies still lag behind the Si or perovskite solar cells, mainly because of the limited thickness of the photoactive layer (< 200 nm).[166] The strategy to enhance sunlight absorption without increasing the film thickness is critical to harvest more photons and thus increase

photovoltaic performance. In addition, the interfacial modification in OSCs is also beneficial for device efficiency improvement by optimizing the surface morphology and promoting interfacial contact. Integrating plasmonic metallic nanoparticles on the photoactive layer as sunlight concentrators and interfacial modifiers is an attractive way to simultaneously meet the above requirements, which can effectively increase sunlight absorption, promote charge transport and reduce charge recombination between the photoactive layer and electrode. Herein, by collaborating with Dr. Zhonglin Du, I investigated the structural features of the QDs synthesized by him through using advanced characterization techniques. I further introduced GNRs@PSS as rear interfacial modifiers into non-fullerene-based OSCs to pursue high photovoltaic performance.

1.4.2 Thesis organization

The thesis is divided into three chapters which are organized as follows:

Chapter 1 Introduction: This chapter describes the basic background and working mechanisms of organic photovoltaic devices, and research progress on improving photovoltaic performance. Meanwhile, the objectives are presented here.

Chapter 2 Experimental and Characterization: This section describes the information on chemicals and materials, solution preparation (ZnO precursor solution and photoactive layer solutions), materials synthesis (PDI-EH molecule and GNRs@PSS nanomaterials), and devices fabrication (PTB7: $PC_{61}BM$-based binary and ternary devices, PBDB-T: ITIC-4F-based binary and ternary devices, and GNRs@PSS integrated devices). Moreover, the main characterization techniques of photoactive layers and devices are presented.

Chapter 3 Research Results: This chapter is divided into three parts.

Parts I: Fabricating ternary solar cells containing the PDI-DPP-PDI non-fullerene guest acceptor, and 3D-nanoscale morphology characterization. The related publication is shown:

Ting Yu, Wanting He, Jafari Maziar, Tugrul Guner, Pandeng Li, Mohamed Siaj, Ricardo Izquierdo, Baoquan Sun, Gregory C. Welch, Aycan Yurtsever and Dongling Ma, Three-dimensional nanoscale morphology characterization of ternary organic solar cells, *Small Methods*, 2022, *6*, 2100916.

Part II: Miscibility-driven morphological optimization by introducing the PDI-EH non-fullerene guest acceptor into the photoactive layer and in-depth understanding of relationship between morphology and performance variation. The related publication is shown:

Ting Yu, Francesco Tintori, Yuchen Zhang, Wanting He, Edward Cieplechowicz, Raja Sekhar Bobba, Poojan Indrajeet Kaswekar, Maziar Jafari, Yuxuan Che, Yong Wang, Mohamed Siaj, Ricardo Izquierdo, Dmytro F. Perepichka, Quinn Qiao, Gregory C. Welch and Dongling Ma, Miscibility driven morphology modulation in ternary solar cells, *J. Mater. Chem. A,* **2023**, *11*, 5037-5047.

Part III: Fabricating highly efficient non-fullerene solar cells by integrating GNRs@PSS plasmonic nanoparticles as interfacial modifiers. The related publication is shown:

Zhonglin Du[1], Ting Yu[1], Wanting He, Aycan Yurtsever, Ricardo Izquierdo, Maziar Jafari, Mohamed Siaj and Dongling Ma, Enhancing efficiency of non-fullerene organic solar cells via using polyelectrolyte-coated plasmonic gold nanorods as rear interfacial modifiers, *ACS Appl. Mater. Interfaces* 2022, *14*, 16185-16196.

CHAPTER 2   EXPERIMENTAL AND CHARACTERIZATION

In this chapter, experimental details of materials, solution preparation, photovoltaic device fabrication, and related characterization are described. Firstly, information on chemicals and materials is briefly presented. Next, the solution preparation of photoactive layers is depicted. Then, fabrication processes of ternary devices with PTB7: $PC_{61}BM$: PDI-DPP-PDI and PBDB-T: ITIC-4F: PDI-EH photoactive layers, and PBDB-T: ITIC-4F-based binary device with interfacial modification are described in detail. Finally, performance characterizations on blend films and devices are presented.

2.1 Chemicals and Materials

Polymer donors (PTB7 and PBDB-T), acceptors ($PC_{61}BM$ and ITIC-4F/ITIC-2F), and 1, 8-diiodooctane (DIO) additive were purchased from the 1-Material company (Canada). Patterned ITO-coated glass substrates ($Rs \leq 10\ \Omega$ square^{-1}, $Tr \geq 83\%$) were purchased from Shenzhen Huayu Union Technology Co., Ltd. (China). In addition, zinc acetate dihydrate (Zn $(CH_3COO)_2 \cdot 2H_2O$, 99.9%), ethanolamine ($NH_2CH_2CH_2OH$, 99.5%), 2-methoxyethanol ($CH_3OCH_2CH_2OH$, 99.8%), chlorobenzene (CB), lithium fluoride (LiF), and molybdenum trioxide (MoO_3) were obtained from Sigma-Aldrich without further purification. Poly (3, 4-ethylene dioxythiophene)-poly (styrene sulfonate) (PEDOT: PSS, Clevios™ P VP AI 4083) was obtained from Heraeus. PDI-DPP-PDI and PDI-EH were synthesized by collaborator - Prof. Gregory C. Welch's group. GNRs@PSS nanorods were synthesized by collaborator - Prof. Zhonglin Du.

2.2 Solutions Preparation

2.2.1 Preparation of the ZnO precursor solution

The ZnO precursor solution was prepared according to a reported procedure.[160] Briefly, Zn($CH_3COO)_2 \cdot 2H_2O$, (1 g) was dissolved in the $CH_3OCH_2CH_2OH$ solution (10 mL) followed by the addition of the $NH_2CH_2CH_2OH$ (0.28 g) under vigorous stirring overnight in ambient conditions. Then the resulting ZnO precursor solution was filtered with the PTFE filter (0.45 μm) before use.

2.2.2 Preparation of binary and ternary blend solutions

The PTB7: $PC_{61}BM$-based binary blend solution was prepared by dissolving the PTB7 polymer and $PC_{61}BM$ in the CB solvent with a weight ratio of 1: 1.5 and a concentration of 25 mg mL^{-1}. Then, the resulting solution was stirred and heated at 60 $^{\circ}$C overnight. Before casting the solution on the substrate, 3 % volume ratio of the DIO additive was added and stirred for 30 min. The PTB7: $PC_{61}BM$-based ternary blend solution was prepared in the same way as the binary solution, but with different contents of the PDI-DPP-PDI guest molecule introduced (10%, 20% and 30%).

The PBDB-T: ITIC-4F-based binary blend solution was prepared by dissolving the PBDB-T polymer and ITIC-4F in the CB solvent with a weight ratio of 1: 1 and a concentration of 20 mg mL^{-1}. Then, the resulting solution was stirred and heated at 90 $^{\circ}$C overnight. Before casting the solution on the substrate, 0.5 % volume ratio of the DIO additive was added and stirred for 30 min. The PBDB-T: ITIC-4F-based ternary blend solution was prepared in the same way as the binary solution, but with different contents of the PDI-EH guest molecule introduced (10%, 20% and 50%).

2.3 Synthesis of Materials

2.3.1 Synthesis of PDI-EH molecule

In a 20 mL microwave vial 2,5-bis(1-octyl)-3,6-di(thiophen-2-yl)diketopyrrolopyrrole (76 mg, 1 eq.), 11-bromo-5-ethylhexyl-2,8-bis(1-ethylpropyl)perylene diimide (234 mg, 2.2 eq.), Silia*Cat*® DPP-Pd (29 mg, 5 mol %), pivalic acid (5 mg, 30 mol %) and cesium carbonate (120 mg, 2.5 eq.) were added with a stir bar and sealed with a crimp sealed septa cap. The contents were purged with N_2 gas followed by the addition of degassed anhydrous *N, N'*-dimethylacetamide (5.3 mL) via syringe. The reaction mixture was heated at 100 °C in a LabArmor® beads bath for 24 hours. After 24 hours the reaction mixture was poured into acetone and allowed to stir for one hour. The precipitated product was collected by filtration and the filtrate was discarded. The solid product was subsequently washed with dichloromethane to solubilize and isolate it from the insoluble silica-supported catalyst using a silica gel plug. The filtrate was concentrated by rotary evaporation and solubilized in a minimal amount of $CHCl_3$. Ethyl acetate was added dropwise over several hours to the $CHCl_3$ solution and allowed to stir overnight. The precipitated product was isolated by filtration. This yielded a dark solid product (186 mg, 70 % yield). The synthetic route of PDI-EH molecule was shown in **Figure 2.1**.
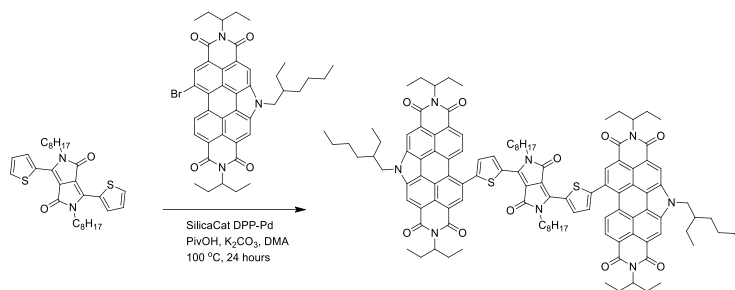
Figure 2.1 The synthetic route of PDI-EH molecule.

2.3.2 Synthesis of GNRs@PSS nanomaterials

Synthesis of cetrimonium bromide (CTAB)-stabilized GNRs: The CTAB-stabilized GNRs were prepared through a seed-mediated growth method in an aqueous solution. Briefly, the fresh seed solution was prepared by the addition of ice-cold $NaBH_4$ solution (0.6 mL, 0.01 M) into a mixture containing $HAuCl_4$ (0.25 mL, 0.01 M) and CTAB (9.75 mL, 0.1 M), and kept at room temperature for 2 h before use. The growth solution was prepared by the sequential addition of $HAuCl_4$ (2 mL, 0.01 M), $AgNO_3$ (0.4 mL, 0.01 M), HCl (0.8 mL, 1.0 M) and ascorbic acid (0.32 mL, 0.1 M) into CTAB (40 mL, 0.1 M). The growth solution was stirred for 30 s and then, the seed solution (0.1 mL) was rapidly added for growing the GNRs. The reaction solution was well mixed by upside-down inversions several times, then kept at 30 °C overnight. After centrifugation, the obtained pellet was redispersed in deionized water.

Synthesis of GNRs@PSS: The GNRs@PSS nanostructures were prepared using the seed-mediated growth method followed by the electrostatic adsorption of PSS.[167] The resulting CTAB-stabilized GNRs (~0.2 mL) were subsequently added into 10 mL of aqueous PSS solution (2 g L^- ^{1}, containing 6 mM NaCl), and the mixture was stirred at room temperature for 6 h. Then, the PSS-encapsulated GNRs were purified by repeating the centrifugation/re-dispersion process three times and finally dispersed into methanol (~1.0 mL) for further use.

2.4 Device Fabrication

First, the patterned ITO glass was washed sequentially in an ultrasonic bath with deionized water, acetone and isopropyl alcohol, and treated in an ultraviolet-ozone chamber for 10 min. Then, the cleaned ITO glass was spin-coated with a ZnO precursor solution at 4500 rpm for 60 s and sintered at 200 °C for 1 h in air. Subsequently, photoactive layers consisting of PBDB-T: ITIC-4F-based binary and ternary blend solutions were spin-coated on the surface of the ZnO layer at 3000 rpm

for 1 min in the glovebox (PTB7: $PC_{61}BM$-based binary and ternary blend solutions were spin-coated on the surface of the ZnO layer at 2000 rpm for 2 min in the glovebox). For the GNRs@PSS integrated OSCs, the moderate GNRs@PSS methanol solution was spin-coated on the PBDB-T: ITIC-4F-based photoactive layer at 3000 rpm for 1 min. Finally, the MoO_3 layer (ca. 25 nm) and Ag electrode (ca. 100 nm) were slowly evaporated onto the surface of the photoactive layer in a vacuum chamber.

2.5 Characterizations

2.5.1 Characterization of photovoltaic performance

The *J-V* curves of OSCs were measured by a Keithley 2400 source meter illuminated under AM 1.5G spectrum from a solar simulator (Oriel, Model No. 94022A). Light intensity was calibrated to be 100 mW cm^{-2} by using an NREL Si solar reference cell. The external quantum efficiency (EQE) measurements were carried out on a Keithley 2000 multimeter under an illumination of 300 W tungsten lamp with a Spectral DK240 monochromator. Raman characterization was performed on a micro-Raman spectrometer (InVia; Renishaw UK) with charge-coupled device detectors. The electron and hole mobility were measured by using the method of space-charge limited current (SCLC) for electron-only devices with the configuration of ITO/ZnO/photoactive layer/LiF/Al and hole-only devices with the configuration of ITO/PEDOT: PSS/photoactive layer/MoO_3/Ag. The charge carrier mobility was determined by fitting the dark current to the model of a single carrier SCLC according to the equation: $J = 9\varepsilon_0\varepsilon_r\mu V^2/8d^3$, where J is the current density, d is the film thickness of the active layer, μ is the charge carrier mobility, ε_r is the relative dielectric constant of the transport medium, and ε_0 is the permittivity of free space. $V = V_{app} - V_{bi}$, where V_{app} is the applied voltage, V_{bi} is the offset voltage. The carrier mobility can be calculated from the slope of the $J^{0.5} \sim V$ curves.

2.5.2 Microscopies and spectroscopies

The transmission electron microscopy (TEM) measurements were performed with accelerating voltage of 200 keV on a JEM-2100PLUS (JEOL) transmission electron microscope. A series of energy-filtered transmission electron microscopy (EF-TEM) images were collected at different central energy of filter with energy slit 4 eV in the range of 16 eV-36 eV. The absorption spectra were measured on a Cary 5000 UV-vis-NIR spectrophotometer (Varian). Atomic force

microscopy (AFM) was conducted to obtain the topography images of active layers on Bruker MultiMode & AFM in the ScanAsyst mode.

The photoinduced force microscopy (PiFM) data were acquired on a VistaScope-infrared (IR) microscope from Molecular Vista, Inc, using PtIr-coated silicon cantilevers (PtIr-NCHR) from Nanosensors. The microscope was operated in dynamic mode using the first mechanical mode of the cantilever to detect the PiFM and the second mechanical mode to detect the topography of the sample. The IR source used to excite the sample was manufactured from Block Engineering at the tunable range of 770 cm^{-1} to 1950 cm^{-1}. Spectral acquisition time was 30 seconds for the presented spectra. All spectra have been normalized against the power profile of the laser. Python programming, a major tool for image processing, was applied here in order to get quantitative information on domain size distribution and composition. We first developed our own Python script, and 99.8% Gaussian distribution of contrast was chosen, showing the values of μ-3σ to μ+3σ (99.8%, μ = mean, σ = standard deviation) in original data of PTB7-based and $PC_{61}BM$-based PiFM images. We then normalized the contrasted PiFM images using the min-max normalization approach before image analysis. Then, the normalized PiFM images were integrated through manual thresholding, resulting in the segmentation of domains in the integrated PiFM image well matched with original, superimposed PiFM image. The percentages of three regions, mixed, PTB7-rich and $PC_{61}BM$-rich, were accordingly extracted. From these processed images, the size distribution of the aggregated $PC_{61}BM$ domain was further acquired by conducting a contour detection algorithm, which permits the detection and size calculation of the object of interest.

Transient photo-response atomic force microscopy (TP-AFM) mounted on the conductive AFM (Agilent 5500) was conducted to measure local transient photovoltage (TPV) and transient photocurrent (TPC) decays at different locations on the donor-acceptor blend by using the contact mode. The green laser (MGL-I-532 DPSS; 532 nm) was illuminated from the bottom of ITO glass. A budget sensor (platinum/ chromium coated silicon conductive tip) was used in this measurement. A breakout box (Agilent N9447A) was connected to the oscilloscope (Agilent MSOX4154A) to receive the transient signal from the AFM.

Grazing-incidence X-ray diffraction (GIXRD) measurement was carried out at the BL14B1 beamline of the Shanghai Synchrotron Radiation Facility using incident X-ray with a wavelength

of 1.24 Å. The 2D-GIXRD pattern, out-of-plane (OOP) and in plane (IP) curves were analyzed by using the Fit 2D software. Differential scanning calorimetry (DSC) measurements were carried out in the temperature range from 30 ºC to 350 ºC under the nitrogen stream with a heating rate of 10 ºC /min. Baseline and temperature were calibrated with Indium and Zinc. Photoluminescence (PL) spectra were acquired on a Fluorolog-3 system (Horiba Jobin Yvon) using an excitation wavelength of 500 nm. Photoluminescence (PL) spectra were acquired on a Fluorolog®-3 system (Horiba Jobin Yvon) using an excitation wavelength of 500 nm.

2.5.3 Contact angle measurements

Contact angle measurements were performed on a contact angle analyzer equiped with an AM211 Dino-Lite camera under the ambient temperature. A deionized water and ethylene glycol droplet of 6 µL volume was placed on the dry surface. The surface tension values of films were calculated using the Owens-Wendt model:

$$\gamma_L (1+\cos\theta) = 2\sqrt{\gamma_s^d \, \gamma_L^d} + 2\sqrt{\gamma_s^p \, \gamma_L^p}$$

where γ_s^d and γ_L^d refer to dispersion tension of plane surface and liquid, γ_s^p and γ_L^p refer to polar components of the surface energy of plane surface and liquid, while γ_L refers to total tension of liquid.

2.5.4 Cyclic voltammetry measurement

The instrument used for the electrochemical measurements was a CH instrument 620E potentiostate. The instrument used a standard three-electrode configuration: Ag wire pseudo-reference electrode, Pt wire counter electrode, and glassy carbon working electrode. Experiments were performed in anhydrous dichloromethane (CH_2Cl_2), which was further degassed with a N_2 gas spurge for 10 minutes. Tetrabutylammonium hexafluorophosphate ($TBAPF_6$) was used as the supporting electrolyte. CV sample concentration was ~0.4 mg/mL. The ionization potentials (IP) and electron affinities (EA) were estimated by correlating the onsets of ferrocene (Fc)/Fc^+ redox couple (E_{ox} $^{Fc/Fc+}$, E_{red} $^{Fc/Fc+}$) to the normal hydrogen electrode (NHE), assuming the IP of Fc/Fc^+ redox couple to be 4.80 eV.

$$E(IP) = (E_{ox}+4.80), \quad E(EA) = (E_{red}+4.80)$$

CHAPTER 3   RESEARCH RESULTS

3.1 3D Nanoscale Morphology Characterization of Ternary Organic Solar Cells

Ting Yu, Wanting He, Maziar Jafari, Tugrul Guner, Pandeng Li, Mohamed Siaj, Ricardo Izquierdo, Baoquan Sun, Gregory C. Welch, Aycan Yurtsever, and Dongling Ma
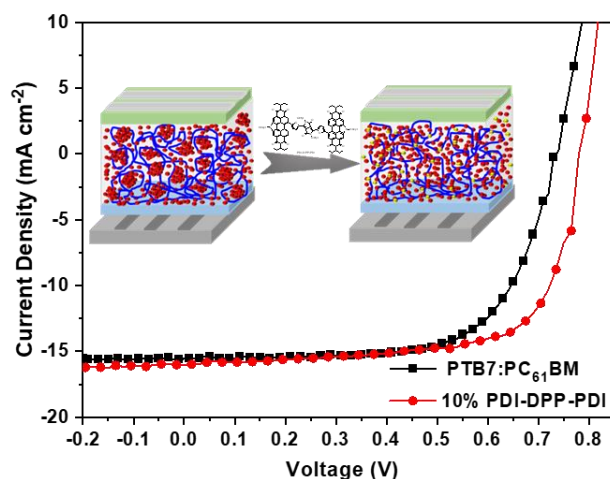
As introduced in Chapter 1, organic solar cells (OSCs) are considered to be one of the promising photovoltaic devices because of their low cost, lightweight, good processability, and ease of fabrication into large-area devices. However, the efficiency and stability of OSCs are still important factors limiting their practical application. Constructing ternary OSCs with complementary absorption spectra and well-matched energy structure of three components in the photoactive layer is an efficient method to enhance the photocurrent and photovoltage of single-junction devices while remaining a simple fabrication process. Meanwhile, the morphology of the photoactive layer can be finely optimized by selecting a suitable guest component and thus improve the performance of ternary OSCs. More importantly, the development of advanced characterization techniques can resolve the complex morphology of the ternary blend film, which provides an effective guidance for device optimization.

In this work, we integrated highly air-stable perylene diimide (PDI)-based non-fullerene acceptor (PDI-DPP-PDI) into PTB7: $PC_{61}BM$-based OSCs as the third component to fabricate ternary OSCs. This cascade band structure showed a better energy level alignment and complementary

absorption, thus demonstrating increased efficiency of ternary devices. Besides, the three-dimensional (3D) nanoscale morphology of ternary blend films was characterized in depth by photo-induced force microscopy (PiFM) coupled with infrared (IR) laser spectroscopy and energy-filtered transmission electron microscopy (EF-TEM), which could qualitatively and quantitatively "view" the surface and cross-sectional morphology. The results provided strong evidence that the PDI-DPP-PDI guest acceptor could suppress the aggregation of the fullerene molecules and generate the homogenous morphology with a higher-level of the molecularly mixed phase, thereby inhibiting charge recombination and stabilizing the morphology of the photoactive layer. Our work represents the first exploration of morphology characterization in a real device setting using advanced characterization techniques and provides a very promising approach to achieve highly stable devices and simultaneously improve photovoltaic performance.

3D Nanoscale Morphology Characterization of Ternary Organic Solar Cells

Ting Yu, Wanting He, Maziar Jafari, Tugrul Guner, Pandeng Li, Mohamed Siaj,
Ricardo Izquierdo, Baoquan Sun, Gregory C. Welch, Aycan Yurtsever, and Dongling Ma*

It is highly desired to develop advanced characterization techniques to explore the 3D nanoscale morphology of the complicated blend film of ternary organic solar cells (OSCs). Here, ternary OSCs are constructed by incorporating the nonfullerene acceptor perylenediimide (PDI)-diketopyrrolopyrrole (DPP)-PDI and their morphology is characterized in depth to understand the performance variation. In particular, photoinduced force microscopy (PiFM) coupled with infrared laser spectroscopy is conducted to qualitatively study the distribution of donor and acceptors in the blend film by chemical identification and to quantitatively probe the segmentation of domains and the domain size distribution after PDI-DPP-PDI acceptor incorporation by PiFM imaging and data processing. In addition, the energy-filtered transmission electron microscopy with energy loss spectra is utilized to visualize the nanoscale morphology of ultrathin cross-sections in the configuration of the real ternary device for the first time in the field of photovoltaics. These measurements allow to "view" the surface and cross-sectional morphology and provide strong evidence that the PDI-DPP-PDI acceptor can suppress the aggregation of the fullerene molecules and generate the homogenous morphology with a higher-level of the molecularly mixed phase, which can prevent the charge recombination and stabilize the morphology of photoactive layer.

1. Introduction

Solar energy is a renewable green energy, which can be directly converted to electricity through solar cells. Among different types of solar cells, organic solar cells (OSCs) are considered as the promising, next generation of photovoltaic technology because of their low cost, lightweight, good processability, and easy fabrication into large-area devices in various shapes.[1] At the present, the power conversion efficiency (PCE) of the most common single junction devices based on fullerene acceptors and their derivatives already exceeds 11%;[2] the further increase of PCE is however required for practical application. To this end, enhancement of photon absorption by, for example, constructing tandem OSCs with two or more sub-cells of complementary absorption spectra is an attractive strategy. But it remains very challenging to engineer each active layer and the intermediate layer of tandem OSCs.[3] Recently, developing the ternary OSCs with three photoactive materials turns out to be an efficient way to enhance the photon harvesting of single junction devices while maintaining a relatively simple fabrication process.[4,5] Importantly, introducing the third component as a charge cascade material, which can act as a charge-gradient bridge, could help effectively transfer the electron and hole to the cathode and anode, resulting in the significant increase of short-circuit current (J_{sc}). In this regard, nonfullerene acceptors offer many appealing features, including structural versatility, and tunable optical and electronic properties, which allow to realize the appropriate energy level alignment and the complementary absorption for ternary OSCs.[6–9]

Optimizing morphology is another critical approach for improving device performance.[10–13] A continuous

T. Yu, W. He, T. Guner, P. Li, A. Yurtsever, D. Ma
Énergie, Matériaux et Télécommunications
Institut National de la Recherche Scientifique (INRS)
Varennes, Québec J3X 1S2, Canada
E-mail: ma@emt.inrs.ca
M. Jafari, M. Siaj
Département de Chimie
Université du Québec à Montréal
Montréal, Québec H2L 2C4, Canada
R. Izquierdo
Département de Génie Électrique
École de Technologie Supérieure
Montréal, Québec H3C 1K3, Canada

B. Sun
Jiangsu Key Laboratory for Carbon-Based Functional Materials and Devices Institute of Functional Nano and Soft Materials (FUNSOM)
Joint International Research Laboratory of Carbon-Based Functional Materials and Devices
Soochow University
Suzhou 215123, P. R. China
G. C. Welch
Department of Chemistry
University of Calgary
Calgary, Alberta T2N 1N4, Canada

**ADVANCED
SCIENCE NEWS**
www.advancedsciencenews.com

**small
methods**
www.small-methods.com

interpenetrating network structure is indispensable to achieve the effective charge transfer at the donor/acceptor interface. In contrast, an inappropriate domain size would highly likely result in undesirable geminate recombination.[14] Besides, incomplete phase separation and the incompatibility of donor and acceptor materials in blend films can cause an inhomogeneous phase morphology, thereby leading to the interfacial defect that may act as charge carrier trap sites.[15] Introducing the third component is an effective way to fine-tune the morphology in the blend film in addition to commonly used strategies of solvent additive engineering, and thermal and solvent vapor annealing.[16,17] To date, the efforts on ternary OSCs have been mainly focused on the use of nonfullerene acceptors as the third component, which appears as a promising way for the morphological optimization. For example, Chen et al. fabricated highly efficient ternary solar cells including a nonfullerene acceptor composed of tetraphenylethylene core and four perylenediimide (PDI) as the third component, which played an active role in tuning morphology and promoting charge generation, separation, and collection.[18]

Stability is as crucial as the high PCE for the commercial application of the OSCs. The OSCs based on poly[[4,8-bis [(2-ethylhexyl) oxy] benzo [1,2-b:4,5-b′] dithiophene-2,6-diyl] [3-fluoro-2-[(2-ethylhexyl) carbonyl] thieno [3,4-b] thiophenediyl]]: phenyl-C_{61}-butyric acid methyl ester (PTB7:PC_{61}BM) blend films have been extensively studied in recent years, showing good photovoltaic performance. However, the PTB7:PC_{61}BM blend film presents the intrinsic drawbacks of air and light instability.[19–22] Different strategies, such as employing an inverted device structure,[23] adjusting manufacturing processes,[24,25] and using air-stable materials,[26,27] have been explored to enhance device stability. Among them, introducing air-stable and photostable materials into the PTB7:PC_{61}BM blend film seems most convenient and effective. Further considering that nonfullerene materials exhibit high thermal, light and chemical stability, using nonfullerene materials in OSCs is an attractive option.

Based on the aforementioned discussion, integrating the complementarily absorbing, energy-level-matching, stable nonfullerene acceptor as the third component can potentially contribute to both enhanced efficiency and stability of OSCs with the morphological optimization of the photoactive layer being a key factor. Although a series of techniques have been used to characterize the morphology of the surface of blend films, such as atomic force microscopy (AFM) and scanning electron microscopy (SEM),[5,28] it is challenging to visualize 3D morphology, in particular, in real device setting.

In this work, for the first time, we analyze the nanoscale morphology of the cross-section of the photoactive layer in real ternary OSC device setting by combining energy-filtered transmission electron microscopy (EFTEM) imaging with electron energy loss spectra (EELS) in addition to qualitatively and quantitatively probing the distribution of the donor and acceptor on the surface of the photoactive layer by photoinduced force microscopy (PiFM). A PDI flanked diketopyrrolopyrrole (DPP) π-conjugated small molecule PDI-DPP-PDI, recently synthesized by our team, was selected to be the third component to be added into PTB7:PC_{61}BM blend film due to its good air stability and photostability over a 35-day evaluation period.[29]

PDI-DPP-PDI acceptor has good absorption in a range of 400–650 nm, which gives good complementary absorption with PTB7 donor and PC_{61}BM acceptor, resulting in overall more photons absorption. By adjusting the contents of PDI-DPP-PDI, 10% PDI-DPP-PDI incorporation in ternary OSCs could inhibit the aggregation of PC_{61}BM acceptor in a molecularly mixed continuous phase to get homogeneous morphology due to the improved compatibility of donor and acceptors, which is beneficial for charge transfer. As a result, we achieved a high fill factor (FF) of 70.02% and a high PCE of 8.71%, representing 14.6% enhancement with respect to the corresponding binary OSCs. Meanwhile, optimized morphology of the active layer with air-stable and photostable PDI-DPP-PDI could reduce the charge trapping and recombination so that the encapsulated ternary OSCs have better air stability, humidity resistance, and photostability with respect to the corresponding binary OSCs. With in-depth investigations, the favorable role of PDI-DPP-PDI was clearly revealed. We report the photo- and device-physics that are responsible for this significant improvement in ternary device performance. Moreover, the explored characterization techniques may be extended to other solar cell systems and provide more understanding and thus contributing to the general development of solar cells.

2. Results and Discussion

Chemical structures and energy levels of PTB7, PC_{61}BM, and PDI-DPP-PDI of ternary OSCs are presented in **Figure 1**a,b. The highest occupied molecular orbital/lowest unoccupied molecular orbital energy levels of PDI-DPP-PDI are -5.30/-3.70 eV based on cyclic voltammetry measurements, respectively, which are in between PTB7 (−5.15/−3.31 eV) and PC_{61}BM (−5.85/−3.89 eV),[30,31] and are thus appropriate to form an excellent charge-cascade structure. The charge-cascade structure with good energy level alignment could simultaneously promote both the hole and electron transportation, which is beneficial for improving the J_{sc}. Additionally, the ultraviolet-visible (UV–vis) absorption of pristine PTB7, PC_{61}BM, and PDI-DPP-PDI thin films was measured to investigate the optical properties. As shown in Figure 1c, the main absorption range of PDI-DPP-PDI thin film was from 400 to 650 nm, which effectively compensates for the weak absorption of PTB7 and PC_{61}BM in the wavelength ranging from 400 to 600 nm, and thus increases overall photon absorption of OSCs.

We fabricated the ternary OSCs with an inverted structure of indium tin oxides (ITO) glass/ZnO/ternary blend film/MoO_3/Ag (Figure 1a). For the active layer fabrication, we kept the ratio of donor to acceptor at 1:1.5 (w/w), while adding different weight percentages of PDI-DPP-PDI into the blend solution with 3% 1,8-diiodooctane (DIO) as a solvent additive. DIO was applied to promote the dispersion of PC_{61}BM in the blend film and thereby be beneficial for OSC performance.[32] From the UV–vis absorption spectra of binary or ternary blend films fabricated with or without involving 3% DIO in Figure S1 in the Supporting Information, it can be seen that adding 3% DIO additive significantly increased the absorption intensity and further redshifted the maximum absorption peak. **Figure 2**a

**ADVANCED
SCIENCE NEWS**
www.advancedsciencenews.com

**small
methods**
www.small-methods.com
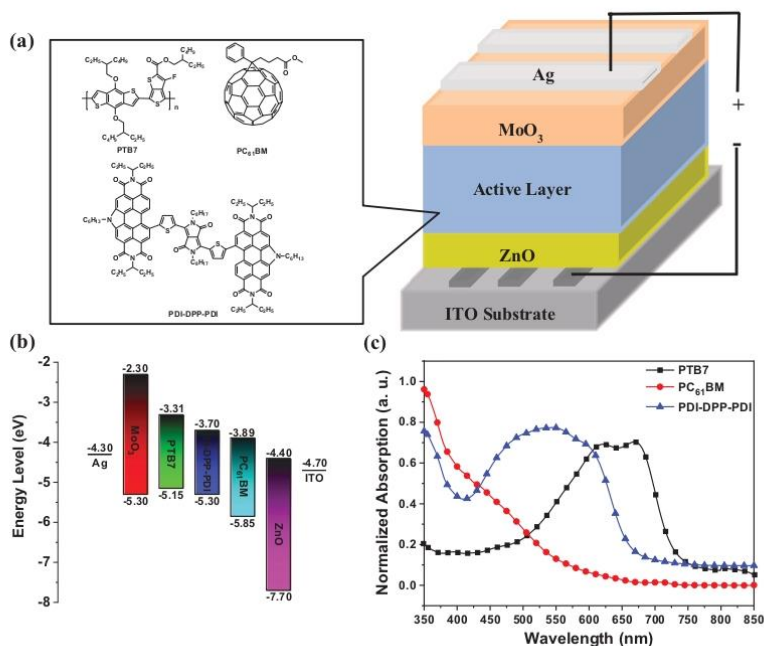
Figure 1. a) Schematic of the chemical structure of the materials in the active layer and device structure. b) Energy level diagram of the OSCs. c) Normalized UV–vis absorption spectra of pristine PTB7, $PC_{61}BM$, and PDI-DPP-PDI films.

illustrates the current density versus voltage ($J–V$) characteristics of the binary and ternary devices with different contents of PDI-DPP-PDI (10%, 20%, and 30%) under simulated air mass 1.5 G illumination at 100 mW cm^{-2}, respectively. The corresponding photovoltaic performance parameters (V_{oc}, J_{sc}, FF, and PCE) are summarized in Table S1 in the Supporting Information. The PCE of PTB7:$PC_{61}BM$ binary device was 7.60% with a V_{oc} of 0.74 V, a J_{sc} of 15.51 mA cm^{-2}, and an FF of 66.80%. Adding 10% PDI-DPP-PDI into the host binary blend film, the V_{oc}, J_{sc}, FF, and PCE values simultaneously increased to 0.78 V, 15.95 mA cm^{-2}, 70.02%, and 8.71%, respectively, which is the best ternary OSCs in this study. However, more than 10%

PDI-DPP-PDI addition deteriorated the photovoltaic performance gradually, mainly due to the reduction of J_{sc} and FF. The ternary devices with 20% PDI-DPP-PDI and 30% PDI-DPP-PDI presented lower J_{sc} at 13.33 mA cm^{-2} and 12.40 mA cm^{-2} and lower FF at 64.59% and 61.52%, resulting in the reduction of PCE to 6.85% and 5.97%, respectively. The poor device performance could be attributed to high crystallinity and easy aggregation of PDI-DPP-PDI within the host blend film. Figure 2b displays the external quantum efficiency (EQE) spectrum for binary device and ternary devices containing different contents of PDI-DPP-PDI. The EQE response of the ternary OSCs with 10% PDI-DPP-PDI was enhanced in the 450–700 nm spectral
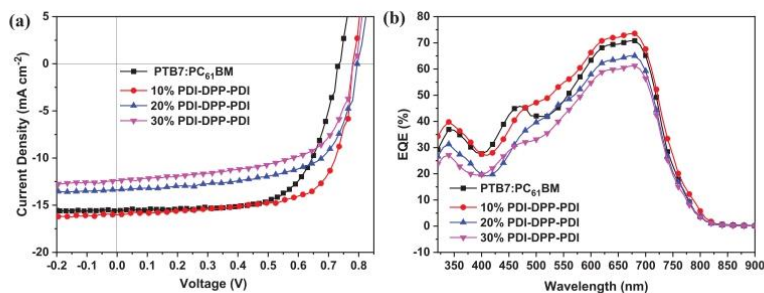
Figure 2. a) $J–V$ characteristics and b) EQE spectra of the devices based on PTB7:$PC_{61}BM$ binary blend film and ternary blend films with different contents of PDI-DPP-PDI (10%, 20%, and 30%).

48

**ADVANCED
SCIENCE NEWS**
www.advancedsciencenews.com

**small
methods**
www.small-methods.com
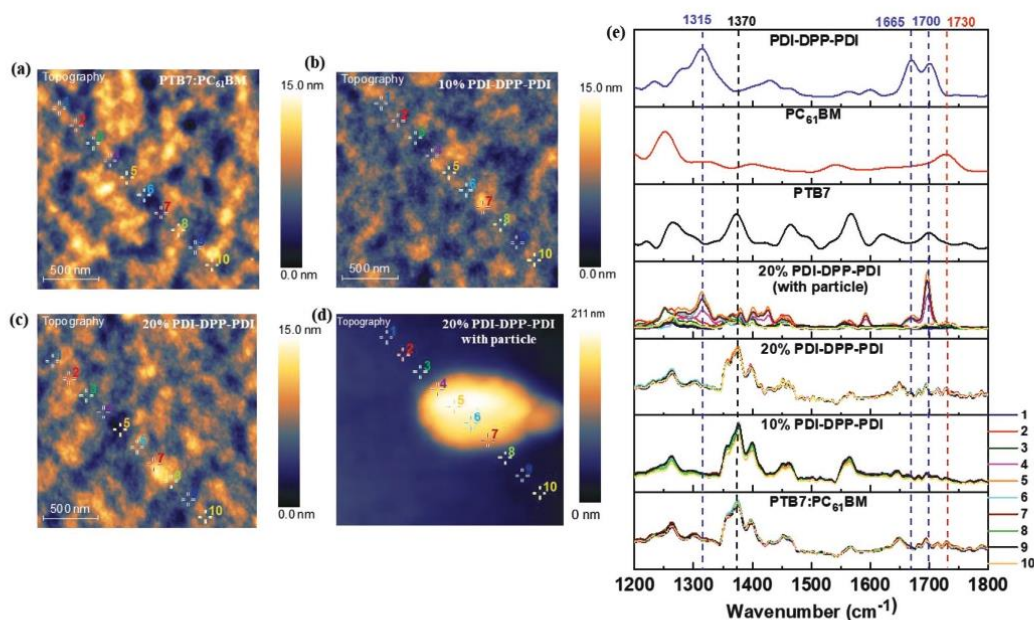
Figure 3. Topography images (left) of a) PTB7:PC$_{61}$BM film and ternary films containing b) 10% PDI-DPP-PDI, c) 20% PDI-DPP-PDI (with the focus on the area without any large particles), and d) 20% PDI-DPP-PDI (with the focus on the area showing large particles. e) PiFM spectra of pristine PTB7, PC$_{61}$BM, PDI-DPP-PDI films and blend films taken from ten locations as marked in corresponding images. The characteristic peaks of PTB7, PC$_{61}$BM, and PDI-DPP-PDI at 1370, 1730, and 1665 cm^{-1}, respectively, were selected for PiFM imaging. Topography image size: 2 μm × 2 μm. All the PTB7:PC$_{61}$BM and ternary films were fabricated with 3% DIO as an additive.

range, which might be due to the absorption of PDI-DPP-PDI and the morphology optimization.

To investigate the surface morphology of the active layer, optical images were first taken. As shown in Figure S2a–d in the Supporting Information, the binary and ternary blend films with 10% PDI-DPP-PDI exhibit smooth morphology. However, with the increase of PDI-DPP-PDI to 20% and 30%, we observed some large PDI-DPP-PDI particles (to be discussed in later text), which suggested that 20% and 30% PDI-DPP-PDI could not be completely dissolved during the solution processing or is not very compatible with the host materials so as to form agglomerates in the film. To explore the distribution of PDI-DPP-PDI in the ternary blend film at a higher resolution, we used a recent PiFM technique that combines the high spatial resolution of AFM microscopy with infrared (IR) spectroscopy to characterize the distribution of organic materials in donor/acceptor phases by chemical identification.[33,34] Figure S3 in the Supporting Information shows the comparison between PiFM spectrum and Fourier transform infrared (FTIR) spectrum of PTB7:PC$_{61}$BM blend film, where major peaks, such as 1370 cm^{-1} (the CH$_3$ symmetric bend mode of PTB7), 1400 cm^{-1} (C−F stretch within the conjugated portion of PTB7), and 1569 cm^{-1} (C=C aromatic backbone), were found to overlap well, despite certain minor differences.[35] The disappearance of the FTIR peak at 1650 cm^{-1} and a slight shift of the 1730 cm^{-1} peak could be caused by different laser profiles and

spectral test modes (for instance, PiFM spectra were taken by a sideband mode to enhance the sensitivity). **Figure 3** presents the topography images (2 μm × 2 μm) of PTB7:PC$_{61}$BM binary blend film and ternary blend films containing 10% and 20% PDI-DPP-PDI and PiFM spectra corresponding to ten different regions in topography images. All films were processed with 3% DIO additive. It should be noted that for the 20% PDI-DPP-PDI ternary film, we focused mainly on the smooth regions without big particles, as shown in Figure 3c and Figure S4e,f in the Supporting Information, for comparing with the 0% and 10% PDI-DPP-PDI samples. In Figure 3e, three characteristic, not-overlapped peaks of PTB7, PC$_{61}$BM and PDI-DPP-PDI in PiFM spectra of pristine films were chosen for close examination and PiFM imaging, which were 1370 cm^{-1} for the CH$_3$ symmetric bend mode of PTB7, 1730 cm^{-1} for C=O mode in ester group of PC$_{61}$BM, and 1665 cm^{-1} for C=O in lactam carbonyl group of PDI-DPP-PDI.[35,36] PTB7:PC$_{61}$BM binary film displays essentially identical PiFM spectra at different locations throughout the film and presents the characteristic peaks at 1370 and 1730 cm^{-1}. It indicated that PTB7 and PC$_{61}$BM could form a well-mixed, uniform film. The characteristic peak of PDI-DPP-PDI measured from ten regions in the topography images of ternary blend film with 10% and 20% PDI-DPP-PDI showed similar intensities, indicating that "dissolved" PDI-DPP-PDI molecules were evenly distributed throughout the donor/acceptor phase and proves that PDI-DPP-PDI had

49

ADVANCED
SCIENCE NEWS

www.advancedsciencenews.com

small
methods

www.small-methods.com
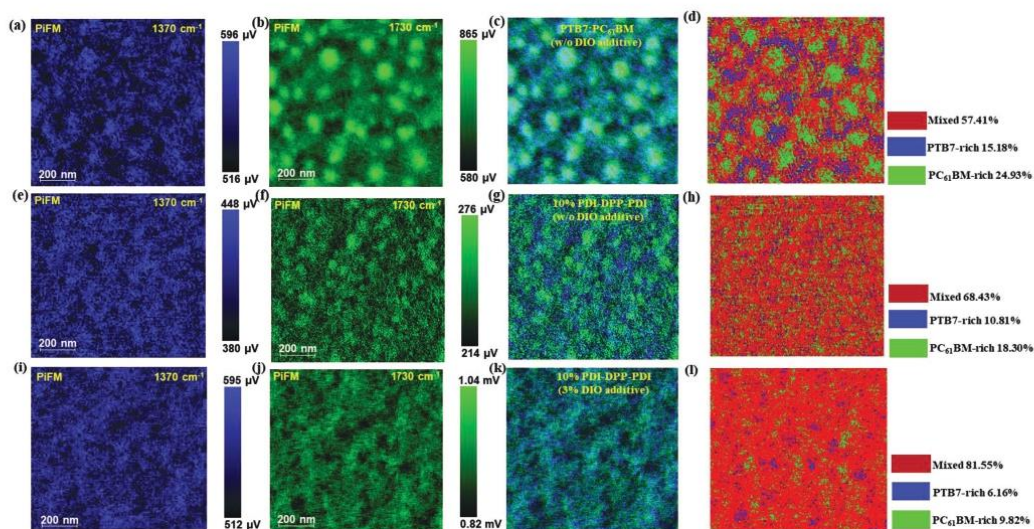
Figure 4. a,b) PiFM images of PTB7:PC$_{61}$BM film without DIO additive, highlighting the PTB7 donor (1370 cm^{-1}), PC$_{61}$BM acceptor (1730 cm^{-1}), and c) the combined PiFM image based on (a) and (b). e,f) PiFM images of PTB7:PC$_{61}$BM film with 10% PDI-DPP-PDI but without DIO additive, highlighting the PTB7 donor (1370 cm^{-1}), PC$_{61}$BM acceptor (1730 cm^{-1}), and g) the combined PiFM image based on (e) and (f). i, j) PiFM images of PTB7:PC$_{61}$BM film with 10% PDI-DPP-PDI and with 3% DIO additive, highlighting the PTB7 donor (1370 cm^{-1}), PC$_{61}$BM acceptor (1730 cm^{-1}), and k) the combined PiFM image based on (i) and (j). d,h,l) Integrated and postprocessed PiFM images based on PTB7-based and PC$_{61}$BM-based PiFM images using homemade Python script, which allowed the segmentation of different regions and corresponding percentage calculations. PiFM image size: 1 μm × 1 μm.

a relatively good compatibility with PTB7 donor and PC$_{61}$BM acceptor under a dissolution condition. As mentioned above, for the 20% PDI-DPP-PDI sample, large particles were observed simultaneously (Figure S2, Supporting Information, and Figure 3d), which were confirmed to be PDI-DPP-PDI aggregates (≈1 μm), as evidenced by the increase of peak intensities at 1315, 1665, and 1700 cm^{-1}, related to PDI-DPP-PDI, in regions 4–7 with respect to other smooth areas without such big particles. It may be argued that the enhanced signal at 1700 cm^{-1} could be related to PTB7. But as the prominent characteristic peak (1370 cm^{-1}) of PTB7 remained relatively low, this possibility can be excluded.

PiFM imaging was then conducted on the binary and ternary films to qualitatively probe the effect of PDI-DPP-PDI on the acceptor and donor distribution in the composite film (processed with or without the DIO additive) and to further quantitatively derive domain size distribution and composition (**Figure 4**).[37] The characteristic peak of PTB7 at 1370 cm^{-1} and PC$_{61}$BM at 1730 cm^{-1} were chosen to obtain the PiFM images that could selectively image the distribution of the corresponding materials, i.e., PTB7 (Figure 4a,e,i) and PC$_{61}$BM (Figure 4b,f,j), in the blend films. These PiFM images, taken at 1370 and 1730 cm^{-1}, were then superimposed to reveal the overall distribution of both donor and acceptor in the same area (Figure 4c,g,k). As clearly shown in Figure 4a–c, the PTB7:PC$_{61}$BM blend film fabricated without the DIO additive treatment presented large size PC$_{61}$BM aggregates, like islands, distributed in a continuous phase containing both PTB7 and PC$_{61}$BM, which is consistent with previous reports.[38] In clear contrast, 10% PDI-DPP-PDI

addition could effectively reduce the PC$_{61}$BM acceptor aggregation (Figure 4e–g). Further, with the DIO additive treatment, the PC$_{61}$BM molecular aggregation basically completely disappeared (Figure 4i–k). The black-and-white and binarized PTB7-based PiFM images and PC$_{61}$BM-based PiFM images are also shown in Figure S5 in the Supporting Information, which yielded the same information.

It is known that bulk heterojunction polymer-fullerene solar cells can mostly be described by the three-phase model proposed by McGehee et al, which refers to a molecularly mixed region and aggregated donor and acceptor phases.[39] In general, for a semi-crystalline polymer, the increase of crystallinity will reduce the level of the molecularly mixed phase and accordingly, increase the level of the aggregated phases. Specific for the PTB7/fullerene system, which usually shows a low level of crystallization, the PC$_{71}$BM acceptor was found to form large agglomerates embedded in a continuous, molecularly mixed matrix, and these aggregates could dissolve and form a finer morphology with the aid of a solvent additive.[38,40] This is exactly what we observed herein upon the introduction of PDI-DPP-PDI and/or DIO, although the involved fullerene derivative, PC$_{61}$BM, is slightly different from PC$_{71}$BM mentioned in the above references. Along with a very low crystallinity (results to be presented and discussed in the later text), we believe that our system has the same basic morphology, i.e., PC$_{61}$BM aggregates distributed in a molecularly mixed continuous phase.

But what are the percentages of these phases? Is the ratio of PC$_{61}$BM-to-PTB7 uniform in the continuous phase? What is the size distribution of aggregated PC$_{61}$BM domains? In order to

answer these questions and get the quantitative information in these regards, we made efforts to develop our own Python script in order to extract the segmentation of $PC_{61}BM$ and PTB7 in integrated PTB7-$PC_{61}BM$ images (Figure 4d,h,l); the algorithmic segmentation analysis of images has been demonstrated to be able to provide structural information quantitatively. The threshold was set to 0.6, which resulted in excellent matching with the original combined PiFM image. A detailed description of image and data processing for PiFM images is presented in the Supporting Information. In Figure 4d,h,l, it can be seen that the continuous matrix is mainly composed of the well-mixed region (containing comparable quantities of PTB7 and $PC_{61}BM$) and a small percentage of the PTB7-rich region (containing >60% of PTB7) and $PC_{61}BM$-rich region (containing >60% of $PC_{61}BM$) as well. The well-mixed region was increased from 57.41% to 81.85% after the introduction of PDI-DPP-PDI acceptor and DIO additive, while the PTB7-rich region and $PC_{61}BM$-rich region (corresponding to mainly the island structure) were decreased from 15.18% to 6.18% and from 24.93% to 9.82%, respectively, suggesting the better mixing of the acceptor and donor throughout the blend film, thanks to the introduction of PDI-DPP-PDI acceptor and DIO additive. In addition, we further obtained the domain size information by conducting a contour detection algorithm, which permits the detection and size calculation of the object of interest.[41] As shown in Figure S6 in the Supporting Information, the size distribution of the $PC_{61}BM$-rich domain in the PTB7:$PC_{61}BM$ film without DIO additive was quite broad, with over 90% central distribution allocated in the range of 40–160 nm. The mean value of the domain size was 90.73 nm. The introduction of 10% PDI-DPP-PDI into the additive-free ternary film could narrow down the distribution of the $PC_{61}BM$-rich domain size to 30–150 nm. Over 90% central distribution of $PC_{61}BM$-rich domain size was in the range of 30–110 nm, with the mean value of 65.60 nm. The reduction of the $PC_{61}BM$-rich domain size due to the inhibition of the $PC_{61}BM$ aggregation is expected to increase the donor/acceptor interface, which could contribute to better exciton dissociation and charge transportation.

In order to gain an understanding of the 3D morphology, we further explored the distribution of organic materials and the domain size in the vertical direction of the device, i.e., by observing the cross-sections of the devices using EFTEM. EFTEM is a technique that can use inelastically scattered electrons to generate an enhanced contrast image by adjusting the central energy of the filter and energy slit. Such a combination allows the selection of only electrons with a certain range of energies, which is based on the fundamental principle that electrons follow different paths depending on their energies while passing through a magnetic prism.[26] Although an EFTEM combined with EELS was previously used to characterize the materials in the blend film, in that case the samples were not prepared under the same processing conditions as those for real devices; instead, the authors deposited the blend film directly on the Cu grids for observations.[42] Moreover, that observation did not yield any information on the morphology in the cross-section of devices. Here, for the first time, we visualized the cross-sectional morphology of OSCs by combining the EFTEM with EELS. Differences in the electronic structure of each organic material can induce distinct and unique electron

loss signals in the bulk-plasmon low loss range (≈10–40 eV) for the EELS spectrum, which can then be used safely to identify and characterize the nanostructure of organic semiconductors. The cross-sections of devices were fabricated by a scanning electron microscope/focused ion beam dual-beam platform.[43,44] A typical bright-field TEM image collected from the cross-section of a device (ITO/ZnO/active layer/MoO_3/Ag as labeled) with an active layer based on PTB7:$PC_{61}BM$ (without DIO treatment) is displayed in **Figure 5**a. Each constituent layer of the device can be clearly resolved. Nonetheless, the image failed to reveal the photoactive layer morphology at the nanoscale level because the bright field image of this area essentially had no contrast, primarily due to similar molecular densities of different components. We thus employed EFTEM to reveal the morphology at the cross-section. To do it, we first normalized the as-acquired EELS signal with the total electron count and then subtracted the background through a custom-made MATLAB code (details are shown in Supporting Information) in order to obtain the EELS spectra for comparison. As shown in Figure 5b, the EELS spectra of pristine PTB7, PDI-DPP-PDI, and $PC_{61}BM$ showed broad bulk plasmon peaks centered at 20.5, 22, and 24 eV, respectively, which significantly overlap with each other. Although challenging, it is still possible to resolve individual components in the blend film because of the different intensity of each material reflected in the lower/higher energy regions (gray and red rectangle regions highlighted in Figure 5b inset) of the EELS spectra. The imaging and analysis in these energy regions can enable the pixelwise integrated electron intensities to reach the highest difference between PTB7 and $PC_{61}BM$. In principle, the PTB7- and $PC_{61}BM$-rich domains should exhibit the opposite intensity contrast when the images are taken/processed at lower/higher energy tail of the bulk plasmon peaks. In this way, we could get an improved-contrast image for the donor and acceptor phase in the blend film. Figure 5c,d shows EFTEM contrast images of cross-sectional PTB7:$PC_{61}BM$ active layer (without DIO treatment; 100 nm thickness TEM lamella) taken at 16.5 and 28.5 eV central energy with 4 eV slit width. It can be seen that the higher intensity regions in Figure 5c (related to the PTB7-rich domains) dimmed, as expected, in Figure 5d, where the higher intensity regions were associated with the $PC_{61}BM$-rich domains. These observations strongly validated our approach in probing the phases in fully organic blend films using EFTEM. After the technique validation, we moved forward to further increase the phase contrast. We achieved it by reducing the TEM lamella thickness to 50 nm to minimize the thickness effect yet still with sufficient signals. As such, we are able to reproducibly acquire the distinct-contrast EFTEM image of cross-sectional PTB7:$PC_{61}BM$ active layer without DIO treatment (Figure S7, Supporting Information). In all the subsequent EFTEM studies, the thickness of all the TEM lamella was controlled between 50 and 70 nm to reduce the film thickness effect on the EFTEM images.

Our developed strategy was finally applied to explore the effect of PDI-DPP-PDI incorporation on the active layer morphology, which was the purpose of this study. A series of EFTEM images, taken at different filtered energy ranges, of the cross-sections of PTB7:$PC_{61}BM$ binary device and ternary device with 10% PDI-DPP-PDI (without the introduction of the DIO additive) are displayed in Figure S8 in the Supporting

ADVANCED
SCIENCE NEWS
www.advancedsciencenews.com

small
methods
www.small-methods.com
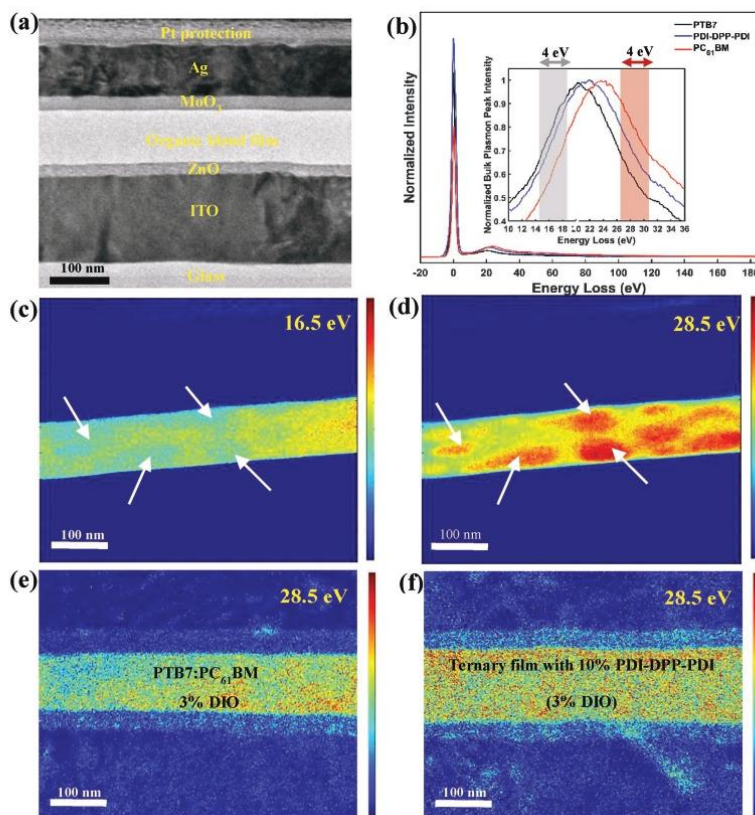
Figure 5. a) A typical bright-field TEM image of the cross section of the PTB7:PC$_{61}$BM photovoltaic device (active layer shows no contrast morphology). b) EELS spectra of pristine PTB7, PDI-DPP-PDI, and PC$_{61}$BM thin layers, and reference bulk plasmon peaks of PTB7, PDI-DPP-PDI, and PC$_{61}$BM at 21, 23, and 24 eV, respectively, are shown in the inset. c,d) Cross-sectional EFTEM images of a PTB7:PC$_{61}$BM device without the DIO treatment (thickness of TEM lamella is 100 nm). Slit was inserted with the central energy set at 16.5 and 28.5 eV and energy width at 4 eV for acquiring these images, with two energy windows highlighted by the colored rectangles energy-loss value slice in (b) by electron spectral imaging, respectively, and its energy width was set as 4 eV. e) EFTEM images of the cross-section of PTB7:PC$_{61}$BM device (with the DIO treatment) and f) PTB7:PC$_{61}$BM:10% PDI-DPP-PDI device (with the DIO treatment). Normalized and background removed images were acquired with a 4 eV wide filter centered at 28.5 eV.

Information. It was found that the highest contrast image for the cross-sectional active layer was obtained using the central energy of filter at 28.5 eV and introducing 10% PDI-DPP-PDI into the active layer could significantly reduce the domain size, in good agreement with the PiFM results for the film surface. Once again, it can be seen that the cross-section of the active layer in the ternary device had more uniform nanoscale morphology. It can thus be concluded that PDI-DPP-PDI can effectively decrease the large-scale aggregation of PC$_{61}$BM molecules, which could facilitate the charge transportation and reduce the charge recombination. Meanwhile, the EFTEM images of the cross-section of the optimal binary device (with the DIO treatment) and ternary device with 10% PDI-DPP-PDI (with the DIO treatment) are shown in Figure 5e,f, respectively. It was noted that adding DIO additive into the active layer can also help eliminate the larger domain size, which is also

consistent with the PiFM results of the film surface. Moreover, EFTEM observations demonstrated that the introduction of PDI-DPP-PDI and DIO additive does not induce the vertical phase segregation, as reported for certain additives.[45]

2D grazing-incidence X-ray diffraction (2D-GIXRD) measurements were employed to investigate the crystallinity of the pristine and blend films, which are given in Figures S9 and S10 in the Supporting Information. The crystallinity of PTB7 in binary blend film would be decreased after mixing with PC$_{61}$BM, leading to the low crystallinity of binary blend film, which is in agreement with the previous work (Figure S10a, Supporting Information).[46] In Figure S10b in the Supporting Information, 2D GIXRD pattern of ternary blend film containing 10% PDI-DPP-PDI was similar to that of PTB7:PC$_{61}$BM binary blend film, which indicates that the PDI-DPP-PDI had good compatibility with PTB7 and PC$_{61}$BM.[47] Moreover, low

**ADVANCED
SCIENCE NEWS**
www.advancedsciencenews.com

**small
methods**
www.small-methods.com
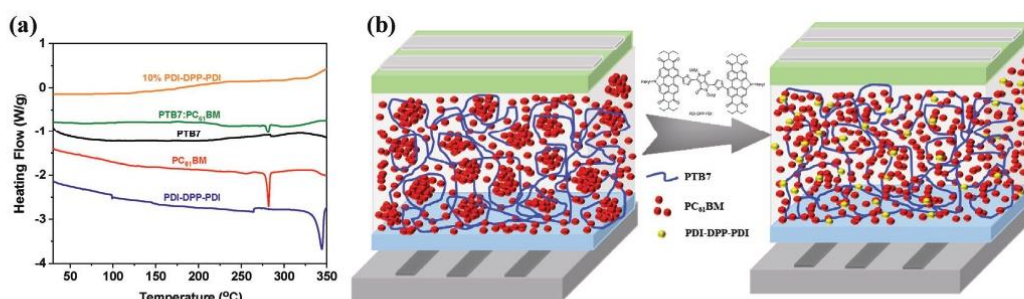
Figure 6. a) The first DSC heating-scan profiles of neat PTB7, $PC_{61}BM$, and PDI-DPP-PDI, PTB7:$PC_{61}BM$ blend (without DIO additive treatment) and 10% PDI-DPP-PDI-based ternary blend (without DIO additive treatment). b) Schematic illustration of binary and ternary OSCs to highlight the morphology variation in the binary and ternary active layers, with the introduction of PDI-DPP-PDI into the latter.

crystallinity of PTB7:$PC_{61}BM$ film and ternary film containing 10% PDI-DPP-PDI allows the high-level presence of the molecularly mixed phase.[37] However, the intensity of lamellar peaks of PDI-DPP-PDI in the 2D GIXRD patterns of ternary blend films with 20% and 30% PDI-DPP-PDI can be observed, owing to the strong agglomeration of PDI-DPP-PDI, which may suppress effective charge transfer.

Differential scanning calorimetry (DSC) measurements were carried out to explore the miscibility of materials in the active layer. The first DSC heating-scan profiles of neat PTB7, $PC_{61}BM$ and PDI-DPP-PDI material, PTB7:$PC_{61}BM$ blend (without DIO additive treatment) and 10% PDI-DPP-PDI-based ternary blend (without DIO additive treatment) are shown in **Figure 6**a. The distinct endothermic peaks, due to the melting of $PC_{61}BM$ and PDI-DPP-PDI, were found at 282 and 344 °C, respectively. The PTB7:$PC_{61}BM$ blend reveals a largely suppressed melting endothermic peak of $PC_{61}BM$, indicating the decreased crystallinity of $PC_{61}BM$ and the increased miscibility in the binary blend film. In the 10% PDI-DPP-PDI-based ternary blend, no endothermic peaks could be observed, which indicates the good miscibility of all the three components in this sample. It can be inferred that PDI-DPP-PDI was able to well mix with PTB7 and $PC_{61}BM$ so as to reduce their aggregation, leading to a molecularly mixed system, in agreement with the results from PiFM and EFTEM measurements (Figures 4 and 5). In Figure 6b, the schematic illustration of the morphology of binary and ternary OSCs was plotted based on the results of PiFM, EFTEM, GIXRD, and DSC, highlighting the influence of PDI-DPP-PDI introduction on the 3D morphology of the active layer, i.e., transforming an island-like $PC_{61}BM$-in-PTB7 structure to a molecularly mixed $PC_{61}BM$/PTB7 system.

The good morphology of ternary blend films will positively affect the charge carrier mobility, which is beneficial for the formation of the effective hole and electron transport channel, and for obtaining higher J_{sc} and FF in ternary OSCs. The more balanced hole mobility (μ_h) and electron mobility (μ_e) can reduce charge accumulation to prevent the large photocurrent loss, resulting in a higher FF value.[48–50] The charge carrier mobility measurement was conducted by using the space charge limited current method to study the charge transfer of ternary blend film.[7] The hole-only device structure was ITO/poly(3,4-ethyle nedioxythiophene):polystyrene sulfonate/active layer/MoO_3/

Ag and the electron-only device structure was ITO/ZnO/ active layer/LiF/Al. **Figure 7**a,b presents the linear fits of J–V curves of the hole-only and electron-only devices. According to the Mott–Gurney square law,[51,52] we could calculate the hole/electron mobility based on binary blend film and ternary blend films with 10%, 20%, and 30% PDI-DPP-PDI. Hole/ electron mobility (Table S2, Supporting Information) was estimated to be $1.37 \times 10^{-4}/2.96 \times 10^{-4}$, $1.57 \times 10^{-4}/3.24 \times 10^{-4}$, $1.54 \times 10^{-4}/3.59 \times 10^{-4}$, and $1.82 \times 10^{-4}/4.47 \times 10^{-4}$ cm^2 V^{-1} s^{-1}, respectively, for these four samples. The most balanced charge carrier mobility ($\mu_e/\mu_h = 2.06$) was achieved by the ternary thin film with 10% PDI-DPP-PDI incorporation, which was related to its good morphology, contributing to a higher FF of 70.02%. In contrast, the ratio of μ_e/μ_h of binary thin film and ternary thin films with 20% PDI-DPP-PDI and 30% PDI-DPP-PDI was higher at 2.16, 2.33, and 2.45, respectively, leading to more charge accumulation.

In order to evaluate the charge transfer between the third component and host binary blends, the photoluminescence (PL) measurements under the excitation wavelength of 500 nm were carried out on the PTB7 film with different contents of PDI-DPP-PDI. As shown in Figure S11 in the Supporting Information, the PL emission peak of pristine PTB7 film was located at 740 nm and its PL intensity was drastically quenched with a small amount of PDI-DPP-PDI incorporation. Therefore, the charge could be transferred from PTB7 to not only $PC_{61}BM$ but also PDI-DPP-PDI, which could reduce the charge accumulation and recombination at the donor/ acceptors interface.

To further explore the charge recombination and transport mechanisms in ternary OSCs, we measured the J_{sc} as a function of light intensity (P_{light}) to study the bimolecular recombination. A power-law equation of $J_{sc} \propto P_{light}^{\alpha}$ could descript the relationship of J_{sc} and P_{light}, where α is the slope of the J_{sc} versus P_{light} curve.[7] According to Figure 7c, the α values of binary OSCs and ternary OSCs with 10%, 20%, and 30% PDI-DPP-PDI were 0.9890, 0.9968, 0.9542, and 0.9478, respectively. It indicated that ternary OSCs with 10% PDI-DPP-PDI incorporation exhibited significantly less bimolecular recombination than the binary OSCs, which is definitely beneficial for exciton dissociation. Figure 7d shows the J_{ph}–V_{eff} plots, where $J_{ph} = J_L - J_D$ (J_{ph} is net photocurrent density, J_L and J_D are current density under
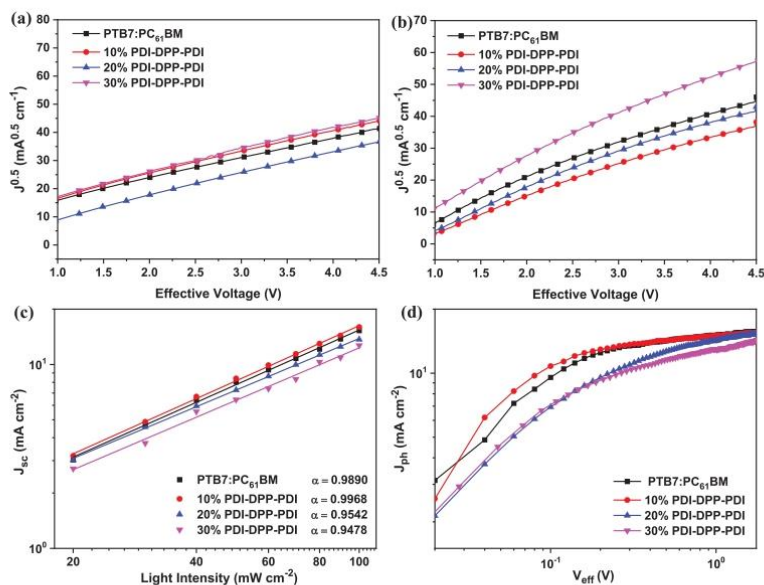
Figure 7. a) Hole mobility and b) electron mobility for binary blend film and ternary blend films with different contents of PDI-DPP-PDI (10%, 20%, and 30%). c) The dependence of short-circuit current density on light intensity and d) the J_{ph}–V_{eff} plots for binary blend film and ternary blend films with different contents of PDI-DPP-PDI (10%, 20%, and 30%).

illumination and in the dark, respectively), and $V_{eff} = V_0 - V$ (V_0 is the voltage at which $J_L = J_D$, V is the applied voltage).[53,54] At the high reverse bias voltage ($V_{eff} > 2V$), J_{ph} reached saturation, indicating that basically all the photogenerated exciton were dissociated to free charge carriers. The exciton dissociation probability (P (E, T)) could be defined as J_{ph}/J_{sat} under the short-circuit condition. The P (E, T) values were thus calculated to be 93.2% for binary OSCs, 97.7% for 10% PDI-DPP-PDI-based ternary OSCs, 87.1% for 20% PDI-DPP-PDI-based ternary OSCs, and 83.5% for 30% PDI-DPP-PDI-based ternary OSCs, respectively. These results suggest that incorporating 10% PDI-DPP-PDI into ternary OSCs could facilitate the exciton dissociation, in line with 3D morphology analysis, and thus contributing to the higher J_{sc} and FF.

In general, PTB7:PC$_{61}$BM OSCs present the distinct degradation under the air and light atmosphere, due to (i) photooxidation and hydroxylation of benzodithiophene unit in the polymer PTB7, leading to the reduction of absorption peak intensity,[20] (ii) photoinduced fullerene dimerization, leading to the aggregation of fullerene,[21] and (iii) enhancement of electronic trap states, increasing charge trapping and recombination and thereby the loss of FF.[22] We expected that air-stable and photostable PDI-DPP-PDI acceptor may act as compatible structure "stabilizers" and help increase the device stability. We thus did device performance stability tests on encapsulated photovoltaic devices based on optimized binary and ternary blend films in ambient conditions and under the high humidity of 70% in air (**Figure 8**a,b). The encapsulated
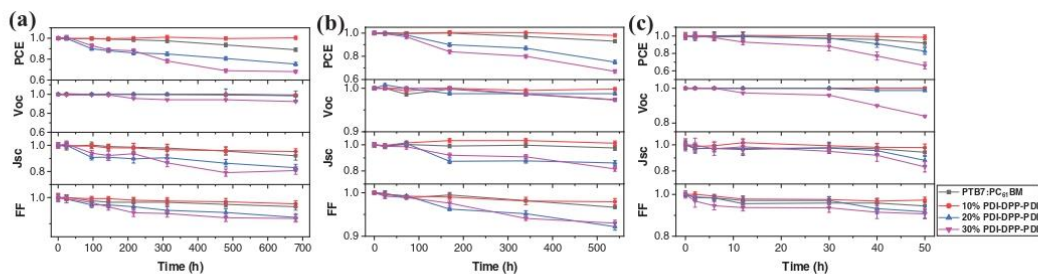
Figure 8. Stability of encapsulated devices for binary blend film and ternary blend films with different contents of PDI-DPP-PDI (10%, 20%, and 30%) a) in air, b) under humidity of 70%, c) under continuous illumination in air. The normalized photovoltaic parameters and error bars were obtained from ten devices.

device containing 10% PDI-DPP-PDI showed excellent air stability, demonstrating almost no degradation after 680 h air exposure. However, the PCE of the binary device and ternary device containing higher concentrations (20% and 30%) of PDI-DPP-PDI exhibited 12%, 25%, and 32% of decay from the initial PCE, respectively. Figure 8b presents the stability of encapsulated devices kept under 70% humidity in air for 540 h. 98% of the initial PCE was remained for the encapsulated ternary device with 10% PDI-DPP-PDI after long-term humidity exposure. It indicated that introducing 10% PDI-DPP-PDI into the ternary device largely increased the stability of the photoactive layer, which could be attributed to the stabilizing effect of PDI-DPP-PDI on the optimized morphology. The degradations of the binary device and ternary device with higher concentrations (20% and 30%) of PDI-DPP-PDI in ambient conditions and under the high humidity of 70% in air are mainly related to the losses of J_{sc} and FF, which are consistent with worse morphology, otherwise, the V_{oc} are slightly dropped. To explore the photostability of devices, we placed the encapsulated devices under continuous illumination in air (Figure 8c). The exposure time is only 50 h due to the photooxidation of PTB7 and photoinduced aggregation of $PC_{61}BM$.[35] Compared to binary and ternary devices with 20% and 30% PDI-DPP-PDI, adding 10% PDI-DPP-PDI was considerably beneficial for increasing the photostability of the ternary device, which was once again since 10% PDI-DPP-PDI incorporation led to the morphological optimization. On the other hand, the role of 10% PDI-DPP-PDI as a chemical structure stabilizer for the PTB7 donor and $PC_{61}BM$ acceptor cannot be excluded. However, the encapsulated devices more than 10% PDI-DPP-PDI decayed after 30 h of continuous illumination, which was caused by the reduction of V_{oc}, J_{sc}, and FF due to the photogenerated charge recombination.[55] It can be concluded that the ternary OSCs with 10% PDI-DPP-PDI incorporation demonstrated higher stability with respect to the binary device fabricated and tested under the same conditions.

3. Conclusions

In summary, in-depth 3D morphological investigations of blend films in the configuration of real devices were accomplished by exploring the combination of PiFM and EFTEM/EELS characterization. The results confirm that incorporating nonfullerene acceptor PDI-DPP-PDI into the PTB7:$PC_{61}BM$ device can better control the donor/acceptor morphology, which can improve the photovoltaic efficiency as well as stability. It was because PDI-DPP-PDI had good compatibility with both PTB7 and $PC_{61}BM$ at an appropriate content. As a result, the optimal ternary device with 10% PDI-DPP-PDI had more balanced hole/electron mobilities to promote the effective charge transfer and reduce the charge recombination, leading to both higher J_{sc} and FF. Meanwhile, the incorporation of 10% stable, nonfullerene PDI-DPP-PDI yielded higher stability to the ternary device, which showed almost no performance decay after 680 h of storage in air, after 540 h exposure to the high humidity of 70% in air, and under continuous long-term illumination in air, much better than that of the corresponding binary devices. Our work represents the first exploration of the morphology characterization in the real

device setting with advanced FETEM/EELS and also provides a very promising approach to get the highly stable device with simultaneously improved photovoltaic performance.

[1] B. C. Thompson, J. M. Fréchet, *Angew. Chem., Int. Ed* **2008**, *47*, 58.
[2] J. Zhao, Y. Li, G. Yang, K. Jiang, H. Lin, H. Ade, W. Ma, Y. Yan, *Nat. Energy* **2016**, *1*, 15027.
[3] Y. Cui, H. Yao, B. Gao, Y. Qin, S. Zhang, B. Yang, C. He, B. Xu, J. Hou, *J. Am. Chem. Soc.* **2017**, *139*, 7302.
[4] N. Gasparini, X. Jiao, T. Heumueller, D. Baran, G. J. Matt, S. Fladischer, E. Spiecker, H. Ade, C. J. Brabec, T. Ameri, *Nat. Energy* **2016**, *1*, 16118.
[5] W. Li, Y. Yan, Y. Gong, J. Cai, F. Cai, R. S. Gurney, D. Liu, A. J. Pearson, D. G. Lidzey, T. Wang, *Adv. Funct. Mater.* **2018**, *28*, 1704212.
[6] T. Yu, X. Xu, G. Zhang, J. Wan, Y. Li, Q. Peng, *Adv. Funct. Mater.* **2017**, *27*, 1701491.
[7] A. Tang, W. Song, B. Xiao, J. Guo, J. Min, Z. Ge, J. Zhang, Z. Wei, E. Zhou, *Chem. Mater.* **2019**, *31*, 3941.
[8] N. An, Y. Cai, H. Wu, A. Tang, K. Zhang, X. Hao, Z. Ma, Q. Guo, H. S. Ryu, H. Y. Woo, Y. Sun, E. Zhou, *Adv. Mater.* **2020**, *32*, 2002122.
[9] Y. Cui, Y. Xu, H. Yao, P. Bi, L. Hong, J. Zhang, Y. Zu, T. Zhang, J. Qin, J. Ren, Z. Chen, C. He, X. Hao, Z. Wei, J. Hou, *Adv. Mater.* **2021**, *33*, 2102420.

[10] H. Tang, H. Chen, C. Yan, J. Huang, P. W. K. Fong, J. Lv, D. Hu, R. Singh, M. Kumar, Z. Xiao, Z. Kan, S. Lu, G. Li, *Adv. Energy Mater.* **2020**, *10*, 2001076.

[11] F. Zhao, C. Wang, X. Zhan, *Adv. Energy Mater.* **2018**, *8*, 1703147.

[12] J. Lv, H. Tang, J. Huang, C. Yan, K. Liu, Q. Yang, D. Hu, R. Singh, J. Lee, S. Lu, G. Li, Z. Kan, *Energy Environ. Sci.* **2021**, *14*, 3044.

[13] S. F. Hoefler, G. Haberfehlner, T. Rath, R. Canteri, M. Barozzi, F. Hofer, G. Trimmel, *Adv. Mater. Interfaces* **2019**, *6*, 1901053.

[14] C. M. Proctor, M. Kuik, T.-Q. Nguyen, *Prog. Polym. Sci.* **2013**, *38*, 1941.

[15] S. R. Cowan, A. Roy, A. J. Heeger, *Phys. Rev. B* **2010**, *82*, 245207.

[16] J. Hou, O. Inganäs, R. H. Friend, F. Gao, *Nat. Mater.* **2018**, *17*, 119.

[17] D. Zomerman, J. Kong, S. M. McAfee, G. C. Welch, T. L. Kelly, *ACS Appl. Energy Mater.* **2018**, *1*, 5663.

[18] Y. Chen, P. Ye, Z. G. Zhu, X. Wang, L. Yang, X. Xu, X. Wu, T. Dong, H. Zhang, J. Hou, *Adv. Mater.* **2017**, *29*, 1603154.

[19] S. A. Thomson, S. C. Hogg, I. D. Samuel, D. J. Keeble, *J. Mater. Chem. A* **2017**, *5*, 21926.

[20] J. Razzell-Hollis, J. Wade, W. C. Tsoi, Y. Soon, J. Durrant, J.-S. Kim, *J Mater. Chem. A* **2014**, *2*, 20189.

[21] M. M. Roubelakis, G. C. Vougioukalakis, L. C. Nye, T. Drewello, M. Orfanopoulos, *Tetrahedron* **2010**, *66*, 9363.

[22] H. Cha, J. Wu, A. Wadsworth, J. Nagitta, S. Limbu, S. Pont, Z. Li, J. Searle, M. F. Wyatt, D. Baran, *Adv. Mater.* **2017**, *29*, 1701156.

[23] J. Chang, Z. Lin, C. Jiang, J. Zhang, C. Zhu, J. Wu, *ACS Appl. Mater. Interfaces* **2014**, *6*, 18861.

[24] Z. He, C. Zhong, S. Su, M. Xu, H. Wu, Y. Cao, *Nat. Photonics* **2012**, *6*, 591.

[25] S. Holliday, C. K. Luscombe, *Adv. Electron. Mater.* **2018**, *4*, 1700416.

[26] F. Bonaccorso, N. Balis, M. M. Stylianakis, M. Savarese, C. Adamo, M. Gemmi, V. Pellegrini, E. Stratakis, E. Kymakis, *Adv. Funct. Mater.* **2015**, *25*, 3870.

[27] P. Li, M. Mainville, Y. Zhang, M. Leclerc, B. Sun, R. Izquierdo, D. Ma, *Small* **2019**, *15*, 1804671.

[28] C. Wang, X. Xu, W. Zhang, S. B. Dkhil, X. Meng, X. Liu, O. Margeat, A. Yartsev, W. Ma, J. Ackermann, *Nano Energy* **2017**, *37*, 24.

[29] S. M. McAfee, S. V. Dayneko, P. Josse, P. Blanchard, C. Cabanetos, G. C. Welch, *Chem. Mater.* **2017**, *29*, 1309.

[30] T. Goh, J. Huang, B. Bartolome, M. Y. Sfeir, M. Vaisman, M. Lee, A. D. Taylor, *J. Mater. Chem. A* **2015**, *3*, 18611.

[31] M.-A. Pan, T.-K. Lau, Y. Tang, Y.-C. Wu, T. Liu, K. Li, M.-C. Chen, X. Lu, W. Ma, C. Zhan, *J Mater. Chem. A* **2019**, *7*, 20713.

[32] F. Liu, W. Zhao, J. R. Tumbleston, C. Wang, Y. Gu, D. Wang, A. L. Briseno, H. Ade, T. P. Russell, *Adv. Energy Mater.* **2014**, *4*, 1301377.

[33] K. L. Gu, Y. Zhou, W. A. Morrison, K. Park, S. Park, Z. Bao, *ACS Nano* **2018**, *12*, 1473.

[34] J. Jahng, D. A. Fishman, S. Park, D. B. Nowak, W. A. Morrison, H. K. Wickramasinghe, E. O. Potma, *Acc. Chem. Res.* **2015**, *48*, 2671.

[35] S. Shah, R. Biswas, T. Koschny, V. Dalal, *Nanoscale* **2017**, *9*, 8665.

[36] D. G. Farnum, G. Mehta, G. G. Moore, F. P. Siegal, *Tetrahedron Lett.* **1974**, *15*, 2549.

[37] H. Sun, F. Pan, H. Bin, J. Zhang, L. Xue, B. Qiu, Z. Wei, Z. Zhang, Y. Li, *Nat. Commun.* **2018**, *9*, 743.

[38] B. A. Collins, Z. Li, J. R. Tumbleston, E. Gann, C. R. McNeill, H. Ade, *Adv. Energy Mater.* **2013**, *3*, 65.

[39] T. M. Burke, M. D. McGehee, *Adv. Mater.* **2014**, *26*, 1923.

[40] W. Chen, T. Xu, F. He, W. Wang, C. Wang, J. Strzalka, Y. Liu, J. Wen, D. J. Miller, J. Chen, K. Hong, L. Yu, S. B. Darling, *Nano Lett.* **2011**, *11*, 3707.

[41] C. Zhang, J. Yan, C. Li, R. Bie, *Neurocomputing* **2018**, *275*, 2702.

[42] N. Rujisamphan, R. E. Murray, F. Deng, C. Ni, S. I. Shah, *ACS Appl. Mater. Interfaces* **2014**, *6*, 11965.

[43] H. J. Jung, D. Kim, S. Kim, J. Park, V. P. David, B. Shin, *Adv. Mater.* **2018**, *30*, 1802769.

[44] C. Guo, F. I. Allen, Y. Lee, T. P. Le, C. Song, J. Ciston, A. M. Minor, E. D. Gomez, *Adv. Funct. Mater.* **2015**, *25*, 6071.

[45] W. Xu, B. Wu, F. Zheng, H. Wang, Y. Wang, F. Bian, X. Hao, F. Zhu, *Org. Electron.* **2015**, *25*, 266.

[46] S. Das, J. K. Keum, J. F. Browning, G. Gu, B. Yang, O. Dyck, C. Do, W. Chen, J. Chen, I. N. Ivanov, *Nanoscale* **2015**, *7*, 15576.

[47] J. Zhang, Y. Zhang, J. Fang, K. Lu, Z. Wang, W. Ma, Z. Wei, *J. Am. Chem. Soc.* **2015**, *137*, 8176.

[48] B. Fan, W. Zhong, X. F. Jiang, Q. Yin, L. Ying, F. Huang, Y. Cao, *Adv. Energy Mater.* **2017**, *7*, 1602127.

[49] Q. An, F. Zhang, W. Gao, Q. Sun, M. Zhang, C. Yang, J. Zhang, *Nano Energy* **2018**, *45*, 177.

[50] X. Xu, Z. Li, Z. Wang, K. Li, K. Feng, Q. Peng, *Nano Energy* **2016**, *25*, 170.

[51] J. A. Röhr, D. Moia, S. A. Haque, T. Kirchartz, J. Nelson, *J. Phys.: Condens. Matter* **2018**, *30*, 105901.

[52] T. Yu, X. Xu, Y. Li, Z. Li, Q. Peng, *ACS Appl. Mater. Interfaces* **2017**, *9*, 18142.

[53] Z. He, C. Zhong, X. Huang, W. Y. Wong, H. Wu, L. Chen, S. Su, Y. Cao, *Adv. Mater.* **2011**, *23*, 4636.

[54] L. Zhang, X. Xing, L. Zheng, Z. Chen, L. Xiao, B. Qu, Q. Gong, *Sci. Rep.* **2014**, *4*, 5071.

[55] N. K. Elumalai, A. Uddin, *Energy Environ. Sci.* **2016**, *9*, 391.

WILEY-VCH

Supporting Information

Three-dimensional Nanoscale Morphology Characterization of Ternary Organic

Solar Cells

Ting Yu, Wanting He, Jafari Maziar, Tugrul Guner, Pandeng Li, Mohamed Siaj, Ricardo Izquierdo,

Baoquan Sun, Gregory C.Welch, Aycan Yurtsever and Dongling Ma*

Dr. T. Yu, W. He, T. Guner, P. Li, Prof. A. Yurtsever, Prof. D. Ma
Énergie, Matériaux et Télécommunications, Institut National de la Recherche Scientifique (INRS),
1650 Boul. Lionel-Boulet, Varennes, Québec, Canada, J3X 1S2
E-mail: ma@emt.inrs.ca
Prof. G. C. Welch
Department of Chemistry, University of Calgary, 2500 University Drive N. W., Calgary, Alberta,
Canada, T2N 1N4
E-mail: gregory.welch@ucalgary.ca
Prof. B. Sun
Jiangsu Key Laboratory for Carbon-Based Functional Materials and Devices Institute of Functional
Nano and Soft Materials (FUNSOM)
Joint International Research Laboratory of Carbon-Based Functional Materials and Devices,
Soochow University, 199 Ren'ai Road, Suzhou 215123 P. R. China
E-mail: bqsun@suda.edu.cn
Dr. J. Maziar, Prof. M. Siaj
Université du québec à montréal, Montréal, Québec, Canada, H2L 2C4
E-mail: siaj.mohamed@uqam.ca
Prof. R. Izquierdo
Département de génie électrique, École de technologie supérieure, Montréal, Québec, Canada, H3C
1K3
E-mail: ricardo.izquierdo@etsmtl.ca

Experimental Section

Reagents and Materials: poly [[4, 8-bis [(2-ethylhexyl) oxy] benzo [1, 2-b : 4, 5-b′] dithiophene-2, 6-diyl] [3-fluoro-2-[(2 ethylhexyl) carbonyl] thieno [3, 4-b] thiophenediyl]] (PTB7) polymer and phenyl-C_{61}-butyric acid methyl ester ($PC_{61}BM$) $PC_{61}BM$ were purchased from 1-Material company (Canada). Patterned ITO-coated glass substrates (Rs $\leq$ 10 Ω square^{-1}, Tr $\geq$ 83%) was purchased from Shenzhen Huayu Union Technology Co., Ltd. (China). In addition, zinc acetate dihydrate ($Zn(CH_3COO)_2 \cdot 2H_2O$, 99.9%), ethanolamine ($NH_2CH_2CH_2OH$, 99.5%), 2-methoxyethanol ($CH_3OCH_2CH_2OH$, 99.8%), chlorobenzene (CB) and molybdenum trioxide interlayer (MoO_3) were obtained from Sigma-Aldrich without further purification. According to previous work,[1] PDI-DPP-PDI was synthesized by using the direct heteroarylation between diketopyrrolopyrrole precursors and N-annulated perylene diimide precursor and employing a silica-supported catalyst.

Devices Fabrication and Testing: The ternary organic solar cells were fabricated with an inverted structure of indium tin oxides (ITO) glass/zinc oxide (ZnO)/active layer/MoO_3/Ag. ZnO precursor solution was prepared according to a reported procedure.[2] The patterned ITO glass substrates were cleaned by sequential ultrasonication in detergent, deionized water, acetone, and isopropanol. Then, they were dried by the high-pressure nitrogen stream and followed by treatment with plasma for 10 min. ZnO precursor solution was spin-coated onto the ITO substrate at 4500 rpm for 60 s and then baked in dried air at 200 $^{\circ}$C for 1h to form a thin ZnO layer. For ternary devices, PTB7:$PC_{61}BM$ with different contents of PDI-DPP-PDI solution was spin-coated onto the above substrate in glovebox at the optimized spin-speed of 2000 rpm for 120 s to form the active layer. The optimized concentration was 25 mg mL^{-1} with D:A ratio of 1:1.5 (w/w) (adding 3 v% 1,8-diiodooctane (DIO)). Finally, MoO_3 (25 nm) and silver (Ag, 100 nm) were deposited onto the surface of the active layer

2

in an evaporation chamber under a high vacuum of 1×10^{-6} mbar). The effective device area was 0.06 cm^2. The current density versus voltage (*J-V*) characterization was measured by using a class ABA LED solar simulator under AM 1.5G (100 mW cm^{-2}), which was calibrated using a standard KG5 filtered silicon solar cell. The external quantum efficiency (EQE) measurement was conducted on an IQE200B system (Newport Corporation) in a high purity nitrogen-filled glovebox.

Device Cross-section Fabrication for EFTEM: The cross-sections of solar cell devices were fabricated by a scanning electron microscope/focused ion beam (SEM/FIB) dual-beam platform (TESCAN LYRA 3). Platinum pads acted as a shield and protection layers were deposited on the region of interest via electron and ion beam assisted deposition. The milling and polishing of the cross-sections were then switched from high accelerating voltage and high current density to lower accelerating voltage and lower current density. First, two opposing trenches were milled away, leaving behind a 2-3 μm thin section on the bulk sample performed at an accelerating voltage of 30 keV and a current of 10 nA. A fine polishing step created a smooth surface leaving behind a 1-2 μm thin section on the block sample. This pre-lamella could be welded to the micromanipulator using ion beam assisted platinum deposition lifted out from the bulk sample, transferred, and attached to a FIB half TEM grid. Afterwards, final low ion polishing with an accelerating voltage 5 keV and current of 20 pA was achieved using low incident angles and low ion currents for both sides. The final thickness of the lamella was approximately 50-70 nm for TEM analysis.

Characterization: The absorption spectra were measured on a Cary 5000 UV-vis-NIR spectrophotometer (Varian). Photoluminescence (PL) spectra were acquired on a Fluorolog®-3 system (Horiba Jobin Yvon) using an excitation wavelength of 500 nm. The topography of the active layer was obtained on Bruker MultiMode & AFM in the ScanAsyst mode. Grazing-incidence

3

X-ray diffraction (GIXRD) measurement was carried out at the BL14B1 beamline of the Shanghai Synchrotron Radiation Facility using incident X-ray with a wavelength of 1.24 Å. The 2D-GIXRD pattern, out-of-plane (OOP) and in plane (IP) curves were analyzed by using the Fit 2D software. The transmission electron microscopy (TEM) measurements were performed with accelerating voltage of 200 keV on a JEM-2100PLUS (JEOL) transmission electron microscope. A series of energy-filtered transmission electron microscopy (EFTEM) images were collected at different central energy of filter with energy slit 4 eV in the range of 16 eV-36 eV. Differential scanning calorimetry (DSC) measurements were carried out in the temperature range from 30 $^{\circ}$C to 350 $^{\circ}$C under the nitrogen stream with a heating rate of 10 $^{\circ}$C /min. Baseline and temperature were calibrated with Indium and Zinc.

The photoinduced force microscopy (PiFM) data were acquired on a VistaScope-infrared (IR) microscope from Molecular Vista, Inc, using PtIr-coated silicon cantilevers (PtIr-NCHR) from Nanosensors. The microscope was operated in dynamic mode using the first mechanical mode of the cantilever to detect the PiFM and the second mechanical mode to detect the topography of the sample. The IR source used to excite the sample was manufactured from Block Engineering at the tunable range of 770 cm^{-1} to 1950 cm^{-1}. Spectral acquisition time was 30 seconds for the presented spectra. All spectra have been normalized against the power profile of the laser.

Python programming, a major tool for image processing, was applied here in order to get quantitative information on domain size distribution and composition. We first developed our own Python script and 99.8% Gaussian distribution of contrast was chosen, showing the values of μ-3σ to μ+3σ (99.8%, μ = mean, σ = standard deviation) in original data of PTB7-based and PC$_{61}$BM-based PiFM images. We then normalized the contrasted PiFM images using the min-max

4

normalization approach before image analysis. Then, the normalized PiFM images were integrated through manually thresholding, resulting in the segmentation of domains in the integrated PiFM image well matched with original, superimposed PiFM image. The percentages of three regions, mixed, PTB7-rich and $PC_{61}BM$-rich, were accordingly extracted. From these processed images, the size distribution of the aggregated $PC_{61}BM$ domain was further acquired by conducting a contour detection algorithm, which permits the detection and size calculation of the object of interest.

5
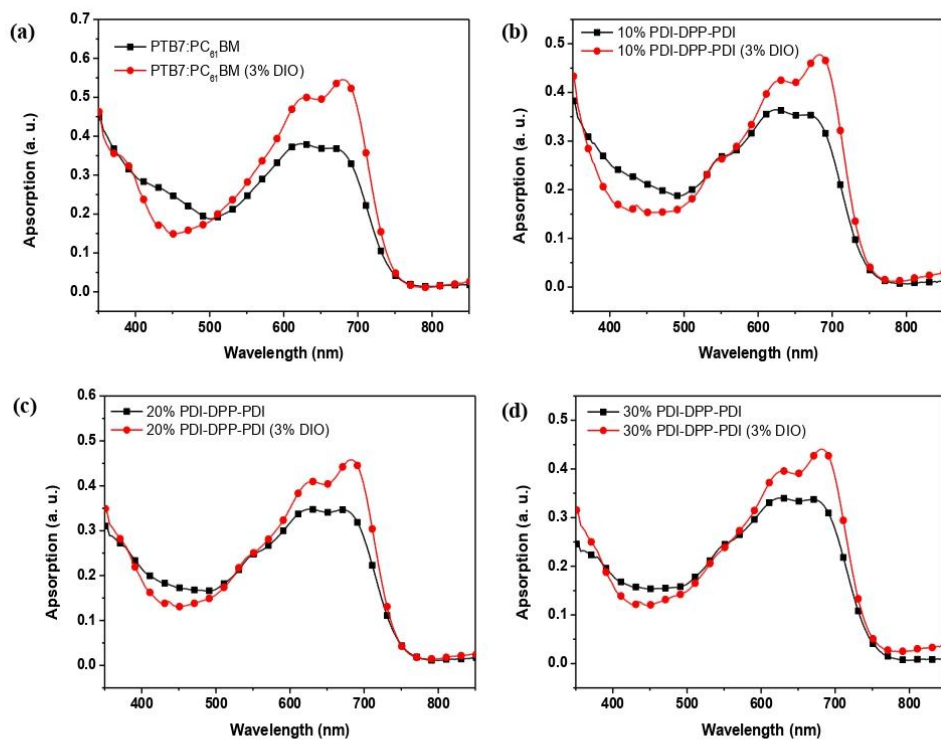
Figure S1. a-d) UV-vis absorption spectra of binary blend film and ternary blend films with or without the DIO treatment.

6
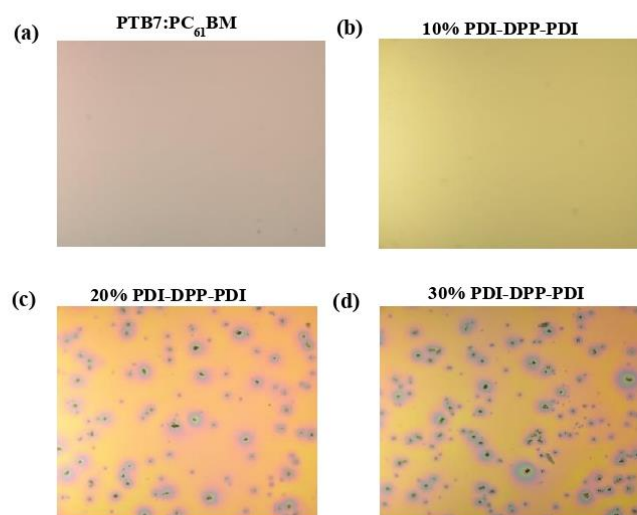
Figure S2. Optical microscopy images of a) PTB7:PC$_{61}$BM blend film and ternary blend films containing b) 10%, c) 20% and d) 30% PDI-DPP-PDI. The large particles in (c) and (d) are composed of undissolved PDI-DPP-PDI based on PiFM measurements.

7
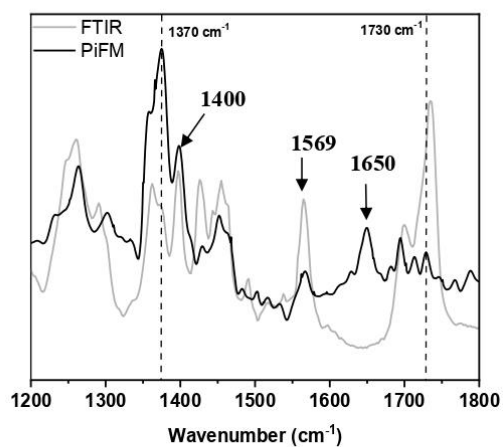
Figure S3. FTIR and PiFM spectra of PTB7:PC$_{61}$BM blend film. The characteristic peak of PTB7 donor at 1370 cm^{-1} and the characteristic peak of PC$_{61}$BM acceptor at 1730 cm^{-1} were chosen for PiFM imaging to show the distribution of PTB7 donor and PC$_{61}$BM acceptor in the film.

8
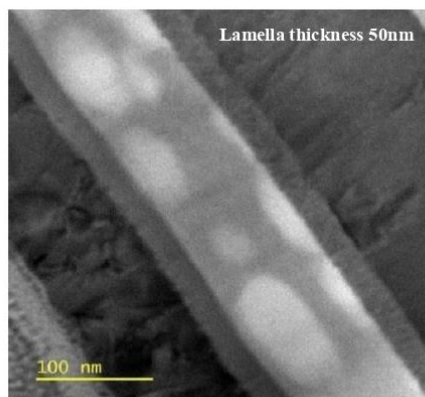
Figure S7. EFTEM images of the cross-sections of PTB7:PC$_{61}$BM device (without the DIO treatment) acquired with a 4 eV wide filter centered at 28.5 eV. TEM lamella thickness is 50 nm.

12
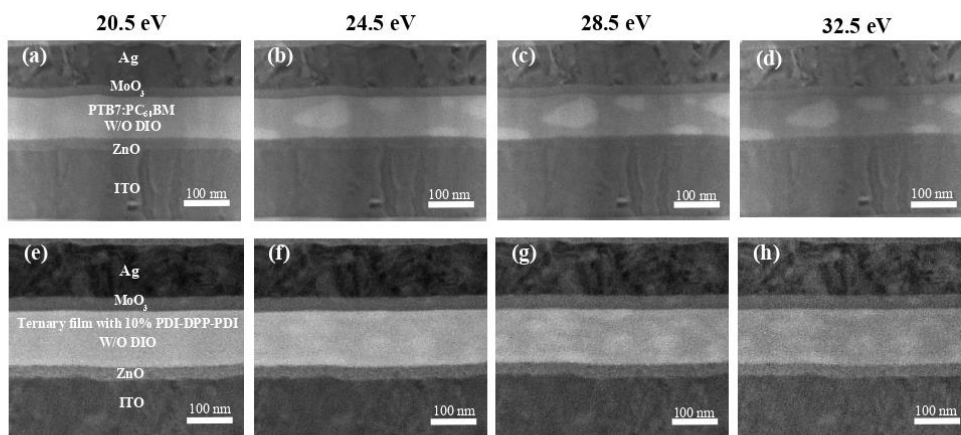
Figure S8. EFTEM images of the cross-sections of a-d) PTB7:PC$_{61}$BM device (without the DIO treatment) and e-h) PTB7:PC$_{61}$BM:10% PDI-DPP-PDI device (without the DIO treatment). Images were acquired with a 4 eV wide filter centered at 20.5 eV, 24.5 eV, 28.5 eV and 32.5 eV.

13
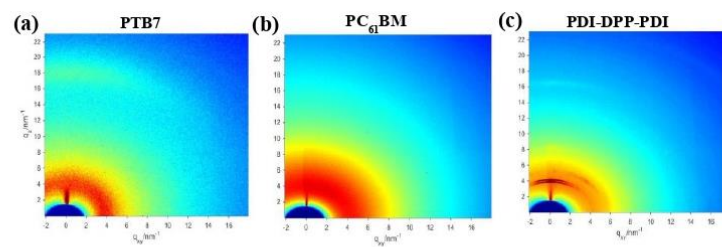
Figure S9. a-c) 2D GIXRD patterns of the pristine PTB7, $PC_{61}BM$, and PDI-DPP-PDI films.

14
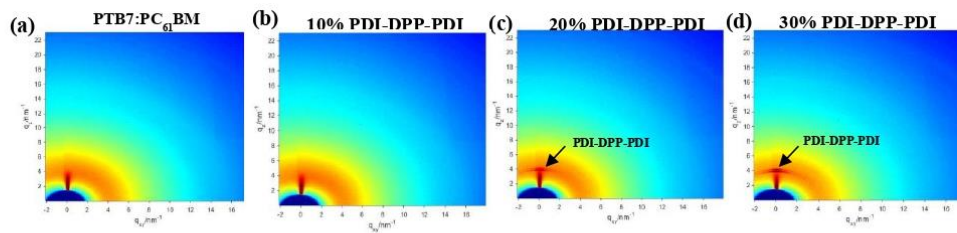
Figure S10. a-d) 2D GIXRD patterns of the binary blend film and ternary blend films containing different contents of PDI-DPP-PDI (10%, 20%, and 30%).

15
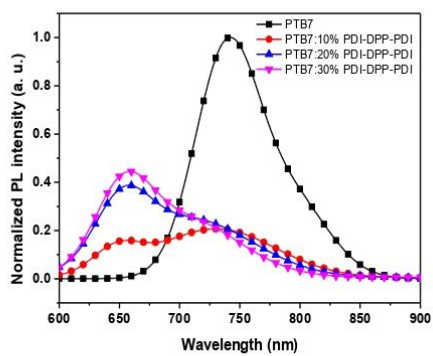
Figure S11. Photoluminescence spectrum of PTB7 film with different contents of PDI-DPP-PDI (10%, 20%, and

30%) with the excitation wavelength of 500 nm.

16

Table S1. Photovoltaic parameters of binary and ternary inverted solar cells under AM 1.5G, 100 mW cm^{-2}

Active layer	Voc [V]	Jsc [mA cm^{-2}]	FF [%]	PCE $_{max\ (ave)}$ [%]^a
PTB7 : PC$_{61}$BM	0.74	15.51	66.80	7.60 (7.45±0.20)
10% PDI-DPP-PDI	0.78	15.95	70.02	8.71 (8.60±0.19)
20% PDI-DPP-PDI	0.80	13.33	64.59	6.85 (6.61±0.22)
30% PDI-DPP-PDI	0.78	12.40	61.52	5.97 (5.55±0.27)

[a] The average values and standard deviation values are obtained from ten devices with two batches.

17

Table S2. Hole mobility, electron mobility and the ratio of hole/electron mobility values for binary blend film and ternary blend films with different contents of PDI-DPP-PDI (10%, 20%, and 30%)

Active layer	Hole mobility(μ_h) cm^2 V^{-1} s^{-1}	Electron mobility(μ_e) cm^2 V^{-1} s^{-1}	μ_e/μ_h
PTB7:PC$_{61}$BM	1.37×10^{-4}	2.96×10^{-4}	2.16
10% PDI-DPP-PDI	1.57×10^{-4}	3.24×10^{-4}	2.06
20% PDI-DPP-PDI	1.54×10^{-4}	3.59×10^{-4}	2.33
30% PDI-DPP-PDI	1.82×10^{-4}	4.47×10^{-4}	2.45

References

[1]   S. M. McAfee, S. V. Dayneko, P. Josse, P. Blanchard, C. Cabanetos, G. C. Welch, *Chem. Mater.* **2017**, *29*, 1309.

[2]   Y. Sun, J. H. Seo, C. J. Takacs, J. Seifter, A. J. Heeger, *Adv. Mater.* **2011**, *23*, 1679.

18

3.2 Miscibility Driven Morphology Modulation in Ternary Solar Cells

Ting Yu, Francesco Tintori, Yuchen Zhang, Wanting He, Edward Cieplechowicz, Raja Sekhar Bobba, Poojan Indrajeet Kaswekar, Maziar Jafari, Yuxuan Che, Yong Wang, Mohamed Siaj, Ricardo Izquierdo, Dmytro F. Perepichka, Quinn Qiao, Gregory C. Welch and Dongling Ma
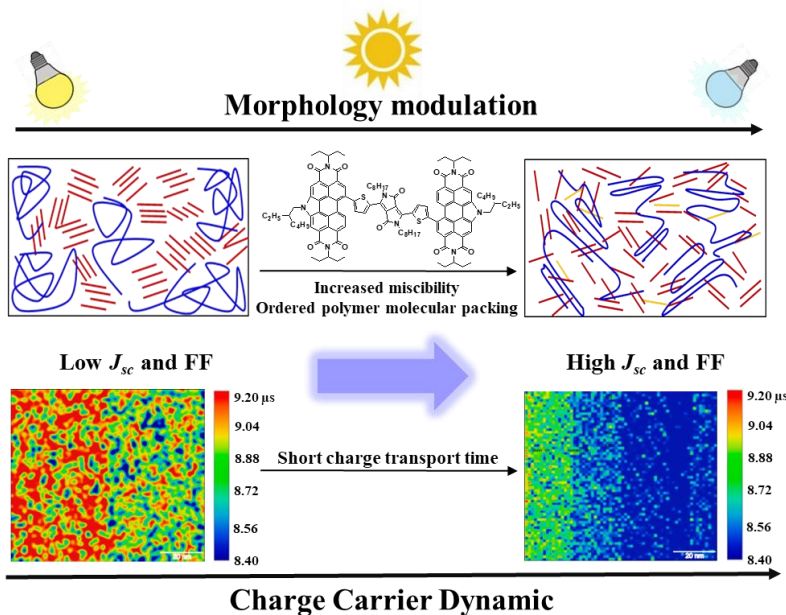
Non-fullerene-based OSCs have made great progress in device performance due to the significant advantages of non-fullerene acceptors (NFAs), such as the wide tunability of chemical structures and properties compared to fullerene acceptors. Therefore, incorporating NFA as an additional component to construct the non-fullerene-based ternary OSC is a convenient and effective strategy to broaden spectral absorption, form charge cascades, and optimize morphology, thereby increasing photon absorption and charge transport as well as reducing charge recombination. Specifically, a judicious selection of the NFA guest material can fine-tune the miscibility of the components, which is highly correlated with the morphology of the photoactive layer. Because of the lack of the quantitative information on the tunability of the miscibility, empirical fine-tuning of the miscibility remains critical for achieving the optimal morphology and device performance of OSCs based on given host donor and acceptor materials.

In this work, a nearly orthogonal structure of PDI-based non-fullerene acceptor, PDI-EH, was designed and synthesized to suppress its aggregation and then integrated into ternary OSCs. It revealed that the PDI-EH could fine-tune the miscibility of host donor and acceptor materials to form an optimally intermixed phase with short-range molecular order by Flory-Huggins interaction parameters and differential scanning calorimetry (DSC) measurements. Selective PiFM imaging of donor and acceptor materials exhibited the formation of well-mixed films after the PDI-EH incorporation. Additionally, the relationship between the optimized morphology and charge carrier dynamics at the nanoscale was explored by a novel transient photo-response atomic force microscopy (TP-AFM) technique. The results revealed a desirable charge carrier dynamic behavior with reduced charge transport time, increased charge recombination lifetime and extended charge diffusion length. As a result, the introduction of the PDI-EH led to improved performance of OSCs under 1-sun, and indoor 2700 K and 6500 K LED illuminations with efficiency enhancement of 12%, 14% and 16%, respectively. This work offers insights into morphology modulation and the resulting local charge carrier dynamic, thereby facilitating the future development of OSCs.

Journal of Materials Chemistry A

PAPER

Check for updates

Miscibility driven morphology modulation in ternary solar cells†

Ting Yu, [a] Francesco Tintori, [b] Yuchen Zhang, [c] Wanting He, [a] Edward Cieplechowicz, [b] Raja Sekhar Bobba, [c] Poojan Indrajeet Kaswekar, [c] Maziar Jafari, [d] Yuxuan Che, [e] Yong Wang, [a] Mohamed Siaj, [d] Ricardo Izquierdo, [f] Dmytro F. Perepichka, [e] Quinn Qiao, [c] Gregory C. Welch [*b] and Dongling Ma [*a]

Organic solar cells (OSCs) are viable power sources for photovoltaic applications. In this work, a non-fullerene acceptor, PDI-EH, was designed to form a nearly orthogonal structure to suppress its aggregation, and integrated into ternary OSCs. In addition to enhanced photon absorption and matched charge cascade, a PDI-EH acceptor modulated the morphology, which is crucial to affect device efficiency. Detailed analysis revealed that PDI-EH can fine-tune the miscibility of the host donor and acceptor (D/A) materials to form an optimally intermixed phase with short-range molecular order. Photo-induced force microscopy (PiFM) for selective PiFM imaging of D/A materials provided strong evidence that D/A materials formed well-mixed films after PDI-EH incorporation. Additionally, nanoscale spatial mapping of charge carrier dynamics was realized for the first time in a ternary film using a novel transient photo-response atomic force microscopy (TP-AFM) technique. The resulting TP-AFM data revealed a reduced charge transport time, increased charge recombination lifetime and extended charge diffusion length. These improvements brought about by PDI-EH benefit the photovoltaic performance of ternary OSCs under both 1-sun and indoor illuminations. Our work offers insights into morphology modulation and the resulting local charge carrier dynamic, thereby facilitating the development of OSCs in practical applications.

Introduction

Organic solar cells (OSCs) are considered one of the most promising technologies for utilizing solar energy in wearable electronics and indoor power generation devices, due to their light weight, flexibility, ease of processing, compatibility with large-scale fabrication (*e.g.* roll-to-roll processing) and short energy payback time.[1,2] Since Heeger and Wudl's concept of 'bulk heterojunction' (BHJ) OSCs comprising of a phase-separated mixture of donor and acceptor molecules in 1995,[3] the power conversion efficiencies (PCEs) of BHJ-OSCs have grown tremendously through the design of new organic donor/acceptor (D/A) materials and device architectures, now exceeding 18%.[4-6] Further improvements, however, will be extremely challenging and require the simultaneous enhancement of photon absorption, exciton generation and dissociation, and charge transport to improve the key performance parameters (open-circuit voltage (V_{oc}), short-circuit current density (J_{sc}), and fill factor (FF)). Significant efforts have been expended in design and synthesis of new D/A materials with complementary absorption and well-matched energy level alignment so as to maximize the photon harvesting and charge transfer.[7,8] Besides, the optimization of the BHJ morphology in the blend film is also crucial and cannot be neglected, since the optimal morphology with suitable phase separation, proper domain size (10–20 nm), high domain purity and interpenetrating nanostructures is of vital importance for effective photo-generated charge carrier dynamics, which are directly correlated with device performance.[9]

Many factors including the molecular properties of materials, D/A ratios and post-treatment processing influence the crystallinity, miscibility and molecular stacking in the blend film, resulting in different BHJ morphologies.[10] Unfortunately,

[a]Énergie, Matériaux et Télécommunications, Institut National de la Recherche Scientifique (INRS), 1650 Boul. Lionel-Boulet, Varennes, Québec, J3X 1P7, Canada. E-mail: Dongling.ma@inrs.ca

[b]Department of Chemistry, University of Calgary, 2500 University Drive N. W., Calgary, T2N 1N4, Alberta, Canada

[c]Department of Mechanical and Aerospace Engineering, Syracuse University, NY, 13244, USA

[d]Département de Chimie, Université du Québec à Montréal, 405 Rue Sainte-Catherine Est, Montréal, H2L 2C4, Québec, Canada

[e]Department of Chemistry, McGill University, Montreal, H3A 0B8, Quebec, Canada

[f]Département de Génie électrique, École de Technologie Supérieure, Montréal, H3C 1K3, Québec, Canada

† Electronic supplementary information (ESI) available. See DOI: https://doi.org/10.1039/d2ta09928d

the lack of common approaches for quantitative analysis of polymer crystallinity and the structural complexity of polymer composites, as well as inconsistent classifications for the molecular ordering of polymer donors in the literature lead to imprecise interpretation of morphologic results. Ade *et al.*[11] classified the molecular ordering of polymers by combining grazing incidence wide-angle X-ray scattering (GIWAXS) and differential scanning calorimetry (DSC) measurements and proposed a consistent terminology: amorphous, oriented amorphous, highly disordered, paracrystalline and crystalline. Among them, amorphous polymers and highly disordered polymers both have no observable endothermal melting temperature (T_m) in DSC scans. However, the amorphous polymers exhibit a glass transition temperature (T_g) and no obvious pattern other than halo scattering in GIWAXS, while highly disordered polymers have no T_g due to the rigidity of the conjugated backbones, but often have a (100) lamellar peak and a (010) π–π stacking peak without any higher order (h00) peaks. The clear interpretation and classification of polymer crystallization are essential for understanding the complex morphology of OSCs and its effects on the device performance.

In most BHJ OSCs, an amorphous/highly disordered polymer donor usually displays good miscibility with small molecular acceptors, and forms a two-phase morphology consisting of mixed phases with suppressed crystallization of the small molecular acceptor and pure acceptor aggregates. A crystalline polymer donor shows low miscibility with the acceptor and facilitates the formation of three-phase morphology including donor aggregates, acceptor aggregates and a mixed phase.[10,12] Because of the short exciton diffusion length (~5–15 nm) in organic semiconductors, manipulating the composition of the mixed phase can generate the proper domain size (10–20 nm), thus favoring exciton diffusion into the donor and acceptor interface, and dissociation. It should be noted that too low or too high miscibility of D/A materials can degrade photovoltaic performance by forming large-scale phase separations or fully mixed D/A structures, which are detrimental to exciton dissociation and charge transport, respectively. However, there is no quantitative information about what miscibility is required for optimal morphology. Considering the high relevance between the miscibility and morphology, empirically fine-tuning the miscibility remains critical for achieving the optimal morphology and device performance of OSCs based on given D/A materials. Incorporating an additional component to construct ternary OSCs is a convenient strategy for fine tuning miscibility and morphology of OSCs. Among various potential "third components", non-fullerene acceptors (NFAs) seem most promising because of their wide tunability of chemical structures and properties. When well designed, they can help adjust the miscibility of host D/A materials for regulation of the phase separation at the nanoscale, and moreover, extend the spectral absorption for harvesting more photons and form the cascade-structural energy levels for efficient charge transfer.[13–15]

In this work, we chose a PBDB-T donor and ITIC-4F acceptor (Fig. 1a) to serve as host photoactive layer materials in ternary OSCs due to their extraordinary photo-stability approaching 10
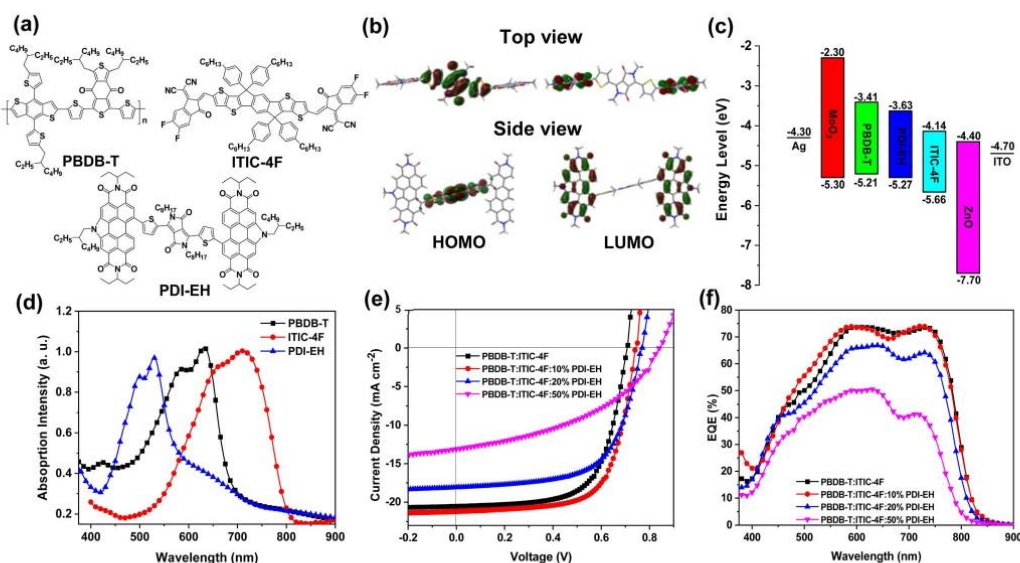
Fig. 1 (a) Molecular structures of PBDB-T, PDI-EH and ITIC-4F; (b) optimized molecular geometries and HOMO/LUMO level of PDI-EH calculated with DFT at the B3LYP/6-31G(d) level of theory. All alkyl side chains were replaced with methyl groups; (c) schematic energy-level diagram of all materials involved in OSC devices; (d) UV-vis absorption spectra of pristine PBDB-T, ITIC-4F and PDI-EH films; (e) J–V characteristics of PBDB-T/ITIC-4F binary and ternary devices under 1-sun illumination, and (f) EQE spectra of PBDB-T/ITIC-4F binary and ternary devices.

years.[16] It was suggested that the high energy offset of the lowest unoccupied molecular orbital (LUMO) levels between the PBDB-T donor and ITIC-4F acceptor ($\Delta E_{LUMO} = D_{LUMO} - A_{LUMO}$) is detrimental for exciton dissociation.[17,18] The ternary blend strategy can help to solve this problem by forming a cascade energy alignment, and then increasing the photovoltage. In addition, a judicious selection of the guest material can fine-tune the miscibility of the components and the morphology of the film, improving the charge separation and transport.

Here, we synthesized an organic solvent-soluble diketo-pyrrolopyrrole (DPP) small molecule with appended ethylhexyl (EH) substituted N-annulated perylenediimide (PDI) end capping units. This molecule named PDI-EH exhibits a highly twisted confirmation with the PDI units out-of-plane from the DPP core. The compound was incorporated as the third component into the PBDB-T/ITIC-4F blend film to fabricate ternary OSCs. The PDI-EH acceptor improves the absorption of the PBDB-T/ITIC-4F film and forms a cascade of energy levels, resulting in harvesting of more photons and increasing of the photovoltage of OSCs. Equally importantly, the PDI-EH acceptor fine-tunes the miscibility of the D/A components, leading to an appropriately mixed phase, as suggested by Flory–Huggins interaction parameters and supported by DSC measurements. Combined with the results of GIWAXS measurements, it shows that PDI-EH incorporation promotes local short-range molecular ordering in an appropriately mixed phase, which can produce fewer morphological defects and crystal boundaries to inhibit charge recombination. In particular, a novel, lab-made transient photo-response atomic force microscopy (TP-AFM) was used for the first time in ternary OSCs for the nanoscale spatial mapping of charge carrier dynamics to reveal improved charge transport and reduced charge recombination due to the optimized morphology by introducing PDI-EH. As a result, the introduction of PDI-EH led to improved performance of OSCs under 1-sun, and indoor 2700 K and 6500 K LED illuminations with an efficiency enhancement of 12%, 14% and 16%, respectively.

Results and discussion

PDI derivatives are promising candidates for electron acceptors in OSCs due to their high electron-affinity and outstanding stability.[19] However, the strong aggregation tendency of PDI derivatives results in the formation of large crystalline domains, inhibiting charge separation. Such a strong aggregation of polycyclic aromatic molecules could often be suppressed by distorting their backbone.[20,21] Thus, we synthesized a highly twisted PDI-EH acceptor featuring PDI terminal units separated by a DPP core based on our previous approach,[22,23] and its synthetic route is shown in Scheme S1† and nuclear magnetic resonance spectra can be found in Fig. S9–10 (ESI†). The molecular structure of PDI-EH is presented in Fig. 1a. As predicted by density functional theory (DFT) calculations (B3LYP/6-31G(d)), the PDI and DPP units are nearly orthogonal ($\varphi = 87°$) to each other in the optimized geometry (Fig. 1b). Such a conformation is expected to hinder intermolecular π-stacking and suppress aggregation. The highest occupied molecular

orbital (HOMO) and LUMO wavefunction densities are distributed almost exclusively on the DPP and PDI units, respectively. Therefore, electron transport of PDI-EH is expected to take place through LUMO orbital couplings from π-stacked PDI terminal units. Cyclic voltammetry (CV) measurements found the HOMO and LUMO levels of PDI-EH at −5.27 and −3.63 eV, respectively, by comparison with ferrocene/ferrocenium oxidation (Fc^+/Fc assumed at −4.80 eV, Fig. S1, ESI†). These energy levels are positioned between the HOMO/LUMO levels of PBDB-T and ITIC-4F (−5.21/−3.41 eV and −5.66/−4.14 eV, respectively), allowing formation of an energy cascade (Fig. 1c).[24,25] The ultraviolet-visible (UV-vis) absorption spectra of pristine donor and acceptors films are displayed in Fig. 1d. It shows that the absorption of PDI-EH at 415–550 nm compensates for the weak absorption of PBDB-T and ITIC-4F films in this spectral range.

Considering the potential benefits of the molecular design of PDI-EH and the rational combination of these three components, we moved forward to fabricate devices with a configuration of indium tin oxide (ITO) glass/ZnO/active layer/MoO₃/Ag.[19] The current density versus voltage (J–V) characteristics of the binary and ternary devices with different contents of PDI-EH (10%, 20%, and 50%) were measured under simulated AM 1.5 G illumination at 100 mW cm^{-2} (Fig. 1e). The increased V_{oc} in all the ternary OSCs with respect to that of binary OSCs is consistent with the formation of the cascade structure. In addition, the ternary device incorporated with 10% PDI-EH led to the best PCE of 10.6% with a V_{oc} of 0.74 V, a J_{sc} of 21.17 mA cm^{-2} and a FF of 67.1% (Table 1). In contrast, 20% and 50% PDI-EH introduction into active layers reduced J_{sc} and FF, but increased V_{oc}, causing an overall decrease in the device performance. In particular, the device with 50% PDI-EH gave the worst performance with dramatically reduced J_{sc} and FF, which is very likely due to an inappropriate morphology formed due to the full mixing of PBDB-T and ITIC-4F, to be discussed later on. As shown in Fig. 1f, the external quantum efficiency (EQE) spectrum of the 10% PDI-EH-based ternary device was enhanced in a wavelength range of 450–590 nm, which is in line with the absorption feature of the PDI-EH acceptor.

Since the performance of OSCs is determined by many factors, including, but not limited to absorption and energy levels, the contribution of PDI-EH is worth further investigation. Among different factors, morphology is an important one, since it is directly related to exciton dissociation, charge transport and recombination. Appropriate morphology of the active layer could favor exciton dissociation and charge transport, which can be driven by the miscibility of the donor and acceptor. Contact angle measurements were conducted to investigate the

Table 1 Photovoltaic parameters of binary and ternary solar cells under simulated AM 1.5 G illumination, 100 mW cm^{-2}

Active layer	V_{oc} [V]	J_{sc} [mA cm^{-2}]	FF [%]	PCE max. (ave.) [%]
PBDB-T: ITIC-4F	0.70	20.50	65.7	9.5 (9.4 ± 0.03)
10% PDI-EH	0.74	21.17	67.1	10.6 (10.4 ± 0.02)
20% PDI-EH	0.77	18.06	62.9	8.7 (8.6 ± 0.01)
50% PDI-EH	0.83	13.17	42.7	4.7 (4.6 ± 0.02)
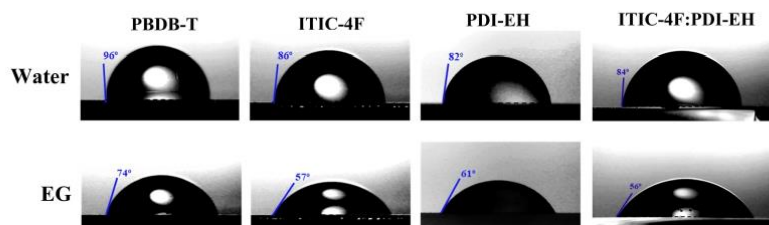
Fig. 2 Water and EG contact angles on pristine PBDB-T, ITIC-4F, and PDI-EH films, and the ITIC-4F/PDI-EH blend film.

miscibility of the donor and acceptor. The surface energies (γ) of PBDB-T, ITIC-4F and PDI-EH films were calculated to be 21.1 mN m^{-1}, 32.3 mN m^{-1} and 26.6 mN m^{-1}, respectively, *via* the contact angle data of water and ethylene glycol (EG) on these pristine films.[26,27] The contact angles and surface energies are displayed in Fig. 2 and Table 2. Based on the equation of $\chi \propto \left(\sqrt{\gamma_1} - \sqrt{\gamma_2}\right)^2$, where γ_1 and γ_2 refer to the surface energies of the PBDB-T donor and acceptors, the Flory–Huggins interaction parameter (χ) was estimated to be 1.21, 0.31 and 0.29 for the PBDB-T donor with ITIC-4F, PDI-EH, and ITIC-4F/PDI-EH acceptors, respectively.[27,28] These values suggest that the PBDB-T donor has good miscibility with the PDI-EH acceptor. Moreover, compared to the χ value of PBDB-T and ITIC-4F, the χ value of PBDB-T and ITIC-4F/PDI-EH decreases to 1.02, suggesting that PDI-EH can increase the miscibility of PBDB-T and ITIC-4F.

DSC measurements were performed to explore the effect of PDI-EH incorporation on the crystallization and miscibility of the PBDB-T donor and ITIC-4F acceptor in blend films. The first DSC heating-scan profiles of pristine and blend films are shown in Fig. 3a. The PBDB-T polymer had no obvious thermal transition peaks due to its amorphous or highly disordered characteristics, and thus, in our system, the PBDB-T polymer is conducive to exist in the mixed phase.[11] On the other hand, ITIC-4F and PDI-EH small molecule acceptors showed distinct endothermic peaks at 322 °C and 343 °C, respectively. Notably, after a sharp endothermic peak at 322 °C, ITIC-4F had a broad exothermic peak at 331 °C, indicative of the melting and recrystallization processes.[29] Besides, the ITIC-4F in the PBDB-T/ITIC-4F binary blend underwent the same thermodynamic

process as the neat ITIC-4F, judging from their similar thermal transition peaks. Also, the binary blend showed a distinct and sharp endothermic peak at 316 °C, which indicated that the ITIC-4F in the binary blend featured considerable crystallization. Compared to the binary blend, ternary blends containing 10% and 20% PDI-EH exhibited the exothermal cold crystallization temperatures (T_{cc}) of ITIC-4F at 205 °C and 214 °C, respectively. The exothermic cold crystallization behavior took place before the melting temperature, indicating the crystallization of the initially amorphous phase and defect-rich crystal rearrangement.[30–32] The enthalpies of the cold crystallization peak (ΔH_{cc}) and the endothermic peak (ΔH_{m}) of ternary blends showed that the ΔH_{cc} of 10% and 20% PDI-EH-containing blends (29.7 and 25.8 J g^{-1}, respectively) was more than half of their ΔH_{m} (59.2 and 49.3 J g^{-1} respectively). It may be interpreted that the crystallization of ITIC-4F was hindered by the PBDB-T polymer matrix due to enhanced miscibility between PBDB-T and ITIC-4F after PDI-EH incorporation.[32] Furthermore, the T_{cc} and the T_{m} disappeared after 50% PDI-EH incorporation due to the overmixing of ITIC-4F and PBDB-T, which led to no detectable ITIC-4F crystallites in the DSC scan. This morphology may increase charge recombination, which leads to the large deterioration of the efficiency of the 50% PDI-EH-containing ternary device.

Two-dimensional (2D)-GIWAXS measurements were conducted to better understand the film microstructure. 2D-GIWAXS patterns of pristine and blend films and the related 1D out-of-plane (OOP) and in-plane (IP) curves are displayed in Fig. 3b–e and Fig. S2 (ESI†). The pristine PBDB-T film showed a lamellar (100) peak in the IP direction at $q = 0.29$ Å^{-1}, a lamellar (100) peak in the OOP direction at $q = 0.26$ Å^{-1} and a π–π stacking (010) peak in the OOP direction at $q = 1.67$ Å^{-1}, indicating that the PBDB-T polymer formed both edge-on and face-on orientations with respect to the substrate.[17,33] Although PBDB-T exhibited distinct scattering peaks in the 2D-GIWAXS pattern, the lack of T_{m} and T_{g} in its DSC profile still points to a global disorder (*i.e.* lack of long-range order), according to the classification of Ade *et al.*[11] Pristine ITIC-4F and PDI-EH films presented broad and isotropic diffraction scattering in the 2D-GIWAXS patterns (Fig. S2b and c, ESI†), which suggests that ITIC-4F and PDI-EH acceptors had no preferential orientation. It is well-known that the π–π stacking (010) in the OOP of blend films can be beneficial for charge transport.[34–36] Comparing the 2D-GIWAXS of the binary and ternary films (Fig. 3b–e),

Table 2 Contact angles of water and EG on pristine films, and related surface energy parameters

Films	θ_{water} (°)	θ_{EG} (°)	γ (mN m^{-1})[a]	χ^{D-A}[b]
PBDB-T	96	74	21.1	
ITIC-4F	86	57	32.3	1.21
PDI-EH	82	61	26.6	0.31
ITIC-4F:PDI-EH	84	56	31.5	1.02

[a] γ represents the surface energies *via* the contact angle data of water and EG on these films. [b] The Flory–Huggins interaction parameters between the donor (PBDB-T) and acceptors (ITIC-4F and PDI-EH) were calculated by following the formula: $\chi \propto \left(\sqrt{\gamma_D} - \sqrt{\gamma_A}\right)^2$.

Paper
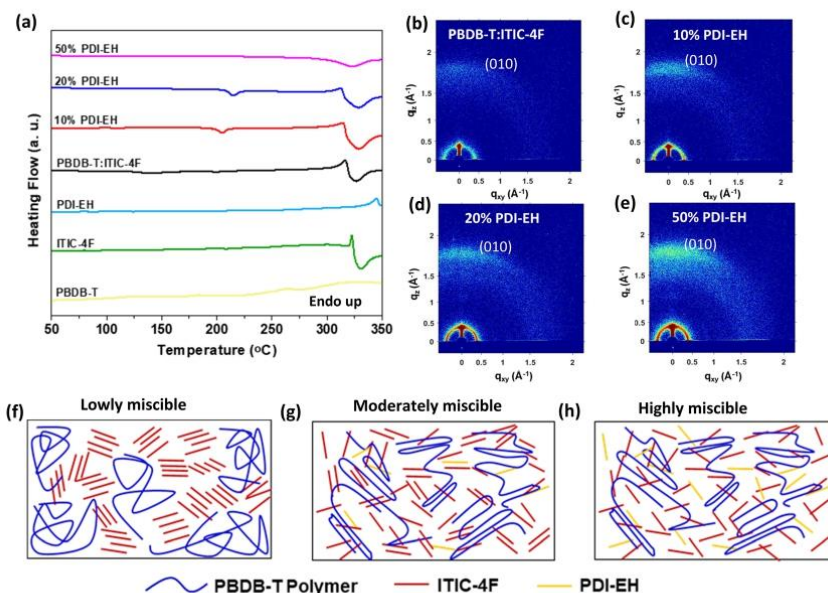
Fig. 3 (a) The first DSC heating-scan profiles from 50 °C to 360 °C of pristine materials, the PBDB-T/ITIC-4F blend, and ternary blends containing 10%, 20% and 50% PDI-EH (pristine materials, and binary and ternary blends were obtained by chlorobenzene solution casting). 2D-GIWAXS patterns of the PBDB-T/ITIC-4F binary blend film (b), ternary blend films containing 10% PDI-EH (c), 20% PDI-EH (d), and 50% PDI-EH (e); (f–h) schematic illustration of the morphology of blend films, which represents the different degrees of miscibility (lowly, moderately and highly miscible) based on results of DSC and 2D-GIWAXS measurements.

intensities of π–π stacking (010) peaks in the OOP of ternary films were found to obviously increase. In addition, the coherence length (L_c) can be measured from the full width at half-maximum (FWHM) of the (010) diffraction peak by using Scherrer's equation to reveal the size of coherently diffracting regions.[37–40] L_c values associated with the OOP (010) peak were calculated to be 20.4 Å, 19.9 Å and 19.7 Å for ternary films containing 10%, 20% and 50% PDI-EH, respectively, which are larger than that of the binary film (16.2 Å), indicating that the PDI-EH incorporation could improve the local π–π stacking short molecular order. By understanding the effect of PDI-EH on the miscibility and molecular ordering through the results of DSC and 2D-GIWAXS measurements, we presented the schematic illustration of the morphology of blend films in Fig. 3f–h. The binary film showed a relatively large volume of crystalline ITIC-4F and relatively low miscibility (Fig. 3f), leading to the formation of more acceptor aggregates and less mixed phase, which is not conducive to exciton dissociation at the donor and acceptor interface. Conversely, the 50% PDI-EH-containing ternary film presented high miscibility with the overmixing of the donor and acceptors (Fig. 3h), thereby increasing charge recombination and decreasing the device FF. Accordingly, the moderate miscibility achieved by introducing 10% PDI-EH favored the charge separation and suppressed charge recombination, and PDI-EH incorporation simultaneously induced short-range molecular order of the PBDB-T polymer, facilitating charge transport, as schematically presented in Fig. 3g. We also

include the 20% sample into this category of 'moderate miscibility', because ITIC-4F still showed observable crystallinity, similar to that of the 10% sample and distinctively different from that of the 50% sample based on DSC measurements. Nevertheless, the photovoltaic performance of the 20% blend under AM 1.5 illumination was slightly weaker than that of the binary device, highlighting the performance's sensitivity to the film morphology and importance of morphology fine tuning.

The surface morphology of the active layer was explored by atomic force microscopy (AFM). Ternary films containing 10%, 20% and 50% PDI-EH showed uniform morphology and reduced root-mean-square (RMS) roughness values (2.47 nm, 2.56 nm and 2.95 nm, respectively), compared to the binary film (3.37 nm), attributed to the increased miscibility after PDI-EH incorporation (Fig. S3, ESI†). The slightly lower RMS values for the 10% PDI-EH blend is consistent with a more uniform morphology, as could be expected based on the observed higher J_{sc} and FF values than other cases. In addition, AFM topography images of the binary film and ternary films exhibited distinct fibril-like morphology, which was believed to mainly consist of the fibrous skeleton of the PBDB-T donor mixed with acceptors, based on the observation of the distinct fibril-like morphology of the pristine PBDB-T film and no obvious phase-separated morphology of two acceptors from the AFM topography and phase images (Fig. S4, ESI†). In addition, the pristine PBDB-T film exhibited distinct fibril-like morphology, which could provide a channel to promote hole transport. Meanwhile, the

decreased roughness of acceptor-only blend films suggests that PDI-EH and ITIC-4F acceptors could form an intermixed phase due to their excellent miscibility, which can speed up the electron transport from the LUMO level of PBDB-T to ITIC-4F through the PDI-EH acceptor as a bridge in the ternary film.

To further explore the distribution and compatibility of materials in the active layer, advanced photo-induced force microscopy (PiFM) coupling AFM with infrared (IR) spectroscopy was used, allowing the characterization of the distribution of different components in the blend film with a high spatial resolution.[15] The topography images of the binary and ternary films (10%, 20% and 50% PDI-EH), and corresponding PiFM spectra are shown in Fig. S5 (ESI†). The blend films displayed similar PiFM spectra taken from ten locations in the corresponding topography image, indicating relatively good mixing of the donor and acceptors. The non-overlapping peaks of PBDB-T at 1641 cm^{-1} (the benzoquinone group of PBDB-T)[41-43] and ITIC-4F at 1540 cm^{-1} (stretching of the CC bond)[44] were chosen for PiFM imaging of the distribution of these two components, which allowed study of the degree of component mixing. PiFM images from the same area in Fig. 4a–p, highlighting the distribution of PBDB-T imaged at 1641 cm^{-1} and ITIC-4F at 1540 cm^{-1}, yielded a similar fibrous feature. The ITIC-4F-based binary image of the PBDB-T/ITIC-4F blend film (Fig. 4m) showed an uneven fiber size (as marked by the red rectangle) attributed to ITIC-4F aggregates, while the PDI-EH

introduction facilitated the formation of a more uniform dispersion of ITIC-4F (Fig. 4j–l) due to better mixing of PBDB-T and ITIC-4F, which is supported by the above results of DSC and 2D-GIWAXS. This point is even more apparent from the superimposed images (Fig. 4q–t) based on the distribution of the PBDB-T donor (green area) and ITIC-4F acceptor (red area). In Fig. 4q, the superimposed PiFM image of the PBDB-T/ITIC-4F blend film showed relatively low mixing along with distinct ITIC-4F aggregates (red area), compared to that of ternary films. Thus, these observations showed the delicate tuning of the morphology with the introduction of PDI-EH.

Morphology variation can be directly reflected from charge transport and recombination behavior. Thus, we conducted space charge limited current (SCLC) measurements to study the charge carrier mobility of blend films and to correlate it with morphology and superior performance of the optimized ternary device. J–V curves of hole-only devices and electron-only devices are shown in Fig. 5a and b. Hole/electron mobilities of binary and 10% PDI-EH-containing ternary devices were estimated to be $1.2 \times 10^{-4}/4.1 \times 10^{-5}$ cm^2 V^{-1} s^{-1} and $1.6 \times 10^{-4}/5.8 \times 10^{-5}$ cm^2 V^{-1} s^{-1}, respectively, based on the Mott–Gurney square law equation.[45,46] According to the charge mobility parameters summarized in Table S1,† it is clear that 10% PDI-EH introduction would contribute to improving electron mobility and achieving the most balanced charge carrier mobility $\mu_h/\mu_e = 2.8$ (vs. 3.0 for the binary device, 3.8 for the 20% PDI-EH ternary
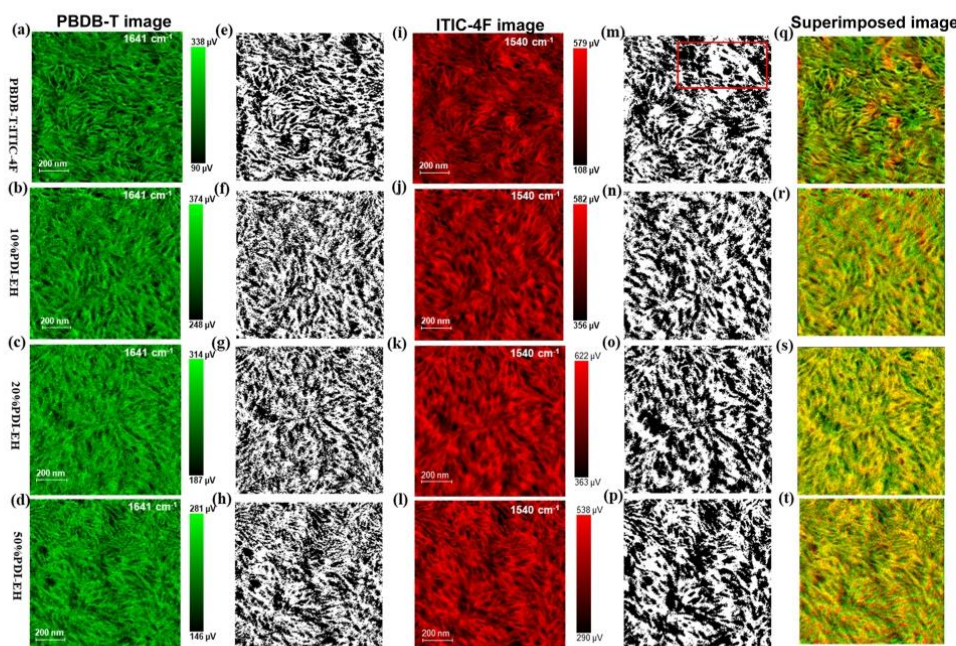
Fig. 4 PiFM images of the PBDB-T/ITIC-4F blend film scanned at 1641 cm^{-1} (a) and 1540 cm^{-1} (i), and the related binary images (e and m); (q) the superimposed PiFM image. PiFM images of ternary blend films containing 10%, 20% and 50% PDI-EH taken at 1641 cm^{-1} (b–d) and 1540 cm^{-1} (j–l), and the related binary images (f–h and n–p); (r–t) the superimposed PiFM images. PiFM image size: 1 μm × 1 μm.

Paper
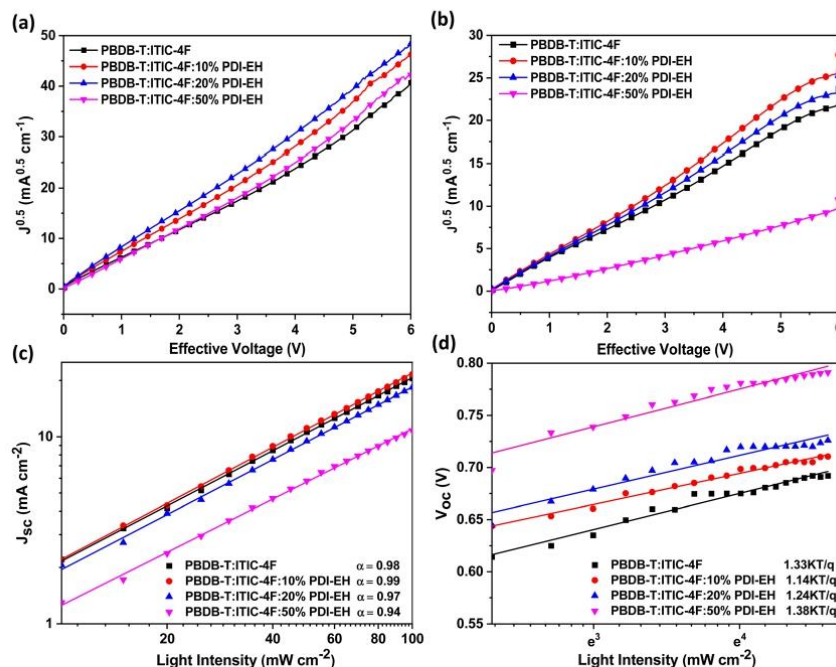
Fig. 5 (a) Hole mobility and (b) electron mobility for the binary blend film and ternary blend films containing 10%, 20% and 50% PDI-EH; (c) the dependence of J_{sc} on P_{light}, and (d) the dependence of V_{oc} on P_{light} for the binary blend film and ternary blend films containing 10%, 20% and 50% PDI-EH.

device, and 18.4 for the 50% PDI-EH ternary device), which explained its higher J_{sc} value. Furthermore, 10% PDI-EH proved beneficial for increasing the exciton dissociation possibility of the ternary device from 94.4% to 95.6% as revealed by plotting the photocurrent density *versus* effective voltage ($J_{ph} - V_{eff}$) plots (Fig. S6, ESI†). This balanced charge carrier mobility and increased exciton dissociation of 10% PDI-EH blends should result from their optimal morphology.

We explored the charge recombination dynamics according to the relationship between J_{sc} and light intensity (P_{light}) as well as that between V_{oc} and P_{light} (Fig. 5c and d).[7,8] The relationship of J_{sc} and P_{light} could be expressed by using an equation of $J_{sc} \propto P_{light}^{\alpha}$. The 10% PDI-EH-containing ternary device showed a higher α value of 0.99, compared to the α value of binary device (0.98), suggesting that 10% PDI-EH introduction can effectively reduce bimolecular recombination. Moreover, ternary devices with 20% and 50% PDI-EH with reduced α values of 0.97 and 0.94, respectively, indicated increased bimolecular recombination. Thus, significantly unbalanced charge mobility and much lower α values of the ternary device containing 50% PDI-EH proved that too much PDI-EH introduction could induce excessive mixing of donor and acceptors, and thus reduced charge transport and increased bimolecular recombination. Additionally, the dependence of V_{oc} on the P_{light} for the binary and ternary devices containing 10%, 20% and

50% PDI-EH was measured with a slope of 1.33, 1.14, 1.24 and 1.38 KT/q, respectively. The smallest slope of the 10% PDI-based ternary device suggested that trap-assisted recombination can be suppressed due to ideal miscibility, complying well with the high J_{sc} and FF values.[47] After introducing 20% and 50% PDI-EH, the slopes were gradually increased, which is consistent with their surface morphology in AFM measurements. The results confirmed that the 10% sample showed both decreased bimolecular recombination and trap-assisted recombination, suggesting its better morphology under the moderate D/A mixing condition.

Transient photo-response AFM (TP-AFM) with high spatial resolution (~9.26 nm by the actual measurement) was further conducted to gain insights into the charge carrier dynamics by nanoscale visualization and mapping of the charge carrier recombination lifetime (τ_r), charge carrier transport time (τ_t) and charge carrier diffusion length (L_D) with a correlation to the influence of PDI-EH incorporation on nanoscale morphology.[48] A green laser (532 nm) pulse with temporal resolution that reaches nanosecond as an excitation source was directed through the bottom of an inverted structure ITO glass/ZnO/active layer to generate charge carriers. Current sensing AFM (C-AFM) was employed to record the topography and current images of the binary film and the optimal ternary film containing 10% PDI-EH to distinguish the donor-rich and acceptor-

Journal of Materials Chemistry A

rich regions, where the donor-rich regions were associated with less conductive regions, whereas acceptor-rich regions were related to more conductive regions.[49,50] The C-AFM images of the binary and 10% PDI-EH-containing ternary films and related topography images are shown in Fig. S7 (ESI†), where red rectangle regions (100 nm × 100 nm) were used to map charge carrier dynamics by collecting the local transient photovoltage (TPV) decays using 1.0 MΩ input impedance from an oscilloscope and transient photocurrent (TPC) decays using 50 Ω input impedance. Fig. 6 displays the nanoscale mapping of τ_r, τ_t, and L_D, where the white dashed lines were presented to show the donor-rich regions and acceptor-rich regions. The τ_r value

can be obtained by fitting TPV decays based on the mono-exponential model (eqn (1)), which is related to trap-assisted charge recombination,[39] and τ_t can be acquired by fitting TPC decays based on eqn (2).

$$V(t) = V_0 \exp\left(-\frac{t}{\tau_r}\right) \tag{1}$$

$$I(t) = I_0 \exp\left(-\frac{t}{\tau_t}\right) \tag{2}$$

where V_0 and I_0 are the steady-state photovoltage and photocurrent, respectively. Fig. 6a and b show TP-AFM nanoscale
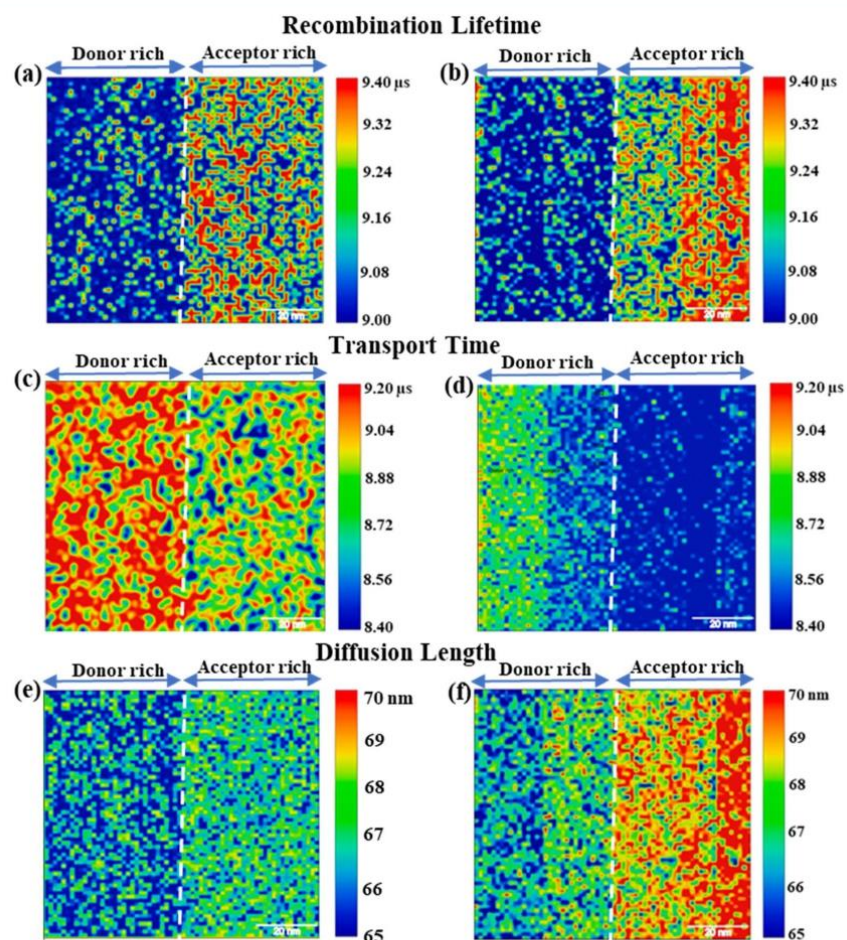
Fig. 6 Spatially resolved TP-AFM mapping of the charge carrier recombination lifetime for the binary film (a) and ternary blend film containing 10% PDI-EH (d), charge-carrier transport time for the binary film (b) and ternary blend film containing 10% PDI-EH (e), and charge–carrier diffusion length for the binary film (c) and ternary blend film containing 10% PDI-EH (f), related to the 100 nm × 100 nm red rectangle in Fig. S7 (ESI†).

mapping of τ_r for the binary and 10% PDI-EH-containing ternary films. Also, the histogram distribution of τ_r for the binary film and ternary film from the mapping in red rectangles is shown in Fig. S8a and d (ESI†). The average τ_r value for the binary film was 9.11 ± 0.14 µs and ~25% of τ_r values > 9.20 µs, while the average τ_r value for the 10% PDI-EH-containing ternary film was increased to 9.22 ± 0.15 µs and ~50% of τ_r values > 9.20 µs. It suggested that trap-assisted charge recombination was suppressed due to smoother morphology driven by the fine-tuned moderate miscibility after PDI-EH incorporation. Based on Fig. 6c and d, the average τ_t value was decreased from 9.04 ± 0.23 µs for the binary film to 8.41 ± 0.10 µs for the 10% PDI-EH-containing ternary film. Moreover, the τ_t mapping of the ternary film (Fig. 6d) presented an obviously smaller τ_t distribution and all τ_t values in the histogram < 8.80 µs, while ~90% of τ_t values > 8.80 µs for the binary film, which is attributed to the formation of local short-range molecular packing in appropriately mixed phases after 10% PDI-EH incorporation, significantly favoring charge transport. Therefore, the L_D value can be calculated by using the formula (eqn (3))

$$L_D = L \times \left(\frac{\tau_r}{\tau_t}\right)^{\frac{1}{2}} \qquad (3)$$

where L is the thickness of the active layer. The ternary film containing 10% PDI-EH showed a longer L_D (the average value of 68.3 ± 0.7 nm) than that (65.5 ± 1.0 nm) of the binary film. It can be noted that the main distribution (~72%) of L_D values for the binary film was smaller than 66.0 nm, but for the 10% PDI-EH-containing ternary film, ~83% of L_D values were larger than 67.5 nm. The obviously increased charge diffusion length results from an ordered molecular packing. Thus, 10% PDI-EH incorporation provides beneficial charge carrier dynamics, leading to enhanced device efficiency in OSCs.

We also tested the performance of the developed OSCs under indoor illumination. Indoor power generation devices are considered to be important for rapidly advancing Internet-of-Things applications and replacing/reducing the use of batteries.[45,51] In this work, a warm light 2700 K LED and cold light 6500 K LED were used and their emission spectra are shown in Fig. 7a, with which the combined UV-vis absorption of

PBDB-T, ITIC-4F and PDI-EH was expected to form an excellent match. Notably, the major absorption band of PDI-EH compensated for the weak absorption of PBDB-T and ITIC-4F from 415 nm to 550 nm, which favors more photon harvesting from LED illumination. Besides, as mentioned above, the charge cascade structure is also advantageous for the increase of V_{oc} in indoor OSCs (iOSCs). Therefore, the photovoltaic performance of PBDB-T/ITIC-4F based binary and ternary devices was characterized under a warm light 2700 K LED with 300 µW cm^{-2} power input and a cold light 6500 K LED with 310 µW cm^{-2} power input. J–V curves of the devices under these LED illuminations are shown in Fig. 7b and c and the related photovoltaic parameters are summarized in Table S2.† Ternary devices containing 10% and 20% PDI-EH under 2700 K LED illumination displayed better PCEs of 11.4% and 12.0% compared to the binary device (10.3%). It is worth mentioning that the 20% PDI-EH devices performed slightly better than the 10% PDI-EH devices mainly due to a higher V_{oc}, because they basically represented similar J_{sc} values (99 µA cm^{-2} vs. 100 µA cm^{-2}) and FF values (63% vs. 65%). Under 1-sun illumination, a morphology with an appropriately mixed phase is crucial to suppress the bimolecular and trap-assisted charge recombination. However, under indoor (low-light) illuminations, the much lower photocurrent density makes bimolecular recombination less probable.[2,52] Therefore, trap-assisted charge recombination associated with the leakage current can more significantly affect the efficiency in iOSCs. Furthermore, efficiencies of binary and ternary devices under 6500 K LED illumination had a consistent trend with that of devices under 2700 K LED illumination, where PCEs of the binary device and ternary devices with 10%, 20% and 50% PDI-EH were 9.9%, 10.6%, 11.5% and 7.6%, respectively. It can be inferred that these ternary OSCs will have greater applicability as indoor devices. It may also be noticed that the OSC performance under 6500 K LED illumination was slightly lower compared to that under 2700 K LED illumination, which may be explained by a better match between the spectral features of the latter and the major absorption bands of the host donor and acceptor (Fig. 7a), which results in higher photocurrent density. It can be concluded that the introduction of a PDI-EH acceptor also has a positive influence on the indoor application of these OSCs,
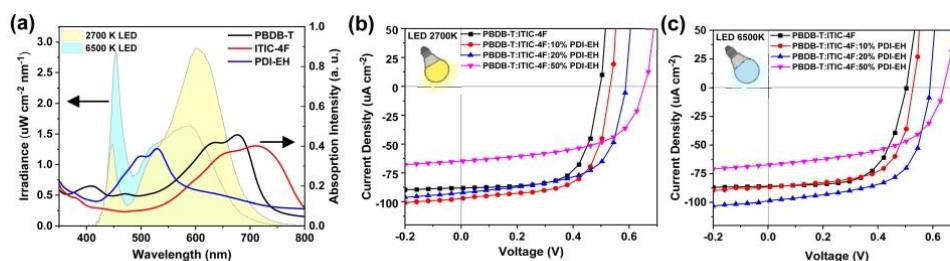
Fig. 7 (a) The irradiance spectra (left Y-axis) with the warm white 2700 K LED and the cold white 6500 K LED as the illumination sources for the iOSC measurement and UV–vis absorption spectra (right Y-axis) of pristine PBDB-T, ITIC-4F and PDI-EH films. J–V characteristics of PBDB-T/ITIC-4F binary and ternary devices (b) under 2700 K LED illumination and (c) under 6500 K LED illumination.

with the moderately mixed sample (20%) leading to the best performance. The indoor studies reveal that the photovoltaic performance depends on the complicated interplay of multiple factors. Depending on the exact conditions of indoor and outdoor applications, the morphology of a given D/A system needs to be respectively optimized, and thus the fine-tuning of morphology can play an important role in performance optimization under different operation conditions.

Conclusion

A highly twisted PDI-EH molecule was synthesized and introduced into the PBDB-T/ITIC-4F film to prepare ternary OSCs, which were applied in versatile photovoltaic applications under AM 1.5 G conditions, and indoor 2700 K and 6500 K LED lamps. The donor and acceptors in the blend film exhibited low, moderate and high miscibility by adjusting the contents of the PDI-EH introduction. It proved that moderate miscibility of the donor and acceptors facilitates the formation of an appropriately mixed phase for effective exciton dissociation. Meanwhile, introducing PDI-EH into blend films would promote the favorable face-on orientation and local short-range ordered molecular packing, favoring charge mobility and inhibiting charge recombination, as evidenced by GIWAXS studies and the observation of the charge carrier dynamics *via* TP-AFM nanoscale mappings. Finally, the synergistic effects in ternary OSCs (enhanced photon absorption, well-matched energy level alignment and optimized morphology) contribute to achieving higher photovoltaic performance under both outdoor and indoor illuminations. Our fundamental studies present promising guidance for the molecular design and morphological regulation of OSCs, thereby facilitating the development of OSCs in practical applications.

Author contributions

Ting Yu: conceptualization, methodology, investigation and writing – original draft. Francesco Tintori: investigation and methodology. Yuchen Zhang: investigation and methodology. Wanting He: methodology. Edward Cieplechowicz: resources. Raja Sekhar Bobba: investigation. Poojan Indrajeet Kaswekar: investigation. Maziar Jafari: investigation. Yuxuan Che: investigation and software. Yong Wang: investigation. Mohamed Siaj: resources and writing – review & editing. Ricardo Izquierdo: resources and writing – review & editing. Dmytro F. Perepichka: resources and writing – review & editing. Quinn Qiao: resources and writing – review & editing. Gregory C. Welch: resources and writing – review & editing. Dongling Ma: conceptualization, supervision and writing – review & editing.

Conflicts of interest

The authors declare no conflict of interests.

Acknowledgements

References

1 K. Fukuda, K. Yu and T. Someya, *Adv. Energy Mater.*, 2020, **10**, 2000765.

2 Y. Cui, Y. Wang, J. Bergqvist, H. Yao, Y. Xu, B. Gao, C. Yang, S. Zhang, O. Inganäs and F. Gao, *Nat. Energy*, 2019, **4**, 768.

3 G. Yu, J. Gao, J. C. Hummelen, F. Wudl and A. J. Heeger, *Science*, 1995, **270**, 1789.

4 K. Jin, Z. Xiao and L. Ding, *J. Semicond.*, 2021, **42**, 060502.

5 Y. Li, Y. Cai, Y. Xie, J. Song, H. Wu, Z. Tang, J. Zhang, F. Huang and Y. Sun, *Energy Environ. Sci.*, 2021, **14**, 5009.

6 Z. Zheng, J. Wang, P. Bi, J. Ren, Y. Wang, Y. Yang, X. Liu, S. Zhang and J. Hou, *Joule*, 2022, **6**, 171.

7 T. Yu, X. Xu, G. Zhang, J. Wan, Y. Li and Q. Peng, *Adv. Funct. Mater.*, 2017, **27**, 1701491.

8 T. Yu, X. Xu, Y. Li, Z. Li and Q. Peng, *ACS Appl. Mater. Interfaces*, 2017, **9**, 18142.

9 F. Zhao, C. Wang and X. Zhan, *Adv. Energy Mater.*, 2018, **8**, 1703147.

10 L. Ye, B. A. Collins, X. Jiao, J. Zhao, H. Yan and H. Ade, *Adv. Energy Mater.*, 2018, **8**, 1703058.

11 Z. Peng, L. Ye and H. Ade, *Mater. Horiz.*, 2022, **9**, 577.

12 M. Ghasemi, H. Hu, Z. Peng, J. J. Rech, I. Angunawela, J. H. Carpenter, S. J. Stuard, A. Wadsworth, I. McCulloch and W. You, *Joule*, 2019, **3**, 1328.

13 N. Gasparini, A. Salleo, I. McCulloch and D. Baran, *Nat. Rev. Mater.*, 2019, **4**, 229.

14 Y. Xie, F. Yang, Y. Li, M. A. Uddin, P. Bi, B. Fan, Y. Cai, X. Hao, H. Y. Woo and W. Li, *Adv. Mater.*, 2018, **30**, 1803045.

15 T. Yu, W. He, M. Jafari, T. Guner, P. Li, M. Siaj, R. Izquierdo, B. Sun, G. C. Welch, A. Yurtsever and D. Ma, *Small Methods*, 2022, **6**, 2100916.

16 X. Du, T. Heumueller, W. Gruber, A. Classen, T. Unruh, N. Li and C. J. Brabec, *Joule*, 2019, **3**, 215.

17 M. Chen, D. Liu, W. Li, R. S. Gurney, D. Li, J. Cai, E. L. Spooner, R. C. Kilbride, J. D. McGettrick and T. M. Watson, *ACS Appl. Mater. Interfaces*, 2019, **11**, 26194.

18 D. Qian, Z. Zheng, H. Yao, W. Tress, T. R. Hopper, S. Chen, S. Li, J. Liu, S. Chen and J. Zhang, *Nat. Mater.*, 2018, **17**, 703.

19 Y. Duan, X. Xu, H. Yan, W. Wu, Z. Li and Q. Peng, *Adv. Mater.*, 2017, **29**, 1605115.

20 P. Li, M. Mainville, Y. Zhang, M. Leclerc, B. Sun, R. Izquierdo and D. Ma, *Small*, 2019, **15**, 1804671.

21 H. Feng, Y. Dai, L. Guo, D. Wang, H. Dong, Z. Liu, L. Zhang, Y. Zhu, C. Su and Y. Chen, *Nano Res.*, 2022, **15**, 3222.

22 S. M. McAfee, S. V. Dayneko, P. Josse, P. Blanchard, C. Cabanetos and G. C. Welch, *Chem. Mater.*, 2017, **29**, 1309.

23 S. M. McAfee, S. V. Dayneko, A. D. Hendsbee, P. Josse, P. Blanchard, C. Cabanetos and G. C. Welch, *J. Mater. Chem. A*, 2017, **5**, 11623.

24 X. Ma, Y. Mi, F. Zhang, Q. An, M. Zhang, Z. Hu, X. Liu, J. Zhang and W. Tang, *Adv. Energy Mater.*, 2018, **8**, 1702854.

25 W. Zhao, S. Li, H. Yao, S. Zhang, Y. Zhang, B. Yang and J. Hou, *J. Am. Chem. Soc.*, 2017, **139**, 7148.

26 D. K. Owens and R. C. Wendt, *J. Appl. Polym. Sci.*, 1969, **13**, 1741.

27 H. Wang, L. Han, J. Zhou, T. Liu, D. Mo, H. Chen, H. Lai, N. Zheng, Z. Xie and W. Zheng, *CCS Chem.*, 2021, **3**, 2591.

28 R. Ma, T. Liu, Z. Luo, K. Gao, K. Chen, G. Zhang, W. Gao, Y. Xiao, T.-K. Lau and Q. Fan, *ACS Energy Lett.*, 2020, **5**, 2711.

29 L. Xiao, B. He, Q. Hu, L. Maserati, Y. Zhao, B. Yang, M. A. Kolaczkowski, C. L. Anderson, N. J. Borys and L. M. Klivansky, *Joule*, 2018, **2**, 2154.

30 L. Yu, D. Qian, S. Marina, F. A. Nugroho, A. Sharma, S. Hultmark, A. I. Hofmann, R. Kroon, J. Benduhn and D.-M. Smilgies, *ACS Appl. Mater. Interfaces*, 2019, **11**, 21766.

31 J. Xin, X. Meng, X. Xu, Q. Zhu, H. B. Naveed and W. Ma, *Matter*, 2019, **1**, 1316.

32 H. Hu, M. Ghasemi, Z. Peng, J. Zhang, J. J. Rech, W. You, H. Yan and H. Ade, *Adv. Mater.*, 2020, **32**, 2005348.

33 Z. Fei, F. D. Eisner, X. Jiao, M. Azzouzi, J. A. Röhr, Y. Han, M. Shahid, A. S. Chesman, C. D. Easton and C. R. McNeill, *Adv. Mater.*, 2018, **30**, 1705209.

34 W. Li, S. Albrecht, L. Yang, S. Roland, J. R. Tumbleston, T. McAfee, L. Yan, M. A. Kelly, H. Ade and D. Neher, *J. Am. Chem. Soc.*, 2014, **136**, 15566.

35 S. Mukherjee, C. M. Proctor, J. R. Tumbleston, G. C. Bazan, T. Q. Nguyen and H. Ade, *Adv. Mater.*, 2015, **27**, 1150.

36 L. Ye, W. Zhao, S. Li, S. Mukherjee, J. H. Carpenter, O. Awartani, X. Jiao, J. Hou and H. Ade, *Adv. Energy Mater.*, 2017, **7**, 1602000.

37 X. Song, N. Gasparini, M. M. Nahid, H. Chen, S. M. Macphee, W. Zhang, V. Norman, C. Zhu, D. Bryant and H. Ade, *Adv. Funct. Mater.*, 2018, **28**, 1802895.

38 L. Zhang and W. Ma, *Chin. J. Polym. Sci.*, 2017, **35**, 184.

39 S. F. Hoefler, G. Haberfehlner, T. Rath, A. Keilbach, M. A. Hobisch, A. Dixon, E. Pavlica, G. Bratina, G. Kothleitner and F. Hofer, *ACS Appl. Energy Mater.*, 2019, **2**, 7535.

40 K. Zhou, Y. Liu, A. Alotaibi, J. Yuan, C. Jiang, J. Xin, X. Liu, B. A. Collins, F. Zhang and W. Ma, *ACS Energy Lett.*, 2020, **5**, 589.

41 N. Y. Doumon, G. Wang, X. Qiu, A. J. Minnaard, R. C. Chiechi and L. Koster, 1, 8-diiodooctane acts as a photo-acid in organic solar cells, *Sci. Rep.*, 2019, **9**, 1.

42 X. Liu, L. Kong, H. Du, Y. Zhang, J. Zhao and Y. Xie, *Org. Electron.*, 2019, **64**, 223.

43 S. Park and H. J. Son, *J. Mater. Chem. A*, 2019, **7**, 25830.

44 S. Hultmark, S. H. K. Paleti, A. Harillo, S. Marina, F. A. A. Nugroho, Y. Liu, L. K. Ericsson, R. Li, J. Martín and J. Bergqvist, *Adv. Funct. Mater.*, 2020, **30**, 2005462.

45 J. A. Röhr, D. Moia, S. A. Haque, T. Kirchartz and J. Nelson, *J. Condens. Matter Phys.*, 2018, **30**, 105901.

46 Z. He, C. Zhong, X. Huang, W. Y. Wong, H. Wu, L. Chen, S. Su and Y. Cao, *Adv. Mater.*, 2011, **23**, 4636.

47 Y. Xie, T. Li, J. Guo, P. Bi, X. Xue, H. S. Ryu, Y. Cai, J. Min, L. Huo and X. Hao, *ACS Energy Lett.*, 2019, **4**, 1196.

48 B. Bahrami, A. H. Chowdhury, A. Gurung, S. Mabrouk, K. M. Reza, S. I. Rahman, R. Pathak and Q. Qiao, *Nano Today*, 2020, **33**, 100874.

49 Y. Kondo, M. Osaka, H. Benten, H. Ohkita and S. Ito, *ACS Macro Lett.*, 2015, **4**, 879.

50 M. Osaka, D. Mori, H. Benten, H. Ogawa, H. Ohkita and S. Ito, *ACS Appl. Mater. Interfaces*, 2017, **9**, 15615.

51 X. Li, W. C. Choy, L. Huo, F. Xie, W. E. Sha, B. Ding, X. Guo, Y. Li, J. Hou and J. You, *Adv. Mater.*, 2012, **24**, 3046.

52 L.-K. Ma, Y. Chen, P. C. Chow, G. Zhang, J. Huang, C. Ma, J. Zhang, H. Yin, A. M. H. Cheung and K. S. Wong, *Joule*, 2020, **4**, 1486.

Support Information

Miscibility Driven Morphology Modulation in Ternary Solar Cells

Ting Yu,[a] Francesco Tintori,[b] Yuchen Zhang,[c] Wanting He,[a] Edward Cieplechowicz,[b] Raja Sekhar Bobba,[c] Poojan Indrajeet Kaswekar,[c] Maziar Jafari,[d] Yuxuan Che,[e] Yong Wang,[a] Mohamed Siaj,[d] Ricardo Izquierdo,[f] Dmytro F. Perepichka,[e] Quinn Qiao,[c] Gregory C. Welch[b]* and Dongling Ma[a]*

[a] Énergie, Matériaux et Télécommunications, Institut National de la Recherche Scientifique (INRS), 1650 Boul. Lionel-Boulet, Varennes, Québec, Canada, J3X 1P7

[b] Department of Chemistry, University of Calgary, 2500 University Drive N. W., Calgary, Alberta, Canada, T2N 1N4

[c] Department of Mechanical and Aerospace Engineering, Syracuse University, NY 13244, USA.

[d] Département de chimie, Université du québec à montréal, 405 Rue Sainte-Catherine Est, Montréal, Québec, Canada, H2L 2C4

[e] Department of Chemistry, McGill University, Montreal, Quebec, Canada, H3A 0B8

[f] Département de génie électrique, École de technologie supérieure, Montréal, Québec, Canada, H3C 1K3

Materials and Methods

Materials: All starting materials and solvents were purchased from Millipore Sigma, unless indicated otherwise. SiliaCat® DPP-Pd heterogeneous catalyst was purchased from silicycle. All chemicals were used without further purification. Poly[[4,8-bis[5-(2-ethylhexyl)-2-thienyl]benzo[1,2-b:4,5-b′]dithiophene-2,6-diyl]-2,5-thiophenediyl[5,7-bis(2-ethylhexyl)-4,8-dioxo-4H,8H-benzo[1,2-c:4,5-c′]dithiophene-1,3-diyl]] (PBDB-T) polymer and 9-Bis(2-methylene-((3-(1,1-dicyanomethylene)-6,7-difluoro)-indanone))-5,5,11,11-tetrakis(4-hexylphenyl)-dithieno[2,3-d:2′,3′-d′]-s-indaceno[1,2-b:5,6-b′]dithiophene (ITIC-4F) were purchased from 1-Material company (Canada). Patterned ITO-coated glass substrates (Rs ≤ 10 Ω square^{-1}, Tr ≥ 83%) was bought from Shenzhen Huayu Union Technology Co., Ltd. (China). In addition, zinc acetate dihydrate (Zn(CH$_3$COO)$_2$·2H$_2$O, 99.9%), ethanolamine (NH$_2$CH$_2$CH$_2$OH, 99.5%), 2-methoxyethanol (CH$_3$OCH$_2$CH$_2$OH, 99.8%), chlorobenzene (CB) and molybdenum trioxide interlayer (MoO$_3$) were obtained from Sigma-Aldrich without further purification.

Materials Characterization:

Nuclear Magnetic Resonance (NMR): ^{1}H and ^{13}C NMR spectra were recorded on Bruker Ascend 500 MHz in solvents as indicated. Chemical shifts (δ) are given in ppm. The residual solvent signals were used as references and the chemical shifts converted to the Tetramethylsilane scale (deuterated chloroform (CDCl$_3$): δH = 7.26 ppm, δC = 77.16 ppm).

Cyclic Voltammetry (CV): The instrument used for the electrochemical measurements was a CH instrument 620E potentiostat. The instrument used a standard three-electrode configuration: Ag wire pseudo-reference electrode, Pt wire counter electrode, and glassy carbon working electrode. Experiments were performed in anhydrous dichloromethane (CH$_2$Cl$_2$), which was further degassed with a N$_2$ gas spurge for 10 minutes. Tetrabutylammonium hexafluorophosphate (TBAPF$_6$) was used as the supporting electrolyte. CV sample concentration was ~0.4 mg/mL. The ionization potentials (IP) and electron affinities (EA) were estimated by correlating the onsets of ferrocene (Fc)/Fc$^+$ redox couple (E$_{ox}$ $^{Fc/Fc+}$, E$_{red}$ $^{Fc/Fc+}$) to the normal hydrogen electrode (NHE), assuming the IP of Fc/Fc$^+$ redox couple to be 4.80 eV. [1]

$$E(IP) = (E_{ox}+4.80), E(EA) = (E_{red}+4.80)$$

Devices Fabrication and Characterization

An inverted structure of ternary organic solar cells (indium tin oxides (ITO) glass/zinc oxide (ZnO)/active layer/MoO$_3$/Ag) was fabricated. ZnO precursor solution was prepared according to a reported procedure.[2] The patterned ITO glass substrates were cleaned by sequential ultrasonication in detergent, deionized water, acetone, and isopropanol, then, dried by the high-pressure nitrogen stream and followed by treatment with

2

plasma for 10 min. ZnO precursor solution was spin-coated onto the ITO substrate at 4500 rpm for 60 s and then baked in dried air at 200 ℃ for 1h to form a thin ZnO layer. Then, the PBDB-T/ITIC-4F binary blend and ternary solution containing 10%, 20% and 50% PDI-EH were spin-coated onto the above substrate in the glovebox at the optimized spin-speed of 3000 rpm for 60 s without thermal-annealing to form the active layer. The optimized concentration was 20 mg mL^{-1} with D/A ratio of 1:1 (w/w) (adding 0.5 v% 1,8-diiodooctane (DIO)). Finally, MoO$_3$ (25 nm) and silver (Ag, 100 nm) were deposited onto the surface of the active layer in an evaporation chamber under a high vacuum of 1×10^{-6} mbar). The effective device area was 0.06 cm^2. The current density versus voltage (J-V) characterization was measured by using a class ABA LED solar simulator under AM 1.5G (100 mW cm^{-2}), which was calibrated using a standard KG5 filtered silicon solar cells. The external quantum efficiency (EQE) measurement was conducted on an IQE200B system (Newport Corporation) in a high purity nitrogen-filled glovebox.

Instruments and Characterizations

The UV-visible absorption spectra were obtained on a Cary 5000 UV-vis-NIR spectrophotometer (Varian).

Atomic force microscopy (AFM) measurements were performed on Bruker MultiMode & AFM in the ScanAsyst mode to acquire the topography and phase images of neat and blend films.

Differential scanning calorimetry (DSC) measurements were carried out on DSC 6000 instrument with a temperature range from 30 ℃ to 360 ℃ under the nitrogen stream with a heating rate of 10 ℃ /min. Baseline and temperature were calibrated with Indium and Zinc. The neat materials and blends were prepared from the evaporation of their CB solutions, and the solidified films were thermally annealed in the same conditions as the OSC devices.

Contact angle measurements were performed on a contact angle analyzer equiped with an AM211 Dino-Lite camera under the ambient temperature. A deionized water and ethylene glycol droplet of 6 μL volume was placed on the dry surface. The surface tension values of films were calculated using the Owens-Wendt model [2, 3]:

$$\gamma_L(1+\cos\theta)=2\sqrt{\gamma_s^d \gamma_L^d}+2\sqrt{\gamma_s^p \gamma_L^p}$$

where γ_s^d and γ_L^d refer to dispersion tension of plane surface and liquid, γ_s^p and γ_L^p refer to polar components of the surface energy of plane surface and liquid, while γ_L refers to total tension of liquid.

Two-dimensional grazing incidence wide-angle X-ray scattering (GIWAXS) measurement was carried out at Xeuss 3.0 instrument of the Suzhou vacuum interconnected nanotech workstation using incident X-ray

3

with a wavelength of 1.34 Å. The 2D-GIWAXS patterns were treated by MATLAB-GIXSGUI software, and 1D out-of-plane (OOP) and in-plane (IP) curves were analyzed by using the Fit 2D software.

The photo-induced force microscopy (PiFM) images and IR spectra were tested on a VistaScope-infrared (IR) microscope from Molecular Vista, Inc, using PtIr-coated silicon cantilevers (PtIr-NCHR) from Nanosensors. The microscope was operated in dynamic mode using the first mechanical mode of the cantilever to detect the PiFM and the second mechanical mode to detect the topography of the sample. The IR source used to excite the sample was manufactured from Block Engineering at the tunable range of 770 cm^{-1} to 1950 cm^{-1}. Spectral acquisition time was 30 seconds for the presented spectra. All spectra have been normalized against the power profile of the laser.

The electron and hole mobility were measured by using the method of space-charge limited current (SCLC) for electron-only devices with the configuration of ITO/ZnO/active layer/LiF/Al and hole-only devices with the configuration of ITO/PEDOT:PSS/active layer/MoO$_3$/Ag. [4, 5] The charge carrier mobility was determined by fitting the dark current to the model of a single carrier SCLC according to the equation: $J = 9\varepsilon_0\varepsilon_r\mu V^2/8d^3$, where J is the current density, d is the film thickness of the active layer, μ is the charge carrier mobility, ε_r is the relative dielectric constant of the transport medium, and ε_0 is the permittivity of free space. $V = V_{app} - V_{bi}$, where V_{app} is the applied voltage, V_{bi} is the offset voltage. The carrier mobility can be calculated from the slope of the $J^{0.5} \sim V$ curves.

Transient photo-response atomic force microscopy (TP-AFM) mounted on the conductive AFM (Agilent 5500) was conducted to measure local transient photovoltage (TPV) and transient photocurrent (TPC) decays at different locations on the donor-acceptor blend by using the contact mode. The green laser (MGL-I-532 DPSS; 532 nm) was illuminated from the bottom of ITO glass. A budget sensor (platinum/ chromium coated silicon conductive tip) was used in this measurement. A breakout box (Agilent N9447A) was connected to the oscilloscope (Agilent MSOX4154A) to receive the transient signal from the AFM.

Synthetic Details
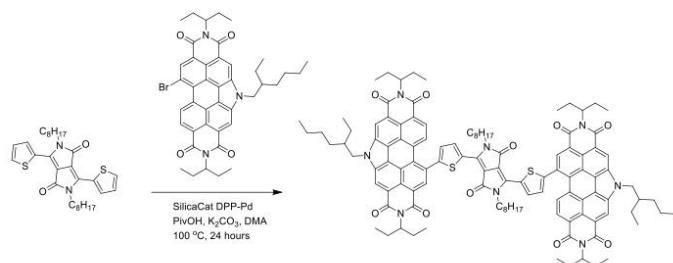
Scheme S1. The synthetic route of PDI-EH molecule.

4

Synthetic Details of PDI-EH: Reactions were carried out on a bench top or under an atmosphere of dry, nitrogen (N₂) where indicated. For reactions requiring heat, the conventional method involved submerging reaction vial/round bottom flask in a LabArmor® bead bath and heating on a hot plate at the desired temperature was used.

Synthesis of PDI-EH: In a 20 mL microwave vial 2,5-bis(1-octyl)-3,6-di(thiophen-2-yl)diketopyrrolopyrrole (76 mg, 1 eq.), 11-bromo-5-ethylhexyl-2,8-bis(1-ethylpropyl)perylene diimide (234 mg, 2.2 eq.), Silia*Cat*® DPP-Pd (29 mg, 5 mol %), pivalic acid (5 mg, 30 mol %) and cesium carbonate (120 mg, 2.5 eq.) were added with a stir bar and sealed with a crimp sealed septa cap. The contents were purged with N₂ gas followed by the addition of degassed anhydrous *N, N'*-dimethylacetamide (5.3 mL) via syringe. The reaction mixture was heated at 100 °C in a LabArmor® beads bath for 24 hours. After 24 hours the reaction mixture was poured into acetone and allowed to stir for one hour. The precipitated product was collected by filtration and the filtrate was discarded. The solid product was subsequently washed with dichloromethane to solubilize, and isolate it from the insoluble silica-supported catalyst using a silica gel plug. The filtrate was concentrated by rotary evaporation and solubilized in a minimal amount of CHCl₃. EtOAc was added dropwise over several hours to the CHCl₃ solution and allowed to stir overnight. The precipitated product was isolated by filtration. This yielded a dark solid product (186 mg, 70 % yield).

¹H NMR (500 MHz, CDCl₃): δ 9.38 (d, *J* = 3.9 Hz, 1H), 9.10 (s, 1H), 9.05 (s, 1H), 8.89 (s, 1H), 8.62 (s, 1H), 8.34 (d, *J* = 8.3 Hz, 1H), 7.63 (d, *J* = 3.9 Hz, 1H), 5.28 – 5.14 (m, 2H), 4.88 – 4.78 (m, 2H), 4.21 – 4.14 (m, 2H), 2.45 – 2.27 (m, 5H), 2.05 – 1.94 (m, 4H), 1.87 (dt, *J* = 15.5, 7.9 Hz, 2H), 1.55 – 1.32 (m, 8H), 1.34 – 1.24 (m, 5H), 1.22 – 1.15 (m, 2H), 1.15 – 1.07 (m, 4H), 0.98 (ddd, *J* = 18.2, 11.2, 4.6 Hz, 14H), 0.87 (t, *J* = 7.3 Hz, 3H), 0.69 (t, *J* = 6.9 Hz, 3H).

¹³C NMR (126 MHz, CDCl₃): δ 161.57, 147.90, 139.82, 137.18, 135.52, 132.64, 132.00, 129.06, 128.22, 125.13, 125.02, 123.22, 123.16, 119.94, 119.85, 108.77, 58.06, 51.15, 42.69, 41.78, 31.78, 31.03, 30.31, 29.26, 28.75, 27.04, 25.35, 24.49, 23.17, 22.64, 14.12, 14.11, 11.56, 10.87. 34/57 carbon peaks obtained, quaternary carbons could not all be obtained.

5
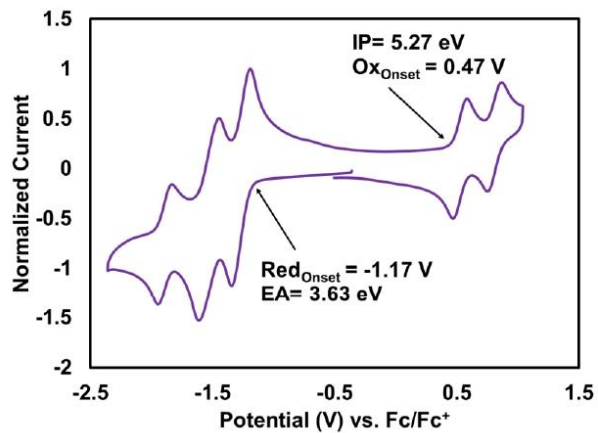
Fig. S1. Cyclic voltammetry curve of PDI-EH, which shows the onsets of oxidation (Ox$_{Onset}$) and reduction (Red$_{Onset}$), ionization potentials (IP) and electron affinities (EA), respectively.

6
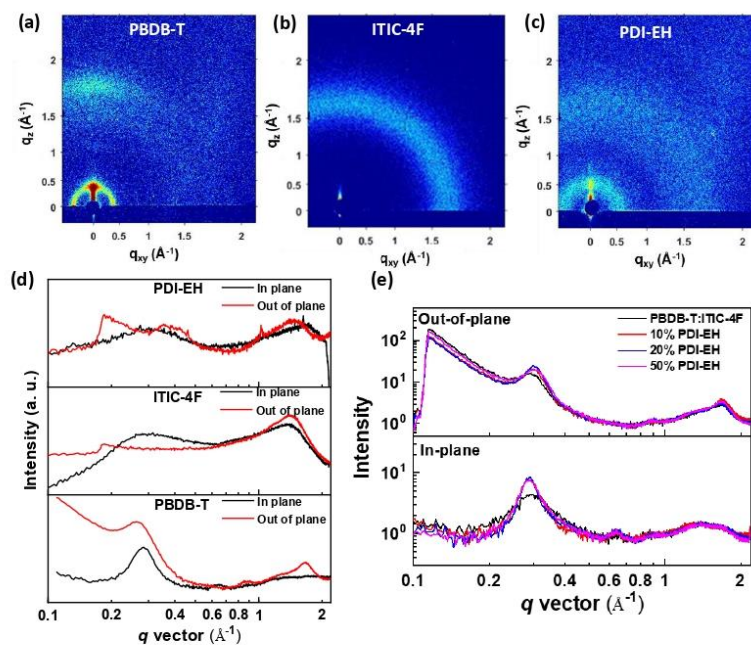
Fig. S2. (a-c) 2D GIWAXS patterns of the pristine PBDB-T, ITIC-4F and PDI-EH films; (d) the out-of-plane and in-plane curves of pristine films related to 2D-GIWAXS patterns; (e) the out-of-plane and in-plane curves of the binary film and ternary films containing 10%, 20% and 50% PDI-EH.

7
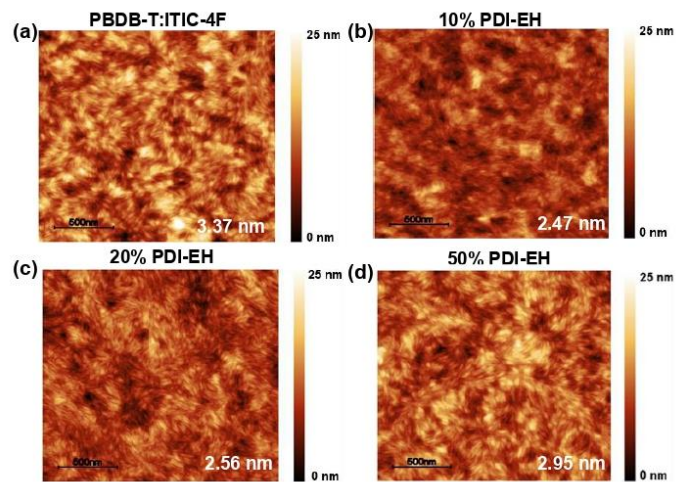
Fig. S3. AFM topography images of PBDB-T/ITIC-4F blend film (a) and ternary blend films containing 10%, 20% and 50% PDI-EH (b-d), AFM images size: 2 um × 2 um. The numbers inside of topography images denote the average RMS roughness value.

8
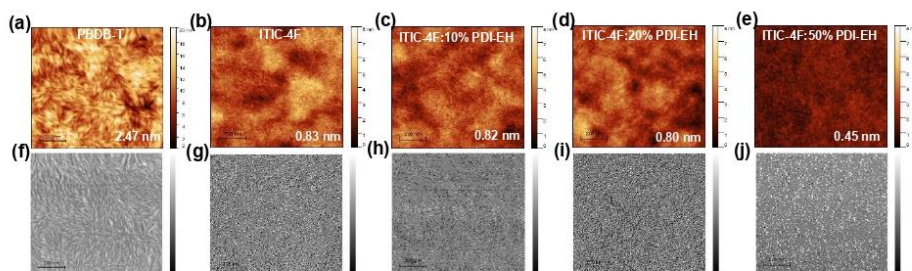
Fig. S4. AFM topography images (a-e) and phase images (f-j) of pristine PBDB-T film (a, f), pristine ITIC-4F film (b, g), ITIC-4F/10% PDI-EH blend film (c, h), ITIC-4F/20% PDI-EH blend film (d, i), and ITIC-4F/50% PDI-EH blend film (e, j). AFM images size: 1 um × 1 um. The numbers inside (a-e) denote the average RMS roughness value.

9
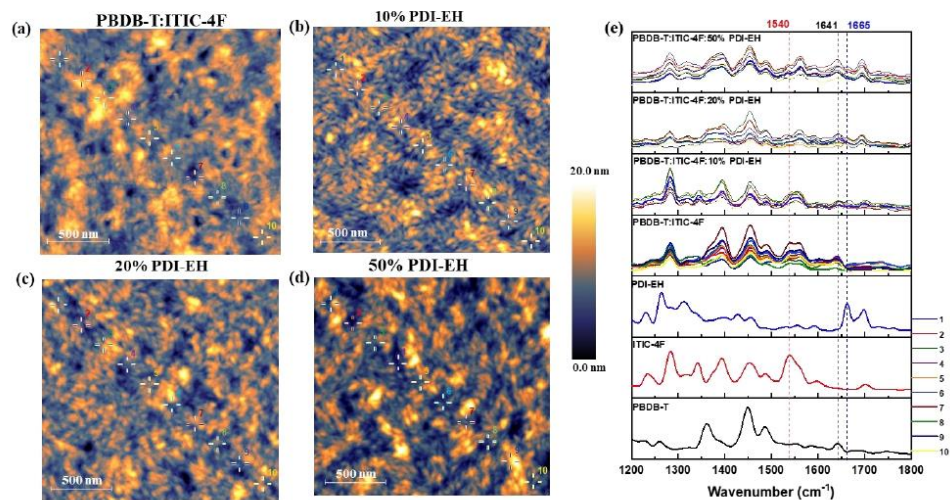
Fig. S5. PiFM topography images of PBDB-T/ITIC-4F blend film (a) and ternary blend films containing 10%, 20% and 50% PDI-EH (b-d); (e) PiFM spectra of the binary film and ternary films containing 10%, 20% and 50%PDI-EH taken from 10 locations as marked in corresponding images. For comparison, PiFM spectra of pristine PBDB-T, ITIC-4F, PDI-EH films are also shown. Topography image size: 2 μm × 2 μm.

10

94
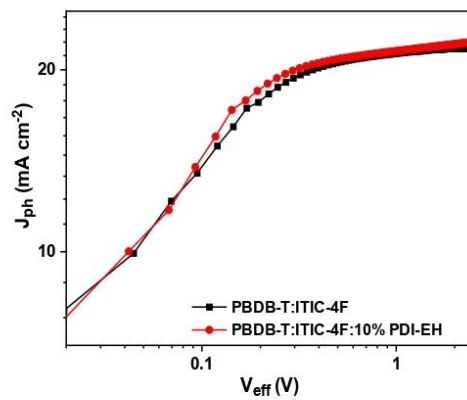
Fig. S6. The J_{ph}-V_{eff} plots for binary blend film and ternary blend films containing 10% PDI-EH.

11
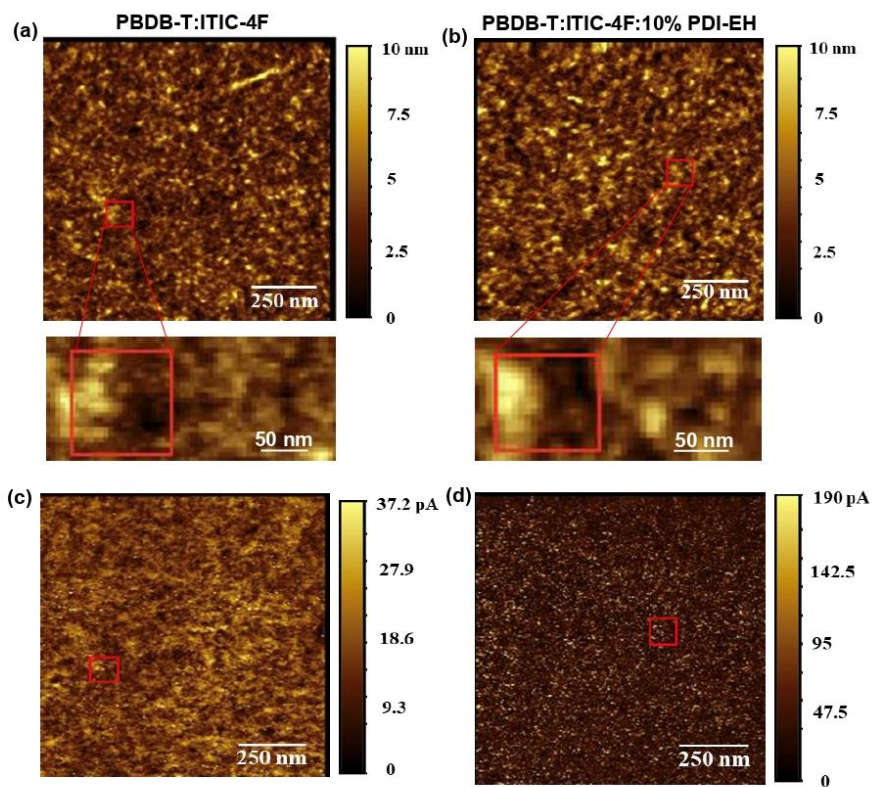
Fig. S7. Topography AFM images of the PBDB-T/ITIC-4F binary film (a) and the 10% PDI-EH-containing ternary film (b); current sensing AFM images of the PBDB-T/ITIC-4F binary film (c) and the 10% PDI-EH-containing ternary film (d). Red rectangles (100 × 100 nm) marked in AFM images were used for nanoscale mappings of τ_r, τ_t and L_D.
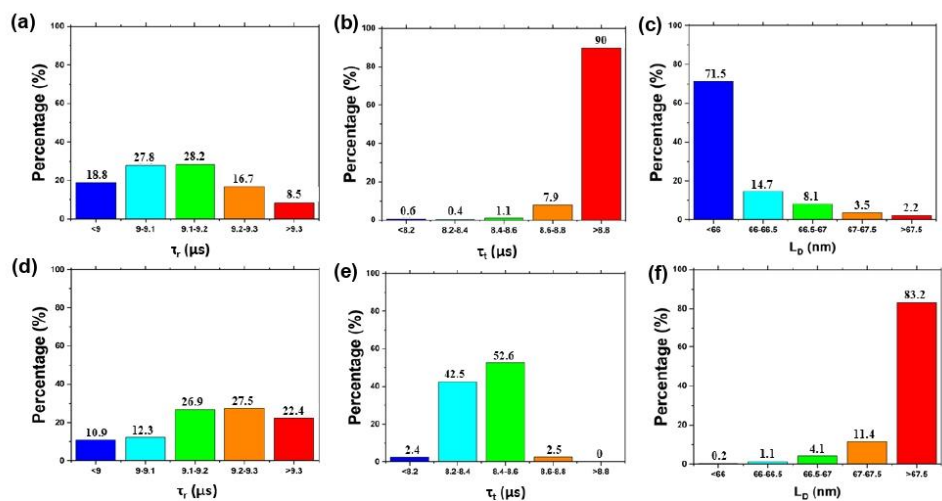
Fig. S8. Histogram distribution of τ_r for (a) PBDB-T/ITIC-4F film and (d)10% PDI-EH-containing ternary film, τ_t for (b) PBDB-T/ITIC-4F film and (e) 10% PDI-EH-containing ternary film, and L_D for (c) PBDB-T/ITIC-4F film and (f) 10% PDI-EH-containing ternary film.

13
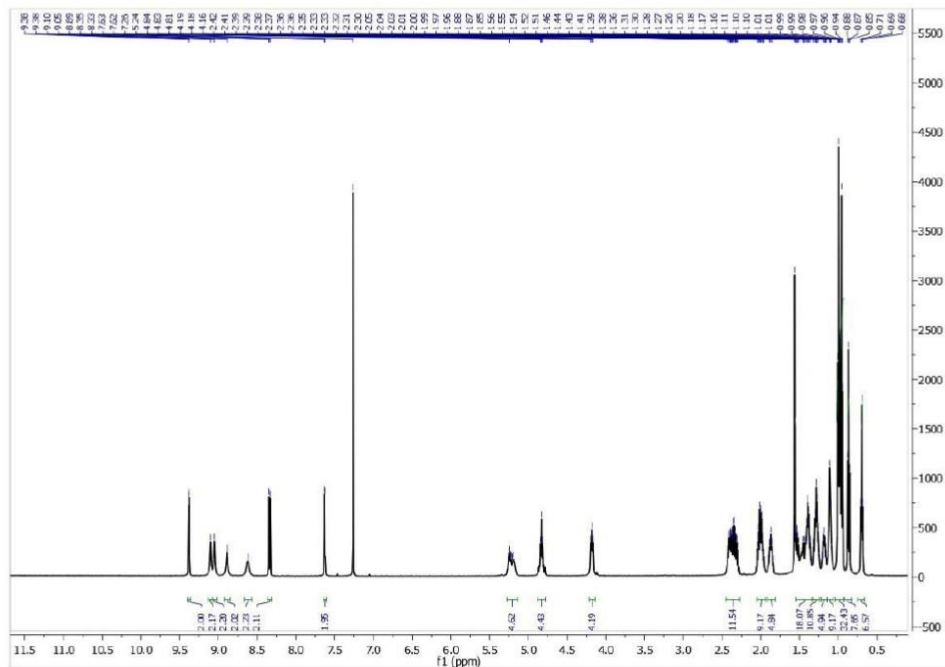
Fig. S9. ^{1}H NMR spectrum of PDI-EH in CDCl$_3$ solution.

14

Fig. S10. ^{13}C NMR spectrum of PDI-EH molecule in CDCl$_3$ solution.

15

Table S1. Hole mobility, electron mobility and the ratio of hole/electron mobility values for binary blend film and ternary blend films with different contents of PDI-EH (10%, 20%, and 50%).

Active layer	Hole mobility(μ_h)	Electron mobility(μ_e)	μ_h/μ_e
PBDB-T : ITIC-4F	1.2×10^{-4}	4.1×10^{-5}	3.0
10% PDI-EH	1.6×10^{-4}	5.8×10^{-5}	2.8
20% PDI-EH	1.8×10^{-4}	4.6×10^{-5}	3.8
50% PDI-EH	1.4×10^{-4}	7.4×10^{-6}	18.4

16

Table S2. Photovoltaic parameters of binary and ternary inverted solar cells under 6500 K LED and 2700 K LED illuminations.

	Active layer	V_{oc} [V]	J_{sc} [uA cm^{-2}]	FF [%]	PCE (max.)[c] [%]
2700 K LED [a]	**PBDB-T : ITIC-4F**	0.51 (0.52 ± 0.013)	97 (93 ± 3.59)	61 (59 ± 2.40)	10.5 (9.7 ± 0.59)
	10% PDI-EH	0.53 (0.53 ± 0.008)	100 (96 ± 4.13)	65 (65± 2.21)	11.4 (11.1 ± 0.41)
	20% PDI-EH	0.59 (0.59 ± 0.004)	99 (95 ± 5.68)	63 (63± 2.26)	12.0 (11.6 ± 0.44)
	50% PDI-EH	0.64 (0.65± 0.005)	73 (70 ± 4.87)	55 (55± 1.76)	8.5 (8.2 ± 0.26)
6500 K LED [b]	**PBDB-T : ITIC-4F**	0.52 (0.51 ± 0.015)	87 (86± 5.32)	65 (63 ± 2.50)	9.9 (9.1 ± 0.67)
	10% PDI-EH	0.55 (0.53 ± 0.014)	90 (87 ± 3.24)	67 (65 ± 1.70)	10.6 (9.7 ± 0.49)
	20% PDI-EH	0.59 (0.59± 0.005)	95 (89 ± 4.33)	63 (63 ± 1.33)	11.5 (10.1 ± 0.48)
	50% PDI-EH	0.64 (0.64± 0.003)	67 (66 ± 3.86)	55 (55 ± 2.01)	7.6 7.5 ± 0.18

[a] measured under 2700 K LED of 300 uW/cm^2 power input.

[b] measured under 6500 K LED of 310 uW/cm^2 power input.

[c] average values and standard deviation were obtained over 10 devices, which are shown in brackets.

17

101

Reference

[1] J. Pommerehne, H. Vestweber, W. Guss, R. F. Mahrt, H. Bässler, M. Porsch, J. Daub, *Adv.Mater.* **1995**, *7*, 551.

[2] D. K. Owens, R. C. Wendt, *J. Appl. Polym. Sci.* **1969**, *13*, 1741.

[3] H. Wang, L. Han, J. Zhou, T. Liu, D. Mo, H. Chen, H. Lai, N. Zheng, Z. Xie, W. Zheng, *CCS Chem.* **2021,** *3*, 2591.

[4] S. Hultmark, S. H. K. Paleti, A. Harillo, S. Marina, F. A. A. Nugroho, Y. Liu, *Adv. Funct. Mater.* **2020**, 3*0*, 2005462.

[5] J. A. Röhr, D. Moia, S. A. Haque, T. Kirchartz, J. Nelson, *J. Condens. Matter Phys.* **2018**, *30*, 105901.

18

3.3 Enhancing Efficiency of Nonfullerene Organic Solar Cells via Using Polyelectrolyte-Coated Plasmonic Gold Nanorods as Rear Interfacial Modifiers

Zhonglin Du[1], Ting Yu[1](co-first author), Wanting He, Aycan Yurtsever, Ricardo Izquierdo, Maziar Jafari, Mohamed Siaj, and Dongling Ma
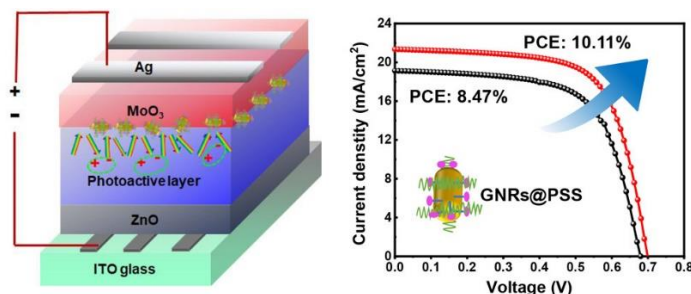
NFA-based OSCs have recently emerged as cost-effective and energy-efficient candidates for green energy resources. Further improvement in power conversion efficiency (PCE) is still required for their practical application. Compared to inorganic solar cells, the thickness of organic absorbers in NFA-based OSCs is usually much thinner (< 200 nm), which results in the inadequate absorption of the incident sunlight. Therefore, it is an urgent task to effectively improve sunlight capture and reduce energy loss. To solve this critical issue, utilizing plasmonic metallic nanoparticles as sunlight concentrators offers the most attractive pathway. However, at present, this approach has not attracted enough attention in the field of NFA-based OSCs.

In this work, Dr. Zhonglin Du synthesized the polyelectrolyte polystyrene sulfonate (PSS)-coated plasmonic gold nanorods (named GNRs@PSS) in a facile way and investigated their structural features by EF-TEM measurements. It revealed that PSS organic layers are uniformly coated on the surface of GNRs with a thickness of ~2.2 nm. Then, I firstly incorporated GNRs@PSS into inverted NFA-based OSCs as rear interfacial modifiers, which resulted in nearly 20% PCE enhancement compared to control devices. This enhancement mainly originated from the improved short-circuit current density (J_{sc}). GNRs could improve the sunlight absorption and exciton generation of NFA-based OSCs via the near-field plasmonic and backscattering effects, arising from their unique surface plasmon resonance (SPR). The SPR effect was revealed by the electrical field distribution of individual GNRs under the irradiation of a tunable laser at different

wavelengths. Likewise, Raman mapping also demonstrated the SPR effect of the GNRs. Meanwhile, the negatively charged PSS shell could ensure the uniform dispersion of GNRS on the surface of the photoactive layer, which thus could improve the interfacial contact and promote hole extraction, leading to enhanced charge mobility. Therefore, this ultrathin PSS organic layer not only guaranteed the strong SPR effect but also prevented direct contact between GNRs and the photoactive layer. Experimental results exhibited that the enhancement of J_{sc} (and thereby PCE) was mainly due to the synergistic effect of plasmonic GNRs and the surface PSS shell.

Enhancing Efficiency of Nonfullerene Organic Solar Cells via Using Polyelectrolyte-Coated Plasmonic Gold Nanorods as Rear Interfacial Modifiers

Zhonglin Du,[⊥] Ting Yu,[⊥] Wanting He, Aycan Yurtsever, Ricardo Izquierdo, Maziar Jafari, Mohamed Siaj, and Dongling Ma*

Read Online

ACCESS | Metrics & More | Article Recommendations | Supporting Information

ABSTRACT: Sufficient sunlight absorption and exciton generation are critical for developing efficient nonfullerene organic solar cells (OSCs). In this work, polyelectrolyte polystyrenesulfonate (PSS)-coated plasmonic gold nanorods (GNRs@PSS) were incorporated, for the first time, into the inverted nonfullerene OSCs as rear interfacial modifiers to improve sunlight absorption and charge generation via the near-field plasmonic and backscattering effects. The plasmonic GNRs effectively improved the sunlight absorption and enhanced the charge generation. Meanwhile, the negatively charged PSS shell ensured the uniform dispersion of the GNRs on the surface of the photoactive layer, optimized the interfacial contact, and further promoted the hole transport to the electrode. These concerted synergistic effects augmented the efficiency (10.11%) by nearly 20% relative to the control device (8.47%). Remarkably, the ultrathin (~2.2 nm) organic layer on the surface of GNRs was closely examined by acquiring the carbon contrast image through energy-filtered transmission electron microscopy (EF-TEM), which clearly confirmed the coating uniformity from the side to end-cap of GNRs. The surface plasmon resonance (SPR) effect of the GNRs@PSS on the surface of the photoactive layer was unprecedentedly mapped by photoinduced force microscopy (PiFM) under the illumination of a tunable wavelength supercontinuum laser mimicking sunlight. Furthermore, investigations into the effect of size, surface coverage, and incorporation location of GNRs@PSS on the performance of OSCs revealed that the appropriate design and incorporation of the plasmonic nanostructures are crucial, otherwise the performance can be decreased, as evidenced in the case of front interface integration.

KEYWORDS: organic solar cells, nonfullerene solar cells, gold nanorods, surface plasmon resonance, interfacial modifiers
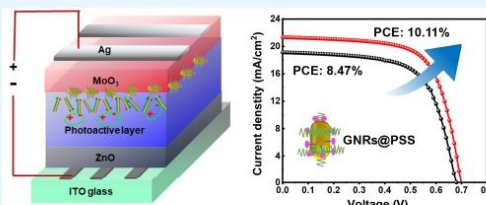
1. INTRODUCTION

Nonfullerene organic solar cells (OSCs) are considered as one of the most likely commercialized solar cells in a short term period.[1−5] Currently, although enormous efforts have been made on different aspects from donor/acceptor materials design and interfacial modification to device architecture engineering, the power conversion efficiency (PCE) of nonfullerene OSCs still lags behind that of the popular perovskite solar cells.[2,6−10] One of the critical issues is that the nonfullerene photoactive materials usually possess low charge carrier mobilities and short diffusion lengths, which largely limit the thickness of optimal bulk heterojunction (BHJ) photoactive films to <200 nm in most cases.[11,12] Such thin photoactive layers inevitably result in the inadequate absorption of the incident sunlight and thus limit the number of photogenerated charge carriers.[12] Clearly, improving light absorption without increasing the film thickness is critical, although challenging, to increase the photocurrent intensity and thereby the device efficiency. To this end, various

strategies have been explored, and among them, utilizing plasmonic metallic nanoparticles (NPs) as sunlight concentrators offers the most attractive pathway.[13−18]

Metallic NPs possess the unique surface plasmon resonance (SPR) effect in the visible and near-infrared wavelength ranges. It arises from the coherent oscillation of their conduction band electrons and leads to greatly enhanced extinction and/or local electromagnetic fields.[19] The SPR effect depends strongly on the size, shape, and type of metal NPs and their dielectric environments. Specifically for solar cells, the SPR effect is able to improve sunlight absorption mainly via the near field and/or light scattering effects generated by metallic NPs.[16,17] In the

16185

former case, the rate of electron−hole formation in the photoactive layer scales up in line with the near field intensity. In the latter case, the optical path of incident photons in the photoactive layer is largely elongated. Hitherto, various metallic NPs have been successfully employed in OSCs.[20−24] However, the current research on plasmonic NPs incorporated nonfullerene OSCs remains very limited. Compared to other NPs, gold nanorods (GNRs) are particularly attractive considering the facile and large tunability of the SPR wavelengths from the visible to near-infrared regions simply by adjusting their aspect ratios.[25,26] Considering that the backward scattered light could be efficiently reused by the devices if the GNRs are located at the real part of devices,[27,28] an attractive strategy is to position the plasmonic GNRs as rear interfacial modifiers, immediately close to the photoactive layer.

In designing plasmon-enhanced OSCs, another important factor to consider is the possible detrimental phenomenon of enhanced charge recombination on the surface of metallic NPs. To address this issue, a rational approach is to wrap metal NPs with an ultrathin, nonmetal shell. Currently, mostly inorganic SiO_2 is applied to inhibit direct contact between metallic NPs and the photoactive layer in OSCs.[29] However, this insulating layer can have a negative effect on the overall charge carrier transport. The inorganic shell formation process is also time-consuming and technically demanding. Controlling ultrathin and uniform thickness can be difficult under certain circumstances. Consequently, selecting suitable organic coating materials, allowing for the facile coating and acting as interfacial contact between metallic NPs and the photoactive layers, is an attractive alternative applicable to OSCs. In principle, polyelectrolytes can load straightforwardly on the surface of GNRs and form the ultrathin and uniform shell layer due to the electrostatic interactions, as already demonstrated for certain metallic NPs.[30,31] Polyelectrolytes were employed as the interlayer in OSCs to improve the charge carriers collection efficiency through the interfacial dipole effect.[32−34] However, to our knowledge, no studies have been performed regarding the application of the polyelectrolyte capped plasmonic metallic NPs into nonfullerene OSCs to improve their PCEs.

Herein, we demonstrate a significant enhancement on the performance of the inverted nonfullerene OSCs via incorporating the negatively charged polystyrenesulfonate (PSS)-coated GNRs as rear interfacial modifiers between the photoactive layer and the back-contact hole transport layers (HTLs). On the one hand, the plasmonic GNRs not only accelerate the charge generation via the near-field SPR effect but also enhance the photon reabsorption via the backscattering effect. On the other hand, the ultrathin PSS shell ascertains the uniform dispersion of the GNRs on the surface of photoactive layer, improves the interface contact, and promotes the hole transport from the photoactive layer to the HTLs. Benefiting from the synergistic effect of GNRs and PSS, a champion PCE of 10.11% (short-circuit current density J_{sc} = 21.34 mA·cm^{-2}, open-circuit voltage V_{oc} = 0.702 V, and fill factor FF = 67.50%) was achieved for the studied nonfullerene OSCs, with an enhancement of near 20% relative to the control device (8.47%). Energy-filtered transmission electron microscopy (EF-TEM) and photoinduced force microscopy (PiFM) were used for probing the ultrathin organic layer on the GNR surface and the near field of GNRs@PSS, respectively. Further investigations unraveled the effect of size, surface coverage, and incorporation locations of GNRs@PSS on the

performance of nonfullerene OSCs. This work provides a versatile and effective strategy for performance improvement of nonfullerene OSCs.

2. EXPERIMENTAL SECTION

2.1. Materials. Gold(III) chloride trihydrate (HAuCl$_4$·H$_2$O, 99.9%), sodium borohydride (NaBH$_4$, 98%), ʟ-ascorbic acid (AA, reagent grade), silver nitrate (AgNO$_3$), cetyltrimethylammonium bromide (CTAB, 99%), polystyrenesulfonate (PSS, Mw ∼ 70 000, powder), zinc acetate dihydrate (Zn(CH$_3$COO)$_2$·2H$_2$O, 99.9%), ethanolamine (NH$_2$CH$_2$CH$_2$OH, 99.5%), 2-methoxyethanol (CH$_3$OCH$_2$CH$_2$OH, 99.8%), lithium fluoride (LiF), and molybdenum trioxide interlayer (MoO$_3$) were obtained from Sigma-Aldrich. Poly[(2,6-(4,8-bis(5-(2-ethylhexyl)thiophen-2-yl)benzo [1,2-b:4,5-b']-dithiophene)-co-(1,3-di(5-thiophen-2-yl)-5,7-bis(2-ethylhexyl)-benzo[1',2'-c:4,5-c']dithiophene-4,8-dione))] (PBDB-T) polymer, 3,9-bis(2-methylene-((3-(1,1-dicyanomethylene)-6,7-difluoro)-indanone))-5,5,11,11-tetrakis(4-hexylphenyl)-dithieno[2,3-d:2',3'-d']-s-indaceno[1,2-b:5,6-b']dithiophene (ITIC-2F) molecule, and poly-(3,4-ethylenedioxythiophene) polystyrenesulfonate (PEDOT:PSS) were purchased from 1-Material company. Patterned indium tin oxide (ITO) glass substrates ($R_s \leq 10\ \Omega$ square^{-1}, $T_r \geq 83\%$) was purchased from Shenzhen Huayu Union Technology Co., Ltd. All chemicals were used as received without further treatment.

2.2. Preparation of GNRs@PSS Nanostructures. The GNRs@PSS nanostructures were prepared using the seed-mediated growth method followed by the electrostatic adsorption of PSS.[35] First, the GNRs capped with CTAB were prepared through the seed-mediated growth method, and the detailed procedure is shown in the Supporting Information (SI). The positively charged GNRs (∼0.2 mL) were subsequently added into 10 mL of aqueous PSS solution (2 g/L, containing 6 mM NaCl), and the mixture was stirred at room temperature for 6 h. Then, the PSS-encapsulated GNRs were purified by repeating the centrifugation/redispersion process three times and finally dispersed into methanol (∼1.0 mL) for further use.

2.3. Fabrication of GNRs@PSS Incorporated Nonfullerene OSCs. The GNRs@PSS integrated nonfullerene OSCs were fabricated via a solution process. First, the patterned ITO glass was washed sequentially in an ultrasonic bath with ultrapure water, acetone, and isopropyl alcohol and treated in an ultraviolet-ozone chamber for 10 min. Then, the cleaned ITO glass was spin-coated with a ZnO precursor at 4500 rpm for 60 s and sintered at 200 °C for 1 h in air. Here, a ZnO precursor solution was prepared by dissolving zinc acetate dehydrate in a 2-methothyethanol and ethanolamine mixture. Subsequently, the photoactive layer consisting of a chlorobenzene solution of PBDB-T/ITIC-2F (1:1 w/w) and a 0.5% volume ratio of 1,8-diiodooctane (DIO) additive was spin-coated on the surface of ZnO electron transport layer at 4000 rpm for 1 min and sintered at 160 °C for 15 min in the glovebox. Then, moderate GNRs@PSS methanol solution was spin-coated on the active layer at 3000 rpm for 1 min. Finally, the MoO$_3$ layer (ca. 25 nm) and Ag electrode (ca. 100 nm) were slowly evaporated onto the surface of the photoactive layer in a vacuum chamber. The effective device area was 0.06 cm^2. For the space-charge limited current (SCLC) measurements, the architectures of ITO/PEDOT:PSS/active layer/GNRs@PSS/MoO$_3$/Ag and ITO/ZnO/active layer/GNRs@PSS/LiF/Al were built up as the hole-only and the electron-only devices, respectively. For the hole-only device, PEDOT:PSS was first spin-coated on the ITO glass at 4500 rpm for 1 min, and the fabrication procedure of the other layer is similar to those of the solar cell devices. For the electron-only devices, the fabrication procedure is identical with the fabrication of the solar cell devices, except that the LiF layer and Al electrode were evaporated on the surface of the photoactive layer. The thickness of the photoactive layer for space-charge-limited currents (SCLC) measurements was the same as in the solar cells.

2.4. Characterization. The ultraviolet−visible (UV−vis) absorption spectrum of GNRs@PSS solution was collected using a Cary 5000 UV−vis−NIR spectrophotometer (Varian). The UV−vis absorption spectrum of GNRs@PSS on the polymer film was
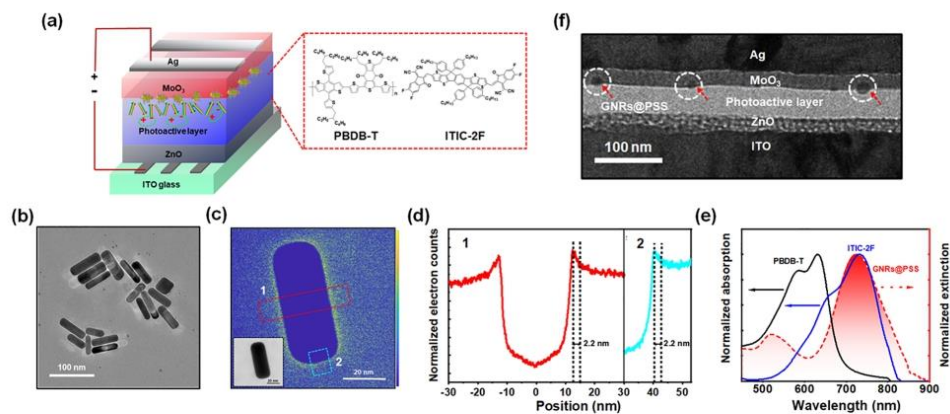
Figure 1. (a) Solar cell device structure and the molecular structure of organic materials in the photoactive layer. (b) Bright-field TEM image of the synthesized GNRs@PSS. (c) EF-TEM image of carbon bulk plasmon peak on the single GNR@PSS, centered at 25 eV with an energy slit 10 eV (inset: gray EF-TEM image of the same GNR@PSS). (d) Normalized electron counts profile along the red and cyan frames marked in (c), respectively, indicating that the uniform thickness of the organic coating shell is ~2.2 ($\pm$0.3) nm. (e) Normalized absorption spectra of PBDB-T (black solid line) and ITIC-2F (blue solid line) and the extinction spectra of GNRs@PSS (red dash line), respectively. (f) Bright-field TEM image of the cross-section of the photovoltaic device, portraying the layered structure of the solar cell device and the GNRs (denoted by circles) at the interface.

measured using a UV−visible−NIR spectrometer (Lambda 750). Photoluminescence (PL) spectra were acquired on a Fluorolog-3 system (Horiba Jobin Yvon) using an excitation wavelength of 500 nm. A transmission electron microscopy (TEM) image of GNRs@PSS was obtained through a JEM-2100PLUS (JEOL) microscope working at an accelerating voltage of 200 kV. The EF-TEM measurements were performed with a silicon monoxide (SiO_x) grid using JEOL JEM-2100 PLUS at 200 kV equipped with an in-column energy filter providing an energy resolution better than 150 meV. EF-TEM images were analyzed by performing integral signal normalization and background subtraction programmatically, using a code implemented in Matlab. The cross-sectional lamella of the device was fabricated by a scanning electron microscope/focused ion beam (SEM/FIB) dual-beam platform (TESCAN LYRA 3). The current density−voltage (*J*−*V*) curves of OSCs were measured by a Keithley 2400 source meter illuminated under AM 1.5G spectrum from a solar simulator (Oriel, Model No. 94022A). Light intensity was calibrated to be 100 mW/cm^2 by using an NREL Si solar reference cell. The external quantum efficiency (EQE) measurements were carried out on a Keithley 2000 multimeter under an illumination of 300 W tungsten lamp with a Spectral DK240 monochromator. Electron and hole mobilities were measured by a Keithley 2400 source meter illuminated under dark conditions. PiFM images were acquired in a noncontact atomic force microscope (AFM) mode using two mechanical modes of a 300 kHz NCHR-PtIr-coated AFM cantilever. The multimodal method of the PiFM technique used the first mechanical vibration mode to measure the PiFM absorption response of the sample, and the second mechanical vibration mode was used to track the topography of the sample, using a 1 nm root-mean-square (RMS) dither amplitude. To isolate the PiFM signal, from the topography signal, the frequency between the first and second mechanical modes were subtracted in the heterodyne signal acquisition. The PiFM images were recorded at 256 × 256 using sample scan speeds between 0.5 and 1.0 Hz. Raman characterization was performed on a micro-Raman spectrometer (InVia; Renishaw UK) with charge-coupled device detectors.

2.5. Finite-Difference Time-Domain Simulations. The three-dimensional finite-difference time-domain (3D-FDTD) method was employed to simulate the local field distribution of GNRs in nonfullerene OSCs according to the solutions of Maxwell's equation. This simulation was performed by introducing the plane-wave

sunlight source with the wavelength lying between 350 to 1000 nm into the entire device structure. The analogue device structure used for the simulation is ITO glass (120 nm)/ZnO (20 nm)/active layer (80 nm)/GNRs@PSS/MoO$_3$ (25 nm)/Ag (100 nm) (*XZ* plane at *Y* = 0). In total, three GNRs@PSS were arranged on the surface of the photoactive layer with an interval of 25 nm. The injection direction of the sunlight is +Z direction and propagates forward. The mesh size of three directions (*XYZ*) was set to 4 nm. In order to obtain the electrical intensity distribution image, three single wavelengths (530, 660, and 740 nm) were extracted from the sunlight to show the electrical field intensity distribution of the whole device.

3. RESULTS AND DISCUSSION

As shown in Figure 1a, the inverted nonfullerene OSCs were fabricated with the structure of ITO/ZnO/PBDB-T/ITIC-2F/MoO$_3$/Ag, and GNRs@PSS wa spin-coated on the surface of the photoactive layer. The photoactive layer was obtained by blending the polymer PBDB-T donor and the small molecule ITIC-2F acceptor, considered as the most photostable BHJ pairs in all the types of nonfullerene OSCs.[36] However, the currently reported efficiency based on this pair is still lower than those of other blends.[36] Here, we tried to use plasmonic GNRs to improve their efficiency, which has not been previously reported in this nonfullerene system, and gain new knowledge.

Plasmonic GNRs were prepared via the seed-mediated growth method with the detailed synthesis process described in the Supporting Information (SI). The morphology of the as-synthesized, CTAB-capped GNRs (Figure S1a) was uniform, and the average size was 24.5 ± 4.0 nm in length and 67.8 ± 7.1 nm in width (Figure S1b). To inhibit the charge recombination caused by direct contact of the GNRs with the PBDB-T and ITIC-2F films, PSS molecules were uniformly deposited onto the GNRs to form the GNRs@PSS nanostructure via the electrostatic interactions between PSS and CTAB-capped GNRs. The TEM image of the GNRs after the PSS shell coating treatment is shown in Figure 1b, and no
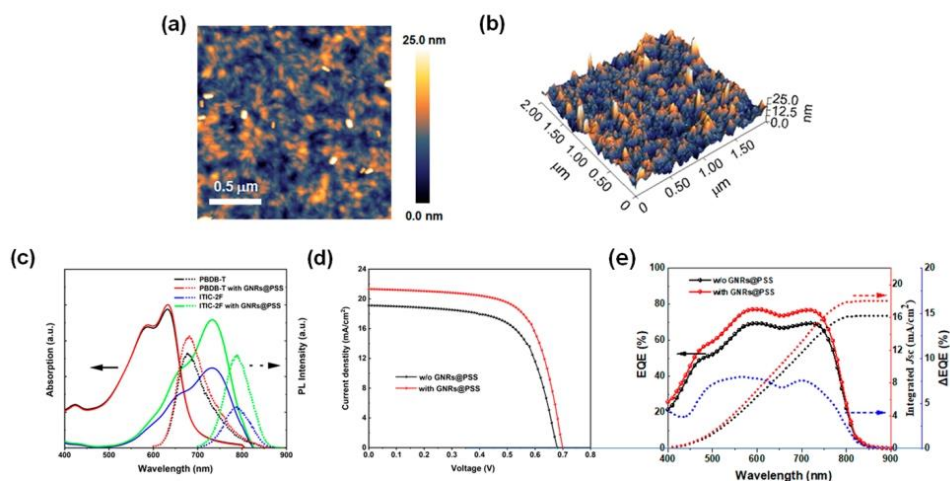
Figure 2. (a) 2D- and (b) 3D-AFM surface topography images of the photoactive layer film with the GNRs@PSS on the surface. (c) Absorption spectra (solid lines) and photoluminescence (dot lines) of the pristine PDBD-T and ITIC-2F films with and without GNRs@PSS. (d) $J-V$ characteristics of the devices with and without GNRs@PSS. (e) EQE, integrated J_{sc}, and corresponding ΔEQE spectra of the devices with and without GNRs@PSS.

obvious structural variation of GNRs was observed. Consistently, the extinction spectrum of GNRs after the PSS shell deposition was invariant (Figure S2).

To probe the thickness of the organic shell, the EF-TEM technique was applied to study a single GNR@PSS. The main composition element of CTAB and PSS is carbon (C), with the bulk plasmon peak located at ~25 eV.[37] Here, the low loss region of electron energy loss spectrum (EELS) was utilized to acquire a carbon contrast image (Figure 1c) by EF-TEM using a 10 eV slit window centered at 25 eV ($\pm$5 eV). The thickness of the organic shell was determined by the profile of the carbon signal intensity. The normalized electron counts profiles along the red frame parallel to the short axis and the cyan frame crossing the end-cap of the GNR (as denoted in Figure 1c) are shown in Figure 1d. The thickness of the organic shell (including both CTAB and PSS) is quite uniform, which is about 2.2 nm everywhere from the side to end-cap, close to the reported thickness value of the PSS layer.[38] In comparison, the zero-loss EF-TEM image (Figure S3) of the single GNR@PSS was taken at 0 eV with a 6 eV slit window (0 $\pm$ 3 eV), where no clear signal variation at the edge was observed, thus validating the use of low-loss carbon signal to probe the organic layer thickness. The successful PSS shell formation was further confirmed by ζ potential measurements. The surface charge reversed from +49.32 to −54.18 mV after PSS coating (Figure S4). The negatively charged GNRs@PSS can facilitate the charge transport from the photoactive layer to the HTL, making GNRs@PSS ideal candidates as the rear interfacial modifiers between the photoactive layer and HTL.[39,40]

The normalized UV−vis absorption spectra of the neat PBDB-T and ITIC-2F films and the extinction spectra of GNRs@PSS are displayed in Figure 1e. PBDB-T and ITIC-2F exhibited strong absorption peaks at 632 and 733 nm, respectively. GNRs marked two extinction peaks centered at 515 and 724 nm, corresponding to the transverse and longitudinal oscillation modes, respectively. The longitudinal

extinction was easily tuned by manipulating the aspect ratio of the GNRs. Here, the longitudinal extinction peak at 724 nm matched well with the absorption of the acceptor ITIC-2F, favoring the effective plasmonic resonance energy transfer process.

The fresh GNRs@PSS solution was spin-coated on the surface of the photoactive layer, immediately before the deposition of the HTL, serving as the sunlight concentrators and interfacial modifiers. The cross-section TEM image (Figure 1f) of the GNRs@PSS incorporated device indicated the GNRs@PSS (highlighted by white broken circles) at the interface between the photoactive layer (~80 nm) and the MoO$_3$ HTL (~25 nm). Specially, GNRs@PSS were partially embedded in the photoactive layer (red arrows in Figure 1f), promoting the near-field and scattering effects. In addition, compared to the pristine photoactive layer (Figure S5), the AFM topography and the corresponding 3D images in Figure 2a,b showed that the GNRs@PSS were randomly distributed on the surface of the photoactive layer without aggregating and disrupting the morphology of photoactive layer.

Although the surface coverage of GNRs@PSS on the photoactive layer was rather low, the enhancement of the device performance was rather effective. The ultrathin PSS shell played a vital role in the solution deposition of GNRs. For the fabrication of OSCs, a common issue encountered during the layer-by-layer solution deposition process is the damage to the previously deposited layers if the subsequent deposition solvent is compatible. It was found that using anhydrous methanol avoided this problem when depositing GNRs, as it was unreactive toward the photoactive layer materials.[41] Meanwhile, methanol solvent is also an excellent candidate to remove the residual DIO additives that deteriorate device performance and stability. Nonetheless, the as-synthesized CTAB-caped GNRs aggregated rapidly in methanol after a few seconds, although they could be easily dispersed in water. With the help of PSS layer, we solved this problem and the GNRs

Table 1. Effects of the GNRs@PSS on the Photovoltaic Performance Parameters (open-circuit voltage V_{oc}, short-circuit current density J_{sc}, fill factor FF, and power conversion efficiency PCE) Extracted from $J{-}V$ Scans under Standard Conditions (simulated AM 1.5 G 100 mW cm^{-2})

configuration	J_{sc} (mA·cm^{-2})[a]	V_{oc} (V)[a]	FF (%)[a]	PCE (%)[a]
w/o GNRs@PSS	19.13	0.686	64.26	8.47
	(18.54 ± 0.36)	(0.682 ± 0.005)	(63.89 ± 0.83)	(8.33 ± 0.49)
with GNRs@PSS	21.34	0.702	67.50	10.11
	(21.08 ± 0.42)	(0.696 ± 0.004)	(67.11 ± 0.68)	(10.02 ± 0.54)

[a]Average values (in parentheses) were obtained from 10 devices.

Figure 3. (a) J_{ph} versus V_{eff}, (b) EIS Nyquist plots, (c) J_{sc} versus light intensity, and (d) V_{oc} versus light intensity for the OSCs based on the PBDB-T/ITIC-2F photoactive layer with and without GNRs@PSS.

can be uniformly dispersed in anhydrous methanol and further deposited on the photoactive layer without deteriorating it. The PSS shell enabled uniform surface distribution of the GNRs and maintained the pristine morphology of the photoactive layer.

To investigate the plasmonic effect on the photoactive materials, the absorption and photoluminescence (PL) spectra of the pristine PBDB-T and ITIC-2F films with and without the GNRs@PSS were measured (Figure 2c). The dipole−dipole coupling strength between the plasmonic and semiconductor materials is strongly dependent on the spectral overlap between the SPR and the acceptor absorption bands.[42] The broken-line PL curves in Figure 2c informed that the incorporation of GNRs@PSS led to the enhancement of the PL intensity for both the PBDB-T and ITIC-2F films due to the escalation in exciton generation, arising from the SPR effect of the GNRs. The current density−voltage ($J{-}V$) curves of the obtained OSCs are shown in Figure 2d. The optimized device with the GNRs@PSS yielded a higher PCE of 10.11% compared to the control device (~8.47%), with improvements of J_{sc} from 19.13 to 21.34 mA/cm^2, V_{oc} from 0.686 to 0.702 V, and FF from 64.26% to 67.50%, respectively (shown in Table

1). To verify that this performance enhancement was mainly due to the introduction of plasmonic GNRs@PSS, we also fabricated OSCs without the GNRs@PSS while going through methanol treatment, where no performance difference was observed (Figure S6) that excluded the solvent (methanol) effect. To extract the mechanism responsible for the enhanced device performance with the plasmonic material, the external quantum efficiency (EQE) of these devices was measured (Figure 2e). The GNRs@PSS integrated devices exhibited a higher EQE than the control over a broad wavelength range from 400 to 850 nm. In particular, the EQE enhancement curve (ΔEQE) showed two distinct peaks at ~520 and 720 nm, which were in line with the transverse and longitudinal SPR of GNRs, respectively. The overall increase in EQE upon the introduction of GNRs@PSS was significant, complying well with the observed enhanced J_{sc}, and ascribed to backscattering and near-field effects of the GNRs@PSS.[43] Meanwhile, the integrated J_{sc} values based on the EQE spectra were 16.23 and 18.14 mA/cm^2 for the control and GNRs@PSS integrated devices, respectively, which were slightly lower than the measured J_{sc} values from $J{-}V$ curves (Figure 2d) as listed in Table 1. However, it should be noted that the discrepancy is

109
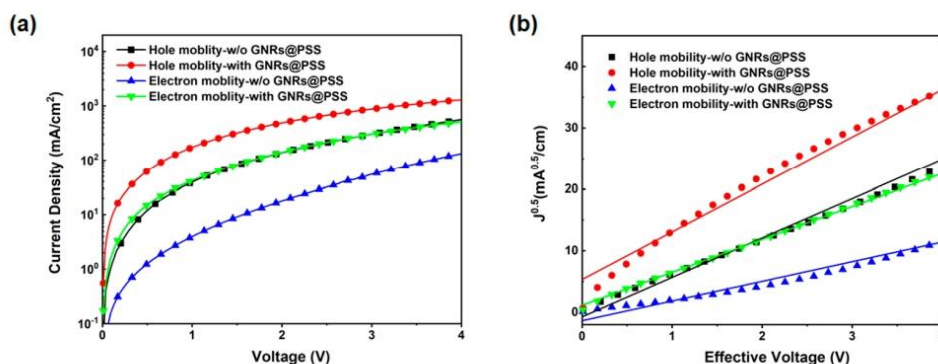
Figure 4. (a) J_D-V characteristics of single carrier devices fabricated with and without the GNRs@PSS. Structures of ITO/PEDOT:PSS/active layer/GNRs@PSS/MoO$_3$/Ag and ITO/ZnO/active layer/GNRs@PSS/LiF/Al were used as the hole-only and the electron-only devices, respectively. (b) Their corresponding $J^{0.5}-V_{eff}$ characteristics for the SCLC single-carrier mobility and fitting lines.

below the 20% threshold, as specified and discussed in the paper by Schmidt-Mende et al.[44]

By further inquiring the plasmonic effect of the GNRs@PSS on the exciton dissociation of OSCs, the photocurrent density (J_{ph}) versus the effective voltage (V_{eff}) of the typical devices were measured and plotted (Figure 3a). J_{ph} is determined as $J_{ph} = J_{light} - J_{dark}$, where J_{light} and J_{dark} are the current densities under illumination and in the dark, respectively. V_{eff} is determined as $V_{eff} = V_0 - V_a$, where V_0 is the voltage at the point of $J_{ph} = 0$ and V_a is the applied bias voltage.[45,46] It is observed that the J_{ph} increases linearly with the voltage at a low value of V_{eff} (<0.1 V) and tends to saturate at a higher value. The saturation photocurrent density (J_{sat}) was determined from Figure 3a. The ratio of J_{ph}/J_{sat} was used to estimate the exciton dissociation and charge collection efficiency under operation conditions. As listed in Table S1, the J_{ph}/J_{sat} ratio was increased from 89.7% to 93.4% under the short circuit condition and from 83.2% to 87.0% under the maximal power output condition. The intensification of the parameters was assigned to the implanted GNRs@PSS. The larger values of J_{ph}/J_{sat} indicate an effective exciton dissociation and a better charge collection efficiency in the GNRs@PSS integrated device, in accordance with the higher FF. Electrochemical impedance spectroscopy (EIS) was further measured, and the resulting Nyquist plots are displayed in Figure 3b. The EIS measurements were carried out at a bias voltage of 0.7 V under dark conditions. The corresponding simulation circuit used for fitting EIS data and the extracted parameters are shown in Figure S7 and Table S2, respectively.[47-49] In this simulation circuit, R_1 is the series resistance of metallic wires and electrodes, R_2 and CPE$_2$ are associated with the contact between the photoactive layer and the MoO$_3$ layer, and R_3 and CPE$_3$ are related with the organic photoactive layer. The devices with GNRs@PSS exhibited a relatively lower R_2 (96.44 Ω cm^2) than the control one (120.7 Ω cm^2), indicating a faster charge transport at the interface due to the negative PSS coating layer on the surface of GNRs.[48,49] The lower R_2 from the EIS measurements was in line with the FF increase of the photovoltaic devices. The R_3 value of the device with GNRs@PSS (171.1 Ω cm^2) was similar to that without GNRs@PSS (172.9 Ω cm^2), suggesting that the GNRs have little effect on the photoactive layer under dark conditions.

Charge recombination behavior of the OSCs with and without GNRs@PSS was also investigated by measuring the J_{sc} and V_{oc} as a function of light intensity (P_{light}). The relationship between J_{sc} and P_{light} is described as $J_{sc} \propto P_{light}^{\alpha}$, where α indicates the degree of the bimolecular recombination.[50,51] As depicted in Figure 3c, the device incorporated with GNRs@PSS obtained a slightly larger α of 0.93 than the pristine one (α = 0.91), indicating less bimolecular recombination, beneficial for effective charge transport. Differently, V_{oc} correlates to the light intensity by the equation, $V_{oc} = (akT/q) \ln(P_{light})$, where V_{oc} is proportional to ln P_{light}, with the slope related to kT/q, where k is Boltzmann's constant, q refers to the elementary charge, and T is the tested temperature. The further the slope is close to 1 kT/q, the less trap-assisted recombination dominates. As shown in Figure 3d, the slope for the GNRs@PSS incorporated device approached 1, implying less trap-assisted recombination.[52]

The carriers transport properties of the PBDB-T/ITIC-2F films fabricated with and without GNRs@PSS were further examined by SCLC mobility measurements. The device architectures of ITO/PEDOT:PSS/active layer/GNRs@PSS/MoO$_3$/Ag and ITO/ZnO/active layer/GNRs@PSS/LiF/Al were built as hole-only and electron-only devices, respectively. Their dark current density-voltage (J_D-V) curves are shown in Figure 4a, and their corresponding $J^{0.5}-V_{eff}$ characteristics and fitting lines are shown in Figure 4b. Both the hole mobility and electron mobility results were calculated by the Mott-Gurney square law and are summarized in Table S3. In the control device, the μ_h and μ_e values were calculated to be (1.35 ± 0.09) × 10^{-4} and (3.20 ± 0.87) × 10^{-5} cm^2 V^{-1} s^{-1}, respectively. After the GNRs@PSS were deposited on the surface of photoactive layer, the μ_h and μ_e were improved to (1.96 ± 0.17) × 10^{-4} and (9.39 ± 0.99) × 10^{-5} cm^2 V^{-1} s^{-1}, respectively. The enhanced charge carrier mobility is likely due to improved interfacial contact and less surface charge trapping. Meanwhile, as shown in Figure S8, the work function of GNRs@PSS-incorporated photoactive layer slightly changed. Furthermore, the GNRs@PSS incorporated devices manifested a more balanced hole and electron mobility than the control one, also explaining the resulting higher FF values.[53] As view of the V_{oc}, on the one hand, the existence of surface PSS can hinder the direct contact between GNRs and
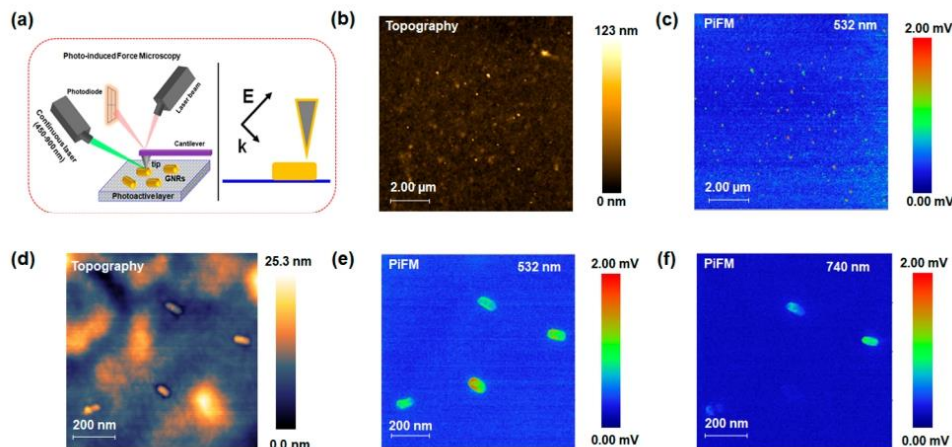
Figure 5. (a) Schematic of the PiFM setup with a supercontinuum wavelength-tunable laser (450−900 nm). (b) Topography and (c) PiFM images of the GNRs@PSS on the surface of the photoactive layer under the 532 nm excitation. The topography and PiFM images size: 10 μm × 10 μm. (d) Magnified topography of the GNRs@PSS on the surface of the photoactive layer with the region size of 1.0 μm × 1.0 μm. Corresponding PiFM images under the excitation of the tunable laser set at (e) 532 nm and (f) 740 nm.
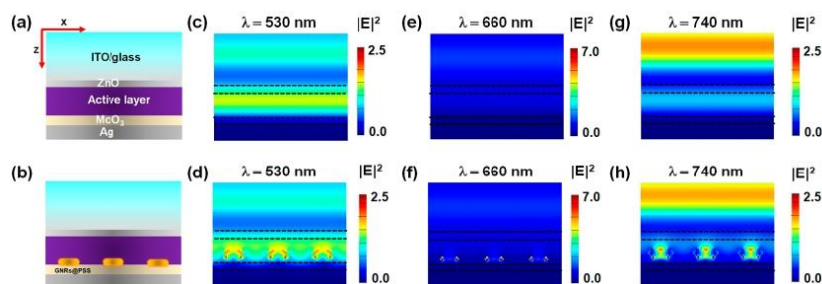
Figure 6. (a and b) Device structures and (c−h) normalized spatial distribution of electric field intensity at three different wavelengths (530, 660, and 740 nm) with and without GNRs@PSS incorporation by FDTD simulations (XZ plane, Y = 0).

photoactive layer materials, which hinders the charge recombination. On the other hand, the GNRs@PSS facilitates the hole transport from the photoactive layer to the HTL. The above advantages of the GNRs@PSS nanostructures finally improved the V_{oc} values.

Interestingly, we were able to locate the local electric field distribution of a single GNR@PSS on the photoactive layer with PiFM measurement.[54−56] Figure 5a illustrates the schematic setup of the PiFM measurements. A PiFM instrument combines an AFM platform with a tunable laser and the necessary optics to tightly focus the laser light onto the tip−sample interface. Herein, we used a supercontinuum laser (from 450 to 900 nm) as the incident light and the incident direction was 45°. The incoming laser beam is a p-polarized uniform plane wave, with the incident electric field denoted by E (Figure 5a). Parts b and c of Figure 5 exhibit the AFM topography and the corresponding PiFM images of GNRs@PSS on the surface of the photoactive layer, respectively. The size of the two images is 10 μm × 10 μm. The PiFM image was recorded under the polarization of the incident laser set at 532 nm. The detected bright spots in the PiFM image reflected the

electron oscillations of the transverse SPR mode mapping of the GNRs on the surface of the photoactive layer. We then focused on the single GNR and observed the near-field plasmonic effect under the laser excitation at different wavelengths specific to the GNR resonance modes. Figure 5d shows the zoomed-in topography image of the GNRs on the photoactive layer (1.0 μm × 1.0 μm). Two different wavelengths (532 and 740 nm) of the laser were applied, which were close to the transverse mode (515 nm) and longitudinal mode (724 nm) of GNRs. As shown in Figure 5e,f, both of the PiFM images were normalized to the maximum PiFM signal of 2.0 mV for comparison. The heterogeneous SPR of GNRs in the PiFM images was observed under the illumination of the tunable laser set at 532 and 740 nm, respectively.

Raman measurements were also applied to verify the plasmonic effect in the PBDB-T/ITIC-2F blend photoactive layer with the incorporation of GNRs@PSS.[57] The sample structure was glass/GNRs@PSS/photoactive materials, and the photoactive layer was much thinner than the real device. The photoactive layer was excited with a 532 nm laser.

111
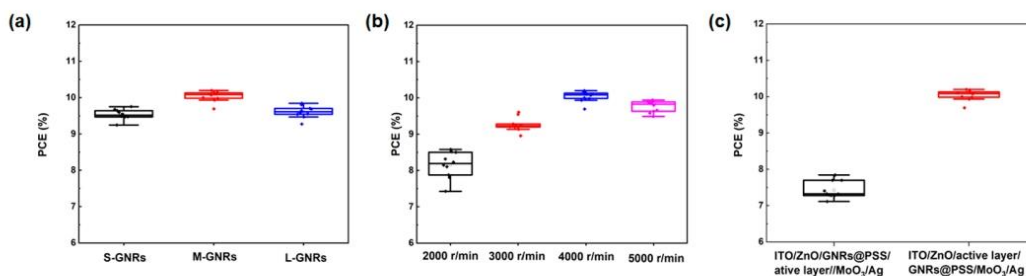
Figure 7. Effect of the optimization conditions on the performance of GNRs@PSS enhanced OSCs: (a) size, (b) surface coverage, and (c) location of the GNRs@PSS.

Reference Raman spectra of the pure PBDB-T and ITIC-2F were measured between 800 and 1900 cm^{-1} (Figure S9). Various Raman vibration modes were identified for these two types of molecules.[58] Raman spectra of the PBDB-T/ITIC-2F blend films with and without GNRs@PSS are exhibited in Figure S10. The peak intensity of the photoactive layer with GNRs@PSS was enhanced significantly due to the plasmonic effect of GNRs. Besides, the Raman mappings (20 μm × 20 μm) with and without GNRs@PSS were collected from 1300 to 1600 cm^{-1} and are shown in Figure S11a,b. The power intensity of the laser for this mapping test was set down to 10% of the maximum value (100 mW), as exposure to a high-intensity laser beam would damage the organic films. Compared to the control one, the bright red spots in the GNRs@PSS incorporated film represented the locally enhanced Raman signal due to the SPR effect of the plasmonic GNRs.

The FDTD calculation is a proven and effective method to simulate the local field distribution.[59,60] Here, in order to further explore the enhancement mechanism in nonfullerene OSCs with GNRs@PSS, the 3D-FDTD method was performed to calculate the normalized electric field intensity in the entire structure. Parts a and b of Figure 6 present the FDTD simulation models. The incident sunlight from the +Z direction crosses the photoactive layers and then is scattered from the GNRs. The complex refraction index n and extinction coefficient k of PBDB-T/ITIC-2F blend film, shown in Figure S12, were obtained from the literature.[61] The normalized spatial distribution regarding the cross-section (XZ, $Y = 0$) of the electric field intensity in the devices with and without GNRs under the illumination of three different wavelengths (530, 660, and 740 nm) are shown in Figure 6c−h. Simulations of the electric field intensity from the other two directions (plane XY, $Z = 0$ and cross-section XZ, $Y = 0$) are available in Figures S13 and S14. Due to the interaction between incident light and reflected light from the electrode, weak interference fringes were observed in the spatial distributions for the control device, especially occurring at a wavelength of 740 nm (as shown in Figure 6c−g). Moreover, as perceived in Figure 6d,f,h, the SPR effect from GNRs contributes to the field enhancements and thus improves sunlight absorption. Allocated to the enhanced light-scattering at plasmon resonance wavelengths of 530 and 740 nm, the coupling of the scattered light into the waveguide modes within the photoactive layer can be observed in Figure 6d,h. Noticeably, the simulated power absorption per unit volume (P_{abs}) of the devices from the planar direction (XY plane at $Z = $

0) are shown in Figure S15, illustrating that the absorption intensity of the device containing GNRs is higher than that of the control one.

It is known that the plasmonic effect of the metallic NPs depends strongly on their size, shape, and dielectric environments. Thus, the selection and incorporation location of GNRs are expected to play important roles in determining the performance enhancement of OSCs. We systematically investigated the effect of the GNRs@PSS incorporation conditions (i.e., the size, surface coverage, and deposition location) on the performance of the nonfullerene OSCs. First, to investigate the size effect of GNRs, we prepared GNRs of three different aspect ratios, designated by S-GNR, M-GNRs, and L-GNRs, respectively. Their TEM images, size distributions, and extinction spectra are shown in Figure S16. With the increase in aspect ratio of GNRs from 2.1 (S-GNRs) to 2.8 (M-GNRs) and 3.4 (L-GNRs), the extinction peak of the longitudinal resonance bands red-shifted, as expected, from 645 to 724 and 801 nm, while the transverse resonance peak stalled at ∼515 nm. As shown in Figure 7a and Table S4, with the increase in an aspect ratio of GNRs, the average PCE was increased first and then decreased. The M-GNRs integrated device obtained a higher PCE (10.11%) than L-GNRs (9.71%) and S-GNRs (9.66%). The corresponding EQE spectra were also measured (Figure S17). The EQE value of the M-GNRs-based solar cell was higher than the other two sizes. This can be reasonably explained by optical observations, where the longitudinal extinction spectrum of M-GNRs showed the balanced overlap with the absorption of both the donor and acceptor (Figure S18), whereas the S-GNRs and the L-GNRs longitudinal modes only overlapped with the absorption of either the acceptor or the donor. The superposition with both the donor and acceptor assured the effective absorption enhancement in both semiconductor materials, hence more exciton generation. The improved exciton generation was indirectly verified by PL measurements (Figure S19), where the M-GNRs were most effective in enhancing the emission of ITIC-2F while the S-GNRs enhanced the PL of PBDB-T. Although S-, M-, and L-GNRs were all able to enhance the exciton generation of photoactive materials, the improvement level on the final performance of the devices was different. It is clear that, in designing plasmon-enhanced OSCs, not only the near field strength (largely relying on the geometry feature of the plasmonic nanostructures themselves) but also the spectra overlap between the plasmonic and photoactive materials need to be taken into consideration to take the greatest possible advantage of SPR effect.

The surface coverage of the GNRs, which is considered as another important factor, also influences the performance of the resulting devices. The surface coverage of the M-GNRs@PSS was optimized systematically by changing the spin-coating rate during the GNR deposition process to obtain the maximum PCE from the OSCs. The higher spin coating rate led to a lower surface coverage of GNRs. With the increase of surface coverage, the PCE first improved and then decreased, possibly because a too-high surface coverage of GNRs@PSS achieved at the lowest deposition speed could hinder the interface contact of the photoactive layer and HTL, thus decreasing the FF and J_{sc} of the devices. The highest PCE of 10.11% was obtained at 4000 r/min (Figure 7b and Table S5).

The effect of GNRs@PSS locations on the performance of OSCs was investigated, and the results are shown in Figure 7c and Table S6. M-GNRs@PSS were spin-coated on the surface of the ZnO electron transport layer before the photoactive layer deposition, which constituted a different device configuration from the above-mentioned cases. In all those cases, the GNRs were located at the interface of the photoactive layer and HTL. The SEM image exhibited that the M-GNRs@PSS were uniformly distributed on the surface of the ZnO layer without agglomeration (Figure S20). Surprisingly, the same plasmonic M-GNRs@PSS had a detrimental impact on the performance of solar cells in this case; the performance was even lower than that without GNRs. The PSS suppressed the electron transfer from the photoactive layer to the ZnO layer, and this negative impact was overwhelmingly larger than the beneficial SPR effect from the GNRs. Therefore, the devices with the M-GNRs@PSS incorporated on the ZnO layer obtained the lower PCE of 7.83%, along with all three major parameters mitigated in contrast to those with the M-GNRs@PSS integrated at the opposite position, as the rear interfacial modifiers, highlighting the importance of appropriate integration location of the GNRs.

It may be argued that the introduction of GNRs can increase heterogeneity and roughness at the interface and thus degrade the device stability. To testify it, the stability involving environmental, thermal, optical, and humidity conditions of the OSCs devices with m-GNRs@PSS were further evaluated, and the temporal evolution of the normalized photovoltaics parameters (PCE, J_{sc}, V_{oc}, and FF) are presented in Figures S21−S24, respectively. For the environmental stability test, the devices were stored upon ambient air exposure and dark conditions. The devices were annealed continuously on a hot plate at 80 °C in the dark for the thermal stability test. As a comparison, the reference devices were examined under the same conditions. As shown in Figures S21 and S22, it is clearly presented that the devices with and without m-GNRs@PSS have similar degradation in both the environmental and thermal stability states during the whole test time (~186 h). Besides, we continued to carry out the stability test of devices with and without m-GNRs@PSS under continuous illumination in the glovebox and under a humidity of 70% in air, respectively. As depicted in Figures S23 and S24, the devices with and without GNRs@PSS display the similar optical stability after 168 h illumination and humidity stability after being stored for 144 h in a humidity of 70%. We did not observe any impact from the GNRs@PSS on the device stability in our experiments. The maintained device stability further reveals that the coated thin PSS layer on the surface of GNRs can increase the interface contact.

4. CONCLUSIONS

In summary, the polyelectrolyte PSS-coated plasmonic GNRs were, for the first time, introduced as the rear interfacial modifier into the inverted PBDB-T/ITIC-2F nonfullerene OSCs. PiFM mapping was explored to visualize the SPR response of individual GNRs on the surface of the photoactive layer under the illumination of the supercontinuum laser mimicking sunlight. The near-field SPR effect and back-scattering effects of plasmonic GNRs led to an increase in the sunlight absorption and exciton generation, as supported by the major increase of the J_{sc}. EF-TEM measurements were performed to probe the thickness (~2.2 nm) of the ultrathin organic shell surrounding GNRs ~2.2 nm. The ultrathin negatively charged PSS shell improved the interface contact and promoted higher excitation dissociation possibilities and more balanced hole/electron mobilities, resulting in the effective charge transport and the reduced charge recombination between the photoactive layer and HTL. Thanks to the synergistic effects of GNRs and PSS, on the basis of the stable PBDB-T/ITIC-2F donor/acceptor pairs, an efficiency of 10.11% was achieved with an enhancement of nearly 20% relative to the control device (8.47%).

■ ASSOCIATED CONTENT

ⓢ Supporting Information

The Supporting Information is available free of charge at https://pubs.acs.org/doi/10.1021/acsami.1c25223.

Discussion of synthesis of CTAB-stabilized gold nanorods, figures of TEM and SEM images, size distribution, UV−vis absorption spectra, zero-loss EF-TEM image, normalized electron count profile, ζ potential, 2D-AFM and 3D-AFM surface topography, $J-V$ characteristics, simulation circuit used for fitting EIS, UPS spectra, Raman spectra, Raman mapping images, refractive index n and k of photoactive layer materials, normalized spatial distribution of electric field intensity at three different wavelengths, calculated absorption spectra, extinction spectra, EQE spectra, PL spectra, and normalized photovoltaic parameters, and tables of effects of the GNRs@PSS on the photocurrent density, saturation photocurrent density, and the ratio values, summary of the fitting parameters of the Nyquist plots of devices with and without the GNRs@PSS, carrier mobilities of the active layers with and without the GNRs@PSS, effects of size of GNRs on the photovoltaic performance parameters, effects of surface coverage of M-GNRs@PSS on the photovoltaic performance parameters, and effect of the incorporation location of the M-GNRs@PSS on the photovoltaic performance parameters extracted under standard conditions (PDF)

■ AUTHOR INFORMATION

Corresponding Author

Dongling Ma − Institut National de la Recherche Scientifique (INRS), Centre Énergie Materiaux et Télécommunications, Varennes, Québec J3X 1P7, Canada; ⓞ orcid.org/0000-0001-8558-3150; Email: ma@emt.inrs.ca

Authors

Zhonglin Du − Institut National de la Recherche Scientifique (INRS), Centre Énergie Materiaux et Télécommunications, Varennes, Québec J3X 1P7, Canada; College of Materials

Science and Engineering, the National Base of International Science and Technology Cooperation on Hybrid Materials, Qingdao University, Qingdao 266071, P. R. China; orcid.org/0000-0001-7629-3717

Ting Yu − *Institut National de la Recherche Scientifique (INRS), Centre Énergie Materiaux et Télécommunications, Varennes, Québec J3X 1P7, Canada*

Wanting He − *Institut National de la Recherche Scientifique (INRS), Centre Énergie Materiaux et Télécommunications, Varennes, Québec J3X 1P7, Canada*

Aycan Yurtsever − *Institut National de la Recherche Scientifique (INRS), Centre Énergie Materiaux et Télécommunications, Varennes, Québec J3X 1P7, Canada*

Ricardo Izquierdo − *Département de Génie Électrique, École de Technologie Supérieure, Montréal, Québec H3C 1K3, Canada*

Maziar Jafari − *Department of Chemistry, Université du Québec à Montréal, NanoQAM/QCAM, Montréal, Québec H3C 3P8, Canada*

Mohamed Siaj − *Department of Chemistry, Université du Québec à Montréal, NanoQAM/QCAM, Montréal, Québec H3C 3P8, Canada;* orcid.org/0000-0003-0499-4260

Complete contact information is available at:
https://pubs.acs.org/10.1021/acsami.1c25223

Author Contributions

[⊥]Z.D. and T.Y. contributed equally. Z.D. and D.M. conceived and supervised the project. Z.D., T.Y., and W.H. performed the measurements and characterizations. Z.D. wrote the draft, and D.M. revised the manuscript. All authors discussed the results and commented on the manuscript.

Notes

The authors declare no competing financial interest.

REFERENCES

(1) Yan, C.; Barlow, S.; Wang, Z.; Yan, H.; Jen, A. K. Y.; Marder, S. R.; Zhan, X. Non-Fullerene Acceptors for Organic Solar Cells. *Nat. Rev. Mater.* **2018**, *3*, 18003.

(2) Meng, L.; Zhang, Y.; Wan, X.; Li, C.; Zhang, X.; Wang, Y.; Ke, X.; Xiao, Z.; Ding, L.; Xia, R.; Yip, H.-L.; Cao, Y.; Chen, Y. Organic and Solution-Processed Tandem Solar Cells with 17.3% Efficiency. *Science* **2018**, *361*, 1094−1098.

(3) Carlé, J. E.; Helgesen, M.; Hagemann, O.; Hösel, M.; Heckler, I. M.; Bundgaard, E.; Gevorgyan, S. A.; Søndergaard, R. R.; Jørgensen, M.; García-Valverde, R.; Chaouki-Almagro, S.; Villarejo, J. A.; Krebs, F. C. Overcoming the Scaling Lag for Polymer Solar Cells. *Joule* **2017**, *1*, 274−289.

(4) Lin, Y.; Wang, J.; Zhang, Z. G.; Bai, H.; Li, Y.; Zhu, D.; Zhan, X. An Electron Acceptor Challenging Fullerenes for Efficient Polymer Solar Cells. *Adv. Mater.* **2015**, *27*, 1170−1174.

(5) Wang, J.; Zhan, X. Fused-Ring Electron Acceptors for Photovoltaics and Beyond. *Acc. Chem. Res.* **2021**, *54*, 132−143.

(6) Luo, Z.; Ma, R.; Liu, T.; Yu, J.; Xiao, Y.; Sun, R.; Xie, G.; Yuan, J.; Chen, Y.; Chen, K.; Chai, G.; Sun, H.; Min, J.; Zhang, J.; Zou, Y.; Yang, C.; Lu, X.; Gao, F.; Yan, H. Fine-Tuning Energy Levels via Asymmetric End Groups Enables Polymer Solar Cells with Efficiencies over 17%. *Joule* **2020**, *4*, 1236−1247.

(7) Jiang, K.; Wei, Q.; Lai, J. Y. L.; Peng, Z.; Kim, H. K.; Yuan, J.; Ye, L.; Ade, H.; Zou, Y.; Yan, H. Alkyl Chain Tuning of Small Molecule Acceptors for Efficient Organic Solar Cells. *Joule* **2019**, *3*, 3020−3033.

(8) Yao, H.; Wang, J.; Xu, Y.; Zhang, S.; Hou, J. Recent Progress in Chlorinated Organic Photovoltaic Materials. *Acc. Chem. Res.* **2020**, *53*, 822−832.

(9) Wang, Y.; Li, J.; Li, T.; Wang, J.; Liu, K.; Jiang, Q.; Tang, J.; Zhan, X. Black Phosphorous Quantum Dots Sandwiched Organic Solar Cells. *Small* **2019**, *15*, 1903977.

(10) Chen, M.; Wang, J.; Yin, F.; Du, Z.; Belfiore, L. A.; Tang, J. Strategically Integrating Quantum Dots into Organic and Perovskite Solar Cells. *J. Mater. Chem. A* **2021**, *9*, 4505−4527.

(11) Li, G.; Zhu, R.; Yang, Y. Polymer Solar Cells. *Nat. Photonics* **2012**, *6*, 153−161.

(12) Chueh, C.-C.; Crump, M.; Jen, A. K.-Y. Optical Enhancement via Electrode Designs for High-Performance Polymer Solar Cells. *Adv. Funct. Mater.* **2016**, *26*, 321−340.

(13) Kundu, S.; Patra, A. Nanoscale Strategies for Light Harvesting. *Chem. Rev.* **2017**, *117*, 712−757.

(14) Ueno, K.; Oshikiri, T.; Sun, Q.; Shi, X.; Misawa, H. Solid-State Plasmonic Solar Cells. *Chem. Rev.* **2018**, *118*, 2955−2993.

(15) Green, M. A.; Pillai, S. Harnessing Plasmonics for Solar Cells. *Nat. Photonics* **2012**, *6*, 130−132.

(16) Atwater, H. A.; Polman, A. Plasmonics for Improved Photovoltaic Devices. *Nat. Mater.* **2010**, *9*, 205−213.

(17) Li, Q.; Wang, F.; Bai, Y.; Xu, L.; Yang, Y.; Yan, L.; Hu, S.; Zhang, B.; Dai, S.; Tan, Z. A Decahedral-Shaped Au Nanoparticles as Plasmonic Centers for High Performance Polymer Solar Cells. *Org. Electron.* **2017**, *43*, 33−40.

(18) Li, J.; Bai, Y.; Yang, B.; Zhang, J.; Chen, X.; Hayate, T.; Alsaedie, A.; Yang, Y.; Hou, J.; Tan, Z. Multifunctional Bipyramid-Au@ZnO Core-Shell Nanoparticles as a Cathode Buffer Layer for Efficient Non-Fullerene Inverted Polymer Solar Cells with Improved Near-Infrared Photo Response. *J. Mater. Chem. A* **2019**, *7*, 2667−2676.

(19) Wang, L.; Hasanzadeh Kafshgari, M.; Meunier, M. Optical Properties and Applications of Plasmonic-Metal Nanoparticles. *Adv. Funct. Mater.* **2020**, *30*, 2005400.

(20) Yao, K.; Zhong, H.; Liu, Z.; Xiong, M.; Leng, S.; Zhang, J.; Xu, Y.-x.; Wang, W.; Zhou, L.; Huang, H.; Jen, A. K. Y. Plasmonic Metal Nanoparticles with Core−Bishell Structure for High-Performance Organic and Perovskite Solar Cells. *ACS Nano* **2019**, *13*, 5397−5409.

(21) Bao, Z. Y.; Liu, S.; Hou, Y.; Shang, A.; Yan, F.; Wu, Y.; Lei, D.; Dai, J. Hollow Au Nanorattles for Boosting the Performance of Organic Photovoltaics. *J. Mater. Chem. A* **2019**, *7*, 26797−26803.

(22) Cui, X.; Chen, Y.; Zhang, M.; Harn, Y. W.; Qi, J.; Gao, L.; Wang, Z. L.; Huang, J.; Yang, Y.; Lin, Z. Tailoring Carrier Dynamics in Perovskite Solar Cells via Precise Dimension and Architecture Control and Interfacial Positioning of Plasmonic Nanoparticles. *Energy Environ. Sci.* **2020**, *13*, 1743−1752.

(23) Dang, X.; Qi, J.; Klug, M. T.; Chen, P. Y.; Yun, D. S.; Fang, N. X.; Hammond, P. T.; Belcher, A. M. Tunable Localized Surface Plasmon-Enabled Broadband Light-Harvesting Enhancement for High-Efficiency Panchromatic Dye-Sensitized Solar Cells. *Nano Lett.* **2013**, *13*, 637−642.

(24) Gonfa, B. A.; Kim, M. R.; Zheng, P.; Cushing, S.; Qiao, Q.; Wu, N.; El Khakani, M. A.; Ma, D. Investigation of the Plasmonic Effect in Air-Processed PbS/CdS Core−Shell Quantum Dot Based Solar Cells. *J. Mater. Chem. A* **2016**, *4*, 13071−13080.

(25) Chen, H.; Shao, L.; Li, Q.; Wang, J. Gold Nanorods and Their Plasmonic Properties. *Chem. Soc. Rev.* **2013**, *42*, 2679−2724.

(26) Du, Z.; Yin, F.; Han, D.; Mao, S.; Wang, J.; Aleem, A. R.; Pan, Z.; Tang, J. Plasmonic Effect with Tailored Au@TiO$_2$ Nanorods in Photoanode for Quantum Dot Sensitized Solar Cells. ACS Appl. Energy Mater. 2019, 2, 5917−5924.

(27) Kakavelakis, G.; Vangelidis, I.; Heuer-Jungemann, A.; Kanaras, A. G.; Lidorikis, E.; Stratakis, E.; Kymakis, E. Plasmonic Back-scattering Effect in High-Efficient Organic Photovoltaic Devices. Adv. Energy Mater. 2016, 6, 1501640.

(28) Beck, F. J.; Polman, A.; Catchpole, K. R. Tunable Light Trapping for Solar Cells Using Localized Surface Plasmons. J. Appl. Phys. 2009, 105, 114310.

(29) Wadams, R. C.; Yen, C.-W.; Butcher, D. P.; Koerner, H.; Durstock, M. F.; Fabris, L.; Tabor, C. E. Gold Nanorod Enhanced Organic Photovoltaics: the Importance of Morphology Effects. Org. Electron. 2014, 15, 1448−1457.

(30) Burrows, N. D.; Lin, W.; Hinman, J. G.; Dennison, J. M.; Vartanian, A. M.; Abadeer, N. S.; Grzincic, E. M.; Jacob, L. M.; Li, J.; Murphy, C. J. Surface Chemistry of Gold Nanorods. Langmuir 2016, 32, 9905−9921.

(31) Hao, H.; Wang, L.; Ma, X.; Cao, K.; Yu, H.; Wang, M.; Gu, W.; Zhu, R.; Anwar, M. S.; Chen, S.; Huang, W. Improved Efficiency of Inverted Perovskite Solar Cells Via Surface Plasmon Resonance Effect of Au@PSS Core-Shell Tetrahedra Nanoparticles. Solar RRL 2018, 2, 1800061.

(32) Liu, P.-H.; Chuang, C.-H.; Zhou, Y.-L.; Wang, S.-H.; Jeng, R.-J.; Rwei, S.-P.; Liau, W.-B.; Wang, L. Conjugated Polyelectrolytes as Promising Hole Transport Materials for Inverted Perovskite Solar Cells: Effect of Ionic Groups. J. Mater. Chem. A 2020, 8, 25173−25177.

(33) Metzman, J. S.; Khan, A. U.; Magill, B. A.; Khodaparast, G. A.; Heflin, J. R.; Liu, G. Critical Role of Polystyrene Layer on Plasmonic Silver Nanoplates in Organic Photovoltaics. ACS Appl. Energy Mater. 2019, 2, 2475−2485.

(34) Kim, H.; Nam, S.; Lee, H.; Woo, S.; Ha, C.-S.; Ree, M.; Kim, Y. Influence of Controlled Acidity of Hole-Collecting Buffer Layers on the Performance and Lifetime of Polymer:Fullerene Solar Cells. J. Phys. Chem. C 2011, 115, 13502−13510.

(35) Ni, W.; Chen, H.; Su, J.; Sun, Z.; Wang, J.; Wu, H. Effects of Dyes, Gold Nanocrystals, pH, and Metal Ions on Plasmonic and Molecular Resonance Coupling. J. Am. Chem. Soc. 2010, 132, 4806−4814.

(36) Du, X.; Heumueller, T.; Gruber, W.; Classen, A.; Unruh, T.; Li, N.; Brabec, C. J. Efficient Polymer Solar Cells Based on Non-fullerene Acceptors with Potential Device Lifetime Approaching 10 Years. Joule 2019, 3, 215−226.

(37) McKenzie, D. R.; Muller, D.; Pailthorpe, B. A. Compressive-Stress-Induced Formation of Thin-Film Tetrahedral Amorphous Carbon. Phys. Rev. Lett. 1991, 67, 773−776.

(38) Kim, J. Y.; Han, M. G.; Lien, M. B.; Magonov, S.; Zhu, Y.; George, H.; Norris, T. B.; Kotov, N. A. Dipole-Like Electrostatic Asymmetry of Gold Nanorods. Sci. Adv. 2018, 4, 1700682.

(39) Sorrentino, R.; Kozma, E.; Luzzati, S.; Po, R. Interlayers for Non-Fullerene Based Polymer Solar Cells: Distinctive Features and Challenges. Energy Environ. Sci. 2021, 14, 180−223.

(40) Xu, H.; Yuan, F.; Zhou, D.; Liao, X.; Chen, L.; Chen, Y. Hole Transport Layers for Organic Solar Cells: Recent Progress and Prospects. J. Mater. Chem. A 2020, 8, 11478−11492.

(41) Guo, S.; Cao, B.; Wang, W.; Moulin, J. F.; Müller-Buschbaum, P. Effect of Alcohol Treatment on the Performance of PTB7:PC$_{71}$BM Bulk Heterojunction Solar Cells. ACS Appl. Mater. Interfaces 2015, 7, 4641−4649.

(42) Banerjee, S.; Preeyanka, N.; Dey, H.; Seth, S.; Rahaman, A.; Sarkar, M. Highly Efficient Energy Transfer from Fluorescent Gold Nanoclusters to Organic J-Aggregates. J. Phys. Chem. C 2020, 124, 5009−5020.

(43) Chan, K.; Wright, M.; Elumalai, N.; Uddin, A.; Pillai, S. Plasmonics in Organic and Perovskite Solar Cells: Optical and Electrical Effects. Adv. Opt. Mater. 2017, 5, 1600698.

(44) Zimmermann, E.; Ehrenreich, P.; Pfadler, T.; Dorman, J. A.; Weickert, J.; Schmidt-Mende, L. Erroneous Efficiency Reports Harm Organic Solar Cell Research. Nat. Photoncis 2014, 8, 669−672.

(45) Wang, Y. W.; Wu, B.; Wu, Z. H.; Lan, Z. J.; Li, L. F.; Zhang, M. J.; Zhu, F. R. Origin of Efficient Inverted Nonfullerene Organic Solar Cells: Enhancement of Charge Extraction and Suppression of Bimolecular Recombination Enabled by Augmented Internal Electric Field. J. Phys. Chem. Lett. 2017, 8, 5264−5271.

(46) Xu, G. Y.; Bi, P. Q.; Wang, S. H.; Xue, R. M.; Zhang, J. W.; Chen, H. Y.; Chen, W. J.; Hao, X. T.; Li, Y. W.; Li, Y. F. Integrating Ultrathin Bulk-Heterojunction Organic Semiconductor Intermediary for High-Performance Low-Bandgap Perovskite Solar Cells with Low Energy Loss. Adv. Funct. Mater. 2018, 28, 1804427.

(47) Li, W.; Cai, J.; Yan, Y.; Cai, F.; Li, S.; Gurney, R. S.; Liu, D.; McGettrick, J. D.; Watson, T. M.; Li, Z.; Pearson, A. J.; Lidzey, D. G.; Hou, J.; Wang, T. Correlating Three-dimensional Morphology With Function in PBDB-T:IT-M Non-Fullerene Organic Solar Cells. Sol. RRL 2018, 2, 1800114.

(48) Liu, X.; Liu, Z.; Sun, B.; Tan, X.; Ye, H.; Tu, Y.; Shi, T.; Tang, Z.; Liao, G. 17.46% Efficient and Highly Stable Carbon-Based Planar Perovskite Solar Cells Employing Ni-Doped Rutile TiO$_2$ as Electron Transport Layer. Nano Energy 2018, 50, 201−211.

(49) Christians, J.; Fung, R. C. M.; Kamat, P. V. An Inorganic Hole Conductor for Organo-Lead Halide Perovskite Solar Cells. Improved Hole Conductivity with Copper Iodide. J. Am. Chem. Soc. 2014, 136, 758−764.

(50) Mihailetchi, V. D.; Wildeman, J.; Blom, P. W. Space-Charge Limited Photocurrent. Phys. Rev. Lett. 2005, 94, 126602.

(51) Bi, D.; Yang, L.; Boschloo, G.; Hagfeldt, A.; Johansson, E. M. Effect of Different Hole Transport Materials on Recombination in CH$_3$NH$_3$PbI$_3$ Perovskite-Sensitized Mesoscopic Solar Cells. J. Phys. Chem. Lett. 2013, 4, 1532−1536.

(52) Hwang, H.; Sin, D. H.; Park, C.; Cho, K. Ternary Organic Solar cells Based on a Wide-Bandgap Polymer with Enhanced Power Conversion Efficiencies. Sci. Rep. 2019, 9, 12081.

(53) Xu, X.; Li, Z.; Wang, Z.; Li, K.; Feng, K.; Peng, Q. 10.20% Efficiency Polymer Solar Cells via Employing Bilaterally Hole-Cascade Diazaphenanthrobisthiadiazole Polymer Donors and Electron-Cascade Indene-C70 Bisadduct Acceptor. Nano Energy 2016, 25, 170−183.

(54) Jahng, J.; Fishman, D. A.; Park, S.; Nowak, D.; Morrison, W. A.; Wickramasinghe, H. K.; Potma, E. O. Linear and Nonlinear Optical Spectroscopy at the Nanoscale With Photoinduced Force Micros-copy. Acc. Chem. Res. 2015, 48, 2671−2679.

(55) Tumkur, T. U.; Yang, X.; Cerjan, B.; Halas, N. J.; Nordlander, P.; Thomann, I. Photoinduced Force Mapping of Plasmonic Nanostructures. Nano Lett. 2016, 16, 7942−7949.

(56) Nowak, D.; Morrison, W.; Wickramasinghe, H. K.; Jahng, J.; Potma, E.; Wan, L.; Ruiz, R.; Albrecht, T. R.; Schmidt, K.; Frommer, J. Nanoscale Chemical Imaging by Photoinduced Force Microscopy. Sci. Adv. 2016, 2, 1501571.

(57) Baek, S.-W.; Park, G.; Noh, J.; Cho, C.; Lee, C.-H.; Seo, M.-K.; Song, H.; Lee, J.-Y. Au@Ag Core-Shell Nanocubes for Efficient Plasmonic Light Scattering Effect in Low Bandgap Organic Solar Cells. ACS Nano 2014, 8, 3302−3312.

(58) Hoang, M. H.; Park, G. E.; Choi, S.; Park, C. G.; Park, S. H.; Nguyen, T. V.; Kim, S.; Kwak, K.; Cho, M. J.; Choi, D. H. High-Efficiency Non-Fullerene Polymer Solar Cell Fabricated by A Simple Process Using New Conjugated Terpolymers. J. Mater. Chem. C 2019, 7, 111−118.

(59) Kumar, K.; Das, A.; Kumawat, U. K.; Dhawan, A. Tandem Organic Solar Cells Containing Plasmonic Nanospheres and Nano-stars for Enhancement in Short Circuit Current Density. Opt Express 2019, 27, 31599−31620.

(60) Huang, J.; Zhao, D.; Dou, Z.; Fan, Q.; Li, N.; Peng, S.; Liu, H.; Jiang, Y.; Yu, L.; Li, C. Z. Highly Efficient ITO-Free Organic Solar Cells with A Column-Patterned Microcavity. Energy Environ. Sci. 2021, 14, 3010−3018.

115

(61) Kerremans, R.; Kaiser, C.; Li, W.; Zarrabi, N.; Meredith, P.; Armin, A. The Optical Constants of Solution-Processed Semiconductors-New Challenges with Perovskites and Non-Fullerene Acceptors. *Adv. Opt. Mater.* **2020**, *8*, 2000319.

▥ Recommended by ACS

Supporting Information

Enhancing Efficiency of Non-Fullerene Organic Solar Cells via Using Polyelectrolyte-Coated Plasmonic Gold Nanorods as Rear Interfacial Modifiers

Zhonglin Du,[†,‡,#] Ting Yu,[†,#] Wanting He,[†] Aycan Yurtsever,[†] Ricardo Izquierdo,[§] Maziar Jafari,[‖] Mohamed Siaj,[‖] and Dongling Ma*,[†]

[†]*Institut National de la Recherche Scientifique (INRS), Centre Énergie Materiaux et Télécommunications, 1650 Boulevard Lionel-Boulet, Varennes, Québec, J3X 1S2, Canada*

[‡]*College of Materials Science and Engineering, the National Base of International Science and Technology Cooperation on Hybrid Materials, Qingdao University, 308 Ningxia Road, Qingdao 266071, PR China*

[§]*Département de Génie Électrique, École de Technologie Supérieure, Montréal, Québec, H3C 1K3, Canada*

[‖]*Department of Chemistry, Université du Québec à Montréal, NanoQAM/QCAM, Montréal, Québec, H3C 3P8, Canada*

To whom correspondence should be addressed. E-mail: ma@emt.inrs.ca (D.M.)

Synthesis of CTAB-stabilized gold nanorods (GNRs).

The CTAB-stabilized GNRs were prepared through a seed-mediated growth method in aqueous solution. Briefly, the fresh seed solution was prepared by the addition of ice-cold $NaBH_4$ solution (0.6 mL, 0.01 M) into a mixture containing $HAuCl_4$ (0.25 mL, 0.01 M) and CTAB (9.75 mL, 0.1 M), and kept at room temperature for 2 h before use. The growth solution was prepared by the sequential addition of $HAuCl_4$ (2 mL, 0.01 M), $AgNO_3$ (0.4 mL, 0.01 M), HCl (0.8 mL, 1.0 M) and ascorbic acid (0.32 mL, 0.1 M) into CTAB (40 mL, 0.1 M). The growth solution was stirred for 30 s and then, the seed solution (0.1 mL) was rapidly added for growing the GNRs. The reaction solution was well mixed by upside-down inversions for several times, then kept at 30 °C overnight. After centrifugation, the obtained pellet was redispersed in deionized water.
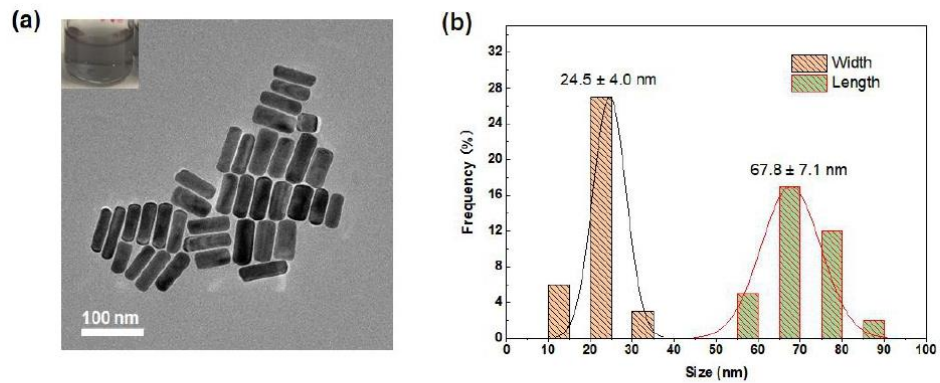
Figure S1 (a) TEM of as synthesized GNRs capped by CTAB (inset: the photo of the GNRs solution); and (b) size distribution of as synthesized GNRs.
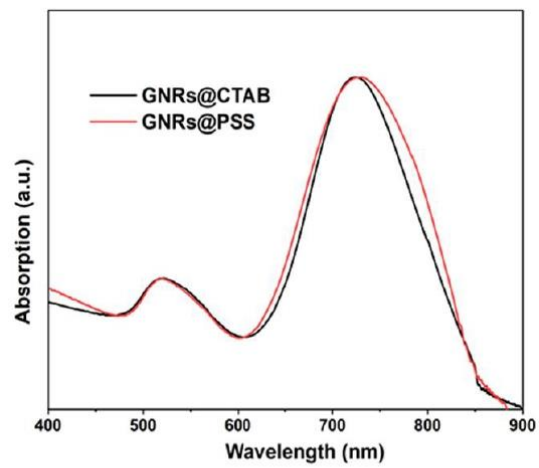
Figure S2 UV-vis absorption spectra of the GNRs before and after the PSS coating treatment.
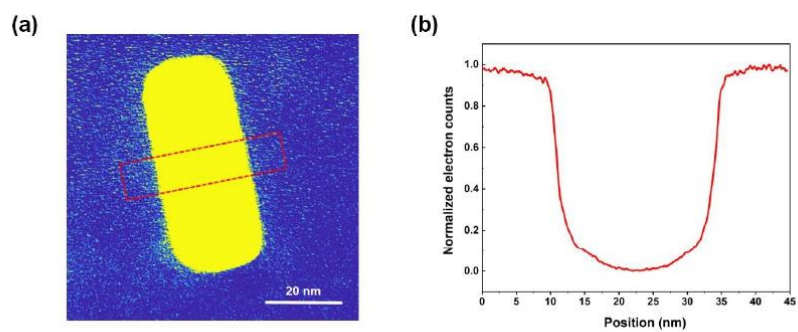
Figure S3 (a) image of Zero-loss EF-TEM image of the single GNR, with an energy slit set at 0±3 eV; (b) normalized electron count profile along the red frame in (a).
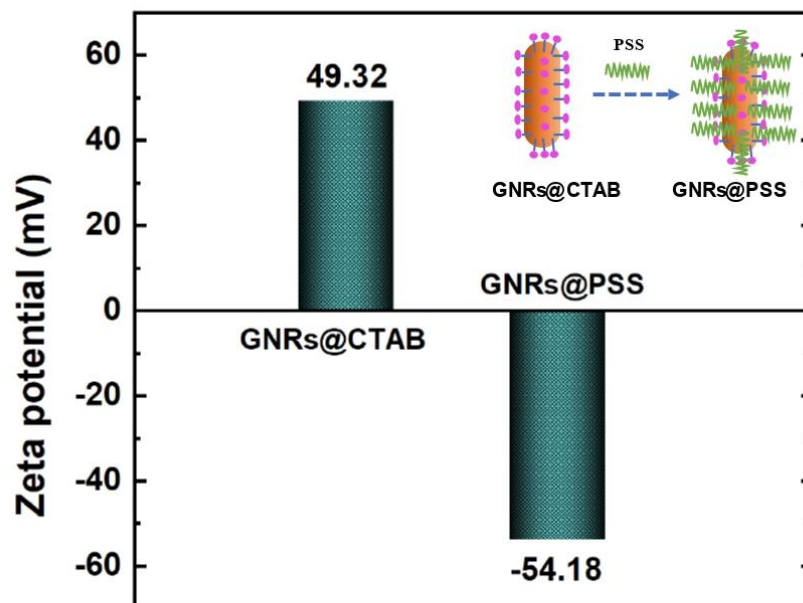
Figure S4 Zeta potential of the GNRs before and after the PSS coating treatment. The dispersion pH was 7.0.
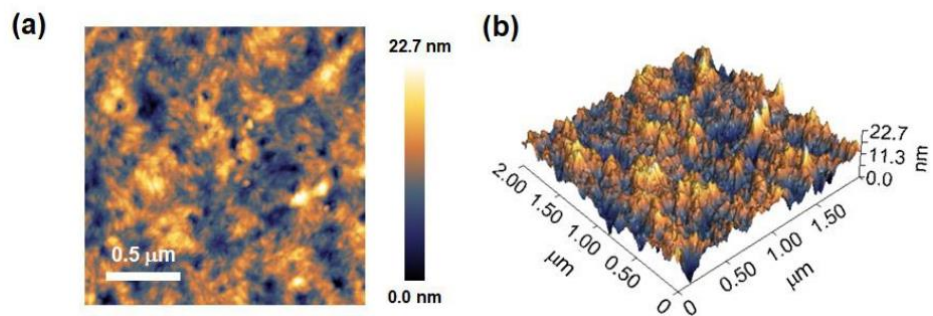
Figure S5 (a) 2D-AFM and (b) 3D-AFM surface topography of the pristine photoactive layer film without GNRs@PSS.
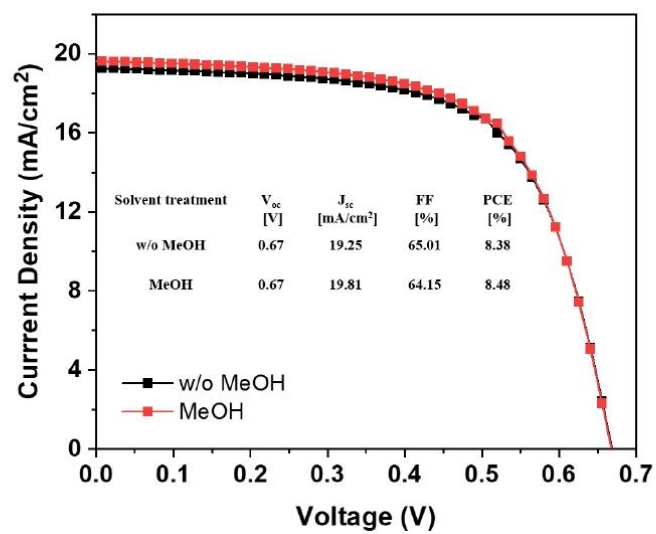
Figure S6 *J-V* characteristics of the devices with and without methanol treatment.

Table S1 Effects of the GNRs@PSS on the photocurrent density (J_{ph}), saturation photocurrent density (J_{sat}) and the ratio (J_{ph}/J_{sat}) values of the OSCs.

devices	$J_{ph}{}^{a}$	$J_{ph}{}^{b}$	J_{sat}	$J_{ph}{}^{a}/J_{sat}$ (%)	$J_{ph}{}^{b}/J_{sat}$ (%)
with GNRs@PSS	21.29	19.83	22.80	93.4	87.0
w/o GNRs@PSS	19.13	17.75	21.33	89.7	83.2

[a] short-circuit condition, [b] maximal power output condition.
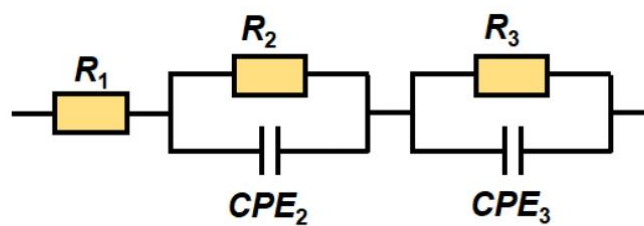
Figure S7 Simulation circuit used for fitting EIS. R_1 accounts for series resistance, R_2 and *CPE*$_2$ are associated with the contact between the photoactive layer and the MoO$_3$ layer, while R_3 and *CPE*$_3$ are related with the organic photoactive layer.

Table S2 Summary of the fitting parameters of the Nyquist plots of devices with and without the GNRs@PSS.

Devices	R_1 (Ω cm^2)	CPE_2 (F/cm^2)	R_2 (Ω cm^2)	CPE_3 (F/cm^2)	R_3 (Ω cm^2)
w/o GNRs@PSS	3.56	4.4×10^{-7}	120.7	1.2×10^{-7}	172.9
with GNRs@PSS	4.17	5.4×10^{-7}	96.44	1.2×10^{-7}	171.1

Table S3 The carrier mobilities of the active layers with and without the GNRs@PSS.

	Hole mobility μ_h (cm^2 V^{-1} s^{-1}) [a]	Electron mobility μ_e (cm^2 V^{-1} s^{-1}) [a]	μ_h/μ_e
with GNRs@PSS	$(1.96\pm0.17)\times10^{-4}$	$(9.39\pm0.99)\times10^{-5}$	2.09
w/o GNRs@PSS	$(1.35\pm0.09)\times10^{-4}$	$(3.20\pm0.87)\times10^{-5}$	4.22

[a]Average values (in parentheses) were obtained from 5 devices.
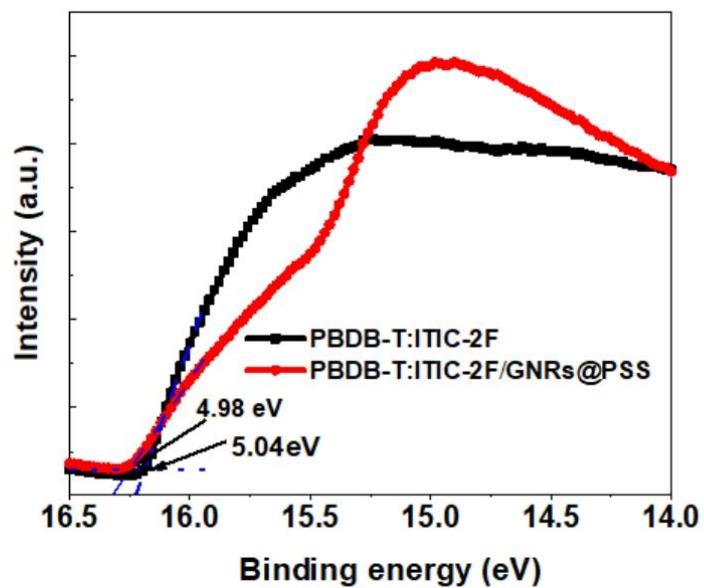
Figure S8 UPS spectra of the photoactive layer with and without GNRs@PSS. The spectra were acquired by UPS (He I, 21.22 eV).

S13

129
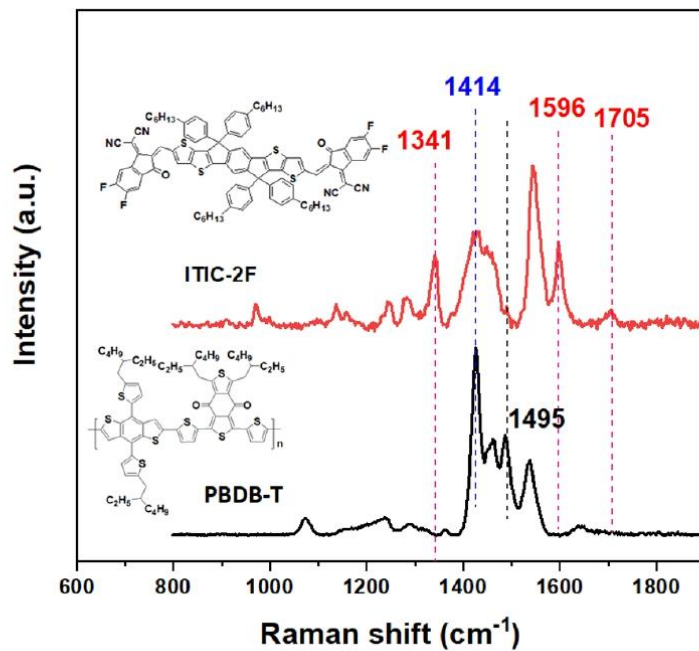
Figure S9 Raman spectra of the PBDB-T polymer and ITIC-2F small molecule between 800 cm^{-1} and 1900 cm^{-1}, respectively. Raman peaks at 1341 cm^{-1}, 1414 cm^{-1}, 1495 cm^{-1}, 1596 cm^{-1} and 1705 cm^{-1} are assigned to C - C and C - H, to C-N, C=S and H-H, to the C-H central ring vibration, to the C=C and central benzene vibration, and to the C=N linkage vibration.[1]
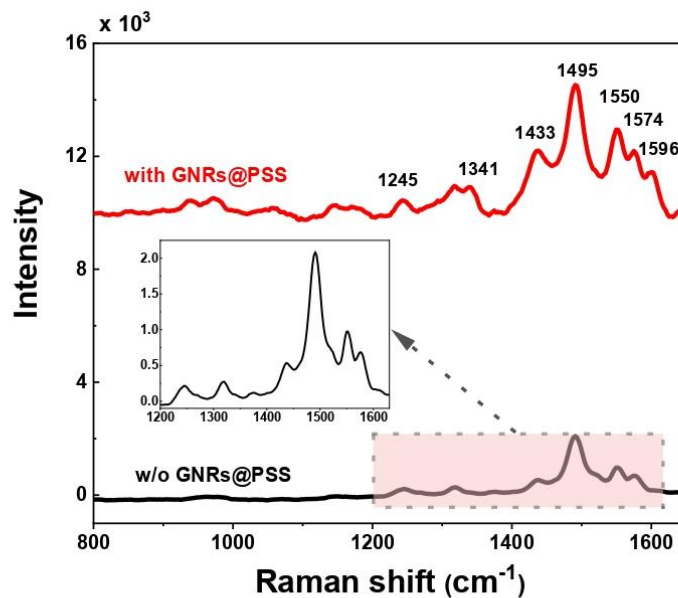
Figure S10 Raman spectra of PBDB-T:ITIC-2F blend films with and without the GNRs@PSS between 800 cm^{-1} and 1650 cm^{-1}. The samples were excited by a 532 nm laser (100 mW/cm^2). Raman peaks at 1341 cm^{-1}, 1433 cm^{-1}, 1495 cm^{-1}, 1550 cm^{-1} and 1596 cm^{-1} are assigned to C - C and C - H, to C-N, C=S and H-H, to the C-H central ring vibration, and to the C=C and central benzene vibration. Inset is the zoomed-in view of the PBDB-T:ITIC-2F blend films without GNRs@PSS between 1200 cm^{-1} and 1630 cm^{-1}.
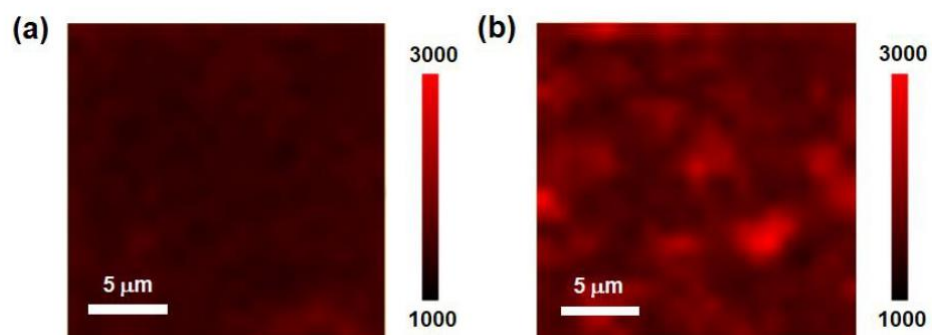
Figure S11 The Raman mapping images of the films without (a) and with (b) GNRs@PSS (20 μm × 20 μm). The data were integrated from 1300-1600 cm^{-1}; The samples were excited by a 532 nm laser (10 mW/cm^2).
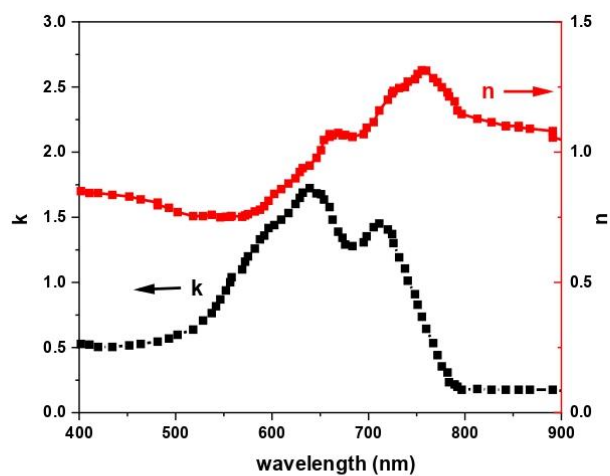
Figure S12 The refractive index n and k of photoactive layer materials (PBDB-T:ITIC-2F) used in this work.
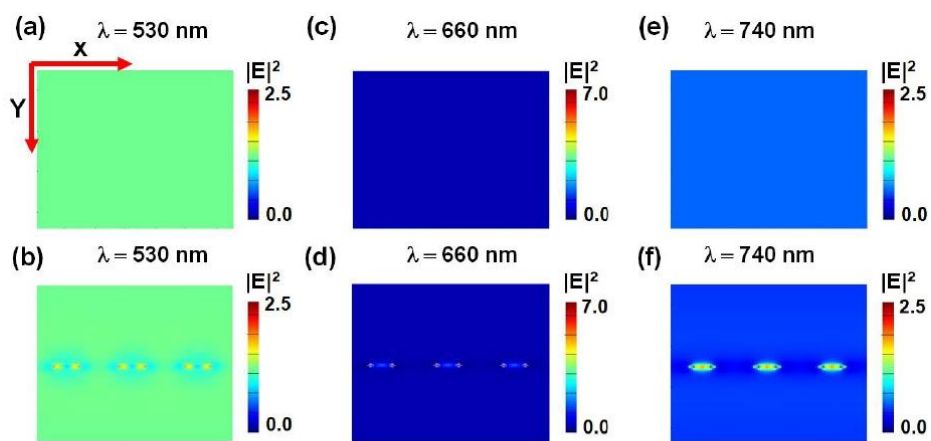
Figure S13 (a-f) Normalized spatial distribution of electric field intensity at three different wavelengths (530 nm, 660 nm, and 740 nm) with and without GNRs@PSS incorporation by FDTD simulations (XY plane, Z=0).
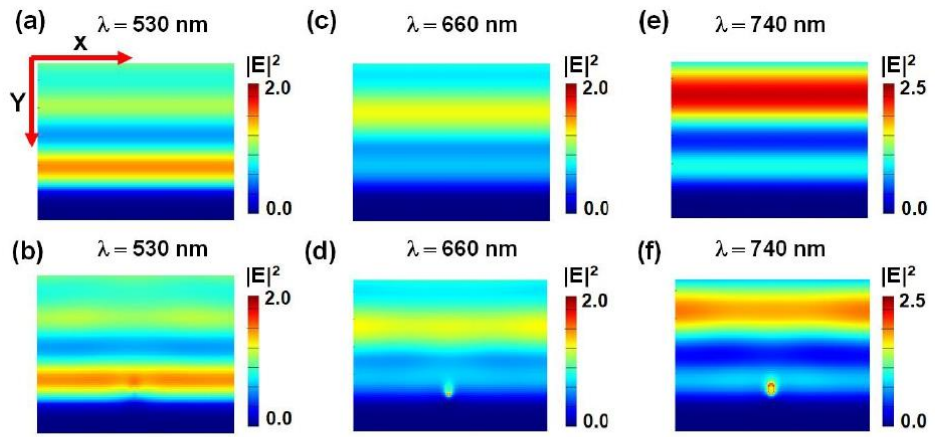
Figure S14 (a-f) Normalized spatial distribution of electric field intensity at three different wavelengths (530 nm, 660 nm, and 740 nm) with and without GNRs@PSS incorporation by FDTD simulations (YZ plane, X=0).
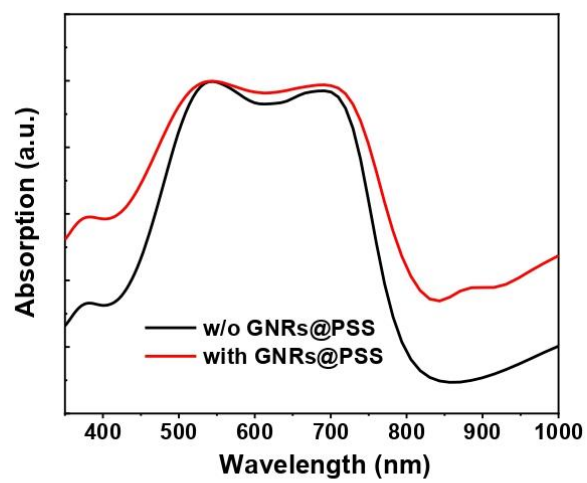
Figure S15 Calculated absorption spectra of the devices with and without GNRs@PSS.
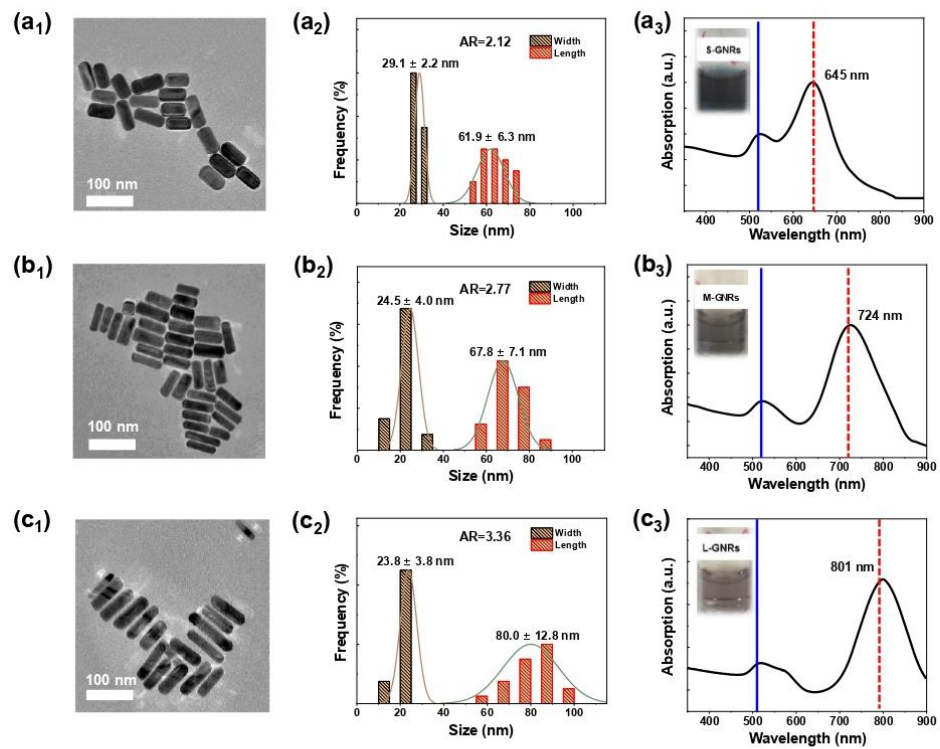
Figure S16 TEM images (a₁, b₁ and c₁), size distributions (a₂, b₂ and c₂), and extinction spectra (a₃, b₃ and c₃) of the three different sizes of GNRs. The transverse SPR was at 518 nm (blue solid line) and the longitudinal SPR (red dashed line) was at 645 nm, 724 nm and 801 nm for S-, M- and L-GNRs, respectively.
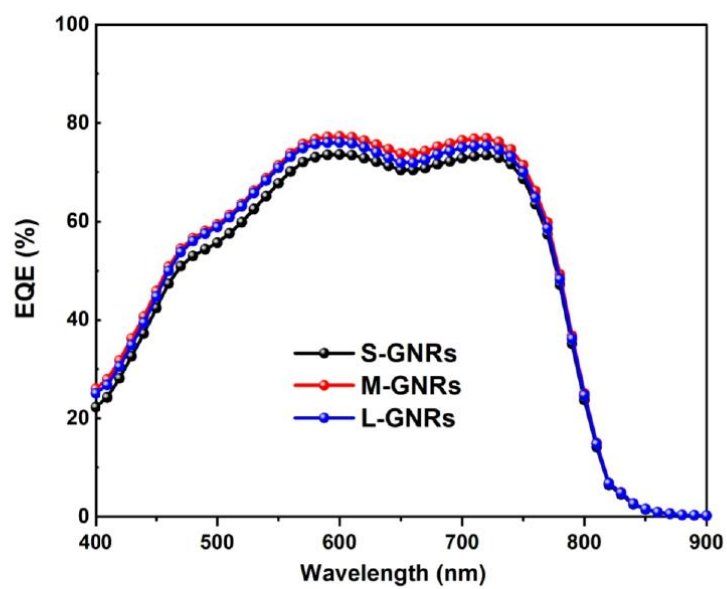
Figure S17 EQE spectra of the devices containing GNRs of different sizes.
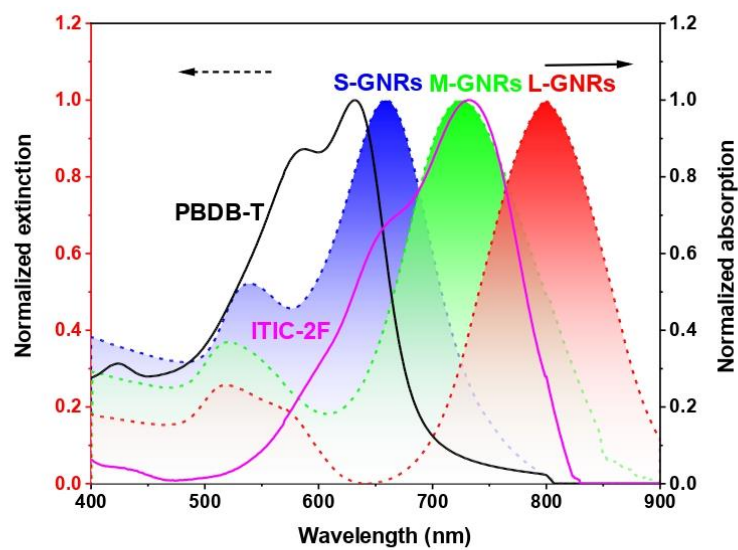
Figure S18 Normalized extinction spectra of S-, M-, and L-GNRs (dashed lines), and UV-*vis* absorption spectra of PBDB-T and ITIC-2F films spin-coated on ITO glass (solid lines).
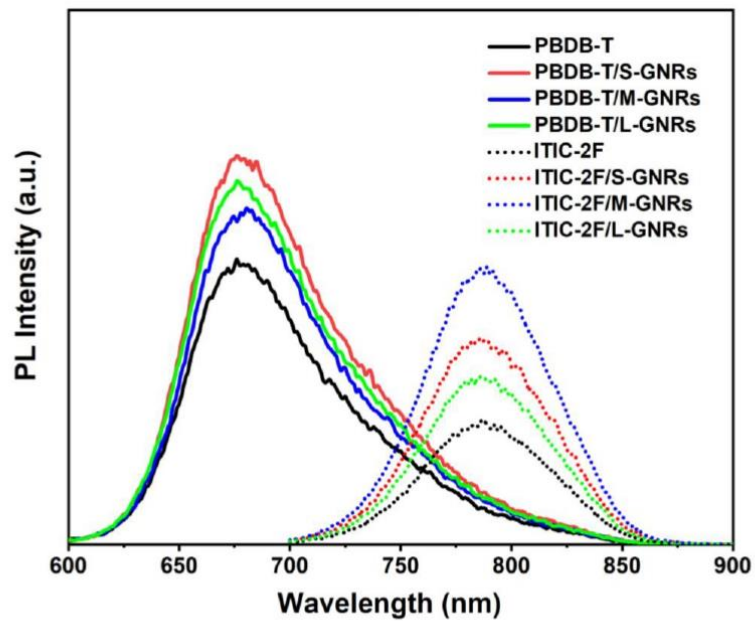
Figure S19 PL spectra of PBDB-T and ITIC-2F films with the GNRs@PSS of three different sizes spin-coated on the surface.

Table S4 Effects of size of GNRs on the photovoltaic performance parameters (open circuit voltage (V_{oc}), short circuit current density (J_{sc}), fill factor (FF), and power conversion efficiency (PCE) extracted from device *J-V* scans under standard conditions (simulated AM 1.5 G 100 mW cm^{-2}).

Size	J_{sc} (mA·cm^{-2})[a]	V_{oc} (V)[a]	FF (%)[a]	PCE (%)[a]
S-GNRs	20.86 (20.87±0.29)	0.694 (0.697±0.01)	66.75 (65.65±0.78)	9.66 (9.55±0.14)
M-GNRs	21.33 (21.37±0.31)	0.703 (0.696±0.006)	67.38 (67.32±0.69)	10.11 (10.02±0.18)
L-GNRs	21.26 (21.18±0.29)	0.698 (0.693±0.012)	65.42 (64.84±0.94)	9.71 (9.62±0.16)

[a] Average values (in parentheses) were obtained from 10 devices.
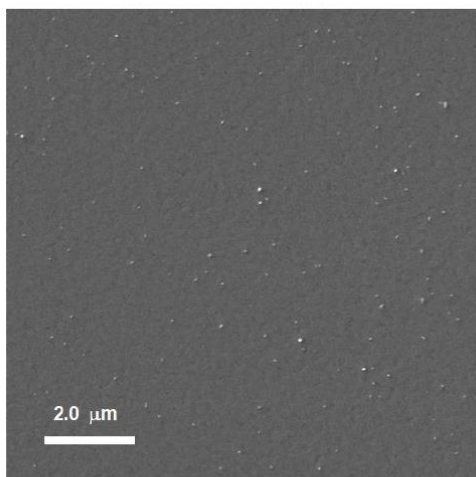
Figure S20 SEM image of the GNRs@PSS spin-coated onto the surface of ZnO layer.
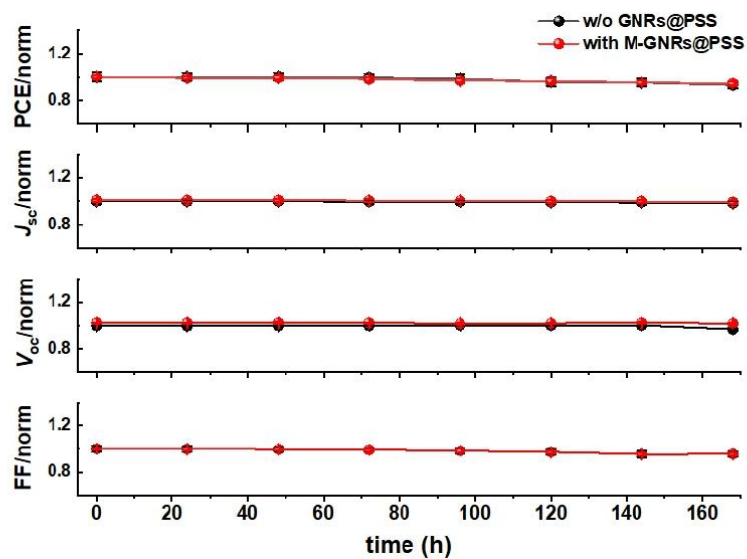
Figure S21 Normalized photovoltaic parameters (PCE, J_{sc}, V_{oc}, and FF) of the devices incorporated with and without M-GNRs@PSS (devices stored upon ambient air exposure, and dark condition).
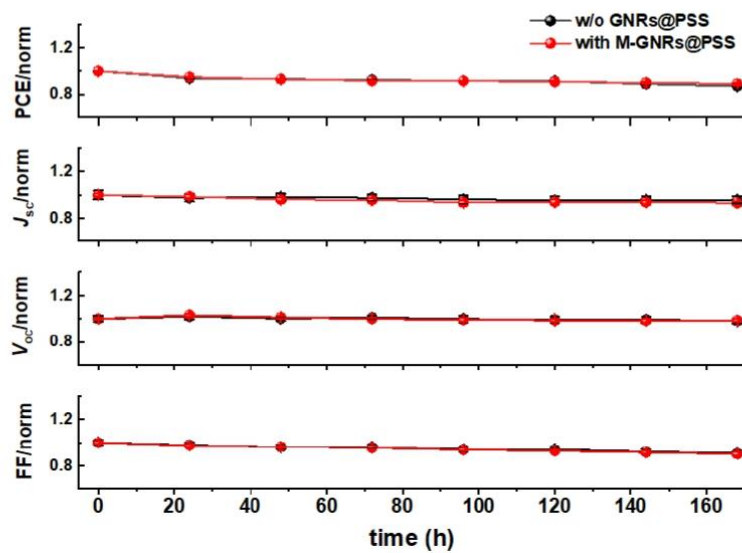
Figure S22 Normalized photovoltaic parameters (PCE, J_{sc}, V_{oc}, and FF) of the devices with and without M-GNRs@PSS annealed continuously on a hot plate at 80 °C in the dark.
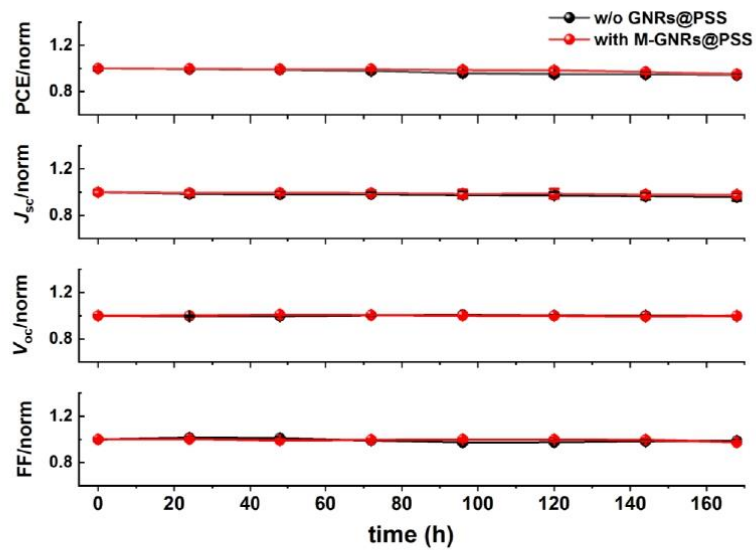
Figure S23 Normalized photovoltaic parameters (PCE, J_{sc}, V_{oc}, and FF) of devices with and without M-GNRs@PSS under continuous illumination in the glovebox.
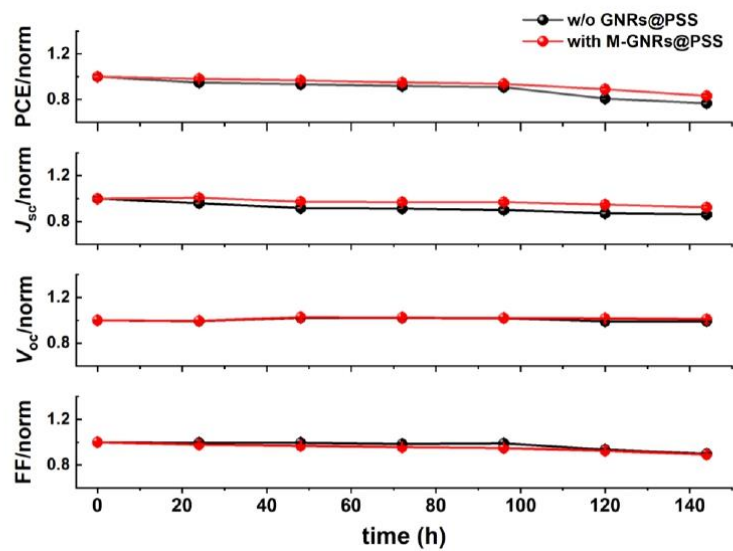
Figure S24 Normalized photovoltaic parameters (PCE, J_{sc}, V_{oc}, and FF) of devices with and without M-GNRs@PSS under humidity of 70% in air.

Table S5 Effects of surface coverage of M-GNRs@PSS on the photovoltaic performance parameters extracted from device *J-V* scans under standard conditions (simulated AM 1.5 G 100 mW cm^{-2}).

Spin Coating Rate	J_{sc} (mA·cm^{-2})[a]	V_{oc} (V)[a]	FF (%)[a]	PCE (%)[a]
2000 rpm/s	20.04 (20.34±0.40)	0.674 (0.681±0.007)	60.95 (58.78±0.18)	8.23 (8.15±0.36)
3000 rpm/s	20.71 (21.11±0.45)	0.684 (0.689±0.005)	64.63 (0.637±0.10)	9.60 (9.26±0.19)
4000 rpm/s	21.33 (21.37±0.31)	0.703 (0.696±0.006)	67.38 (67.32±0.69)	10.11 (10.02±0.18)
5000 rpm/s	21.45 (21.39±0.19)	0.702 (0.700±0.004)	66.04 (65.20±0.59)	9.94 (9.76±0.16)

[a] Average values (in parenthese) were obtained from 10 devices.

Table S6 Effect of the incorporation location of the M-GNRs@PSS on the photovoltaic performance parameters extracted under standard conditions (simulated AM 1.5 G 100 mW cm^{-2}).

Configuration	J_{sc} (mA·cm^{-2})[a]	V_{oc} (V)[a]	FF (%)[a]	PCE (%)[a]
ITO/ZnO/GNRs@PSS/ PBDB-T:ITIC-2F/MoO₃/Ag	19.06 (18.51±0.62)	0.685 (0.682±0.006)	59.95 (58.87± 0.38)	7.83 (7.43 ± 0.23)
ITO/ZnO/PBDB-T:ITIC-2F/ GNRs@PSS/MoO₃/Ag	21.33 (21.37±0.31)	0.703 (0.696±0.006)	67.38 (67.32±0.69)	10.11 (10.02±0.18)

[a] Average values (in parentheses) were obtained from 10 devices.

Reference

1. Hoang, M. H.; Park, G. E.; Choi, S.; Park, C. G.; Park, S. H.; Nguyen, T. V.; Kim, S.; Kwak, K.; Cho, M. J.; Choi, D. H. High-Efficiency Non-Fullerene Polymer Solar Cell Fabricated by A Simple Process Using New Conjugated Terpolymers. *J. Mater. Chem. C*, **2019**, *7*, 111-118.

CHAPTER 4   CONCLUSIONS AND PERSPECTIVES

4.1 Conclusions

To date, significant progress has been made in the field of OSCs in terms of photovoltaic performance, but further enhancement of device efficiency remains a major research topic. The ternary blend strategy, especially the introduction of non-fullerene guest acceptors, is an effective way to enhance sunlight absorption, match charge cascades and optimize morphology, so it needs to be carefully studied. In particular, in-depth understanding the complex morphology of ternary blend films through advanced characterization techniques can provide guidance for achieving the optimal morphology, which can help exciton dissociation and charge transport. Additionally, the characterization of the local charge carrier dynamic can aid in morphological modulation, thus leading to high-efficient device performance. Lastly, to overcome the issue of sunlight absorption limited by the thin photoactive layer in OSCs, integrating a sunlight concentrator on the photoactive layer can effectively enhance photon harvesting. Meanwhile, this sunlight concentrator can act as an interfacial modifier to optimize surface morphology and improve interfacial contact, thus improving charge transport and reducing charge recombination on the surface of the photoactive layer. Accordingly, this thesis mainly focuses on ternary blend strategy, morphology optimization, and interfacial modification to increase device performance, and the results of this thesis are divided into three parts.

In the first part, the highly air-stable PDI-DPP-PDI non-fullerene guest acceptor was incorporated into PTB7: $PC_{61}BM$-based OSCs, which could extend the spectral absorption, form charge cascaded structure and control the nanoscale morphology. Combined advanced PiFM and EF-TEM characterization, the 3D morphology of the blend film could be visualized in the configuration of real devices. It was found that the introduction of an appropriate content of the PDI-DPP-PDI was able to suppress the aggregation of host donor and acceptor materials as well as form a higher level of the molecularly mixed phase. As a result, the ternary blend film with an optimized morphology had balanced charge mobility and reduced charge recombination, resulting in higher J_{sc} and FF. Meanwhile, the incorporation of the highly stable PDI-DPP-PDI guest acceptor and optimized morphology facilitated the achievement of better air stability, humidity resistance and photostability of ternary OSCs.

In the second part, the PBDB-T: ITIC-4F-based ternary OSCs with a highly twisted PDI-EH non-fullerene guest acceptor were applied in versatile photovoltaic applications under 1-sun and indoor LED illuminations, and achieved high device efficiencies. The host donor and acceptor materials showed low miscibility, which led to undesirable exciton dissociation and charge transport. Adjusting the content of the PDI-EH guest acceptor could effectively improve the miscibility, since PDI-EH had good compatibility with the host donor and acceptor, as supported by Flory-Huggins interaction parameters and DSC measurements. It was found that moderate miscibility of the donor and acceptors promoted the formation of an appropriately mixed phase with local short-range ordered molecular packing, resulting in effective charge carrier dynamics. In addition, TP-AFM nanoscale mappings demonstrated reduced charge transport lifetime, increased charge recombination lifetime and extended charge diffusion length for the ternary blend film with moderate miscibility, suggesting a promising approach to understanding the relationship between the optimized morphology and the resulting local charge carrier dynamic. Finally, the synergistic effects of ternary OSCs with enhanced photon absorption, well-matched energy level alignment and optimized morphology are beneficial for the improvement of photovoltaic performance.

In the third part, the polyelectrolyte PSS-coated plasmonic GNRs nanoparticles were designed and synthesized by Dr. Zhonglin Du, to be integrated on the surface of the photoactive layer as rear interfacial modifiers in non-fullerene OSCs, which could promote the enhancement of photovoltaic performance. PiFM measurements were performed to visualize the near-field SPR effect of plasmonic GNRs on the photoactive layer under the tunable laser illumination. Moreover, Raman measurements and 3D finite-difference time-domain (FDTD) calculation revealed the field enhancement due to the SPR effect and back scattering effect of plasmonic GNRs, resulting in increased sunlight absorption and exciton generation. In addition, EF-TEM measurements were conducted to probe the thickness of an ultrathin PSS organic shell, which could improve the interface contact without affecting the plasmonic effects of GNRs. Therefore, the integration of GNRs@PSS on the photoactive layer could not only promote exciton generation and dissociation, but also increase charge transport and reduce charge recombination between the photoactive layer and HTL, leading to an enhancement of nearly 20% in GNRs@PSS integrated devices relative to control devices.

4.2 Perspectives

Although many strategies have been adopted to improve device efficiency, such as high-efficient donor and acceptor materials design in ternary OSCs, morphology control, and interface engineering, future research still faces significant challenges for the practical application of OSC technologies. Therefore, some perspectives are proposed for advancing the future development of organic photovoltaics.

4.2.1 The visualization of complex morphology by advanced characterization techniques

As we introduced in part I, advanced characterization techniques are essential to visualize the 3D morphology of real devices, laying the foundation of nanoscale morphology optimization. Firstly, EF-TEM is an advanced electron imaging technique that uses inelastically scattered electrons to obtain enhanced contrast images and resolve the distribution of components in the photoactive layer by adjusting the central energy of the filter and energy slit. Compared to the traditional TEM, EF-TEM is able to generate distinct-contrast images of the cross-section of the real device. In addition, the application of PiFM coupling the AFM with a wavelength-tunable laser enables the chemical imaging of three components in the ternary blend film at a high spatial resolution (~ 10 nm). Combined with algorithm-driven analysis in PiFM images, the donor- and acceptor-rich domain sizes in the blend film could be calculated and their compatibility was quantitatively assessed. Therefore, advanced characterization techniques combined with algorithm-driven data analysis can qualitatively and quantitatively 'view' surface and cross-sectional morphology, thus providing a deeper understanding of morphology modulation in OSCs.

4.2.2 Creative design of advanced functional materials

In the third part, plasmonic metallic nanoparticles as sunlight concentrators were integrated in non-fullerene OSCs, which provide an attractive way to enhance sunlight absorption without increasing the thickness of the photoactive layer. Additionally, the introduction of the organic shell on metallic nanoparticles can reduce charge recombination on the surface of metallic nanoparticles and increase the compatibility with the organic photoactive layer, leading to better interfacial contact for effective charge transport. Therefore, the creative design of advanced functional nanomaterials can further contribute the photovoltaic performance. For example, like the design of GNRs@PSS, other plasmonic nanomaterials can be rationally designed to improve light

absorption in OSCs due to their SPR effect by tuning their nanostructure size, shape, metal types and surrounding dielectric environments.[168] In addition, Type-II heterojunction nanomaterials have provoked a surge of research in photovoltaics because of the efficient spatial separation of electrons and holes at the junction interface.[169] The integration of rationally designed Type-II heterojunction nanomaterials into OSCs can broaden the spectral absorption of the photoactive layer and promote spatial charge separation, enabling the construction of high-efficient OSCs.

4.2.3 The applications of organic photovoltaics

Recently, researchers made numerous efforts to improve device stability and extend device versatile applications. In the first part, we introduced the PDI-DPP-PDI guest acceptor into OSCs to control morphology and suppress the aggregation of polymer donor and fullerene acceptor. PDI-DPP-PDI acts as structural and morphological 'stabilizer' to help achieve stable photovoltaic devices under ambient atmosphere, high humidity, and light illumination. In the second part, the PDI-EH molecule was synthesized and introduced into non-fullerene OSCs to modulate the miscibility of materials in the photoactive layer to form an optimal morphology. Therefore, the optimized morphology could reduce the trap-assisted charge recombination, leading to achieving high-efficient indoor OSCs under LED illumination. Accordingly, selecting an appropriate guest component for morphology optimization in ternary OSCs is a promising approach to improve the OSC applications, facilitating the future development of OSC technologies.

REFERENCES

1. Weinberg, C. J.; Williams, R. H., Energy from the sun. *Sci. Am.* **1990,** *263* (3), 146-155.

2. Yoshikawa, K.; Kawasaki, H.; Yoshida, W.; Irie, T.; Konishi, K.; Nakano, K.; Uto, T.; Adachi, D.; Kanematsu, M.;Uzu, H., Silicon heterojunction solar cell with interdigitated back contacts for a photoconversion efficiency over 26%. *Nat. energy* **2017,** *2* (5), 1-8.

3. Bhattacharya, S.; John, S., Beyond 30% conversion efficiency in silicon solar cells: a numerical demonstration. *Sci. Rep.* **2019,** *9* (1), 1-15.

4. Wilson, G. M.; Al-Jassim, M.; Metzger, W. K.; Glunz, S. W.; Verlinden, P.; Xiong, G.; Mansfield, L. M.; Stanbery, B. J.; Zhu, K.; Yan, Y., The 2020 photovoltaic technologies roadmap. *J Phys. D: Appl. Phys.* **2020,** *53* (49), 493001.

5. Conibeer, G., Third-generation photovoltaics. *Mater. Today* **2007,** *10* (11), 42-50.

6. Hu, Z.; Wang, J.; Ma, X.; Gao, J.; Xu, C.; Yang, K.; Wang, Z.; Zhang, J.; Zhang, F., A critical review on semitransparent organic solar cells. *Nano Energy* **2020,** *78*, 105376.

7. Lin, Y.; Firdaus, Y.; Isikgor, F. H.; Nugraha, M. I.; Yengel, E.; Harrison, G. T.; Hallani, R.; El-Labban, A.; Faber, H.; Ma, C., Self-assembled monolayer enables hole transport layer-free organic solar cells with 18% efficiency and improved operational stability. *ACS Energy Lett.* **2020,** *5* (9), 2935-2944.

8. Lin, Y.; Nugraha, M. I.; Firdaus, Y.; Scaccabarozzi, A. D.; Aniés, F.; Emwas, A.-H.; Yengel, E.; Zheng, X.; Liu, J.; Wahyudi, W., A simple n-dopant derived from diquat boosts the efficiency of organic solar cells to 18.3%. *ACS Energy Lett.* **2020,** *5* (12), 3663-3671.

9. Zhu, L.; Zhang, M.; Xu, J.; Li, C.; Yan, J.; Zhou, G.; Zhong, W.; Hao, T.; Song, J.; Xue, X., Single-junction organic solar cells with over 19% efficiency enabled by a refined double-fibril network morphology. *Nat. Mater.* **2022,** *21* (6), 656-663.

10. Cui, Y.; Xu, Y.; Yao, H.; Bi, P.; Hong, L.; Zhang, J.; Zu, Y.; Zhang, T.; Qin, J.; Ren, J., Single-junction organic photovoltaic cell with 19% efficiency. *Adv. Mater.***2021,** *33* (41), 2102420.

11. Li, L.; Yang, M.; Zhang, S.; Liu, P.; Li, G.; Wen, W.; Zhang, H.; Zhao, H., The fabrication of CNTs/TiO2 photoanodes for sensitive determination of organic compounds. *Nanotechnology* **2010,** *21* (48), 485503.

12. Weinberger, B.; Akhtar, M.; Gau, S., Polyacetylene photovoltaic devices. *Synth. Met.* **1982,** *4* (3), 187-197.

13. Tang, C. W., Two-layer organic photovoltaic cell. *Appl. Phys. Lett.***1986,** *48* (2), 183-185.

14. Yu, G.; Gao, J.; Hummelen, J. C.; Wudl, F.; Heeger, A. J., Polymer photovoltaic cells: enhanced efficiencies via a network of internal donor-acceptor heterojunctions. *Science* **1995,** *270* (5243), 1789-1791.

15. Rafique, S.; Abdullah, S. M.; Sulaiman, K.; Iwamoto, M., Fundamentals of bulk heterojunction organic solar cells: An overview of stability/degradation issues and strategies for improvement. *Renewable Sustainable Energy Rev.* **2018,** *84*, 43-53.

16. Ke, J.-C.; Wang, Y.-H.; Chen, K.-L.; Huang, C.-J., Effect of open-circuit voltage in organic solar cells based on various electron donor materials by inserting molybdenum trioxide anode buffer layer. *Sol. Energy Mater. Sol. Cells* **2015,** *133*, 248-254.

17. Zhao, F.; Wang, C.; Zhan, X., Morphology control in organic solar cells. *Adv. Energy Mater.* **2018,** *8* (28), 1703147.

18. Blom, P. W.; Mihailetchi, V. D.; Koster, L. J. A.; Markov, D. E., Device physics of polymer: fullerene bulk heterojunction solar cells. *Adv. Mater.* **2007,** *19* (12), 1551-1566.

19. Kroon, R.; Lenes, M.; Hummelen, J. C.; Blom, P. W.; De Boer, B., Small bandgap polymers for organic solar cells (polymer material development in the last 5 years). *Polym. Rev.* **2008,** *48* (3), 531-582.

20. Sariciftci, N. S.; Smilowitz, L.; Heeger, A. J.; Wudl, F., Photoinduced electron transfer from a conducting polymer to buckminsterfullerene. *Science* **1992,** *258* (5087), 1474-1476.

21. Kim, H. U.; Kim, J.-H.; Kang, H.; Grimsdale, A. C.; Kim, B. J.; Yoon, S. C.; Hwang, D.-H., Naphthalene-, anthracene-, and pyrene-substituted fullerene derivatives as electron acceptors in polymer-based solar cells. *ACS Appl. Mater. Interfaces* **2014,** *6* (23), 20776-20785.

22. Moriwaki, K.; Matsumoto, F.; Takao, Y.; Shimizu, D.; Ohno, T., Synthesis and properties of novel methanofullerenes having ethylthienyl and/or n-pentyl group for photovoltaic cells. *Tetrahedron* **2010,** *66* (36), 7316-7321.

23. Choi, J. H.; Son, K.-I.; Kim, T.; Kim, K.; Ohkubo, K.; Fukuzumi, S., Thienyl-substituted methanofullerene derivatives for organic photovoltaic cells. *J. Mater. Chem.* **2010,** *20* (3), 475-482.

24. Zhao, G.; He, Y.; Xu, Z.; Hou, J.; Zhang, M.; Min, J.; Chen, H. Y.; Ye, M.; Hong, Z.; Yang, Y., Effect of carbon chain length in the substituent of PCBM-like molecules on their photovoltaic properties. *Adv. Funct. Mater.* **2010,** *20* (9), 1480-1487.

25. Troshin, P. A.; Hoppe, H.; Renz, J.; Egginger, M.; Mayorova, J. Y.; Goryachev, A. E.; Peregudov, A. S.; Lyubovskaya, R. N.; Gobsch, G.; Sariciftci, N. S., Material solubility-photovoltaic performance relationship in the design of novel fullerene derivatives for bulk heterojunction solar cells. *Adv. Funct. Mater.* **2009,** *19* (5), 779-788.

26. Mikroyannidis, J.; Kabanakis, A.; Suresh, P.; Sharma, G., Efficient bulk heterojunction solar cells based on a broadly absorbing phenylenevinylene copolymer containing thiophene and pyrrole rings. *J. Phys. Chem. C* **2011,** *115* (14), 7056-7066.

27. Mikroyannidis, J. A.; Kabanakis, A. N.; Sharma, S.; Sharma, G. D., A simple and effective modification of PCBM for use as an electron acceptor in efficient bulk heterojunction solar cells. *Adv. Funct. Mater.* **2011,** *21* (4), 746-755.

28. Wienk, M. M.; Kroon, J. M.; Verhees, W. J.; Knol, J.; Hummelen, J. C.; Van Hal, P. A.; Janssen, R. A., Efficient methano [70] fullerene/MDMO-PPV bulk heterojunction photovoltaic cells. *Angew. Chem., Int. Ed. Engl.* **2003,** *115* (29), 3493-3497.

29. Ganesamoorthy, R.; Sathiyan, G.;Sakthivel, P., Fullerene based acceptors for efficient bulk heterojunction organic solar cell applications. *Sol. Energy Mater. Sol. Cells* **2017,** *161*, 102-148.

30. Kowalik, J.; Tolbert, L. M.; Narayan, S.; Abhiraman, A., Electrically conducting poly (undecylbithiophene) s. 1. regioselective synthesis and primary structure. *Macromolecules* **2001,** *34* (16), 5471-5479.

31. Dang, M. T.; Hirsch, L.; Wantz, G., P3HT: PCBM, best seller in polymer photovoltaic research. *Adv. Mater.* **2011,** *23* (31), 3596-3602.

32. Laird, D. W.; Vaidya, S.; Li, S.; Mathai, M.; Woodworth, B.; Sheina, E.; Williams, S.; Hammond, T. In Advances in Plexcore active layer technology systems for organic photovoltaics: roof-top and accelerated lifetime analysis of high performance organic photovoltaic cells, *Org. Photovoltaics,* **2007,** *6656*, 157-164.

33. Yu, T.; Xu, X.; Zhang, G.; Wan, J.; Li, Y.; Peng, Q., Wide bandgap copolymers based on quinoxalino [6, 5-f]. quinoxaline for highly efficient nonfullerene polymer solar cells. *Adv. Funct. Mater.* **2017,** *27* (28), 1701491.

34. Al-Azzawi, A. G.; Aziz, S. B.; Dannoun, E.; Iraqi, A.; Nofal, M. M.; Murad, A. R.; M Hussein, A., A mini review on the development of conjugated polymers: steps towards the commercialization of organic solar cells. *Polymers* **2023,** *15* (1), 164.

35. Duren, van J. K. J.; Dhanabalan, A.; Hal, van P. A.; Janssen, R. A. J.*,* Low-bandgap polymer photovoltaic cells. *Synth. Met.***2001,** *121* (1), 1587-1588.

36. Jo, J. W.; Bae, S.; Liu, F.; Russell, T. P.; Jo, W. H., Comparison of two D-A type polymers with each being fluorinated on D and A unit for high performance solar cells. *Adv. Funct. Mater.* **2015,** *25* (1), 120-125.

37. Jheng, J. F.; Lai, Y. Y.; Wu, J. S.; Chao, Y. H.; Wang, C. L.; Hsu, C. S., Influences of the non-covalent interaction strength on reaching high solid-state order and device performance of a low bandgap polymer with axisymmetrical structural units. *Adv. Mater.* **2013,** *25* (17), 2445-2451.

38. Chen, Z.; Cai, P.; Chen, J.; Liu, X.; Zhang, L.; Lan, L.; Peng, J.; Ma, Y.; Cao, Y., Low band-gap conjugated polymers with strong interchain aggregation and very high hole mobility towards highly efficient thick-film polymer solar cells. *Adv. Mater.* **2014,** *26* (16), 2586-2591.

39. Biniek, L.; Chochos, C. L.; Leclerc, N.; Hadziioannou, G.; Kallitsis, J. K.; Bechara, R.; Lévêque, P.; Heiser, T., A [3,2-b]thienothiophene-alt-benzothiadiazole copolymer for photovoltaic applications: design, synthesis, material characterization and device performances. *J. Mater. Chem.* **2009,** *19* (28), 4946.

40. Venkatesan, S.; Ngo, E. C.; Chen, Q.; Dubey, A.; Mohammad, L.; Adhikari, N.; Mitul, A. F.; Qiao, Q., Benzothiadiazole-based polymer for single and double junction solar cells with high open circuit voltage. *Nanoscale* **2014,** *6* (12), 7093-7100.

41. Pal, S. K.; Kesti, T.; Maiti, M.; Zhang, F.; Inganas, O.; Hellstrom, S.; Andersson, M. R.; Oswald, F.; Langa, F.; Osterman, T.; Pascher, T.; Yartsev, A.; Sundstrom, V., Geminate charge recombination in polymer/fullerene bulk heterojunction films and implications for solar cell function. *J. Am. Chem. Soc.* **2010,** *132* (35), 12440-12451.

42. Zhang, F.; Jespersen, K. G.; Björström, C.; Svensson, M.; Andersson, M. R.; Sundström, V.; Magnusson, K.; Moons, E.; Yartsev, A.; Inganäs, O., Influence of Solvent Mixing on the Morphology and Performance of Solar Cells Based on Polyfluorene Copolymer/Fullerene Blends. *Adv. Funct. Mater.* **2006,** *16* (5), 667-674.

43. Liu, J.; Choi, H.; Kim, J. Y.; Bailey, C.; Durstock, M.; Dai, L., Highly crystalline and low bandgap donor polymers for efficient polymer solar cells. *Adv. Mater.* **2012,** *24* (4), 538-542.

44. Song, K. W.; Song, H. J.; Lee, T. H.; Heo, S. W.; Moon, D. K., An effect on the side chain position of D-π-A-type conjugated polymers with sp2-hybridized orbitals for organic photovoltaics. *Polym. Chem.* **2013,** *4* (11), 3225.

45. Liu, Q.; Li, C.; Jin, E.; Lu, Z.; Chen, Y.; Li, F.; Bo, Z., 9-arylidene-9H-fluorene-containing polymers for high efficiency polymer solar cells. *ACS Appl. Mater. Interfaces* **2014,** *6* (3), 1601-1607.

46. Kim, J.; Kim, S. H.; Jung, I. H.; Jeong, E.; Xia, Y.; Cho, S.; Hwang, I.-W.; Lee, K.; Suh, H.; Shim, H.-K.; Woo, H. Y., Synthesis and characterization of indeno[1,2-b]fluorene-based low bandgap copolymers for photovoltaic cells. *J. Mater. Chem.* **2010,** *20* (8), 1577.

47. Zheng, Q.; Jung, B. J.; Sun, J.; Katz, H. E., Ladder-type oligo-p-phenylene-containing copolymers with high open-circuit voltages and ambient photovoltaic activity. *J. Am. Chem. Soc.* **2010,** *132* (15), 5394-5404.

48. Blouin, N.; Michaud, A.; Gendron, D.; Wakim, S.; Blair, E.; Neagu-Plesu, R.; Belletete, M.; Durocher, G.; Tao, Y.; Leclerc, M., Toward a rational design of poly(2,7-carbazole) derivatives for solar cells. *J. Am. Chem. Soc.* **2008,** *130* (2), 732-742.

49. Gevaerts, V. S.; Furlan, A.; Wienk, M. M.; Turbiez, M.; Janssen, R. A., Solution processed polymer tandem solar cell using efficient small and wide bandgap polymer:fullerene blends. *Adv. Mater.* **2012,** *24* (16), 2130-2134.

50. Zhang, Y.; Zhou, H.; Seifter, J.; Ying, L.; Mikhailovsky, A.; Heeger, A. J.; Bazan, G. C.; Nguyen, T. Q., Molecular doping enhances photoconductivity in polymer bulk heterojunction solar cells. *Adv. Mater.* **2013,** *25* (48), 7038-7044.

51. Mühlbacher, D.; Scharber, M.; Morana, M.; Zhu, Z.; Waller, D.; Gaudiana, R.; Brabec, C., High photovoltaic performance of a low-bandgap polymer. *Adv. Mater.* **2006,** *18* (21), 2884-2889.

52. Zhu, Z.; Waller, D.; Gaudiana, R.; Morana, M.; Mühlbacher, D.; Scharber, M.; Brabec, C., Panchromatic conjugated polymers containing alternating donor/acceptor units for photovoltaic applications. *Macromolecules* **2007,** *40* (6), 1981-1986.

53. Albrecht, S.; Janietz, S.; Schindler, W.; Frisch, J.; Kurpiers, J.; Kniepert, J.; Inal, S.; Pingel, P.; Fostiropoulos, K.; Koch, N.; Neher, D., Fluorinated copolymer PCPDTBT with enhanced open-circuit voltage and reduced recombination for highly efficient polymer solar cells. *J. Am. Chem. Soc.* **2012,** *134* (36), 14932-14944.

54. Scharber, M. C.; Koppe, M.; Gao, J.; Cordella, F.; Loi, M. A.; Denk, P.; Morana, M.; Egelhaaf, H. J.; Forberich, K.; Dennler, G.; Gaudiana, R.; Waller, D.; Zhu, Z.; Shi, X.; Brabec, C. J., Influence of the bridging atom on the performance of a low-bandgap bulk heterojunction solar cell. *Adv. Mater.* **2010,** *22* (3), 367-370.

55. Liang, Y.; Xu, Z.; Xia, J.; Tsai, S. T.; Wu, Y.; Li, G.; Ray, C.; Yu, L., For the bright future-bulk heterojunction polymer solar cells with power conversion efficiency of 7.4%. *Adv. Mater.* **2010,** *22* (20), E135-138.

56. He, Z.; Xiao, B.; Liu, F.; Wu, H.; Yang, Y.; Xiao, S.; Wang, C.; Russell, T. P.; Cao, Y., Single-junction polymer solar cells with high efficiency and photovoltage. *Nat. Photon.* **2015,** *9* (3), 174-179.

57. Huang, J.; Zhang, X.; Zheng, D.; Yan, K.; Li, C.-Z.; Yu, J., Boosting Organic Photovoltaic Performance Over 11% Efficiency With Photoconductive Fullerene Interfacial Modifier. *Solar RRL* **2017,** *1* (1), 1600008.

58. Usmani, B.; Ranjan, R.; Gupta, S. K.; Gupta, R. K.; Nalwa, K. S.; Garg, A., Inverted PTB7-Th: PC$_{71}$BM organic solar cells with 11.8% PCE via incorporation of gold nanoparticles in ZnO electron transport layer. *Sol. Energy* **2021,** *214*, 220-230.

59. Zhang, Y.; Lang, Y.; Li, G., Recent advances of non-fullerene organic solar cells: From materials and morphology to devices and applications. *EcoMat* **2022**, e12281.

60. He, Y.; Li, Y., Fullerene derivative acceptors for high performance polymer solar cells. *Phys. Chem. Chem. Phys.* **2011,** *13* (6), 1970-1983.

61. Armin, A.; Li, W.; Sandberg, O. J.; Xiao, Z.; Ding, L.; Nelson, J.; Neher, D.; Vandewal, K.; Shoaee, S.; Wang, T., A history and perspective of non-fullerene electron acceptors for organic solar cells. *Adv. Energy Mater.* **2021,** *11* (15), 2003570.

62. Wang, J.; Zhan, X., Rylene diimide electron acceptors for organic solar cells. *Trends in Chem.* **2019,** *1* (9), 869-881.

63. Li, Z.; Ying, L.; Zhu, P.; Zhong, W.; Li, N.; Liu, F.; Huang, F.; Cao, Y., A generic green solvent concept boosting the power conversion efficiency of all-polymer solar cells to 11%. *Energy Environ. Sci.* **2019,** *12* (1), 157-163.

64. Zhang, J.; Li, Y.; Huang, J.; Hu, H.; Zhang, G.; Ma, T.; Chow, P. C.; Ade, H.; Pan, D.; Yan, H., Ring-fusion of perylene diimide acceptor enabling efficient nonfullerene organic solar cells with a small voltage loss. *J. Am. Chem. Soc.* **2017,** *139* (45), 16092-16095.

65. Zhu, L.; Zhong, W.; Qiu, C.; Lyu, B.; Zhou, Z.; Zhang, M.; Song, J.; Xu, J.; Wang, J.; Ali, J., Aggregation-induced multilength scaled morphology enabling 11.76% efficiency in all-polymer solar cells using printing fabrication. *Adv. Mater.* **2019,** *31* (41), 1902899.

66. Rajaram, S.; Armstrong, P. B.; Kim, B. J.; Frechet, J. M., Effect of addition of a diblock copolymer on blend morphology and performance of poly (3-hexylthiophene): perylene diimide solar cells. *Chem. Mater.* **2009,** *21* (9), 1775-1777.

67. Zhao, D.; Wu, Q.; Cai, Z.; Zheng, T.; Chen, W.; Lu, J.; Yu, L., Electron acceptors based on α-substituted perylene diimide (PDI) for organic solar cells. *Chem. Mater.* **2016,** *28* (4), 1139-1146.

68. Wu, Q.; Zhao, D.; Schneider, A. M.; Chen, W.; Yu, L., Covalently bound clusters of alpha-substituted PDI-rival electron acceptors to fullerene for organic solar cells. *J. Am. Chem. Soc.* **2016,** *138* (23), 7248-7251.

69. Sharma, G.; Balraju, P.; Mikroyannidis, J. A.; Stylianakis, M. M., Bulk heterojunction organic photovoltaic devices based on low band gap small molecule BTD-TNP and perylene–anthracene diimide. *Sol. Energy Mater. Sol. Cells* **2009,** *93* (11), 2025-2028.

70. Kozma, E.; Kotowski, D.; Luzzati, S.; Catellani, M.; Bertini, F.; Famulari, A.; Raos, G., Improving the efficiency of P3HT: perylene diimide solar cells via bay-substitution with fused aromatic rings. *RSC Adv.* **2013,** *3* (24), 9185-9188.

71. Jiang, W.; Ye, L.; Li, X.; Xiao, C.; Tan, F.; Zhao, W.; Hou, J.; Wang, Z., Bay-linked perylene bisimides as promising non-fullerene acceptors for organic solar cells. *Chem. Comm.* **2014,** *50* (8), 1024-1026.

72. Sun, D.; Meng, D.; Cai, Y.; Fan, B.; Li, Y.; Jiang, W.; Huo, L.; Sun, Y.; Wang, Z., Non-fullerene-acceptor-based bulk-heterojunction organic solar cells with efficiency over 7%. *J. Am. Chem. Soc.* **2015,** *137* (34), 11156-11162.

73. Meng, D.; Sun, D.; Zhong, C.; Liu, T.; Fan, B.; Huo, L.; Li, Y.; Jiang, W.; Choi, H.; Kim, T., High-performance solution-processed non-fullerene organic solar cells based on selenophene-containing perylene bisimide acceptor. *J. Am. Chem. Soc.* **2016,** *138* (1), 375-380.

74. Yan, Q.; Zhou, Y.; Zheng, Y.-Q.; Pei, J.; Zhao, D., Towards rational design of organic electron acceptors for photovoltaics: a study based on perylenediimide derivatives. *Chem. Sci.* **2013,** *4* (12), 4389-4394.

75. Lin, Y.; Wang, Y.; Wang, J.; Hou, J.; Li, Y.; Zhu, D.; Zhan, X., A star-shaped perylene diimide electron acceptor for high-performance organic solar cells. *Adv. Mater.* **2014,** *26* (30), 5137-5142.

76. Duan, Y.; Xu, X.; Yan, H.; Wu, W.; Li, Z.; Peng, Q., Pronounced effects of a triazine core on photovoltaic performance–efficient organic solar cells enabled by a PDI trimer-based small molecular acceptor. *Adv. Mater.* **2017,** *29* (7), 1605115.

77. Lin, H.; Chen, S.; Hu, H.; Zhang, L.; Ma, T.; Lai, J. Y. L.; Li, Z.; Qin, A.; Huang, X.; Tang, B., Reduced intramolecular twisting improves the performance of 3D molecular acceptors in non-fullerene organic solar cells. *Adv. Mater.* **2016,** *28* (38), 8546-8551.

78. Zhong, Y.; Trinh, M. T.; Chen, R.; Wang, W.; Khlyabich, P. P.; Kumar, B.; Xu, Q.; Nam, C.-Y.; Sfeir, M. Y.; Black, C., Efficient organic solar cells with helical perylene diimide electron acceptors. *J. Am. Chem. Soc.* **2014,** *136* (43), 15215-15221.

79. Zhong, Y.; Trinh, M. T.; Chen, R.; Purdum, G. E.; Khlyabich, P. P.; Sezen, M.; Oh, S.; Zhu, H.; Fowler, B.; Zhang, B., Molecular helices as electron acceptors in high-performance bulk heterojunction solar cells. *Nat. Commun.* **2015,** *6* (1), 1-8.

80. Guo, X.; Watson, M. D., Conjugated polymers from naphthalene bisimide. *Org. lett.* **2008,** *10* (23), 5333-5336.

81. Yan, H.; Chen, Z.; Zheng, Y.; Newman, C.; Quinn, J. R.; Dötz, F.; Kastler, M.; Facchetti, A., A high-mobility electron-transporting polymer for printed transistors. *Nature* **2009,** *457* (7230), 679-686.

82. Hou, J.; Inganäs, O.; Friend, R. H.; Gao, F., Organic solar cells based on non-fullerene acceptors. *Nat. Mater.* **2018,** *17* (2), 119-128.

83. Lin, Y.; He, Q.; Zhao, F.; Huo, L.; Mai, J.; Lu, X.; Su, C.-J.; Li, T.; Wang, J.; Zhu, J., A facile planar fused-ring electron acceptor for as-cast polymer solar cells with 8.71% efficiency. *J. Am. Chem. Soc.* **2016,** *138* (9), 2973-2976.

84. Lin, Y.; Wang, J.; Zhang, Z. G.; Bai, H.; Li, Y.; Zhu, D.; Zhan, X., An electron acceptor challenging fullerenes for efficient polymer solar cells. *Adv. Mater.* **2015,** *27* (7), 1170-1174.

85. Zhao, W.; Qian, D.; Zhang, S.; Li, S.; Inganäs, O.; Gao, F.; Hou, J., Fullerene-free polymer solar cells with over 11% efficiency and excellent thermal stability. *Adv. Mater.* **2016,** *28* (23), 4734-4739.

86. Xu, X.; Yu, T.; Bi, Z.; Ma, W.; Li, Y.; Peng, Q., Realizing over 13% efficiency in green-solvent-processed nonfullerene organic solar cells enabled by 1, 3, 4-thiadiazole-based wide-bandgap copolymers. *Adv. Mater.* **2018,** *30* (3), 1703973.

87. Lin, Y.; Zhao, F.; He, Q.; Huo, L.; Wu, Y.; Parker, T. C.; Ma, W.; Sun, Y.; Wang, C.; Zhu, D., High-performance electron acceptor with thienyl side chains for organic photovoltaics. *J. Am. Chem. Soc.* **2016,** *138* (14), 4955-4961.

88. Li, S.; Ye, L.; Zhao, W.; Zhang, S.; Mukherjee, S.; Ade, H.; Hou, J., Energy-level modulation of small-molecule electron acceptors to achieve over 12% efficiency in polymer solar cells. *Adv. Mater.* **2016,** *28* (42), 9423-9429.

89. Zhao, W.; Li, S.; Yao, H.; Zhang, S.; Zhang, Y.; Yang, B.; Hou, J., Molecular optimization enables over 13% efficiency in organic solar cells. *J. Am. Chem. Soc.* **2017,** *139* (21), 7148-7151.

90. Zhang, H.; Yao, H.; Hou, J.; Zhu, J.; Zhang, J.; Li, W.; Yu, R.; Gao, B.; Zhang, S.; Hou, J., Over 14% efficiency in organic solar cells enabled by chlorinated nonfullerene small-molecule acceptors. *Adv. Mater.* **2018,** *30* (28), 1800613.

91. Lin, Y.; Zhao, F.; Prasad, S. K.; Chen, J. D.; Cai, W.; Zhang, Q.; Chen, K.; Wu, Y.; Ma, W.; Gao, F., Balanced partnership between donor and acceptor components in nonfullerene organic solar cells with > 12% efficiency. *Adv. Mater.* **2018,** *30* (16), 1706363.

92. Zhu, J.; Xiao, Y.; Wang, J.; Liu, K.; Jiang, H.; Lin, Y.; Lu, X.; Zhan, X., Alkoxy-induced near-infrared sensitive electron acceptor for high-performance organic solar cells. *Chem. Mater.* **2018,** *30* (12), 4150-4156.

93. Dai, S.; Zhao, F.; Zhang, Q.; Lau, T.-K.; Li, T.; Liu, K.; Ling, Q.; Wang, C.; Lu, X.; You, W., Fused nonacyclic electron acceptors for efficient polymer solar cells. *J. Am. Chem. Soc.* **2017,** *139* (3), 1336-1343.

94. Yuan, J.; Zhang, Y.; Zhou, L.; Zhang, G.; Yip, H.-L.; Lau, T.-K.; Lu, X.; Zhu, C.; Peng, H.; Johnson, P. A., Single-junction organic solar cell with over 15% efficiency using fused-ring acceptor with electron-deficient core. *Joule* **2019,** *3* (4), 1140-1151.

95. Ma, R.; Liu, T.; Luo, Z.; Guo, Q.; Xiao, Y.; Chen, Y.; Li, X.; Luo, S.; Lu, X.; Zhang, M., Improving open-circuit voltage by a chlorinated polymer donor endows binary organic solar cells efficiencies over 17%. *Sci. China Chem.* **2020,** *63* (3), 325-330.

96. Liu, Q.; Jiang, Y.; Jin, K.; Qin, J.; Xu, J.; Li, W.; Xiong, J.; Liu, J.; Xiao, Z.; Sun, K., 18% efficiency organic solar cells. *Sci. Bull.* **2020,** *65* (4), 272-275.

97. Cui, Y.; Yao, H.; Zhang, J.; Zhang, T.; Wang, Y.; Hong, L.; Xian, K.; Xu, B.; Zhang, S.; Peng, J., Over 16% efficiency organic photovoltaic cells enabled by a chlorinated acceptor with increased open-circuit voltages. *Nat. Commun.* **2019,** *10* (1), 1-8.

98. Zhang, Z.; Li, Y.; Cai, G.; Zhang, Y.; Lu, X.; Lin, Y., Selenium heterocyclic electron acceptor with small urbach energy for as-cast high-performance organic solar cells. *J. Am. Chem. Soc.* **2020,** *142* (44), 18741-18745.

99. Jiang, K.; Wei, Q.; Lai, J. Y. L.; Peng, Z.; Kim, H. K.; Yuan, J.; Ye, L.; Ade, H.; Zou, Y.; Yan, H., Alkyl chain tuning of small molecule acceptors for efficient organic solar cells. *Joule* **2019,** *3* (12), 3020-3033.

100. Cui, Y.; Yao, H.; Hong, L.; Zhang, T.; Tang, Y.; Lin, B.; Xian, K.; Gao, B.; An, C.; Bi, P., Organic photovoltaic cell with 17% efficiency and superior processability. *Natl. Sci. Rev.* **2020,** *7* (7), 1239-1246.

101. Cui, Y.; Yao, H.; Zhang, J.; Xian, K.; Zhang, T.; Hong, L.; Wang, Y.; Xu, Y.; Ma, K.; An, C., Single-junction organic photovoltaic cells with approaching 18% efficiency. *Adv. Mater.* **2020,** *32* (19), 1908205.

102. Li, C.; Zhou, J.; Song, J.; Xu, J.; Zhang, H.; Zhang, X.; Guo, J.; Zhu, L.; Wei, D.; Han, G., Non-fullerene acceptors with branched side chains and improved molecular packing to exceed 18% efficiency in organic solar cells. *Nat. Energy* **2021,** *6* (6), 605-613.

103. Song, J.; Zhu, L.; Li, C.; Xu, J.; Wu, H.; Zhang, X.; Zhang, Y.; Tang, Z.; Liu, F.; Sun, Y., High-efficiency organic solar cells with low voltage loss induced by solvent additive strategy. *Matter* **2021,** *4* (7), 2542-2552.

104. Meng, H.; Liao, C.; Deng, M.; Xu, X.; Yu, L.; Peng, Q., 18.77% efficiency organic solar cells promoted by aqueous solution processed cobalt (II) acetate hole transporting layer. *Angew. Chem., Int. Ed. Engl.* **2021,** *133* (41), 22728-22735.

105. Weng, K.; Ye, L.; Zhu, L.; Xu, J.; Zhou, J.; Feng, X.; Lu, G.; Tan, S.; Liu, F.; Sun, Y., Optimized active layer morphology toward efficient and polymer batch insensitive organic solar cells. *Nat. Commun.* **2020,** *11* (1), 1-9.

106. Shaheen, S. E.; Brabec, C. J.; Sariciftci, N. S.; Padinger, F.; Fromherz, T.; Hummelen, J. C., 2.5% efficient organic plastic solar cells. *Appl. Phys. Lett.* **2001,** *78* (6), 841-843.

107. Park, S. H.; Roy, A.; Beaupré, S.; Cho, S.; Coates, N.; Moon, J. S.; Moses, D.; Leclerc, M.; Lee, K.; Heeger, A. J., Bulk heterojunction solar cells with internal quantum efficiency approaching 100%. *Nat. Photon.* **2009,** *3* (5), 297-302.

108. Wienk, M. M.; Turbiez, M.; Gilot, J.; Janssen, R. A., Narrow-bandgap diketo-pyrrolo-pyrrole polymer solar cells: the effect of processing on the performance. *Adv. Mater.* **2008,** *20* (13), 2556-2560.

109. Zhu, L.; Zhang, M.; Zhou, G.; Hao, T.; Xu, J.; Wang, J.; Qiu, C.; Prine, N.; Ali, J.; Feng, W., Efficient organic solar cell with 16.88% efficiency enabled by refined acceptor crystallization and morphology with improved charge transfer and transport properties. *Adv. Energy Mater.* **2020,** *10* (18), 1904234.

110. Dayneko, S. V.; Hendsbee, A. D.; Welch, G. C., Fullerene-free polymer solar cells processed from non-halogenated solvents in air with PCE of 4.8%. *Chem. Comm.* **2017,** *53* (6), 1164-1167.

111. Park, G. E.; Choi, S.; Park, S. Y.; Lee, D. H.; Cho, M. J.; Choi, D. H., Eco-friendly solvent-processed fullerene-free polymer solar cells with over 9.7% efficiency and long-term performance stability. *Adv. Energy Mater.* **2017,** *7* (19), 1700566.

112. Kim, C.; Chen, S.; Park, J. S.; Kim, G.-U.; Kang, H.; Lee, S.; Phan, T. N.-L.; Kwon, S.-K.; Kim, Y.-H.; Kim, B. J., Green solvent-processed, high-performance organic solar cells achieved by outer side-chain selection of selenophene-incorporated Y-series acceptors. *J. Mater. Chem. A* **2021,** *9* (43), 24622-24630.

113. Pang, S.; Chen, Z.; Li, J.; Chen, Y.; Liu, Z.; Wu, H.; Duan, C.; Huang, F.; Cao, Y., High-efficiency organic solar cells processed from a real green solvent. *Mater. Horiz.* **2023**, *10,* 473-482.

114. Peet, J.; Kim, J. Y.; Coates, N. E.; Ma, W. L.; Moses, D.; Heeger, A. J.; Bazan, G. C., Efficiency enhancement in low-bandgap polymer solar cells by processing with alkane dithiols. *Nat. Mater.* **2007,** *6* (7), 497-500.

115. Lee, J. K.; Ma, W. L.; Brabec, C. J.; Yuen, J.; Moon, J. S.; Kim, J. Y.; Lee, K.; Bazan, G. C.; Heeger, A. J., Processing additives for improved efficiency from bulk heterojunction solar cells. *J. Am. Chem. Soc.* **2008,** *130* (11), 3619-3623.

116. Guo, X.; Zhang, M.; Ma, W.; Ye, L.; Zhang, S.; Liu, S.; Ade, H.; Huang, F.; Hou, J., Enhanced photovoltaic performance by modulating surface composition in bulk heterojunction polymer solar cells based on PBDTTT-C-T/PC$_{71}$BM. *Adv. Mater.* **2014,** *26* (24), 4043-4049.

117. Jacobs, I. E.; Wang, F.; Valdez, Z. I. B.; Oviedo, A. N. A.; Bilsky, D. J.; Moulé, A. J., Photoinduced degradation from trace 1, 8-diiodooctane in organic photovoltaics. *J. Mater. Chem. C* **2018,** *6* (2), 219-225.

118. Holliday, S.; Luscombe, C. K., Low boiling point solvent additives for improved photooxidative stability in organic photovoltaics. *Adv. Electron. Mater.* **2018,** *4* (10), 1700416.

119. Doumon, N. Y.; Wang, G.; Qiu, X.; Minnaard, A. J.; Chiechi, R. C.; Koster, L., 1, 8-diiodooctane acts as a photo-acid in organic solar cells. *Sci. Rep.* **2019,** *9* (1), 1-14.

120. Hu, X.; Wang, M.; Huang, F.; Gong, X.; Cao, Y., 23% enhanced efficiency of polymer solar cells processed with 1-chloronaphthalene as the solvent additive. *Synth. Met.* **2013,** *164*, 1-5.

121. He, X.; Chan, C. C.; Kim, J.; Liu, H.; Su, C. J.; Jeng, U. S.; Su, H.; Lu, X.; Wong, K. S.; Choy, W. C., 1-Chloronaphthalene-induced donor/acceptor vertical distribution and carrier dynamics changes in nonfullerene organic solar cells and the governed mechanism. *Small methods* **2022,** *6* (3), 2101475.

122. Schmidt, K.; Tassone, C. J.; Niskala, J. R.; Yiu, A. T.; Lee, O. P.; Weiss, T. M.; Wang, C.; Fréchet, J. M.; Beaujuge, P. M.; Toney, M. F., A mechanistic understanding of processing additive-induced efficiency enhancement in bulk heterojunction organic solar cells. *Adv. Mater.* **2014,** *26* (2), 300-305.

123. Salim, T.; Wong, L. H.; Bräuer, B.; Kukreja, R.; Foo, Y. L.; Bao, Z.; Lam, Y. M., Solvent additives and their effects on blend morphologies of bulk heterojunctions. *J. Mater. Chem.* **2011,** *21* (1), 242-250.

124. Wang, W.; Song, L.; Magerl, D.; Moseguí González, D.; Körstgens, V.; Philipp, M.; Moulin, J. F.; Müller-Buschbaum, P., Organic photovoltaics: influence of solvent additive 1, 8-octanedithiol on P3HT: PCBM solar cells. *Adv. Funct. Mater.* **2018,** *28* (20), 1870130.

125. Waters, H.; Bristow, N.; Moudam, O.; Chang, S.-W.; Su, C.-J.; Wu, W.-R.; Jeng, U.-S.; Horie, M.; Kettle, J., Effect of processing additive 1, 8-octanedithiol on the lifetime of PCPDTBT based organic photovoltaics. *Org. Electron.* **2014,** *15* (10), 2433-2438.

126. Ye, T.; Jin, S.; Singh, R.; Kumar, M.; Chen, W.; Wang, D.; Zhang, X.; Li, W.; He, D., Effects of solvent additives on the morphology and transport property of a perylene diimide dimer film in perovskite solar cells for improved performance. *Sol. Energy* **2020,** *201*, 927-934.

127. Chen, Y.; Ding, X.; Wang, G.; Xiao, S.; Liu, X.; Zhu, Z.; Wang, C.;Wen, S., Non-halogenated solvent-processed high-efficiency polymer solar cells: the role of diphenyl ether in morphology, light-trapping, transport Pproperties. *Trans. Tianjin Univ.* **2022,** *28* (5), 423-432.

128. Zhao, W.; Ye, L.; Li, S.; Liu, X.; Zhang, S.; Zhang, Y.; Ghasemi, M.; He, C.; Ade, H.; Hou, J., Environmentally-friendly solvent processed fullerene-free organic solar cells enabled by screening halogen-free solvent additives. *Sci. China Mater.* **2017,** *60* (8), 697-706.

129. Wibowo, F. T. A.; Krishna, N. V.; Sinaga, S.; Lee, S.; Hadmojo, W. T.; Do, Y. R.; Jang, S.-Y., High-efficiency organic solar cells prepared using a halogen-free solution process. *Cell Rep. Phys. Sci.* **2021,** *2* (8), 100517.

130. Ye, L.; Xiong, Y.; Zhang, M.; Guo, X.; Guan, H.; Zou, Y.; Ade, H., Enhanced efficiency in nonfullerene organic solar cells by tuning molecular order and domain characteristics. *Nano Energy* **2020,** *77*, 105310.

131. Zhao, W.; Zhang, S.; Zhang, Y.; Li, S.; Liu, X.; He, C.; Zheng, Z.; Hou, J., Environmentally friendly solvent-processed organic solar cells that are highly efficient and adaptable for the blade-coating method. *Adv. Mater.* **2018,** *30* (4), 1704837.

132. Sun, Y.; Cui, C.; Wang, H.; Li, Y., Efficiency enhancement of polymer solar cells based on poly (3-hexylthiophene)/indene-C70 bisadduct via methylthiophene additive. *Adv. Energy Mater.* **2011,** *1* (6), 1058-1061.

133. Majeed, S. M.; Ahmed, D. S.; Mohammed, M. K., A novel 3-methylthiophene additive to boost the performance and stability of perovskite solar cells. *RSC Adv.* **2021,** *11* (18), 10425-10433.

134. Zhao, J.; Li, Y.; Yang, G.; Jiang, K.; Lin, H.; Ade, H.; Ma, W.; Yan, H., Efficient organic solar cells processed from hydrocarbon solvents. *Nat. Energy* **2016,** *1* (2), 1-7.

135. Xue, L.; Liu, X.; Wang, Q.; Yang, M.; Du, S.; Yang, C.; Tong, J.; Xia, Y.; Li, J., Improved performance of organic solar cells by utilizing green non-halogen additive to modulate active-layer morphology. *Energy Technol.* **2022,** *10* (10), 2200504.

136. Li, G.; Shrotriya, V.; Huang, J.; Yao, Y.; Moriarty, T.; Emery, K.; Yang, Y., High-efficiency solution processable polymer photovoltaic cells by self-organization of polymer blends. *Nat. Mater.* **2005,** *4* (11), 864-868.

137. Erb, T.; Zhokhavets, U.; Gobsch, G.; Raleva, S.; Stühn, B.; Schilinsky, P.; Waldauf, C.; Brabec, C. J., Correlation between structural and optical properties of composite polymer/fullerene films for organic solar cells. *Adv. Funct. Mater.* **2005,** *15* (7), 1193-1196.

138. Li, W.; Cai, J.; Yan, Y.; Cai, F.; Li, S.; Gurney, R. S.; Liu, D.; McGettrick, J. D.; Watson, T. M.; Li, Z., Correlating three-dimensional morphology with function in PBDB-T: IT-M non-fullerene organic solar cells. *Solar RRL* **2018,** *2* (9), 1800114.

139. Liang, Q.; Han, J.; Song, C.; Yu, X.; Smilgies, D.-M.; Zhao, K.; Liu, J.; Han, Y., Reducing the confinement of PBDB-T to ITIC to improve the crystallinity of PBDB-T/ITIC blends. *J. Mater. Chem. A* **2018,** *6* (32), 15610-15620.

140. Köntges, W.; Perkhun, P.; Kammerer, J.; Alkarsifi, R.; Würfel, U.; Margeat, O.; Videlot-Ackermann, C.; Simon, J.-J.; Schröder, R. R.; Ackermann, J., Visualizing morphological principles for efficient photocurrent generation in organic non-fullerene acceptor blends. *Energy Environ. Sci.* **2020,** *13* (4), 1259-1268.

141. Zhu, W.; Spencer, A. P.; Mukherjee, S.; Alzola, J. M.; Sangwan, V. K.; Amsterdam, S. H.; Swick, S. M.; Jones, L. O.; Heiber, M. C.; Herzing, A. A., Crystallography, morphology, electronic structure, and transport in non-fullerene/non-indacenodithienothiophene polymer: Y6 solar cells. *J. Am. Chem. Soc.* **2020,** *142* (34), 14532-14547.

142. Li, G.; Yao, Y.; Yang, H.; Shrotriya, V.; Yang, G.; Yang, Y., "Solvent annealing" effect in polymer solar cells based on poly (3-hexylthiophene) and methanofullerenes. *Adv. Funct. Mater.* **2007,** *17* (10), 1636-1644.

143. Hegde, R.; Henry, N.; Whittle, B.; Zang, H.; Hu, B.; Chen, J.; Xiao, K.; Dadmun, M., The impact of controlled solvent exposure on the morphology, structure and function of bulk heterojunction solar cells. *Sol. Energy Mater. Sol. Cells* **2012,** *107*, 112-124.

144. Zhao, Y.; Guo, X.; Xie, Z.; Qu, Y.; Geng, Y.; Wang, L., Solvent vapor-induced self assembly and its influence on optoelectronic conversion of poly (3-hexylthiophene): Methanofullerene bulk heterojunction photovoltaic cells. *J. Appl. Polym. Sci.* **2009,** *111* (4), 1799-1804.

145. Chen, H.; Hsiao, Y.-C.; Hu, B.; Dadmun, M., Control of morphology and function of low band gap polymer–bis-fullerene mixed heterojunctions in organic photovoltaics with selective solvent vapor annealing. *J. Mater. Chem. A* **2014,** *2* (25), 9883-9890.

146. Zheng, Y.; Li, S.; Zheng, D.; Yu, J., Effects of different polar solvents for solvent vapor annealing treatment on the performance of polymer solar cells. *Org. Electron.* **2014,** *15* (11), 2647-2653.

147. Zhang, M.; Zhang, F.; An, Q.; Sun, Q.; Wang, W.; Ma, X.; Zhang, J.; Tang, W., Nematic liquid crystal materials as a morphology regulator for ternary small molecule solar cells with power conversion efficiency exceeding 10%. *J. Mater. Chem. A* **2017,** *5* (7), 3589-3598.

148. Jiao, C.; Pang, C.; An, Q., Nonfullerene organic photovoltaic cells exhibiting 13.76% efficiency by employing upside-down solvent vapor annealing. *Int. J. Energy Res.* **2019,** *43* (14), 8716-8724.

149. Qiu, D.; Adil, M. A.; Lu, K.; Wei, Z., The crystallinity control of polymer donor materials for high-performance organic solar cells. *Front. Chem.* **2020,** *8*, 603134.

150. Zhang, L.; Ma, W., Morphology optimization in ternary organic solar cells. *Chinese J. Polym. Sci.* **2017,** *35* (2), 184-197.

151. Zhao, F.; Li, Y.; Wang, Z.; Yang, Y.; Wang, Z.; He, G.; Zhang, J.; Jiang, L.; Wang, T.; Wei, Z., Combining energy transfer and optimized morphology for highly efficient ternary polymer solar cells. *Adv. Energy Mater.* **2017,** *7* (13), 1602552.

152. Zhang, J.; Zhang, Y.; Fang, J.; Lu, K.; Wang, Z.; Ma, W.; Wei, Z., Conjugated polymer–small molecule alloy leads to high efficient ternary organic solar cells. *J. Am. Chem. Soc.* **2015,** *137* (25), 8176-8183.

153. Xie, Y.; Yang, F.; Li, Y.; Uddin, M. A.; Bi, P.; Fan, B.; Cai, Y.; Hao, X.; Woo, H. Y.; Li, W., Morphology control enables efficient ternary organic solar cells. *Adv. Mater.* **2018,** *30* (38), 1803045.

154. Naveed, H. B.; Ma, W., Miscibility-driven optimization of nanostructures in ternary organic solar cells using non-fullerene acceptors. *Joule* **2018,** *2* (4), 621-641.

155. Khlyabich, P. P.; Burkhart, B.; Thompson, B. C., Efficient ternary blend bulk heterojunction solar cells with tunable open-circuit voltage. *J. Am. Chem. Soc.* **2011,** *133* (37), 14534-14537.

156. Gao, J.; Ma, X.; Xu, C.; Wang, X.; Son, J. H.; Jeong, S. Y.; Zhang, Y.; Zhang, C.; Wang, K.; Niu, L., Over 17.7% efficiency ternary-blend organic solar cells with low energy-loss and good thickness-tolerance. *J. Chem. Eng.* **2022,** *428*, 129276.

157. An, Q.; Wang, J.; Ma, X.; Gao, J.; Hu, Z.; Liu, B.; Sun, H.; Guo, X.; Zhang, X.; Zhang, F., Two compatible polymer donors contribute synergistically for ternary organic solar cells with 17.53% efficiency. *Energy Environ. Sci.* **2020,** *13* (12), 5039-5047.

158. Li, Y.; Cai, Y.; Xie, Y.; Song, J.; Wu, H.; Tang, Z.; Zhang, J.; Huang, F.; Sun, Y., A facile strategy for third-component selection in non-fullerene acceptor-based ternary organic solar cells. *Energy Environ. Sci.* **2021,** *14* (9), 5009-5016.

159. Cai, Y.; Li, Y.; Wang, R.; Wu, H.; Chen, Z.; Zhang, J.; Ma, Z.; Hao, X.; Zhao, Y.; Zhang, C., A well-mixed phase formed by two compatible non-fullerene acceptors enables ternary organic solar cells with efficiency over 18.6%. *Adv. Mater.* **2021,** *33* (33), 2101733.

160. Yin, Z.; Wei, J.; Zheng, Q., Interfacial materials for organic solar cells: recent advances and perspectives. *Adv. Sci.* **2016,** *3* (8), 1500362.

161. Li, S.; Fu, Q.; Meng, L.; Wan, X.; Ding, L.; Lu, G.; Lu, G.; Yao, Z.; Li, C.; Chen, Y., Achieving over 18% efficiency organic solar cell enabled by a ZnO-based hybrid electron transport layer with an operational lifetime up to 5 years. *Angew. Chem., Int. Ed. Engl.* **2022,** *134* (34), e202207397.

162. Shrotriya, V.; Li, G.; Yao, Y.; Chu, C.-W.; Yang, Y., Transition metal oxides as the buffer layer for polymer photovoltaic cells. *Appl. Phys. Lett.* **2006,** *88* (7), 073508.

163. Zhang, Z.-G.; Qi, B.; Jin, Z.; Chi, D.; Qi, Z.; Li, Y.; Wang, J., Perylene diimides: a thickness-insensitive cathode interlayer for high performance polymer solar cells. *Energy Environ. Sci.* **2014,** *7* (6), 1966-1973.

164. Yao, J.; Qiu, B.; Zhang, Z.-G.; Xue, L.; Wang, R.; Zhang, C.; Chen, S.; Zhou, Q.; Sun, C.; Yang, C., Cathode engineering with perylene-diimide interlayer enabling over 17% efficiency single-junction organic solar cells. *Nat. Commun.* **2020,** *11* (1), 2726.

165. Liu, F.; Zhou, L.; Liu, W.; Zhou, Z.; Yue, Q.; Zheng, W.; Sun, R.; Liu, W.; Xu, S.; Fan, H., Organic solar cells with 18% efficiency enabled by an alloy acceptor: a two-in-one strategy. *Adv. Mater.* **2021,** *33* (27), 2100830.

166. Chueh, C. C.; Crump, M.; Jen, A. K. Y., Optical enhancement via electrode designs for high-performance polymer solar cells. *Adv. Funct. Mater.* **2016,** *26* (3), 321-340.

167. Ni, W.; Chen, H.; Su, J.; Sun, Z.; Wang, J.; Wu, H., Effects of dyes, gold nanocrystals, pH, and metal ions on plasmonic and molecular resonance coupling. *J. Am. Chem. Soc.* **2010,** *132* (13), 4806-4814.

168. Wang, L.; Hasanzadeh Kafshgari, M.; Meunier, M., Optical properties and applications of plasmonic-metal nanoparticles. *Adv. Funct. Mater.* **2020,** *30* (51), 2005400.

169. Su, Q.; Li, Y.; Hu, R.; Song, F.; Liu, S.; Guo, C.; Zhu, S.; Liu, W.; Pan, J., Heterojunction photocatalysts based on 2D materials: the role of configuration. *Adv. Sustain. Syst.* **2020,** *4* (9), 2000130.

RÉSUMÉ

L'introduction

À mesure que les gens prennent conscience de la protection de l'environnement, le remplacement des combustibles fossiles non renouvelables est imminent pour atténuer les conséquences non durables. L'énergie solaire est une alternative prometteuse pour répondre à la demande croissante d'énergie, qui peut être convertie en électricité grâce à des dispositifs photovoltaïques. En 1954, les laboratoires Bell ont réussi à fabriquer pour la première fois des cellules solaires C-Si et ont obtenu une efficacité de 6 %, ouvrant ainsi de nouveaux horizons à la technologie photovoltaïque pour exploiter l'énergie solaire. Après le développement de première et deuxième génération de cellules solaires, c-Si cellules solaires ont atteint une efficacité de 26% et réalisé la production commerciale et industrielle. Cependant, les processus de fabrication compliqués des cellules solaires à film de Si et inorganique, le coût élevé des matières premières et les limites inhérentes aux matières inorganiques limitent l'utilisation de l'énergie solaire. Afin de résoudre les problèmes ci-dessus, les cellules solaires de troisième génération ont été largement développées, les cellules solaires organiques (OSC) étant l'un des dispositifs photovoltaïques les plus prometteurs en raison de leurs avantages importants tels que le faible coût, la flexibilité, la légèreté, et processus de fabrication simple. Le meilleur rendement de conversion de puissance (PCE) des OSC à jonction unique a maintenant atteint plus de 19 % en laboratoire, ce qui les rend plus attractifs que jamais pour d'éventuelles applications commerciales.

Depuis des décennies, des efforts importants sont déployés pour améliorer les performances photovoltaïques des OSC grâce à l'innovation de la configuration du dispositif et au développement de matériaux en couches photoactivés, couches interfaciales et électrodes. Les chercheurs ont développé trois configurations principales pour l'amélioration de la performance photovoltaïque, y compris les OSC monocouche, les OSC balayeurs et les OSC d'hétérojonction en vrac (BHJ). Parmi eux, les BHJ-OSCs sont considérés comme la structure de dispositif la plus efficace en raison de la zone de contact largement accrue entre le donneur et les matériaux accepteur, qui favorise la dissociation de l'exciton et le transport de charge. De plus, les configurations BHJ-OSC sont optimisées en utilisant une stratégie de mélange ternaire, qui confère une efficacité photovoltaïque de plus de 19%. Il est à noter que la morphologie idéale du film de mélange BHJ avec les nanostructures interpénétratrices, la séparation de phase appropriée et la

165

taille de domaine appropriée est d'une importance vitale pour la réalisation des OSC de pointe. L'introduction des composants invités dans les OSC ternaires est une approche simple et efficace pour obtenir la morphologie souhaitée. Cependant, le film de mélange ternaire avec les trois composants apporte généralement une morphologie plus compliquée. Par conséquent, la morphologie du film de mélange ternaire doit être caractérisée en profondeur, ce qui aide à obtenir des informations sur l'optimisation des performances. En outre, la percée dans les accepteurs non cylindriques a conduit à une augmentation rapide de l'efficacité des appareils. Les contributions des matériaux d'interface aux performances des appareils sont également essentielles.

Objectif de la thèse

Dans le but d'améliorer la performance photovoltaïque grâce à diverses approches, telles que la stratégie de mélange ternaire, la modification interfaciale et la caractérisation de la relation entre les matériaux et la variation de performance, trois parties de la thèse ont été réalisées comme suit :

Partie I: Étude de l'amélioration des performances photovoltaïques des cellules solaires ternaires grâce à une compréhension approfondie de la morphologie 3D des films de mélange ternaires

Comme tout le monde le sait, l'introduction d'un composant invité avec absorption complémentaire et niveau d'énergie bien adapté est une stratégie prometteuse pour améliorer l'efficacité de l'appareil. En outre, la morphologie souhaitable de la couche active avec une séparation de phase appropriée et un réseau d'interpénétration peut être atteint en ajustant le contenu du composant invité. Jusqu'à présent, il est difficile de visualiser la morphologie 3D du film de mélange grâce à des techniques de caractérisation traditionnelles, telles que l'AFM, la MET et la MEB. La microscopie à force photoinduite (PiFM) combinant AFM avec spectroscopie laser infrarouge peut caractériser la distribution des composants dans la couche active par identification chimique, qui peut être utilisé pour étudier la morphologie de la surface. De plus, la microscopie électronique à transmission à filtration d'énergie (EFTEM) avec spectres de perte d'énergie électronique peut sonder la morphologie transversale des OSC. Ici, en combinant ces deux techniques de caractérisation avancées pour la caractérisation morphologique 3D, le rôle de l'accepteur PDI-DPP-PDI dans l'optimisation morphologique du mélange actif peut être exploré en profondeur, contribuant ainsi à atteindre des OSC très efficaces et stables.

Partie II: Optimisation morphologique par miscibilité permettant une haute performance de l'appareil grâce à l'intégration d'un accepteur invité non cylindrique (PDI-EH) avec une structure presque orthogonale

L'optimisation morphologique BHJ dans la couche active est cruciale et ne peut être négligée, car les performances du dispositif sont directement corrélées avec l'interpénétration des nanostructures, la séparation de phase, la taille et la pureté du domaine. Dans la plupart des BSO-BHJ, la cristallinité du matériel donneur et accepteur influence habituellement leur miscibilité du donneur et de l'accepteur et donc la séparation de phase. Une miscibilité trop faible ou trop élevée des matériaux donneurs et accepteurs peut détériorer les performances de l'appareil en formant des phases à grande échelle ou entièrement mixtes. Jusqu'à présent, en raison du manque d'informations quantitatives sur la miscibilité pour obtenir une morphologie optimale, le réglage empirique de la miscibilité est également d'une importance vitale. Dans les OSC ternaires, la sélection d'une molécule hôte appropriée permet de régler efficacement la miscibilité des matériaux hôtes, ce qui facilite ainsi la dynamique des vecteurs de charge photo-générés. Ici, pour collaborer avec le Prof. Gregory C. Welch, un accepteur invité non final (PDI-EH) a été rationnellement conçu et synthétisé pour affiner la miscibilité des matériaux du donneur hôte et de l'accepteur. En outre, une compréhension approfondie de la relation entre la morphologie optimale et la dynamique locale du porteur de charge qui en résulte peut faciliter le développement futur des OSC.

Partie III: Effet synergique de la plasmonique GNRs@PSS en tant que modificateurs interfaciaux arrière sur l'amélioration de l'efficacité des cellules solaires non cylindriques

Les performances photovoltaïques des OSC non cylindriques ont beaucoup progressé. Cependant, leur efficacité est encore inférieure à celle des cellules solaires Si ou pérovskite, principalement en raison de l'épaisseur limitée de la couche active (< 200 nm). La stratégie visant à améliorer l'absorption de la lumière solaire sans augmenter l'épaisseur du film est essentielle pour augmenter davantage les performances photovoltaïques. En outre, la modification interfaciale de la couche active est également cruciale pour optimiser la morphologie de la surface et favoriser le contact interfacial. L'intégration de nanoparticules métalliques plasmoniques sur la couche active en tant que concentrateurs de lumière solaire et modificateurs interfaciaux est un moyen attrayant de répondre simultanément aux exigences ci-dessus, ce qui peut augmenter efficacement

l'absorption de lumière solaire, promouvoir le transport de la charge et réduire la recombinaison de la charge entre la couche active et l'électrode. Ici, en collaboration avec le Prof. Zhonglin Du, les GNR plasmoniques recouverts de polyélectrolyte PSS ont été synthétisés et introduits comme modificateurs interfaciaux arrière dans des OSC non basés sur des cellules afin de poursuivre des performances photovoltaïques élevées.

Résultats

Dans la première partie, un accepteur invité PDI-DPP-PDI non atmosphérique hautement stable a été incorporé dans OSCS basés sur PTB7: $PC_{61}BM$, ce qui pourrait étendre l'absorption spectrale, former une structure en cascade de charge et contrôler la morphologie du donneur/accepteur, comme la montre la **Figure R1**. La combinaison de la caractérisation avancée PiFM et EFTEM/EELS pourrait visualiser la morphologie 3D du film de mélange dans la configuration du dispositif réel. Il a été constaté que l'introduction d'un contenu approprié de la PDI-DPP-PDI était en mesure de supprimer l'agrégation du donneur et de l'accepteur ainsi que de former un niveau plus élevé de la phase mixte moléculaire, comme la montre la **Figure R2 et R3**. En conséquence, le film de mélange ternaire avec une morphologie optimisée avait une mobilité de charge équilibrée et de réduire la recombinaison de charge, résultant en J_{sc}, FF et PCE plus élevés. Les paramètres photovoltaïques des appareils sont indiqués dans le **Tableau R1**. Parallèlement, l'intégration de l'accepteur invité PDI-DPP-PDI hautement stable et une morphologie optimisée ont facilité l'obtention d'une meilleure stabilité de l'air, résistance à l'humidité et photo stabilité des OSC ternaires, comme la montre la **Figure R4**.
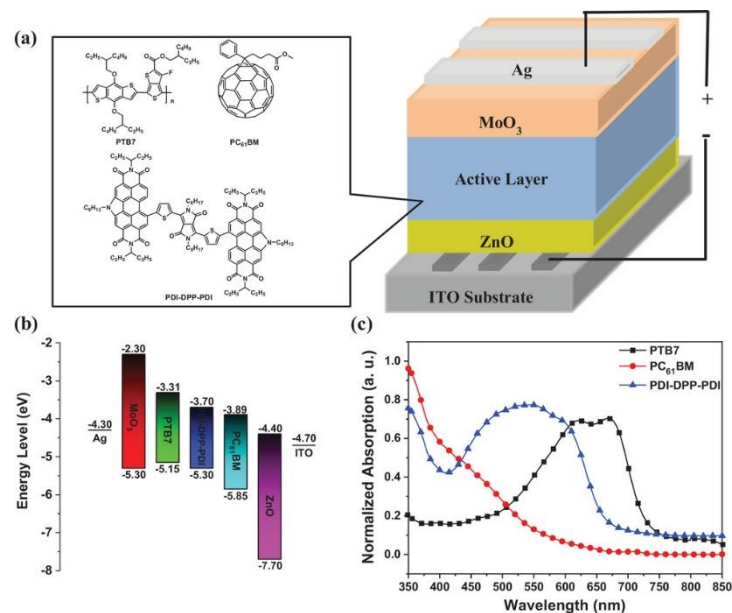
Figure R1 (a) Schéma de la structure chimique des matériaux dans la couche active et de la structure du dispositif. (b) Diagramme du niveau d'énergie des OSC. (c) Spectres d'absorption UV vis normalisés des films PTB7, PC$_{61}$BM et PDI-DPP-PDI.
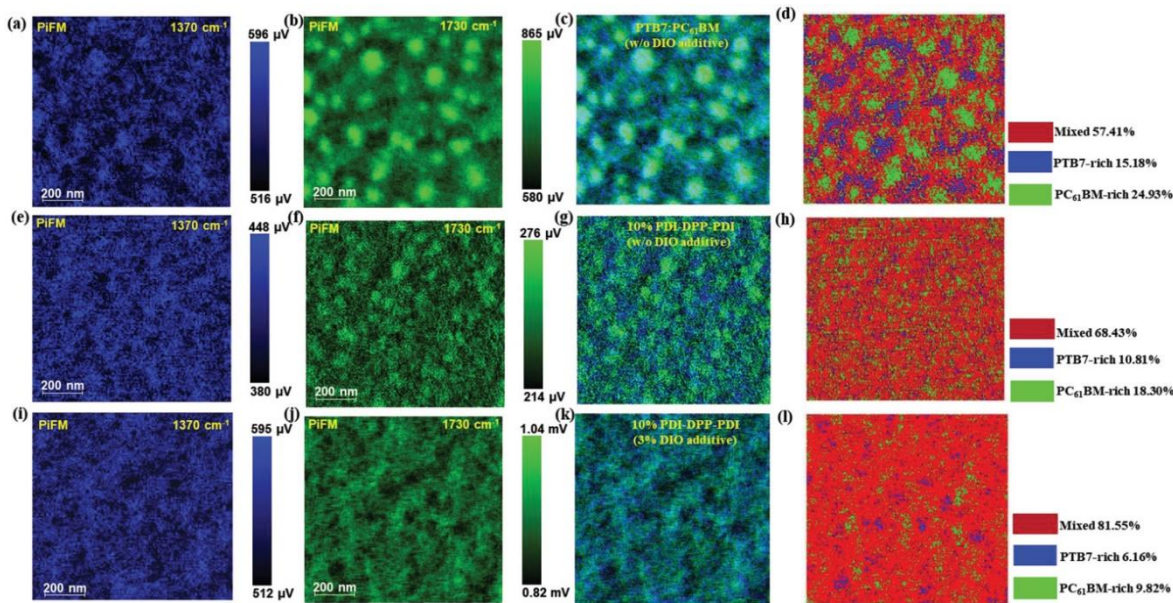
Figure R2 (a, b) Images PiFM de film PTB7: PC$_{61}$BM sans additif DIO, mettant en évidence le donneur PTB7 (1370 cm^{-1}), l'accepteur PC$_{61}$BM (1730 cm^{-1}), et (c) l'image PiFM combinée basée sur (a) et (b). (e, f) Images PiFM de film PTB7:PC$_{61}$BM avec 10 % de PDI-DPP-PDI mais sans additif DIO, mettant en évidence le donneur PTB7 (1370 cm^{-1}), l'accepteur PC$_{61}$BM (1730 cm^{-1}), et (g) l'image PiFM combinée basée sur (e) et (f). (i, j) Images PiFM de film PTB7:PC$_{61}$BM avec PDI-DPP-PDI à 10 % et additif DIO à

3 %, mettant en évidence le donneur PTB7 (1370 cm^{-1}), l'accepteur PC$_{61}$BM (1730 cm^{-1}) et (k) l'image PiFM combinée basée sur (i) et (j). (d, h, l) Images PiFM intégrées et post-traitées basées sur des images PiFM basées sur PTB7 et PC$_{61}$BM utilisant du script Python maison, ce qui a permis la segmentation de différentes régions et les calculs de pourcentage correspondants. Taille de l'image PiFM: 1 μm × 1 μm.
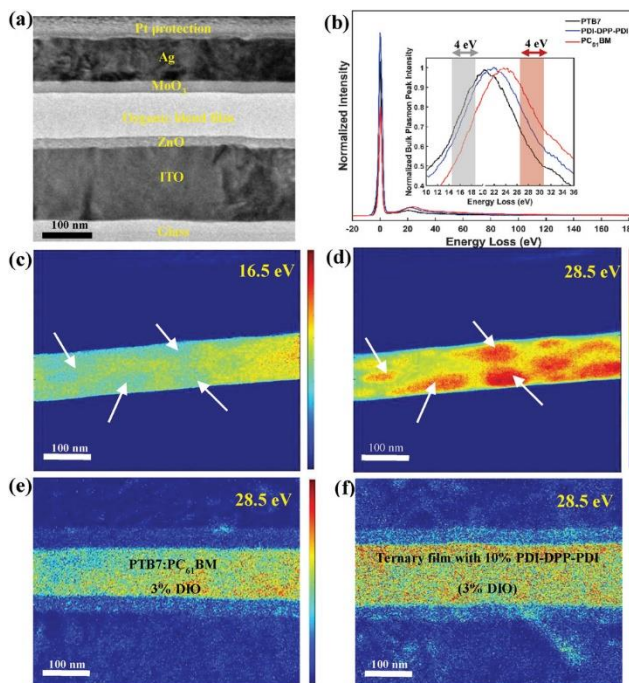
Figure R3 (a) Une image MET typique de la section transversale du dispositif photovoltaïque PTB7: PC$_{61}$BM (la couche active ne montre aucune morphologie de contraste). (b) Les spectres EELS de PTB7, PDI-DPP-PDI et PC$_{61}$BM en couches minces, et les pics de plasmons massifs de référence de PTB7, PDI-DPP-PDI et PC$_{61}$BM à 21, 23 et 24 eV, respectivement, sont indiqués dans l'encadré. (c, d) Images EFTEM transversales d'un dispositif PTB7:PC$_{61}$BM sans traitement DIO (l'épaisseur de lamelle TEM est de 100 nm). La fente a été insérée avec l'énergie centrale réglée à 16.5 et 28.5 eV et la largeur d'énergie à 4 eV pour l'acquisition de ces images, avec deux fenêtres d'énergie mises en évidence par les rectangles colorés coupe de valeur de perte d'énergie en (b) par imagerie spectrale des électrons, et sa largeur d'énergie a été réglée à 4 eV. (e) Images EFTEM de la section transversale du dispositif PTB7: PC$_{61}$BM (avec le traitement DIO) et (f) du dispositif PTB7: PC$_{61}$BM:10 % PDI-DPP-PDI (avec le traitement DIO). Les images normalisées et d'arrière-plan supprimées ont été acquises avec un filtre de 4 eV de large centré à 28.5 eV.

Tableau S1. Paramètres photovoltaïques des cellules solaires inversées binaires et ternaires sous AM 1.5G, 100 mW cm^{-2}

170

Active layer	V_{oc} [V]	J_{sc} [mA cm^{-2}]	FF [%]	PCE $_{max\ (ave)}$ [%][a]
PTB7: PC$_{61}$BM	0.74	15.51	66.80	7.60 (7.45±0.20)
10% PDI-DPP-PDI	0.78	15.95	70.02	8.71 (8.60±0.19)
20% PDI-DPP-PDI	0.80	13.33	64.59	6.85 (6.61±0.22)
30% PDI-DPP-PDI	0.78	12.40	61.52	5.97 (5.55±0.27)

[a] Les valeurs moyennes et les valeurs d'écart type sont obtenues à partir de dix appareils.
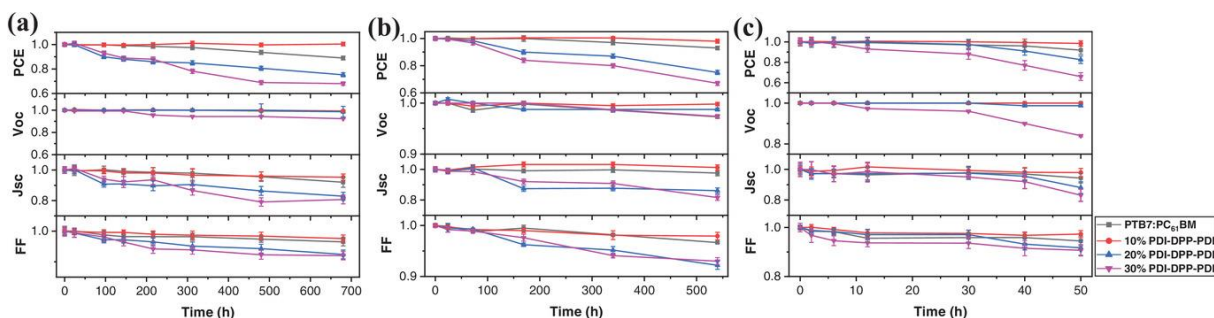
Figure R4 Stabilité des dispositifs encapsulés pour film de mélange binaire et films de mélange ternaire avec différents contenus de PDI-DPP-PDI (10%, 20% et 30%) a) dans l'air, (b) sous humidité de 70%, (c) sous éclairage continu dans l'air. Les paramètres photovoltaïques normalisés et les barres d'erreur ont été obtenus à partir de dix appareils.

Les résultats correspondants dans cette section sont publiés dans l'article suivante:

Ting Yu, Wanting He, Jafari Maziar, Tugrul Guner, Pandeng Li, Mohamed Siaj, Ricardo Izquierdo, Baoquan Sun, Gregory C. Welch, Aycan Yurtsever and Dongling Ma, Three-dimensional nanoscale morphology characterization of ternary organic solar cells, *Small Methods*, 2022, *6*, 2100916.

Dans la deuxième partie, des OSC ternaires basés sur PBDB-T: ITIC-4F avec un accepteur invité non-fullerène PDI-EH à haute torsion ont été appliqués dans des applications photovoltaïques polyvalentes sous des éclairages LED 1 soleil et intérieurs et ont atteint des rendements élevés, comme la montre la **Figure R5**. Le matériel du donneur hôte et de l'accepteur a montré une faible miscibilité, ce qui entraîne une dissociation et un transport de charge indésirables. L'ajustement du contenu de l'accepteur invité PDI-EH pourrait améliorer efficacement la miscibilité, puisque PDI-EH a une bonne compatibilité avec le donneur hôte et l'accepteur pris en charge par les paramètres d'interaction Flory-Huggins et les mesures DSC. On a constaté qu'une miscibilité

modérée du donneur et des accepteurs favorisait la formation d'une phase convenablement mélangée avec un remplissage moléculaire local à courte portée, ce qui résultait en une dynamique porteuse de charge efficace, comme la montre la **Figure R6** et le Tableau R1. En outre, les cartographies nanométriques TP-AFM ont révélé une diminution de la durée de transport de la charge et une augmentation de la durée de vie de la recombinaison de charge et de la durée de diffusion de la charge pour le film de mélange ternaire avec une miscibilité modérée, qui présentait une approche prometteuse pour comprendre la relation entre la morphologie optimisée et la dynamique du porteur de charge local qui en résultait, comme la montre la **Figure R7**. Enfin, les effets synergiques des OSC ternaires avec une absorption accrue des photons, un alignement du niveau d'énergie bien adapté et une morphologie optimisée sont bénéfiques pour la performance photovoltaïque.
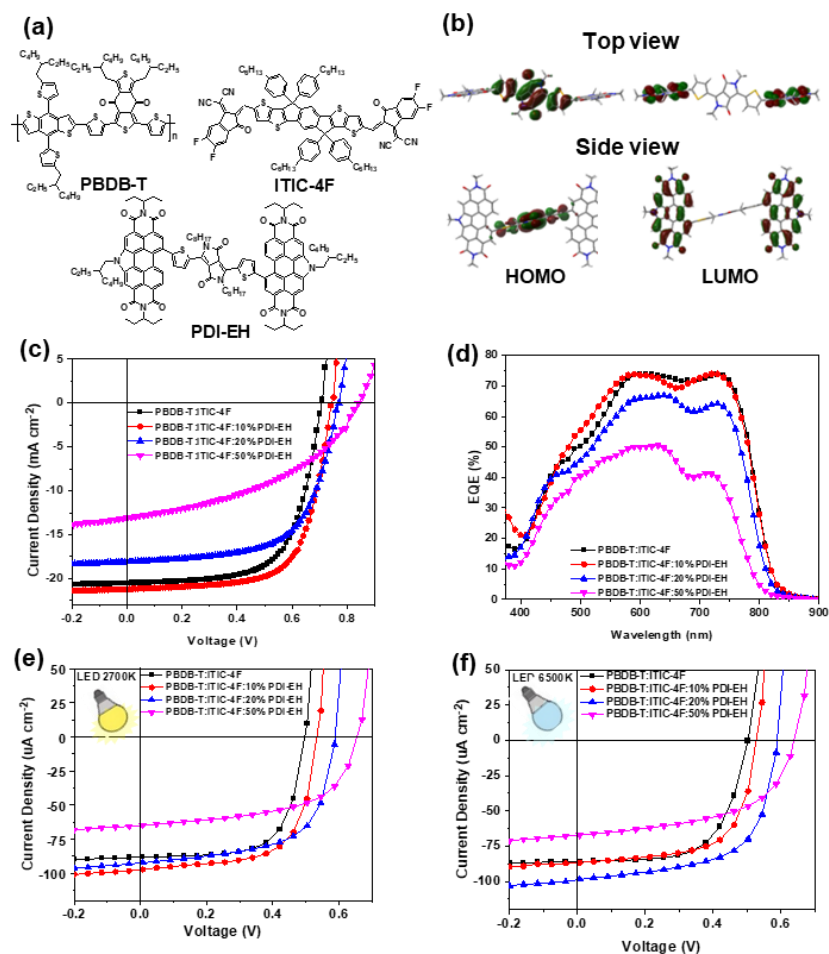
Figure R5 (a) Structures moléculaires de PBDB-T, PDI-EH et ITIC-4F, (b) géométries moléculaires optimisées et niveau HOMO/LUMO de PDI-EH calculé avec DFT au niveau de théorie B3LYP/6-31G(d).

172

Toutes les chaînes latérales alkyles ont été remplacées par des groupes méthyliques, (c) les caractéristiques *J-V* des dispositifs binaires et ternaires PBDB-T: ITIC-4F sous éclairage 1-soleil, et (d) les spectres EQE des dispositifs binaires et ternaires PBDB-T: ITIC-4F. Caractéristiques J-V des dispositifs binaires et ternaires PBDB-T: ITIC-4F (e) sous l'éclairage LED 2700 K et (f) sous l'éclairage LED 6500 K.
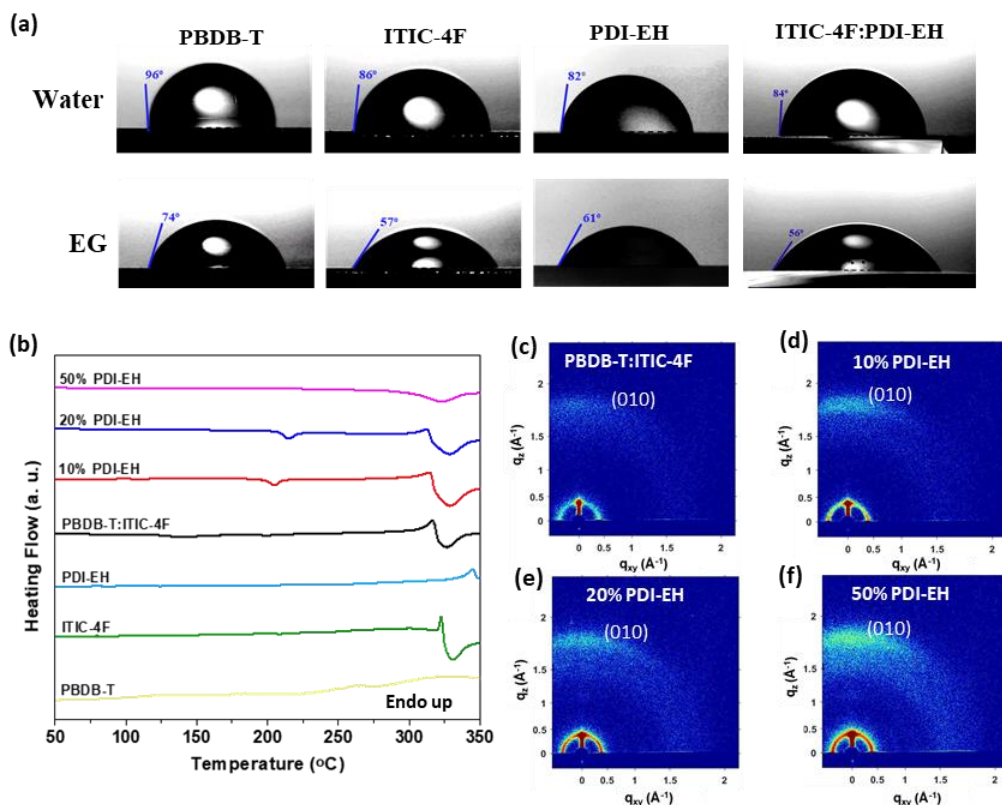
Figure R6. (a) Angles de contact eau et éthylène glycol (EG) sur les films PBDB-T, ITIC-4F, PDI-EH et ITIC-4F: PDI-EH. (b) Les premiers profils chauffants DSC de 50 ºC à 360 ºC de matériaux vierges, de mélange PBDB-T: ITIC-4F et de mélanges ternaires contenant 10 %, 20 % et 50 % de PDI-EH (matériaux vierges, mélanges binaires et ternaires ont été obtenus par coulée en solution de chlorobenzène). Schémas 2D-GIWAXS du film de mélange binaire PBDB-T: ITIC-4F (c), films de mélange ternaire contenant 10 % de PDI-EH (d), 20 % de PDI-EH (e) et 50 % de PDI-EH (f).

Tableau R1 Angles de contact de l'eau et de l'EG sur les films vierges, et paramètres d'énergie de surface connexes

Films	θ_{water} (º)	θ_{EG} (º)	γ (mN m^{-1})[a]	$\chi^{\text{D-A}}$[b]
PBDB-T	96	74	21.1	
ITIC-4F	86	57	32.3	1.21
PDI-EH	82	61	26.6	0.31
ITIC-4F:PDI-EH	84	56	31.5	1.02

a. γ représente les énergies de surface via les données d'angles de contact de l'eau et de l'EG sur ces films.

b. Les paramètres d'interaction Flory-Huggins entre le donneur (PBDB-T) et les accepteurs (ITIC-4F et PDI-EH) ont été calculés selon la formule : $\chi \propto (\sqrt{\gamma_D} - \sqrt{\gamma_A})^2$.
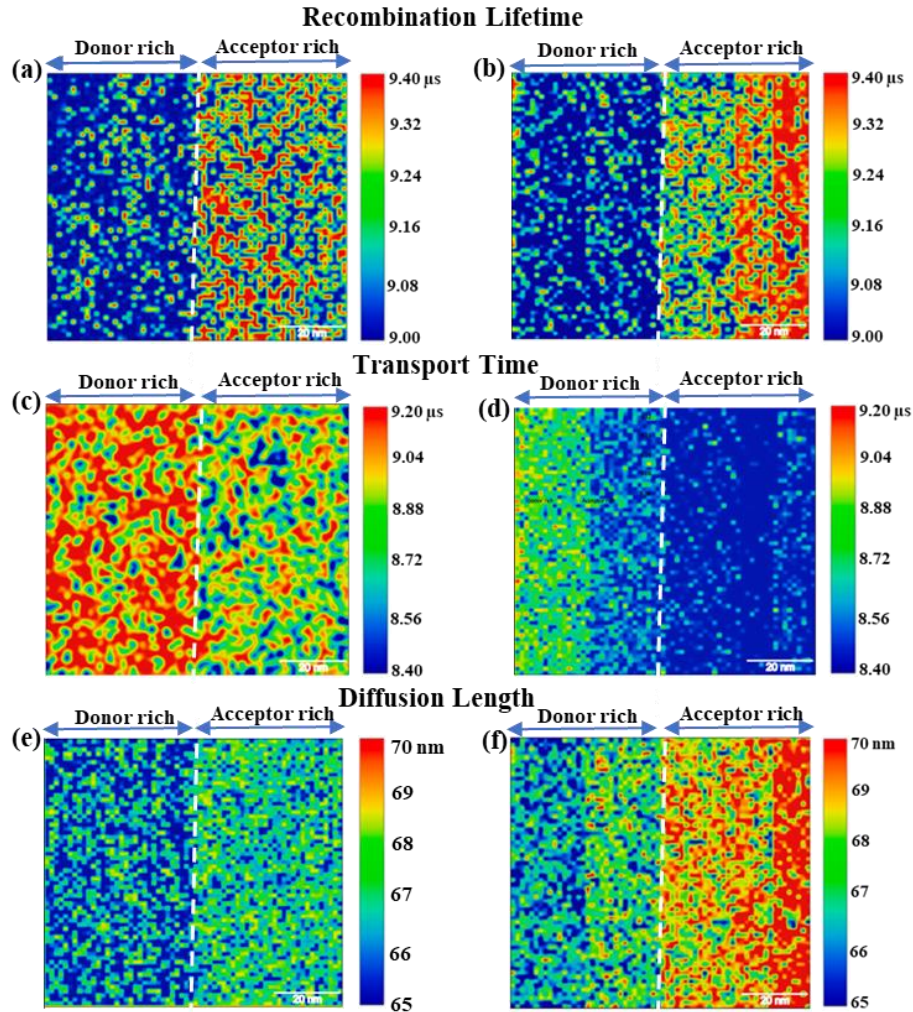
Figure R7 Cartographie TP-AFM à résolution spatiale de la durée de vie de la recombinaison du support de charge pour le film binaire (a) et le film de mélange ternaire contenant 10 % de PDI-EH (d), le temps de transport du support de charge pour le film binaire (b) et le film de mélange ternaire contenant 10 % de PDI-EH (e), et la longueur de diffusion porteuse de la charge pour le film binaire (c) et le film de mélange ternaire contenant 10 % de PDI-EH (f).

Les résultats correspondants dans cette section sont publiés dans l'article suivante:

Ting Yu, Francesco Tintori, Yuchen Zhang, Wanting He, Edward Cieplechowicz, Raja Sekhar Bobba, Poojan Indrajeet Kaswekar, Maziar Jafari, Yuxuan Che, Yong Wang, Mohamed Siaj,

174

Ricardo Izquierdo, Dmytro F. Perepichka, Quinn Qiao, Gregory C. Welch and Dongling Ma, Miscibility driven morphology modulation in ternary solar cells, *J. Mater. Chem. A,* **2023**, *11*, 5037-5047.

Dans la troisième partie, les nanoparticules métalliques, les GNN plasmoniques revêtues de polyélectrolyte PSS, ont été conçues et synthétisées, qui ont été intégrées sur la couche active comme modificateurs interfaciaux arrière dans les OSC non tubulaires pour améliorer les performances photovoltaïques. Comme la montre la **Figure R8**, des mesures EFTEM ont été effectuées pour sonder l'épaisseur d'une enveloppe organique PSS ultramince, ce qui pourrait améliorer le contact interface sans affecter les effets plasmoniques des RNG. En outre, la mesure PiFM a été effectuée pour visualiser l'effet SPR en champ proche des RGN plasmoniques sur la couche active sous un éclairage laser accordable, comme la montre la **Figure R9**. En outre, comme la montre la **Figure R10**, différences finies en 3D FDTD ont révélé l'amélioration du champ en raison de l'effet SPR et de l'effet de rétrodiffusion des GNR plasmoniques, ce qui a entraîné une augmentation de l'absorption de la lumière solaire et de la production d'exciton, comme soutenu par le J_{sc} augmenté, comme la montre la **Figure R10**. Par conséquent, l'intégration de GNRs@PSS sur la couche active pourrait non seulement favoriser la génération et la dissociation d'excitons, mais aussi augmenter le transport de charge et réduire la recombinaison de charge entre la couche active et HTL, conduisant à une amélioration de près de 20% des dispositifs intégrés GNRs@PSS par rapport au dispositif de contrôle, comme la montre le Tableau R2.
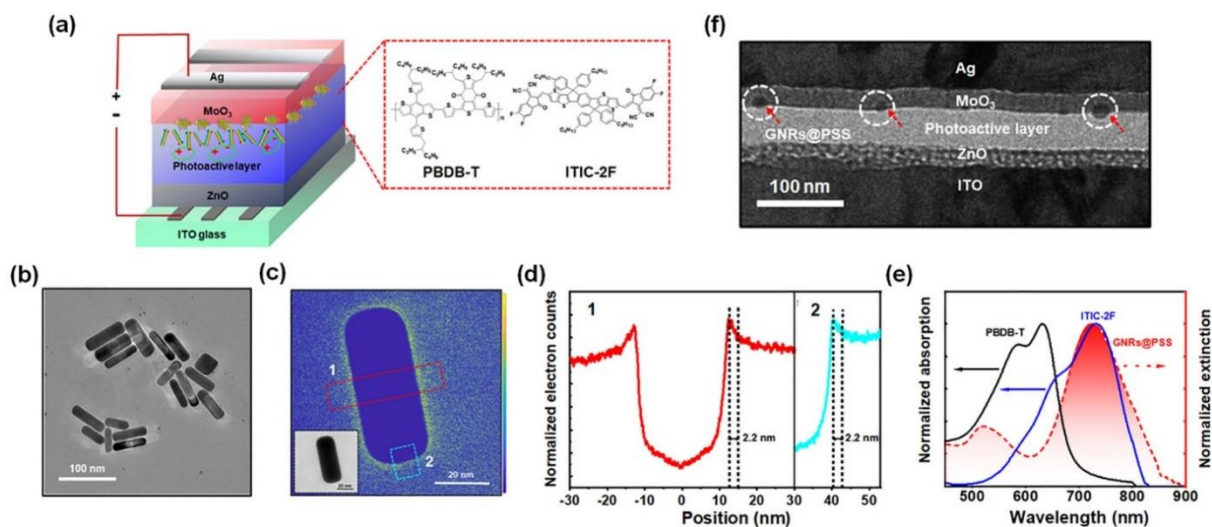
Figure R8 (a) la structure des dispositifs à cellules solaires et la structure moléculaire des matières organiques dans la couche photoactivé. b) Image MET de la synthèse GNRs@PSS. (c) Image EF-TEM du

pic de plasmon en vrac de carbone sur l'unique GNR@PSS, centrée à 25 eV avec une fente d'énergie 10 eV (encart : image EF-TEM grise du même GNR@PSS). (d) Profil des comptages d'électrons normalisés le long des cadres rouge et cyan indiqués en (c), respectivement, indiquant que l'épaisseur uniforme de la coquille de revêtement organique est de ~2.2 (± 0.3) nm. (e) Spectres d'absorption normalisés de PBDB-T (ligne noire) et ITIC-2F (ligne bleue) et spectres d'extinction de GNRs@PSS (ligne rouge), respectivement. (f) Image TEM à champ lumineux de la section transversale du dispositif photovoltaïque, représentant la structure en couches du dispositif de la cellule solaire et des GNR (indiqués par des cercles) à l'interface.
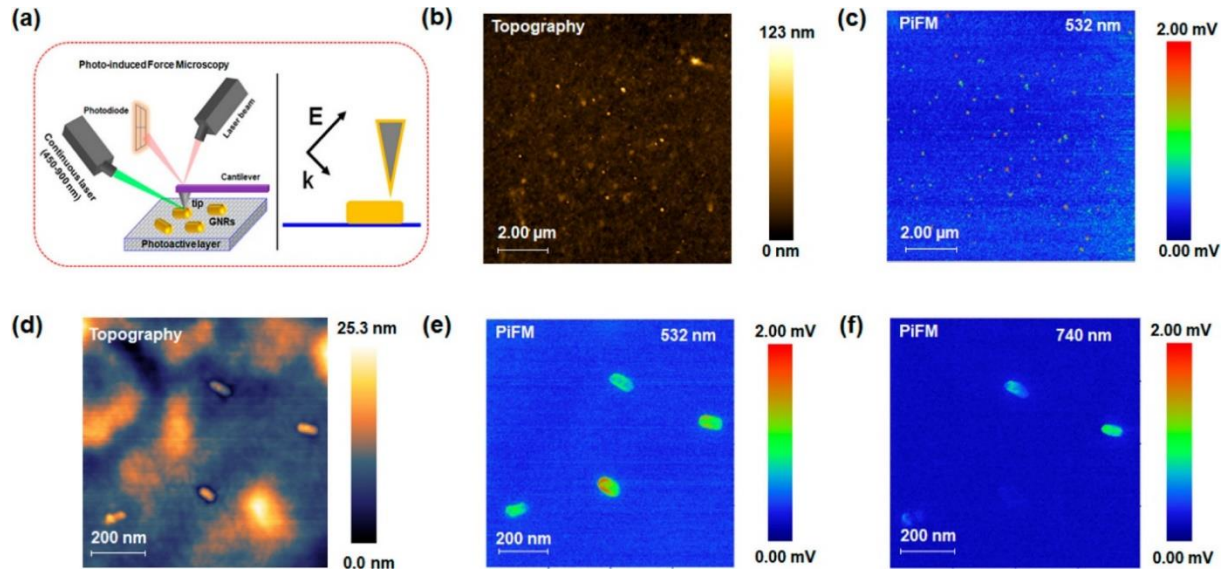
Figure R9 (a) Schéma de la configuration PiFM avec un laser à longueur d'onde réglable en super continuum (450-900 nm). Topographie et (c) images PiFM du GNRs@PSS à la surface de la couche photoactivé sous l'excitation de 532 nm. La topographie et la taille des images PiFM: 10 μm × 10 μm. (d) Topographie agrandie du GNRs@PSS sur la surface de la couche photoactivé avec la taille de la région de 1.0 μm × 1.0 μm. Images PiFM correspondantes sous l'excitation du laser accordable à (e) 532 nm et (f) 740 nm.
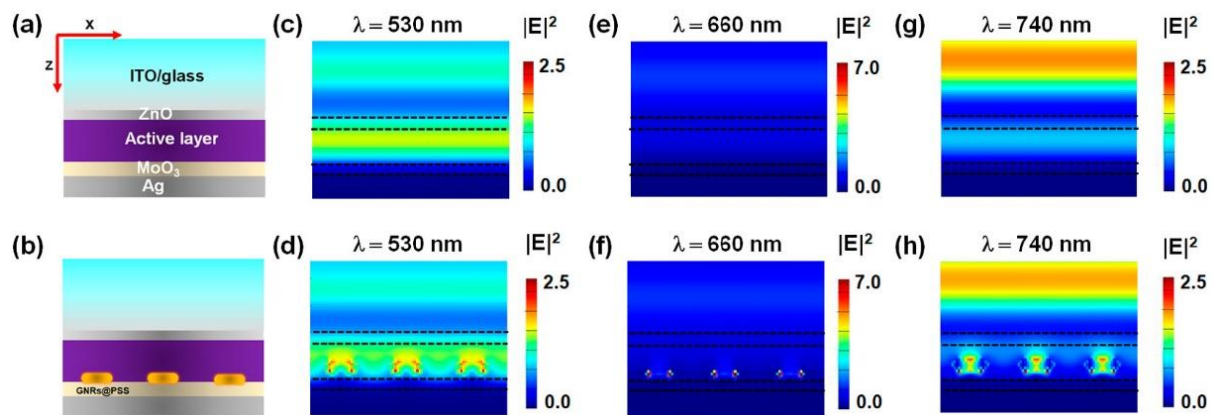
Figure R10 (a, b) Structures du dispositif et (c–h) distribution spatiale normalisée de l'intensité du champ électrique à trois longueurs d'onde différentes (530, 660 et 740 nm) avec et sans intégration GNRs@PSS par simulations FDTD (plan XZ, Y = 0).

Tableau R2 Effets du GNRs@PSS sur les paramètres de performance photovoltaïque extraits des balayages J-V dans des conditions standard AM 1.5 G 100 mW cm^{-2}.

Configuration	J_{sc} (mA·cm^{-2})[a]	V_{oc} (V)[a]	FF (%)[a]	PCE (%)[a]
w/o GNRs@PSS	19.13 (18.54±0.36)	0.686 (0.682±0.005)	64.26 (63.89±0.83)	8.47 (8.33±0.49)
with GNRs@PSS	21.34 (21.08±0.42)	0.702 (0.696±0.004)	67.50 (67.11±0.68)	10.11 (10.02±0.54)

[a]Les valeurs moyennes (entre parenthèses) ont été obtenues à partir de 10 dispositifs.

Les résultats correspondants dans cette section sont publiés dans l'article suivante:

Zhonglin Du[1], Ting Yu[1](co-first author), Wanting He, Aycan Yurtsever, Ricardo Izquierdo, Maziar Jafari, Mohamed Siaj and Dongling Ma, Enhancing efficiency of non-fullerene organic solar cells via using polyelectrolyte-coated plasmonic gold nanorods as rear interfacial modifiers, *ACS Appl. Mater. Interfaces* 2022, *14*, 16185-16196.